Studying galaxy clusters through X-rays and the Sunyaev-Zel'dovich effect: simulations, detection and characterisation

Miriam Elizabeth Ramos Ceja

2016

Studying galaxy clusters through X-rays and the Sunyaev-Zel'dovich effect: simulations, detection and characterisation

Dissertation
zur
Erlangung des Doktorgrades (Dr. rer. nat.)
der
Mathematisch-Naturwissenschaftlichen Fakultät
der
Rheinischen Friedrich-Wilhelms-Universität Bonn

von

Miriam Elizabeth Ramos Ceja

aus

Uruapan, Mexiko

Bonn, 15.02.2016

Dieser Forschungsbericht wurde als Dissertation von der Mathematisch-Naturwissenschaftlichen Fakultät der Universität Bonn angenommen und ist auf dem Hochschulschriftenserver der ULB Bonn http://hss.ulb.uni-bonn.de/diss_online elektronisch publiziert.

1. Gutachter:	Prof. Dr. Frank Bertoldi
2. Gutachter:	Prof. Dr. Thomas H. Reiprich
Tag der Promotion:	08.06.2016
Erscheinungsjahr:	2016

Dedicada a mi Pa’ y Ma’
(Gustavo y Ma. Cruz)

Abstract

Clusters of galaxies are the largest gravitationally-bound objects in the Universe. Thereby clusters are ideal tracers of cosmic expansion and structure formation that allow tight constraints on the average cosmic density of matter and of other fundamental cosmological parameters. Galaxy clusters can be observed over a broad spectral range, in emission from radio wavelengths to X-rays, through their distortion of the cosmic microwave background radiation (the Sunyaev-Zel'dovich Effect), or through their gravitational lensing distortion in the optical appearance of background galaxies. These observables allow detailed measurements of the cluster galaxy populations, of the hot intra-cluster gas, and of the gravitationally dominant dark matter.

This work studies the detection capability and the accuracy of physical constraints derived from present and future X-ray surveys of galaxy clusters. Such imaging-spectroscopy X-ray surveys produce large samples of clusters that allow accurate measures of cosmic structure formation and cosmological parameters only if selection effects are well understood, and the masses of galaxy clusters can be well quantified out to the most distant, i.e. cosmologically earliest, highest-redshift clusters.

In the first part of the thesis, the detection efficiency of galaxy clusters for the upcoming *eROSITA* mission is investigated by means of extensive and dedicated Monte Carlo simulations. Employing a state-of-the-art source detection technique, we determine a cluster detection efficiency based on the cluster fluxes and sizes. Using this *eROSITA* cluster selection function, we found that *eROSITA* will be able to detect a total of $\sim 1.36 \times 10^5$ clusters in the whole sky. This cluster number will allow *eROSITA* to put stringent constraints on the dark matter and dark energy models.

In the second part of the thesis, the galaxy group detection capability of the future *ATHENA* observatory is investigated. The detection of the thermal X-ray emission from the faint and small galaxy groups ($M_{500} \sim 5 \times 10^{13}$ $\mathrm{M}_\odot$) at high redshifts ($z \gtrsim 2.5$) will be accessible only to powerful X-ray telescopes like *ATHENA*. We confirm this assumption by means of detailed simulations. The results confirm that such groups will be detected as extended sources by *ATHENA*, and that the key instrumental parameters are a large effective area (2.1 m^2 at 1 keV) and a good spatial resolution ($\lesssim 10''$).

In the third part of this work, the physical differences between galaxy cluster samples selected in different wavebands are investigated. For this research, $z > 0.8$ mid-infrared (SpARCS) and X-ray (XMM-LSS) selected cluster samples are compared. We show that the X-ray selected clusters have a more compact distribution of the hot gas and galaxies, compared to the mid-infrared selected clusters. Moreover, we found that a sub-sample of the mid-infrared bright clusters have a lack of X-ray emission, making them consistent with non-virialised systems or filamentary structures projected along the line-of-sight.

The final part of the thesis describes a complementary method to probe the baryonic properties of galaxy clusters. The approach consists in constraining the intra-cluster gas pressure model by comparing the predicted thermal Sunyaev-Zel'dovich power spectrum with current Cosmic Microwave Background measurements. We show that a steeper pressure profile in the cluster outskirts, or an evolving gas mass fraction, have mild-to-severe conflicts with the experimental data. It is also shown that the future Sunyaev-Zel'dovich experiments can break the current parameter degeneracies and place simultaneous constraints on the gas pressure profile and its redshift evolution.

The different aspects of the statistical studies based on the galaxy cluster population that we explore in this work, revealed possible sources of uncertainties. These uncertainties deserve careful consideration in order to achieve precision cosmology with future galaxy cluster surveys. Possible routes to improve on this systematics are presented.

List of publications

Chapter 5 is part of the supporting paper:

"The Hot and Energetic Universe: The evolution of galaxy groups and clusters"
Pointecouteau, E., Reiprich, T., [...], **Ramos-Ceja, M. E.**, et al.
2013, URL: http://athena2.irap.omp.eu/IMG/pdf/SP_1.pdf

Chapter 6 will be submitted to MNRAS as:

"Wavelength bias in distant galaxy cluster samples: A case study using the XMM-LSS and SpARCS cluster samples"
Willis, J., **Ramos-Ceja, M. E.**, Pacaud F., Muzzin A.
2016, MNRAS in preparation

Chapter 7 has been published as:

"Constraining the intracluster pressure profile from the thermal SZ power spectrum"
Ramos-Ceja, M. E., Basu, K., Pacaud, F., Bertoldi, F.
2015, A&A, 583, A111

Additional publications that were not incorporated into this thesis:

"The XXL Survey IX: 3 GHz VLA radio observations towards a supercluster at $z = 0.43$"
Baran, N., Smolcic, V., Milakovic, D., Novak, M., Delhaize, J., Gastaldello, F., **Ramos-Ceja, M. E.**, et al.
2015, A&A submitted

"The XXL survey VI. The bright AGN sample"
Fotopoulou, S., Pacaud, F., Paltani, S., Ranalli, P., **Ramos-Ceja, M. E.**, et al.
2015, A&A submitted

"The XXL survey I. Scientific motivations - XMM-Newton observing plan - Follow-up observations and simulation programme"
Pierre, M., Pacaud, F., [...], **Ramos-Ceja, M. E.**, et al.
2015, A&A accepted

"The Hot and Energetic Universe: A White Paper presenting the science theme motivating the Athena+ mission"
Nandra, K., Barret, D., [...], **Ramos-Ceja, M. E.**, et al.
2013, URL: http://x-ifu-resources.irap.omp.eu/PUBLIC/PUBLICATIONS/2013_The_Hot_And_Energetic_universe

Contents

CHAPTER 1

Introduction

Galaxy clusters are the most massive gravitationally bound objects in the Universe. Their study is important as galaxy clusters offer a powerful probe of our cosmological model independent of other methods, such as supernovae type Ia and the Cosmic Microwave Background (CMB). Galaxy clusters have undergone gravitational relaxation and, therefore, are the largest objects whose masses can be measured using independent methods. These measurements allow us to use the observed matter content of clusters and cluster counts at different epochs to constrain the amount of dark matter in the Universe. Moreover, the rate of gravitationally-driven structure formation provides independent constraints on the amount and properties of dark energy in the Universe.

Galaxy clusters are composed of a hot gas called intra-cluster medium (ICM), a galaxy population, and a dark matter halo. These different components offer a unique physical environment in which many relevant astrophysical processes can be extensively studied. For example, galaxy formation and evolution, Active Galactic Nuclei (AGN) feedback, chemical enrichment and non-thermal phenomena. The diverse constituents of galaxy clusters allow them to be studied at different wavelengths: the galaxy population through optical and infrared bands, the ICM in X-rays and via the Sunyaev-Zel'dovich (SZ) effect in sub-millimetre bands, and the dark matter indirectly through the gravitational lensing effect in optical bands.

Multi-wavelength studies of galaxy clusters have come a long way over the past five decades. The first galaxy cluster surveys showed that galaxy clusters are important tracers of cosmic evolution, and many studies thus focus on this aspect. With the advent of high sensitivity and high resolution observing capabilities, deep X-ray and radio observations revealed the complexity of the ICM medium and directed much attention towards detailed studies of the different astrophysical processes in galaxy clusters.

In recent years, a growing number of optical and infrared observations of galaxy clusters at and beyond $z \sim 1$, and the systematic use of gravitational lensing for cluster mass determination have made galaxy clusters important objects that help to constrain the nature of dark matter and dark energy. Recent SZ cluster studies and surveys are enriching and complementing the knowledge of such systems.

Today, the study of galaxy clusters is advancing to cosmological studies with well-defined, large cluster samples. Simple galaxy cluster counts are no longer used for cosmological constraints, but rather cluster samples that are carefully treated by understanding their underlying cluster populations as well as their cluster mass determination and calibration. This has become clear in the recently identified tension between primary CMB and cluster counts constraints on cosmological parameter encountered by the *Planck* collaboration (Planck Collaboration et al. 2014b). Observational bias and the survey strategy must be carefully accounted for in order to provide a sufficiently accurate description of the observed cluster sample (e.g. Mantz et al. 2010a; Pacaud et al. 2015).

Among the observational techniques for the study of galaxy clusters, X-ray imaging is one of the most sensitive and reliable methods to detect and analyse such systems. Todays X-ray missions, such as *XMM-Newton* and *Chandra*, possess a high sensitivity and resolution allowing detailed studies of individual galaxy clusters and the statistical analysis of medium-size cluster samples (hundreds of clusters) up to high-redshifts $z \sim 0.8$ (e.g. Fassbender et al. 2011).

In the near future, a real breakthrough is expected from the new generation of complementary X-ray observatories, specifically the extended ROentgen Survey with an Imaging Telescope Array (*eROSITA*) and the Advanced Telescope for High ENergy Astrophysics (*ATHENA*). *eROSITA* will perform an all-sky survey and detect $\sim 10^5$ new galaxy clusters out to redshift $z = 1$, (Merloni et al. 2012) which will help to constrain cosmological parameters, while *ATHENA* will have better spatial resolution and sensitivity for a detailed exploration of the hot and energetic processes of the Universe out to redshift $z = 1$, and beyond (Nandra et al. 2013).

The above X-ray surveys, together with a series of on-going and planned multi-wavelength cluster surveys, promise an unprecedented amount of galaxy cluster data. To use the observed cluster samples as precision cosmological probes, it is necessary to understand their underlying cluster population and to produce low-bias cluster samples. This cannot be assessed just with observations, but detailed and extensive simulations are required. Therefore, reliable simulators and source properties extraction tools that quantify the differences between observations and theoretical models are needed.

The present thesis work explores the galaxy cluster population that is and will be detected by current and future X-ray missions. The first two chapters give an overview of basic concepts relevant to the studies presented here. Chapter 2 presents an introduction to galaxy clusters and their main components, emphasizing the multi-wavelength signatures of clusters; and the formation and evolution of clusters within the cosmological framework. Chapter 3 provides an introduction to X-ray astronomy, and describes the current and future X-ray missions and the basics concepts of X-ray imaging. This chapter closes with a detailed description of the different X-ray surveys, the determination of the cluster selection function, and a summary of different X-ray image simulators.

Chapter 4 discusses the best methods and strategies to achieve high cluster detection efficiency with future *eROSITA* data. Through extensive and dedicated image simulations, the performance of different source detection algorithms is tested and compared. Furthermore, a 2D cluster selection function, based on source extension and flux, is derived. This provides the means to predict the galaxy cluster population that *eROSITA* will be able to identify.

Chapter 5 addresses the future capabilities of *ATHENA* in detecting high-redshift ($z \gtrsim 2$) galaxy groups. Such capabilities are evaluated through extensive image simulations. Different physically-motivated models are simulated and tested since little is known about the thermo-dynamical state of galaxy groups at high redshifts. Moreover, distinct *ATHENA* instrumental setup models are compared by means of dedicated image simulations. The results of this chapter are part of the supporting paper Pointecouteau et al. (2013), which back up the evolution of galaxy cluster science goals of the *ATHENA* mission (Nandra et al. 2013). In 2014, the *ATHENA* observatory has been chosen as the next generation of Large-class mission in the ESA science programme.

Chapter 6 presents a study of different aspects of wavelength-selection biases in high-redshift galaxy cluster samples. For this, high-redshift $z > 0.8$ mid-infrared (SpARCS) and X-ray (XMM-LSS) selected galaxy cluster samples are used. Two techniques are developed to analyse faint X-ray sources: a Bayesian aperture photometry method and a faint source stacking procedure. Both techniques implement a careful treatment of the Poisson and low-count statistics present in X-ray data. The contents of this chapter are in the process of being submitted. The reference will be Willis, Ramos-Ceja et al. 2016.

Chapter 7 shows how the thermal SZ power spectrum can be used to constrain ICM gas pressure models and other cluster properties. CMB measurements from the South Pole Telescope and Bayesian Markov chain Monte Carlo methods are used to quantify deviations from the standard universal gas pressure model and the agreement between predictions for the thermal SZ power and experimental data. The contents of this chapter have been published in the journal *Astronomy & Astrophysics*. The reference is Ramos-Ceja et al. 2015, A&A, 583, A111.

The main results and conclusions are summarized in the closing Chapter 8.

CHAPTER 2

Galaxy Groups and Clusters

According to the concordance model of cosmology, the structure formation of the Universe is a hierarchical process, where gravity is the main force that assembles large clumps of matter. In this sense, galaxy groups and clusters are the largest gravitationally bound and most recently formed objects of the cosmic structure. They are located at the top level of the large-scale structure of the Universe, which makes them valuable tracers of structure formation and cosmic evolution.

Galaxy groups and clusters are mainly composed of dark matter ($\sim 80\%$*), a hot and highly ionized electron gas (*$\sim 15\%$*), and galaxies (*$\sim 5\%$*). All three components have been slowly gathered and retained by the deep gravitational potential over cosmic times. Since the only direct information from galaxy groups and clusters comes from the baryonic matter, multi-wavelength observations are essential to understand all the different complex physical processes taking place in such objects.*

Galaxy groups and clusters are at the crossroads of cosmology and astrophysics. From a cosmological point of view, these objects are relaxed and virialized, which allows their mass determination. From knowing the mass of such objects helps to understand the structure formation and its evolution, which ultimately helps to constrain and establish the standard model of cosmology. This makes galaxy groups and clusters a complementary cosmological probe. They are also unique astrophysical laboratories where galaxy evolution, thermodynamics of the intra-cluster medium, star formation efficiency, feedback processes, plasma physics, etc., can be studied in great detail.

This chapter briefly reviews the current understanding of the baryonic and dark matter components of galaxy groups and clusters. First, the multi-wavelength observable properties of such systems are described. Then, a brief summary of the current cosmological model is presented. Finally, an explanation of how structure formation and its evolution relates to galaxy groups and clusters is presented.

2.1 Galaxy groups and clusters as astrophysical laboratories

Galaxies are not randomly distributed in the Universe, they tend to group in the so-called galaxy groups and galaxy clusters. Such systems are known as the largest gravitationally bound and relaxed objects in the Universe. Galaxy groups and clusters have evolved from early overdense regions and they have grown under gravitational interaction. They contain from ten to thousands individual galaxies, and the space between such galaxies is filled with huge amounts of hot intra-cluster gas. However, the main component of galaxy clusters is in the form of dark matter. Roughly speaking, galaxy groups and clusters have three main components: dark matter ($80-88\%$), intra-cluster gas ($10-15\%$), and galaxies ($2-5\%$).

The difference between galaxy groups and clusters is not well defined. In the following, general characteristics of both kinds of objects are given. Galaxy groups are the smallest aggregates of galaxies. They typically contain no more than ~ 50 galaxies within a diameter of $\sim 300-800$ kpc. Their total mass is approximately few 10^{12} to few 10^{13} $M_\odot$. The velocity dispersion of the galaxies is about $\sim 100-400$ km/s. On the other hand, galaxy clusters are generally much larger than groups. They contain ~ 50 to $1,000$ galaxies. Their mass is approximately $10^{14}-10^{15}$ $M_\odot$ within a diameter of $\sim 0.8-2$ Mpc. The velocity dispersion of the galaxies is about $400-1000$ km/s. These characteristics show that galaxy groups and clusters are ideal laboratories to study physical processes at large scales, some of which will be explained in the following sections.

In this section, the multi-wavelength properties of galaxy groups and clusters will be briefly reviewed. First, the optical characteristics will be described, putting emphasis on the observables which allow the determination of the galaxy cluster mass. Second, due to the deep gravitational potential where galaxy clusters form, the intra-cluster gas emits strongly in the X-ray waveband. Therefore, the temperature of the gas, as well as its surface brightness, can be determined allowing to study these systems in more detail. Moreover, this hot gas modifies the temperature of the Cosmic Microwave Background radiation, where microwave observations offer another source of information about the state of a galaxy cluster. Finally, for some galaxy clusters, there exists a relativistic population of electrons lying on the intra-cluster gas, which can be observed in radio-frequencies.

2.1.1 Optical properties

Galaxy clusters were first discovered in the optical band as overdensities of galaxies (see the top left panel of Fig. 2.1). They have been recognized as a concentration of galaxies for more than 200 years, but it was not until 1958 that George Abell and collaborators, in a concise and methodological way, built the first cluster catalogues (Abell 1958; Abell et al. 1989). Currently, the optical identification methods of galaxy clusters are an extension and improvement of Abell's basic technique: galaxy cluster members are selected based on their magnitude and colour. This method allows to remove background galaxies more efficiently and to identify high redshift galaxy clusters. The latter because many galaxies in galaxy clusters are redder than other galaxies at similar redshift due to the old population of stars that they contain. By plotting the galaxy colour versus magnitude, the so-called 'red-sequence' plot, the galaxy cluster membership can be determined (Gladders & Yee 2000).

The 'red-sequence' technique has been extensively used in recent years, giving rise to sophisticated red-sequence cluster finder algorithms which also use the cluster redshift information. This information is obtained by either large on-going spectroscopic surveys (e.g. Robotham et al. 2011) or by computing photometric redshift (e.g. Rykoff et al. 2014), which correlate the observed magnitudes with templates of galaxy spectrum to measure the redshift.

Using optical observations, the total mass of a galaxy cluster can be determined by two different methods: measuring the velocity dispersion of the member galaxies, or measuring the proportion of background galaxies affected by gravitational lensing.

Galaxy velocity dispersion

Once a galaxy group or cluster has been optically identified, it is necessary to obtain the radial velocities of the member galaxies. The velocity measurement is based on the redshift of each galaxy, which can be obtained from photometric or spectroscopic observations. Such determination has two purposes: to determine the galaxy membership, and to measure the mass of the galaxy group or cluster. In the former, it is expected that velocity distribution of the cluster members follows a Gaussian since the galaxies are trapped in a common gravitational potential. Therefore, galaxies with velocities falling outside a Gaussian fit are disregarded. If the fit does not follow a Gaussian distribution, then the galaxy cluster candidate is considered as a pure projection effect of different galaxies at different redshift.

As mentioned before, galaxy groups and clusters are gravitationally bound systems, and many of them appear regular and relaxed. Such characteristics allow the use of the virial theorem to calculate the total mass of the systems. The virial theorem states that for a stable, self-gravitating, spherical distribution of equal mass objects (in this case galaxies), the total kinetic energy of the objects is related to the total gravitational potential energy. Then, the total virial mass, $M_{\rm vir}$, of the system is given by

$$M_{\rm vir} = \frac{3 r_{\rm G} \sigma^2}{G}, \tag{2.1}$$

where $r_{\rm G}$ is the gravitational radius assuming a spherically symmetric system, σ^2 is the mass-weighted radial velocity dispersion, and G is the gravitational constant. By using the above relation, Zwicky (1933) was able to determine the mass of the Coma cluster, concluding that the mass of the cluster must be greater than the observed mass in the stars. This discovery represents the first evidence of dark matter in the Universe. Despite the simple approach to measuring the cluster's total mass given by the virial theorem, it is important to note that galaxy groups and clusters are dynamical systems which are undergoing formation and they do not possess a clear size, therefore, they are not in a total steady state.

Gravitational lensing

Nowadays, gravitational lensing represents one of the main methods for galaxy group and cluster mass determination. It was first proposed by Zwicky (1937), and it takes advantage of one prediction of General Relativity: a photon from a background source gets deflected due to a mass concentration, the so-called lens (for a comprehensive treatment of gravitational lensing see Schneider et al. 1993). Such deflection is inversely proportional to the axial distance, i.e. the distortion of the background sources is larger closer to the mass concentration centre than in the edges. Usually, the distortion is seen as a tangential stretching with respect to the projected radius. There exist two main regimes of lensing:

- **Strong lensing**: If the background source is close in projection to the optical axis between the observer and the lens, multiple magnified and distorted images are produced.
- **Weak lensing**: If the alignment between the observer, lens and background sources is not close, slightly distorted single images of the background sources are produced. They must be studied statistically, averaging over many distorted sources. Furthermore, the large-scale structure of the Universe also acts as a weak lens, which is referred to as cosmic shear.

Since not all galaxy clusters present strong lensing effects, the weak lensing regime is more commonly used for mass estimates. In this method, a background galaxy catalogue is created for the galaxy cluster in question. For each background source, the intrinsic ellipticity and gravitational lensing shear is measured. Such measurements are combined to create a shear profile, which is fitted by a model. This model should describe the mass distribution of the system, as a function of radius. Two of the most commonly used models are the singular isothermal sphere (SIS) profile, which is the simplest parameterisation of the mass distribution described as $\rho = \sigma^2/2\pi G r^2$ indicating that the mass of a galaxy group or cluster increases proportionally to r, and the Navarro-Frenk-White profile (NFW, see Section 2.2.2) profile. The accuracy of weak lensing mass estimates is limited by the superposition of mass concentrations along the line of sight.

2.1.2 X-ray properties

As mentioned before, galaxy groups and clusters form in deep gravitational potentials. The majority of the space in such potentials is filled by intra-cluster gas, which is falling towards the centre and, therefore, it is heated to very high temperatures, where it starts to emit in X-ray wavelengths (see the top right panel of Fig. 2.1). Since the majority of the work presented in this thesis is based on X-ray simulations and observations of galaxy groups and clusters, this section will explain their X-ray characteristics in more detail in comparison with their optical counterparts. Further details can be found in the review of Sarazin (1986).

Intra-cluster medium

The hot intra-cluster medium (ICM) is the most massive baryonic component of a galaxy group or cluster. Its mass exceeds the baryonic mass contained in the galaxies by a factor of $\sim 2-7$. The ICM is a hot plasma with very low electron densities of $n_\mathrm{e} \simeq 10^2 - 10^5\ \mathrm{m}^{-3}$ and high temperatures of the order of $T \simeq 10^7 - 10^8$ K, which corresponds to $k_\mathrm{B}T = 1 - 10$ keV. Furthermore, the thermal ICM emission can reach X-ray luminosities of $L_\mathrm{X} \simeq 10^{43} - 10^{45}\ \mathrm{erg\ s^{-1}}$, making galaxy groups and clusters some of the most X-ray luminous objects in the Universe besides Active Galactic Nuclei (AGN). On the one hand, X-ray observations of the ICM enable us to determine the temperature of the ICM, its thermodynamic state and the abundance of elements. On the other hand, the ICM allows studies of hydrodynamical processes, such as shock fronts and propagation, temperature discontinuities, turbulence, etc.

With such high temperatures and low densities that galaxy groups and clusters possess, and with hydrogen being the main component of the ICM, the primary X-ray emission process is thermal bremsstrahlung (free-free). The emissivity at a frequency ν of an ion of charge Z in a plasma with an electron temperature T_e is given by

$$\epsilon_\nu^{ff} = \frac{2^5 \pi e^6}{3 m_\mathrm{e} c^3} \left(\frac{2\pi}{3 m_\mathrm{e} k_\mathrm{B}} \right)^{\frac{1}{2}} Z^2 n_\mathrm{e} n_\mathrm{i} g_{ff}(Z, T_\mathrm{e}, \nu) T_\mathrm{e}^{-\frac{1}{2}} e^{\frac{h_\mathrm{P}\nu}{k_\mathrm{B} T_\mathrm{e}}}, \tag{2.2}$$

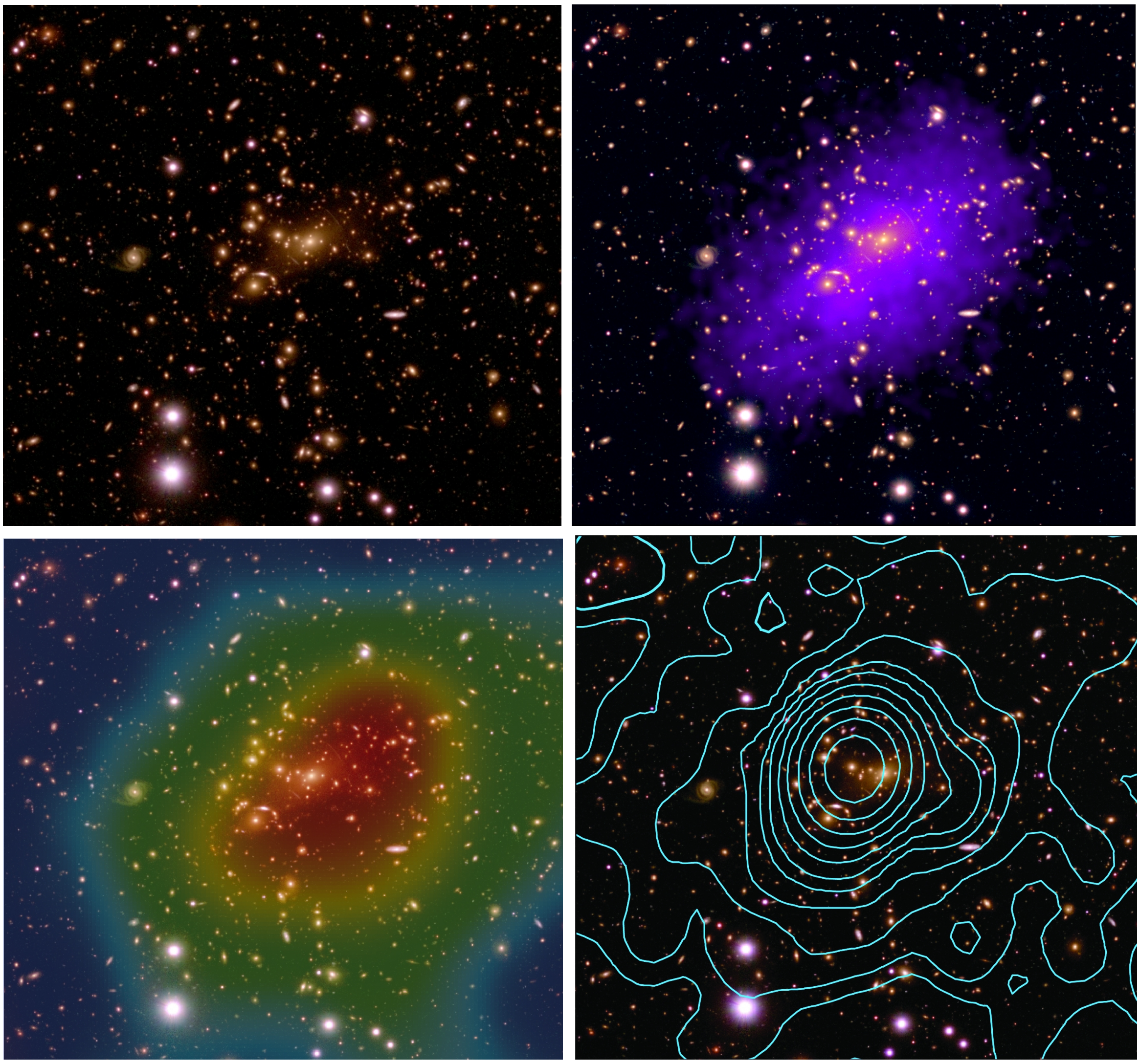

Figure 2.1: Multiwavelength observations of the galaxy cluster Abell 2219. The four panels show a three colour *Subaru* optical image using the Rc, V and B filters, overlaid with: *top right*, *Chandra* X-ray surface brightness (purple); *bottom left*, *CARMA* SZ surface brightness (colours); *bottom right*, radio contours at 1.4 GHz (cyan). Optical image adapted from von der Linden et al. (2014), X-ray image adapted from Canning et al. (2015), and radio contours adapted from Bacchi et al. (2003); SZ image credit: M. Sommer.

where m_e is the electron mass, n_i and Z are the ion number density and charge, respectively. The Gaunt factor $g_{ff}(Z, T_\mathrm{e}, \nu)$ corrects for quantum mechanical effects and for the effect of distant collisions, and is a slowly varying function of frequency and temperature (see Kellogg et al. 1975). h_P and k_B are the Planck and Boltzmann constants, respectively. For low frequencies, $h_\mathrm{P}\nu \ll k_\mathrm{B}T_\mathrm{e}$, the thermal bremsstrahlung spectrum is nearly constant, but for high frequencies, $h_\mathrm{P}\nu \gtrsim k_\mathrm{B}T_\mathrm{e}$, it has a steep exponential cut-off. There exist two other mechanisms of X-ray emission in galaxy groups and clusters: recombination radiation (free-bound emission) and deexcitation radiation (bound–bound emission). The first process also contributes to the continuum radiation spectrum while the latter contributes to line emission. Examples of ICM model X-ray spectra, including bremsstrahlung emission, recombination radiation, and line emission are shown in Fig. 2.2.

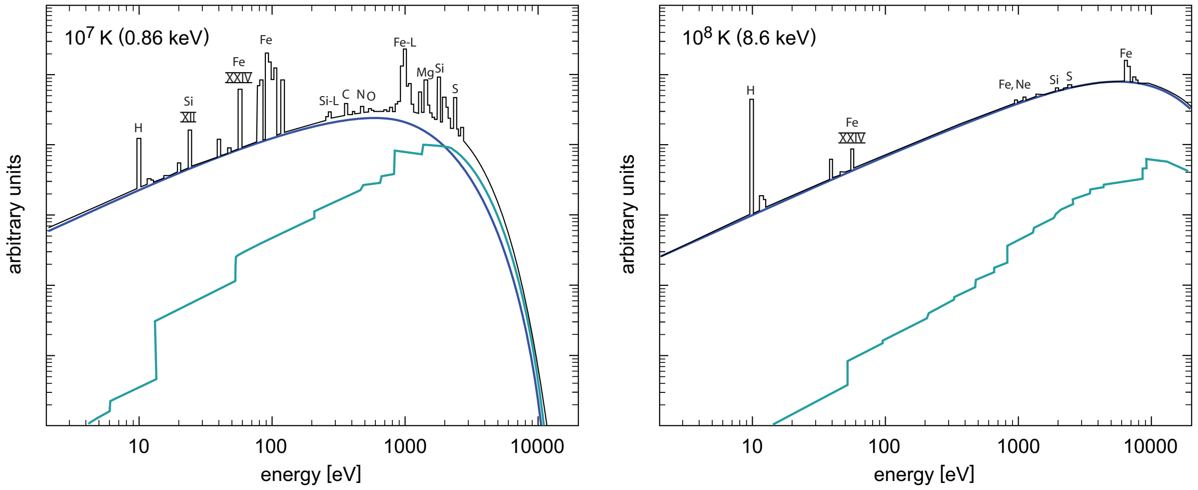

Figure 2.2: X-ray spectra at different plasma temperatures: 10^7 and 10^8 K for left and right panels, respectively. The continuum contributions are shown in blue for bremsstrahlung radiation and in cyan for recombination radiation. Different emission lines are also shown and are labelled according to the elements from which they originate. Image adapted from Böhringer & Werner (2010).

The total integrated (bolometric) emissivity is obtained by integration of Eq. 2.2 over all frequencies:

$$\epsilon_{\rm bol}^{ff} = \int_0^\infty \epsilon_\nu^{ff} {\rm d}\nu = \frac{2^5 \pi e^6}{3 m_{\rm e} h_{\rm P} c^3} \left(\frac{2\pi k_{\rm B}}{3 m_{\rm e}} \right)^{\frac{1}{2}} Z^2 n_{\rm e} n_{\rm i} g_{\rm B}(Z, T_{\rm e}) T_{\rm e}^{\frac{1}{2}}, \tag{2.3}$$

where $g_{\rm B} \approx 1.2$ is calculated by averaging g_{ff} over all frequencies. In the same way, the total luminosity of a galaxy group or cluster is given by integrating the total emissivity over the plasma volume,

$$L_{\rm X} = \int_V \epsilon {\rm d}V. \tag{2.4}$$

Therefore, the X-ray luminosity provides direct observational information of the local electron density in the system.

X-ray surface brightness

The X-ray emission in galaxy groups and clusters is also characterized to be spatially extended rather than point-like (see the top right panel of Fig. 2.1). Such extended emission can be parameterised radially. For this, a number of assumptions have to be made. First, the ICM is assumed to be in hydrostatic equilibrium within the gravitational potential. Then, the ICM can be modelled as an isothermal ideal gas, and the velocity dispersion of the galaxies in the system is considered isotropic. Furthermore, the galaxy density should be described by a King-profile[1], and the system should have spherical symmetry. Following such simplifications, Cavaliere & Fusco-Femiano (1976) proposed a radial parameterisation for the gas density as:

$$\rho_{\rm gas}(r) = \rho_{\rm gas}(0) \left[1 + \left(\frac{r}{r_c} \right)^2 \right]^{-\frac{3}{2}\beta}, \tag{2.5}$$

---

[1] King (1962) showed $\rho(r) \propto [1 + (r/r_c)^2]^{-3/2}$ is an approximation to the inner parts of an isothermal function.

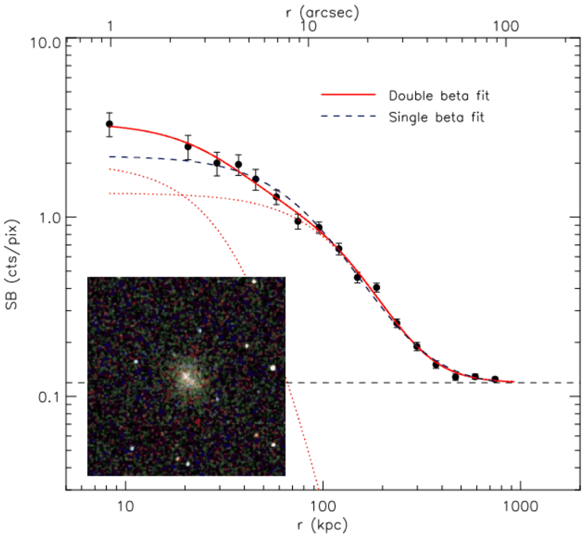

Figure 2.3: Surface brightness profile of a galaxy cluster measured with *Chandra*. The dotted lines indicate the two components of a double β-model fit (red solid line) as the central emission cannot be fitted by a single β-model (blue dashed line). Image adapted from Rosati et al. (2009).

where r_c is a core radius that keeps the profile from becoming singular at the origin, and $\beta = \mu m_\mathrm{p}\sigma^2/k_\mathrm{B}T$ represents the ratio of specific kinetic energies of galaxies and gas. μ and m_p are the mean molecular weight and proton mass, respectively. Such parameterisation is better known as the 'β-model'. In general, r_c determines the characteristic extent scale of the profile, whereas β modulates the overall steepness. By integrating Eq. 2.5 over the volume, the gas mass of the system can be obtained.

The X-ray surface brightness is given by flux, f_X, coming from a solid angle, Ω, of the sky:

$$S_\mathrm{X} = \frac{f_\mathrm{X}}{\Omega} = \frac{L_\mathrm{X}}{\Omega 4\pi D_L^2} = \frac{1}{4\pi\Omega D_L^2}\int_V \epsilon \mathrm{d}V = \frac{A\int_{-\infty}^{\infty}\epsilon \mathrm{d}l}{\Omega 4\pi D_L^2}, \tag{2.6}$$

where the integration is a long the line-of-sight, l. A is the area and D_L is the luminosity distance. It is important to mention that the X-ray surface brightness suffers of 'cosmological dimming', since it has a dependence on the redshift of the source given by $D_L = D_A(1+z)^2$, where D_A is the angular diameter distance. Moreover, since $A = \Omega D_A^2$, then $S_\mathrm{X} \propto (1+z)^{-4}$. This strong dependence on redshift makes the X-ray surface brightness to dim at cosmological distances.

For a typical astrophysical plasma $n_\mathrm{e} \propto n_\mathrm{i}$, the total X-ray emissivity of a galaxy group or cluster is proportional to the square of the electron density. Then, from Eq. 2.6 one obtains $S_\mathrm{X} \propto n_\mathrm{e}^2$. Since $\rho_\mathrm{gas} \propto n_\mathrm{e}$, using Eq. 2.5 the surface brightness is given by

$$S_\mathrm{X} = S_\mathrm{X}(0)\left[1 + \left(\frac{r}{r_c}\right)^2\right]^{-3\beta+\frac{1}{2}}. \tag{2.7}$$

In general, the β-model fits the observed surface brightness well, except for the central part, where it tends to underestimate the central brightness value; and the outer parts, where the gas profile seems to steepen compared to the β-model slope. In such cases it is common practice to fit a 'double β-model', $S_\mathrm{X} = S_{\mathrm{X}_1} + S_{\mathrm{X}_2}$ (see Fig. 2.3).

Gas temperature

The electron temperature of the ICM can be determined by fitting a model to the observed X-ray spectra. The ICM is usually assumed to be in collisional ionization equilibrium, making the ICM electrons and ions to be in thermal equilibrium. Then, the gas temperature is assumed to be equal to the electron temperature.

The determination of the spatial distribution of the ICM temperature is a difficult task to achieve. The main reasons are the limited spatial and spectral resolution, background contamination, etc., that are inherent to X-ray observatories. Observations show two main types of ICM temperature profiles: galaxy clusters with dense ICM cores show a decrement in the temperature profile towards the centre while galaxy clusters with moderate central densities show a flat profile or a slight increment. Such systems are usually referred as cool-core (CC) and non-cool core (NCC) galaxy clusters. CC systems have dense and cool central regions that radiate efficiently in X-rays. These galaxy clusters were long thought to be the result of relaxation from merging events which evolve into a cooling-flow state, i.e. the gas condensates in the central region and then cools through radiative processes (Fabian 1994). However, high-resolution X-ray spectroscopy did not confirm this scenario: the gas was not as cool as predicted (e.g. Peterson et al. 2001). This problem has been investigated, giving as a result the possible existence of a heating mechanism that balances the cooling flow. The most suitable candidate of heating in the ICM s the feedback from AGN in the central galaxy (e.g. McNamara & Nulsen 2007).

The gas temperature of galaxy groups and clusters in hydrostatic equilibrium is related to the total mass of the system. This is derived from the ideal gas equation, $P_{\rm gas} = \rho_{\rm gas} k_{\rm B} T_{\rm gas}/\mu m_{\rm p}$, and the hydrostatic equation for pressure equilibrium,

$$\frac{\mathrm{d}p_{\rm gas}}{\mathrm{d}r} = -\rho_{\rm gas}(r)\frac{GM_{\rm tot}(<r)}{r^2} = \frac{k_{\rm B}}{\mu m_{\rm p}}\frac{\mathrm{d}[\rho_{\rm gas}(r)T_{\rm gas}(r)]}{\mathrm{d}r}. \tag{2.8}$$

Solving for $M_{\rm tot}(<r)$ gives the total hydrostatic mass (total gravitational mass) within a given radius

$$M_{\rm tot}(<r) = -\frac{k_{\rm B}T_{\rm gas}(r)r}{G\mu m_{\rm p}}\left[\frac{\mathrm{d}\ln\rho_{\rm gas}}{\mathrm{d}\ln r} + \frac{\mathrm{d}\ln T_{\rm gas}(r)}{\mathrm{d}\ln r}\right]. \tag{2.9}$$

2.1.3 Microwave properties (Sunyaev-Zel'dovich effect)

The ICM can be also observed in microwave frequencies through the distortion it causes on the Cosmic Microwave Background (CMB) (see the bottom left panel of Fig. 2.1). The CMB radiation has a perfect black body spectrum, which is distorted by the hot electrons of the ICM. This effect was predicted by Sunyaev & Zel'dovich (1972), and it is known as the Sunyaev-Zel'dovich (SZ) effect. The first galaxy clusters observations through this effect were made by Birkinshaw (1991). The SZ effect can be subdivided into the thermal SZ effect and the kinetic SZ effect.

Thermal Sunyaev-Zel'dovich effect

The thermal SZ (tSZ) effect is a small spectral distortion of the CMB spectrum caused by the inverse Compton interaction between the CMB photons and the high-energy electron distribution of the ICM. This interaction boosts the energy of the CMB photon by roughly $k_{\rm B}T_{\rm e}/m_{\rm e}c^2$ per collision, causing a

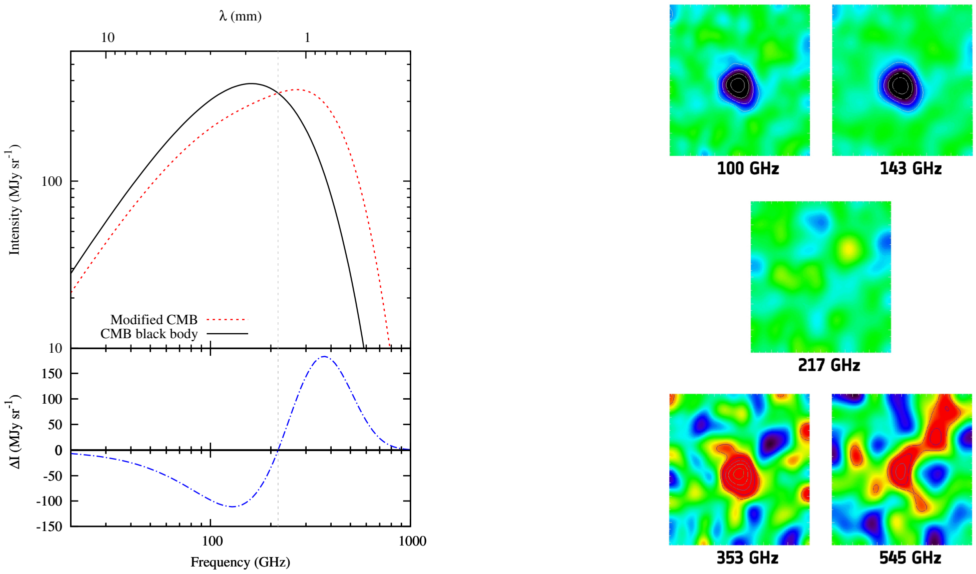

Figure 2.4: *Left*: The CMB spectrum, undistorted (solid line) and distorted by the SZ effect (red dotted line). *Right*: The images show the galaxy cluster Abell 2319 at five different frequencies. The frequency dependence of the SZ effect is clear from the images: at low frequencies the signal is negative (blue), whereas at high frequencies the signal is positive (red) in comparison with the average CMB signal. There is no signal at the null point frequency (217 GHz). SZ images credit: ESA/LFI & HFI Consortia[2].

small ($\lesssim$ 1 mK) distortion in the CMB spectrum (see left panel of Fig. 2.4). The tSZ effect appears as a decrease in the intensity of the CMB at frequencies below ~ 217 GHz and as an increase at higher frequencies (see right panel of Fig. 2.4).

The tSZ spectral distortion on the CMB is usually expressed as a change in the CMB temperature, $\Delta T_{\rm SZ}$,

$$\frac{\Delta T_{\rm SZ}}{T_{\rm CMB}} = f_\nu(x) y = f_\nu(x) \int n_e \frac{k_{\rm B} T_e}{m_e c^2} \sigma_T {\rm d}l, \tag{2.10}$$

where $x \equiv h\nu / k_{\rm B} T_{\rm CMB}$ is a dimensionless frequency, y is the Compton-y parameter, σ_T is the Thomson cross-section, $m_e c^2$ is the electron rest energy, and the integration is performed along the line of sight. The frequency dependence is given by

$$f_\nu(x) = \left(x \frac{e^x + 1}{e^x - 1} - 4 \right) (1 + \delta_{\rm SZ}(x, T_e)) \tag{2.11}$$

where $\delta_{\rm SZ}(x, T_e)$ are the relativistic corrections to the frequency dependence. A comparison of Eq. 2.10 with the ideal gas equation, $P_{\rm e} = n_{\rm e} k_{\rm B} T_{\rm e} / \mu m_{\rm p}$, reveals that the Compton-y parameter is proportional to the integrated pressure along the line of sight. Furthermore, the tSZ effect has a linear dependence on $n_{\rm e}$ compared to the $n_{\rm e}^2$ of the X-ray emission, implying that the tSZ signal is less sensitive to ICM inhomogeneities.

It is important to note that the tSZ is a redshift independent effect. This feature makes the tSZ effect a unique tool for the observation and identification of high redshift galaxy clusters, unlike the X-ray and optical methods.

---

[2] http://sci.esa.int/jump.cfm?oid=47697

When integrating the Compton-y parameter over the projected surface area, the total SZ-signal is obtained

$$Y_{\mathrm{SZ}} = \int y \mathrm{d}\Omega \propto \int n_{\mathrm{e}} T_{\mathrm{e}} \mathrm{d}V \propto M_{\mathrm{gas}} T_{\mathrm{gas}}. \tag{2.12}$$

Y_{SZ} is usually known as the integrated y-parameter, and is directly linked to the galaxy cluster gas mass and temperature, i.e. the total thermal energy of the gas. $M_{\mathrm{gas}} = f_{\mathrm{gas}} M_{\mathrm{tot}}$, is the gas mass, where f_{gas} is the so-called gas mass fraction parameter. Since Y_{SZ} is directly linked to the gas mass and temperature, a tight relation between Y_{SZ} and M_{tot}. However, it needs external data for proper calibration.

Kinetic Sunyaev-Zel'dovich effect

The kinetic SZ (kSZ) effect is due to the motion of a cluster with respect to the CMB rest frame (Sunyaev & Zel'dovich 1980). The kSZ effect acts like a Doppler shift on the CMB photons, and the sign of the distortion depends on the direction of the cluster peculiar velocity with respect to the line of sight. The temperature spectrum of the kinetic effect (ignoring relativistic corrections) is given by

$$\frac{\Delta T_{\mathrm{kSZ}}}{T_{\mathrm{CMB}}} = -\tau_e \left(\frac{v_{\mathrm{pec}}}{c} \right), \tag{2.13}$$

where τ_e is the optical depth of electrons, v_{pec} is the component of the peculiar velocity along the line of sight, and the negative sign indicates that a cluster moving away from us will cause a decrement. It has been suggested that the kSZ can help to measure the peculiar velocity field of galaxy clusters, but the small magnitude of the kSZ effect makes it very difficult to detect. Very recently, the first detections of kSZ have been reported in the literature (Sayers et al. 2013a; Planck Collaboration et al. 2015b).

2.1.4 Radio properties

Some galaxy clusters are known to emit diffuse radio emission that cannot be attributed to single galaxies residing in the system. There are two types of such diffuse emission:

- **Radio haloes** have very low surface brightness and are located at the centre of the galaxy cluster. They appear to have steep spectral index, which makes them distinguishable from a possible distribution of weak radio sources along the line of sight of the cluster ($S_\nu \propto \nu^{-1.2}$), large size (about 1 Mpc, the typical size of a galaxy cluster), and a regular morphology (see bottom right panel of Fig. 2.1).

- **Radio relics** are extended, diffuse emission without any optical counterpart. They also have a steep radio spectrum ($S_\nu \gtrsim \nu^{-1.2}$). However, radio relics are not as extended as radio haloes, they are not centrally located in the galaxy cluster, but in the peripheral regions, and they have an elongated morphology.

Both phenomena are due to synchrotron radiation, but it is not clear where it comes from. One of the most accepted explanations is that the charged particles which produce such radiation, are related to merger events in galaxy clusters. Mergers produce shocks waves which should be effective at amplifying magnetic fields and accelerating charged particles to the necessary relativistic speed for synchrotron emission (e.g. Bonafede et al. 2014).

Individual galaxies in galaxy groups and clusters can emit in radio as well. A radio galaxy is characterized by a *compact radio source*, which is associated with the AGN of its optical counterpart, *radio lobes*, which are extended regions of radio emission located diametrically opposed with respect to and far away from the compact radio source, and *radio jets*, which carry the energy from the compact source out to the radio lobes. However, the hot and dense ICM of galaxy clusters affects the morphology of such radio galaxies. These galaxies are moving at high velocity, v, through the ICM, which causes their radio lobes to be bent by the ram pressure, $P_{\mathrm{ram}} = n_{\mathrm{gas}} v^2$. Depending on the separation angle of such lobes, the radio source morphology can be divided into three types: wide-angle tail (WAT), narrow-angle tail (NAT), and head-tail sources. The detection of such radio morphologies is an indicator of the presence of a galaxy group or cluster.

2.2 Galaxy groups and clusters as cosmological probes

From a cosmological point of view, galaxy groups and clusters are considered as dark matter haloes, which occupy the top level of the cosmic object hierarchy. Numerical simulations have shown dark matter to be an essential ingredient in the formation of cosmic structures. Furthermore, in order to explain the observed properties of galaxy groups and clusters the presence of dark matter and dark energy is necessary. Therefore, galaxy groups and clusters are an important source of information about the underlying cosmological model, making it possible to constrain the value of cosmological parameters and allowing to distinguish between different models that predict distinct structure formation histories and evolution of the Universe.

In this Section, the general framework of the current cosmological model will be briefly reviewed. Then, the main aspects of hierarchical structure formation history will be presented, as well as its growth and evolution. These aspects will get complemented by the description of the abundance and distribution of haloes in the Universe. The mass-observable relations of galaxy groups and clusters will be also introduced. Finally, the current cosmological constraints from galaxy cluster analysis will be summarized. For a comprehensive treatment of the underlying cosmological model see Peacock (1999) and Dodelson (2003).

2.2.1 Cosmological framework

The standard cosmological model is based on the *cosmological principle*: the Universe is homogeneous and isotropic on large-scales. The Theory of General Relativity describes the gravitational attraction between masses as a result of the curvature of space-time induced by matter and energy. To describe the dynamics of the Universe, the theory assumes a space-time described by the Friedman-Lemaître-Robertson-Walker metric. From both assumptions, the Friedman equations are obtained

$$\dot{a}^2 = \frac{8\pi G}{3}\rho a^2 + \frac{1}{3}c^2\Lambda a^2 - kc^2, \tag{2.14a}$$

$$\ddot{a} = -\frac{4\pi G}{3}\left(\rho + \frac{3p}{c^2}\right)a + \frac{1}{3}c^2\Lambda a. \tag{2.14b}$$

Here, $a(t)$ is a time-dependent cosmic scale factor that describes how the Universe is expanding with time (the dots represent time derivatives). By convention, $a(t_0) = 1$ today, where t_0 is the age of the Universe at current epoch ($z = 0$). ρc^2 is the mean density of mass-energy of the Universe, p is the pressure of the energy density, Λ is Einstein's cosmological constant, and k is the space-time curvature constant. The current concordance model is known as the Lambda Cold Dark Matter (ΛCDM) model, and establishes that the Universe is composed of radiation, baryonic matter, *dark matter*, which is a type of matter assumed to be non-collisional and non-baryonic, and *dark energy*, a form of energy density with negative pressure responsible for the current cosmic acceleration of the Universe.

The first Friedman equation (Eq. 2.14a) defines the expansion rate of the Universe

$$H(t) = \frac{\dot{a}(t)}{a(t)}. \tag{2.15}$$

This is commonly known as the *Hubble parameter*. This parameter can be measured from different cosmological probes, the most recent measurement by the *Planck* mission gives $H(t_0) = H_0 = 67.74 \pm 0.46$ km s^{-1} (Planck Collaboration et al. 2015a). H_0 is known as the Hubble constant and is often written as a dimensionless parameter $h = H_0/(100 \text{ km s}^{-1} \text{ Mpc})$.

By assuming that the total energy density ρc^2 follows an equation of state of a perfect fluid, $p = w\rho c^2$, the density of each major energy density components changes with the expansion as $\rho(a) = \rho_0 a^{-3(1+w)}$. The non-relativistic baryonic and dark matter density, ρ_m, components contribute with a negligible pressure, corresponding to $w = 0$. The radiation energy density, ρ_r, exerts a pressure with $w = 1/3$, and the dark energy density, ρ_Λ, remains constant as the Universe is expanding, exerting a pressure $w = -1$. The most general form of dark energy allows for a time evolution of the equation of state, $w(z)$, but in this work the constant value of w is preserved as stated by the ΛCDM model.

The second Friedman equation (Eq. 2.14b) shows that the geometry of the Universe, given by the curvature k, is closely related to the total energy density. In the case of a flat Universe ($k = 0$), a precise relation is obtained for the energy density

$$\rho_\mathrm{cr}(t) = \frac{3H^2(t)}{8\pi G}. \tag{2.16}$$

This quantity is known as the *critical density* of the Universe. At present time ($t = 0$), the current total density is $\rho_\mathrm{cr} \approx 2.775 \times 10^{11}\, h^2\, \mathrm{M}_\odot\, \mathrm{Mpc}^{-3}$.

The individual energy densities can be transformed into dimensionless parameters by stating them in units of the critical energy density ρ_cr. These density parameters are:

$$\Omega_\mathrm{m} \equiv \frac{\rho_\mathrm{m}}{\rho_\mathrm{cr}}; \quad \Omega_\mathrm{r} \equiv \frac{\rho_\mathrm{r}}{\rho_\mathrm{cr}}; \quad \Omega_\Lambda \equiv \frac{\rho_\Lambda}{\rho_\mathrm{cr}} = \frac{\Lambda}{3H_0^2}. \tag{2.17}$$

Then, the total energy density and the curvature of the Universe can be expressed as

$$\Omega_0 = \Omega_\mathrm{m} + \Omega_\mathrm{r} + \Omega_\Lambda, \tag{2.18a}$$
$$\Omega_k = 1 - \Omega_\mathrm{m} - \Omega_\mathrm{r} - \Omega_\Lambda. \tag{2.18b}$$

Ω_m is the total matter density, which can be divided into Ω_b and Ω_c for the baryonic and dark components, respectively. Ω_Λ is the dark energy density, and together with Ω_m are the dominant energy density components in the current Universe. The radiation term, Ω_r is negligible today, but it has an important role at early epochs ($z \gtrsim 1000$). Eq. 2.18b is a dimensionless formulation of the first Friedman equation (Eq. 2.14a) at $z = 0$.

Making use of the definitions in Eq. 2.18, the expansion equation 2.14a becomes

$$H^2(z) = H_0^2 E^2(z) = H_0^2[\Omega_\mathrm{m}(1+z)^3 + \Omega_\mathrm{r}(1+z)^4 + \Omega_\Lambda + \Omega_k(1+z)^2], \tag{2.19}$$

where the scale factor has been rewritten in terms of the observable redshift $a = (1+z)^{-1}$, and $E(z)$ is the cosmic evolution function. Therefore, the understanding of the current cosmological model, and consequently galaxy groups and clusters, depends on the determination of a defined set of parameters, which describe the geometry of the Universe, the mean density of its components, and the initial density perturbations (to be explained in the next section). The latter are the seeds of the cosmic objects in the Universe. The most recent determination of the density components has been done by the *Planck* mission: $\Omega_\mathrm{m} = 0.3089 \pm 0.0062$ and $\Omega_\Lambda = 0.6911 \pm 0.0062$ (Planck Collaboration et al. 2015a). This indicates that the current epoch in the Universe is dominated by the dark energy density.

2.2.2 Cosmic structure formation

At scales smaller than $\sim$ 100 Mpc, the present day Universe is not homogeneous. This implies that, even at early epochs, perturbations to the homogeneous Universe must have existed. A full description of the growth of the initial density perturbations is out of the scope of this thesis. Thus, a very brief and qualitative explanation of such perturbations is presented at first, followed by a more detailed description of the collapse of the density perturbations, which are the seeds of the current galaxy groups and clusters.

Linear growth of density perturbations

In the very early Universe, quantum fluctuations where the seeds of the initial density fluctuations. An early inflation phase (Guth 1981; Linde 1982) is thought to have increased these quantum fluctuations to macroscopic scales. Such an inflation period would also permit to explain how the Universe came to be homogeneous on scales larger than the causality radius in the primordial Universe.

The primordial density field is characterized by the density contrast (or overdensity) field: $\delta(\mathbf{x}) = (\rho(\mathbf{x}) - \bar{\rho}_\mathrm{m})/\bar{\rho}_\mathrm{m}$, where ρ_m is the mean density. By modelling the Universe as a multicomponent fluid in the early epochs, the evolution of such system is described by the standard equations of a self-gravitating medium: the continuity equation, describing the mass conservation, the Euler equation, characterizing the momentum conservation, and the Poisson equation, which includes the gravitational potential and the dark energy in form of a cosmological constant. Using such equations and assuming small perturbations, the *linear* evolution of the density contrast is given by

$$\ddot{\delta} + 2H\dot{\delta} = \delta\left[4\pi G\bar{\rho}_\mathrm{m} - \frac{c_\mathrm{s}^2 k^2}{a^2}\right]. \tag{2.20}$$

Here, c_s is the speed of sound. In this equation, the Hubble parameter acts as a friction force, the so-called Hubble drag, and suppress the growth of δ. The right-hand side of the equation describes the conflict between pressure support and gravity.

The solution to Eq. 2.20 is of the form: $\delta(x,t) = \delta_+(x,t_i)D_+(t) + \delta_-(x,t_i)D_-(t)$, where D_+ and D_- describe the growing and decaying modes of the density perturbation, respectively. The latter solution is of little physical interest and is ignored. For a ΛCDM model, the expression for D_+ is given by

$$D_+(z) = \frac{2}{5}\Omega_\mathrm{m}E(z)\int_z^\infty \frac{1+z'}{E^3(z')}dz'. \tag{2.21}$$

Such parameter is known as the linear growth factor, and it is very sensitive to the cosmological parameters enclosed in $E(z)$ (see Eq. 2.19). Therefore, any observable quantity that measures the evolution of density perturbations with redshift is a sensitive probe of the underlying cosmological model and complements the knowledge from other cosmological tests.

Spherical collapse

Galaxy group and cluster formation can be explained by the spherically symmetric collapse model. This simplest model of non-linear collapse, the so-called *top-hat model*, assumes a spherically symmetric matter density fluctuation of low amplitude embedded in a background field with constant mean density and a given expansion rate. According to Birkhoff's theorem, a closed sphere within a homogeneous medium can evolve independently of its surroundings. Thus, the collapse of the perturbation can be conceived as a two steps process: first, the perturbation expands up to a maximum radius until the turnaround epoch. Then, the perturbation detaches from the general Hubble expansion due to its own gravitational pull, and its radius starts to decrease until the fluctuation collapses, virializes and settles in a final radius (see Fig. 2.5).

In the case of an Einstein-de Sitter cosmology model (i.e. $\Omega_\mathrm{m} = 1,\ \Omega_\Lambda = 0$), the final overdensity at the time of equilibrium has a value of

$$\Delta_\mathrm{vir} \equiv \frac{\rho_\mathrm{coll}}{\bar{\rho}_\mathrm{m}} = 18\pi^2 \simeq 178, \tag{2.22}$$

where ρ_coll is the mean density of the perturbation once it has collapsed. For different values of Ω_m and Ω_Λ, the overdensity can be computed in a similar way from ρ_coll and $\bar{\rho}_\mathrm{m}$ at the time of collapse. It is important to emphasize that such overdensity is widely used in the definition of the *virial radius*, r_vir, of galaxy groups and clusters. Since such systems do not have a well-defined boundary. Their total mass, obtained from optical, X-ray or SZ measurements (e.g. Eqs. 2.1 and 2.9), is usually defined within the radius r_vir, where the average galaxy cluster density is equal to a given overdensity with respect to the critical density at the galaxy cluster redshift z (see Section 2.2.4),

$$M_\Delta = \frac{4\pi}{3}r_\Delta^3\Delta\rho_\mathrm{cr}(z). \tag{2.23}$$

Usually, $\Delta = 200$ is used to express the radius of a virialized galaxy cluster. The linear extrapolation of the density contrast at the virialization time gives $\delta_\mathrm{c} \equiv \delta_+(t_\mathrm{vir}) \simeq 1.69$, which defines the overdensity that a perturbation in the initial density field must have to end up in a virialized structure.

Although the top-hat collapse model gives significant insights of galaxy group and cluster formation process, it is based on simplified assumptions (spherical symmetry, homogeneous mass distribution). Moreover, with more detailed gravitational dynamics the above analytical solutions become too complicated. Therefore, the only alternative is the use of three-dimensional numerical cosmological simulations to explore the properties of the cosmological model in the non-linear regime.

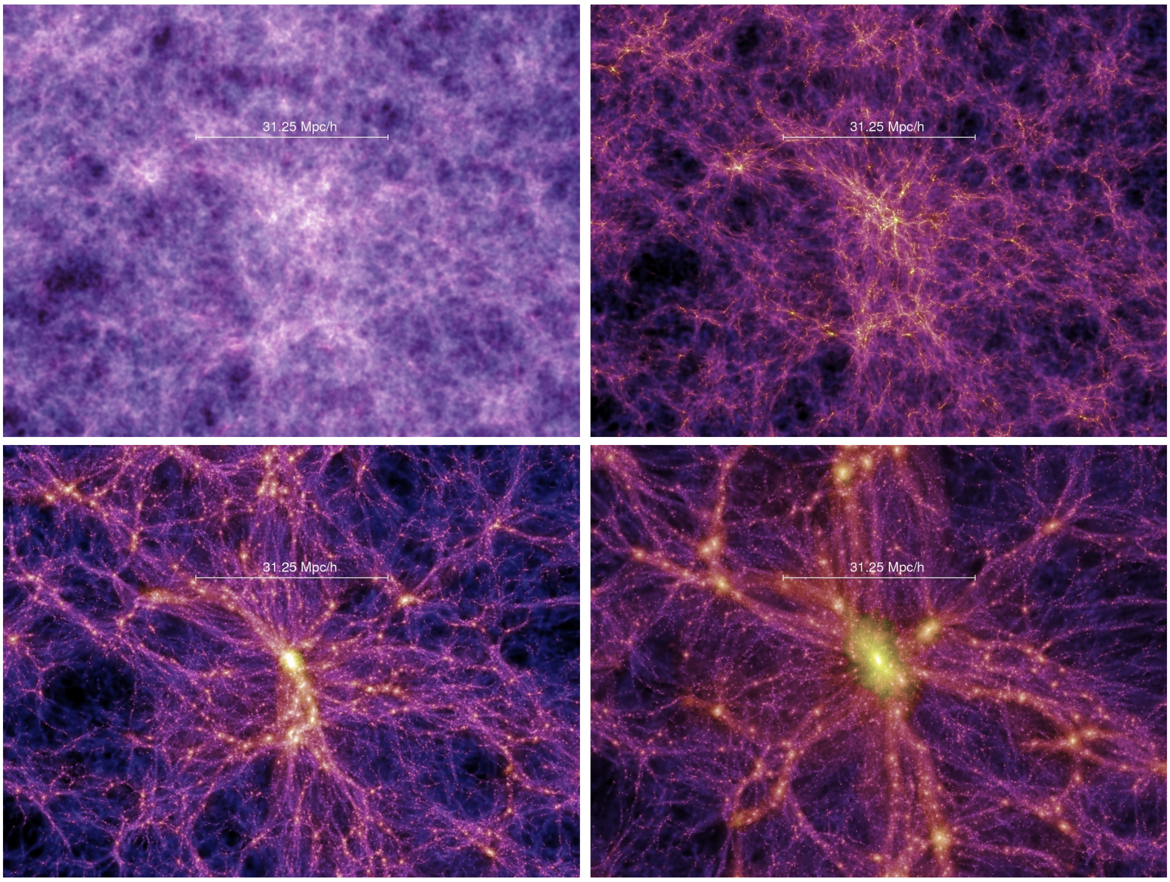

Figure 2.5: Snapshots of the Millennium simulation showing the dark matter distribution for four different redshifts, $z = 18.3$ (*top left*), $z = 5.7$ (*top right*), $z = 1.4$ (*bottom left*), and today, $z = 0$ (*bottom right*). The significant increase of structure is clearly seen as redshift increases, i.e. at high-z the dark matter use to be homogeneously distributed, but already had some density fluctuations, which were the seeds of future collapsed structures at low-z. Furthermore, this figure illustrates the complexity of the collapse process, since there exist strong deviations from spherical symmetry. Figure adapted from Springel et al. (2005).

The largest numerical simulations have been able to simulate only dark matter, since gravity is the only force that needs to be modelled (e.g. Virgo consortium, Jenkins et al. 1998; Millennium simulation, Springel et al. 2005). Simulations including baryons, hydrodynamical simulations, need to model the gas physics and radiation processes, which are more complicated to replicate (e.g. Magneticum Pathfinder simulation, Dolag et al. in preparation). The results of simulations are compared with observations in order to test different models, i.e. simulations help to distinguish between models that reproduce the observations and the ones that do not.

All this analysis and numerical modelling have provided a hierarchical view of galaxy group and cluster formation (see Fig. 2.5): small-mass collapsed objects are the first pieces to detach from the Hubble flow and undergo gravitational relaxation. Then, these small objects merge with others to form progressively larger virialized structures.

Structure of dark matter haloes

The properties of dark matter haloes in which the galaxy groups and clusters form, have been extensively investigated by numerical simulations. Navarro, Frenk & White (1997) found a universal dark matter halo density profile for virialized objects within the ΛCDM cosmological model. This model is known as the NFW profile, and is widely used to model the density profile of dark matter haloes,

$$\rho_{\rm NFW}(r) = \frac{\rho_{\rm s}}{x(1+x)^2}. \tag{2.24}$$

Here $x \equiv r/r_{\rm s}$, $r_{\rm s}$ being the scale radius at which the logarithmic slope of the profile is equal to -2, and $\rho_{\rm s}$ is the characteristic density at $r = r_{\rm s}$. At small radii, $r \ll r_{\rm s}$, the NFW profile has a *cusp* associated with the inner slope $\rho_{\rm NFW}(r) \propto r^{-1}$, whereas at larger distances, $r \gg r_{\rm s}$, the density follows $\rho_{\rm NFW}(r) \propto r^{-3}$. Optical and X-ray observations agree on this profile representation (e.g. Pointecouteau et al. 2005).

2.2.3 Halo mass function

Since the formation and evolution of individual galaxy groups and clusters cannot be observed given the cosmological time scales that such processes take, it is common to study the statistics of the population of such systems as a function of redshift in order to understand their evolution. Given the close relation between cosmological parameters and the formation and evolution of galaxy groups and clusters, constraints on the cosmological model can be established by observations of these objects. The distribution of dark matter haloes is termed the *halo mass function*, and it provides the number density of dark matter haloes, $n(M, z)$, for a given mass at a given redshift. Since galaxy groups and clusters form and evolve together with such haloes, the function can also be interpreted as a galaxy cluster mass function (see Fig. 2.6).

The first model for the halo mass function was developed by Press & Schechter (1974). Such model relates the mass function of objects resulting from non-linear collapse to the statistical properties of the initial linear density contrast field, by calculating the probability that such overdensity will collapse into a halo of a given mass. Thus, the halo mass function can be derived as a fraction of the total volume collapsing into halos of mass M, divided by the comoving volume occupied by each such halo within the initial density field ($M/\bar{\rho}_{\rm m}$):

$$\frac{{\rm d}n(M,z)}{{\rm d}M} = \frac{\bar{\rho}_{\rm m}}{M} g(M,z), \tag{2.25}$$

where $g(M, z)$ is given by the assumptions of the collapse model. Numerical simulations have shown that the shape of $g(M, z)$ predicted by Press & Schechter (1974) deviates by $\gtrsim 50\%$ when compared with the simulations results (e.g. Jenkins et al. 2001). Nowadays the halo abundance is measured and calibrated from large cosmological simulations.

Sheth & Tormen (1999) generalized the expression for the halo mass function in terms of the scaled differential mass function $f(\sigma, z)$, which is given by

$$f(\sigma,z) = \frac{M}{\bar{\rho}_{\rm m}} \frac{{\rm d}n(M,z)}{{\rm d}\ln\sigma^{-1}(M,z)}. \tag{2.26}$$

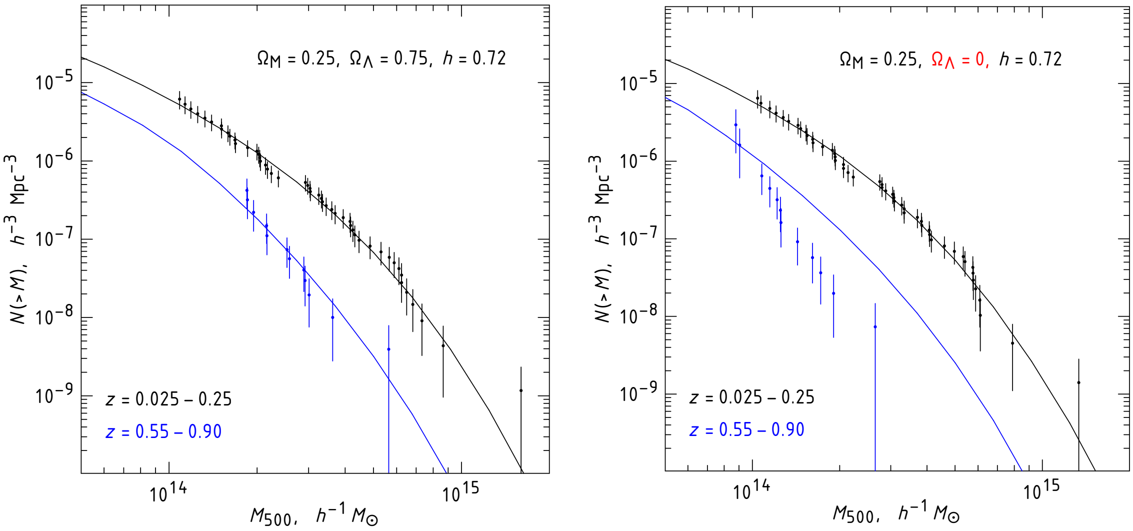

Figure 2.6: Illustration of the sensitivity of the cluster mass function to the cosmological model. *Left panel*: the measured mass function and predicted models are shown for two redshift bins. *Right panel*: same as the right panel, but now the data and the models are computed for a cosmology with $\Omega_\Lambda = 0$. In this case the predicted number density of $z > 0.55$ clusters is in disagreement with the data, and therefore this cosmological model ($\Omega_\Lambda = 0.25$ and $\Omega_\Lambda = 0$) can be rejected. Image adapted from Vikhlinin et al. (2009b).

Here $\bar{\rho}_\mathrm{m} = \rho_\mathrm{cr}\Omega_\mathrm{m}$ is the mean matter density at $z = 0$, and $\sigma(M, z)$ is the variance of the linear density field. Then, the halo mass function is given by,

$$\frac{\mathrm{d}n(M,z)}{\mathrm{d}M} = \frac{\bar{\rho}_\mathrm{m}}{M}\frac{\mathrm{d}\ln\sigma^{-1}(M,z)}{\mathrm{d}M} f(\sigma, z). \tag{2.27}$$

This definition of the halo mass function does not explicitly depend on redshift, power spectrum, or cosmology, all of these are encapsulated in $\sigma(M, z)$, which will be explained more in detail, before presenting a functional form of $f(\sigma, z)$.

It is required that the spatial average of the density contrast, satisfies $\langle\delta(\mathbf{x}, z)\rangle = 0$. By assuming that the initial density field is described by a Gaussian distribution, the mean, together with variance, completely describe the matter density distribution. The density distribution can be also defined in the Fourier space[3], and the variance of $\delta(\mathbf{x}, z)$ is given by

$$\langle\delta^2\rangle = \frac{1}{2\pi^2}\int_0^\infty P(k)k^2\mathrm{d}k, \tag{2.28}$$

where $P(k, z)$ is the power spectrum of the density fluctuations as a function of redshift. Objects of mass M arose from initial perturbations of size $R(M) = (3M/4\pi\rho_\mathrm{m})^{\frac{1}{3}}$. In this case, the density field is filtered[4] with a window function, W, which smoothes out all the fluctuations of scales smaller than R. Therefore,

---

[3] In this case, the density distribution is described as a superposition of plane waves, which evolve independently one of each other during linear evolution, and density contrast is given by $\tilde{\delta}(\mathbf{k}, z) = \int \mathrm{d}^3 x e^{i\mathbf{k}\cdot\mathbf{x}}\delta(\mathbf{x}, z)$.

[4] Mathematically spatial filtering is equivalent to a convolution of the density field with a window function: $\delta(\mathbf{x}) = \int \delta(\mathbf{y})W(|\mathbf{x} - \mathbf{y}|)\mathrm{d}\mathbf{y}$.

the variance of the perturbed field at scale R is given by

$$\sigma^2(M,z) = \frac{1}{2\pi^2}\int P(k)|\tilde{W}(k)|k^2\mathrm{d}k. \tag{2.29}$$

$\tilde{W}(k)$ is the Fourier transform of the window function W. The usual shape for the window function is the top-hat filtering, which is constant within a sphere of radius R and zero outside. Its Fourier transform is given by

$$\tilde{W}(k) = \frac{3[\sin(kR) - kR\cos(kR)]}{(kR)^3}. \tag{2.30}$$

The redshift dependence of $\sigma(M,z)$ enters only through the growth factor $D_+(z)$ (see Eq. 2.21),

$$\sigma(M,z) = \sigma(M,0)\frac{D_+(z)}{D_+(0)}, \tag{2.31}$$

i.e. it is assumed that the density perturbations continue to grow according to the linear growth factor, even when they have entered into the non-linear regime.

The power spectrum in Eq. 2.29 is a statistical description of the large-scale structure of the Universe. In the linear regime of structure formation, each fluctuation evolves independently and hence the evolution density is a linear function of the initial conditions. The growing solution (see Eq. 2.21) is the mode that dominates the evolution, therefore the power spectrum is given by

$$P(k,z) = T^2(k)\left(\frac{D_+(z)}{D_+(0)}\right)^2 P_{\mathrm{in}}(k). \tag{2.32}$$

$T(k)$ is the transfer function which contains all the non-gravitational effects that modify the original linear evolution of the power spectrum. In general, $T(k)$ is redshift dependent. The initial power spectrum, $P_{\mathrm{in}}(k)$, is obtained by normalizing the linear growth factor, $D_+(z)$, to 1 at $z = 0$ in Eq. 2.32: $P_{\mathrm{in}}(k) = Ak^{n_\mathrm{s}}$. Here, n_s is the index of the initial power spectrum, and can be measured through observations ($n_\mathrm{s} \sim 1$), and A is the amplitude at $z = 0$. A is directly linked to the normalization of the power spectrum, which is defined as the variance computed for at top-hat window having a comoving radius of $R = 8\ h^{-1}$ Mpc (see Eq. 2.29). This value of R is motivated by early results of galaxy surveys where it was found that $\delta(R = 8\ h^{-1}\ \mathrm{Mpc}) \simeq \delta M/M \simeq 1$, i.e. the variance of galaxy number density in spatial bins of $8\ h^{-1}$ Mpc is about unity (Davis & Peebles 1983). This variance is better known as σ_8 and determines the height of density peaks and consequently the number of haloes in the Universe. σ_8 and n_s are two of the most important cosmological parameters that can be directly measured. The *Planck* mission has determined $\sigma_8 = 0.8159 \pm 0.0086$ and $n_\mathrm{s} = 0.9667 \pm 0.0040$ (Planck Collaboration et al. 2015a).

Coming back to the halo mass function determination, there have been many attempts to calibrate the halo mass function from cosmological simulations (e.g. Reed et al. 2003; Warren et al. 2006; Reed et al. 2007). In particular, the halo abundance function obtained by Tinker et al. (2008) is one of the most widely used in the galaxy cluster field. The parameterised Tinker et al. (2008) mass function is given by

$$f(\sigma) = A_\mathrm{T}\left[\left(\frac{\sigma}{b_\mathrm{T}}\right)^{-a_\mathrm{T}} + 1\right]\mathrm{e}^{-c_\mathrm{T}/\sigma^2}. \tag{2.33}$$

Here, A_T sets the overall amplitude of the mass function, a_T and b_T are the slope and amplitude of the low-mass power law, respectively. c_T determines the cut-off scale at which the abundance of halos exponentially decreases. An advantage of this study is the publication of the fitting parameters as a function of the overdensity Δ. Tinker et al. (2008) also found that the overall shape of the halo mass function has a redshift dependence. The redshift evolution of the parameters is given by

$$\begin{aligned} A_{\rm T}(z) &= A_{\rm T,0}(1+z)^{-0.14}, & (2.34)\\ a_{\rm T}(z) &= a_{\rm T,0}(1+z)^{-0.06}, & (2.35)\\ b_{\rm T}(z) &= b_{\rm T,0}(1+z)^{-\alpha_{\rm T}}, & (2.36)\\ \log_{10}\alpha_{\rm T}(\Delta) &= -\left[\frac{0.75}{\log_{10}(\Delta/75)}\right]^{1.2}. & (2.37) \end{aligned}$$

The simulations by Tinker et al. (2008) have a 5% statistical precision in halo number at $z = 0$ for a ΛCDM cosmology.

A final remark on the importance of the halo mass function is that it depends strongly (through $\sigma(M, z)$) on all the cosmological parameters that have been mentioned throughout this entire section ($\Omega_{\rm m}$, Ω_Λ, h, w, σ_8, and $n_{\rm s}$, see Fig. 2.6). Therefore, the abundance of massive systems, such as galaxy groups and clusters, is a determining probe of the current cosmological model[5]. Several on-going and future surveys that aim to detect galaxy groups and clusters via optical, X-ray, and SZ observations (see Chapter 4). It is expected that the number of detected galaxy groups and clusters will range from thousands to tens thousands. Then, in order to maximize the extraction of cosmological information from such surveys, the halo mass function should be known to a few per cent accuracy.[6].

2.2.4 Self-similar model

Kaiser (1986) developed a model to describe the observable properties of galaxy groups and clusters. This modelling is based on three key assumptions:

1. Galaxy groups and clusters form via gravitational collapse from initial peaks of the density field. Therefore, the gravitational collapse is scale-free or *self-similar*.
2. The initial fluctuations do not have a preferred scale. Hence, the amplitude of the density contrast can be described by a power-law, $\Delta(k) \propto k^n$.
3. The physical processes that take place during the formation and evolution of galaxy groups and clusters do not introduce new scales in the problem, i.e. the only source of energy input into the ICM is gravitational.

This modelling has a major effect on the description and study of galaxy groups and clusters: when describing such systems as self-similar it means that they are simply scaled versions of each other, i.e. all galaxy groups and clusters are essentially identical. The self-similarity can be split into two regimes:

- **Strong self-similarity:** all galaxy clusters of different masses are identical scaled versions of each other.
- **Weak self-similarity:** the density of the Universe changes as a function of redshift, $\rho_{\rm cr}(z) = \rho_{\rm cr}(0)E^2(z)$, i.e. the density was higher at early epochs. This change has to be taken into

---

[5] Although, the halo mass determination depends also on the precise determination of the galaxy group and cluster masses.

[6] In this sense, the halo mass function should be calibrated for a wider range of masses and redshifts, as well to include the effects of baryonic matter, which can be significant (e.g. Bocquet et al. 2015).

account when comparing low and high redshift galaxy clusters, and it is known as self-similar redshift evolution.

Although the assumptions made by Kaiser (1986) oversimplify the problem of galaxy group and cluster formation and evolution, they predict simple *power-law* relationships between the different properties of such systems. Since such relations are very important for studies of galaxy groups and clusters, they will be explained in more detail in the following.

Scaling relations

As mentioned before, scaling relations are relations that describe the relationship between different galaxy cluster properties. Such relations are very important since they relate easily observable quantities to other properties which are difficult to determine by observations. For example, the galaxy group and cluster mass is one of the most essential properties to be determined, but cannot be measured directly. In this sense, precise measurements of galaxy cluster masses and their evolution with time are important because they provide constraints on cosmological models (see Section 2.2.3).

Some galaxy groups and cluster scaling relations have been already presented throughout this chapter. For example, one of the most obvious is the relation between the mass and radius (Eq. 2.23): $M \propto r^3$. However, such relation should also be translated into its equivalent at earlier epochs, i.e. expressed as a function of redshift. Voit (2005) discusses three different forms of redshift parameterisation for scaling relations, in this work the third form will be used since the scaling involves the analytical solution from the spherical collapse model. Therefore, the mass-radius $M - r$ relations states:

$$M \propto r^3 \Delta(z) E^2(z). \tag{2.38}$$

Such relation indicates that objects at high redshift have smaller sizes. Bryan & Norman (1998) provide an approximation for $\Delta(z) = 18\pi^2 + 82[\Omega_{\mathrm{m}}(z) - 1] - 39[\Omega_{\mathrm{m}}(z) - 1]^2$, where $\Omega_{\mathrm{m}}(z) = (1+z)^3 E^{-2}(z)$.

Since most of the work presented in this thesis focuses on the X-ray aspects of galaxy clusters, the following scaling relations will be related with X-ray observables, skipping the optical and SZ properties (for a more complete review on scaling relations see Böhringer et al. 2012 and Giodini et al. 2013). From X-ray observations one can directly derive the following galaxy cluster properties:

- **Mass-Temperature relation, $M - T$.** The self-similar model relates the cluster mass and temperature from Eq. 2.8

  $$M \propto T^{\frac{3}{2}} \Delta^{-\frac{1}{2}}(z) E^{-1}(z). \tag{2.39}$$

  Conversely, one can obtain the $T - M$ relation: $T \propto M^{\frac{2}{3}} \Delta^{\frac{1}{3}} E^{\frac{2}{3}}(z)$. This relation shows that objects of the same mass are hotter at higher redshifts. It is one of the most fundamentals scaling laws since it is obtained directly from the energy budget of the cluster gas. As explained in Section 2.1.2, the global temperature can be obtained from the observed spectrum. Observations of galaxy clusters are consistent with such scaling relation (e.g. Reichert et al. 2011).

- **Mass-Luminosity relation,** $M - L_{\mathrm{X}}$. The X-ray luminosity is obtained by integrating the bolometric emissivity (Eq. 2.3) over the volume: $L_{\mathrm{X}} = \int_V \epsilon \mathrm{d}V \propto \rho_{\mathrm{gas}}^2 T^{\frac{1}{2}} r^3 \propto \Delta(z) E^2(z) T^{\frac{1}{2}} M \propto M^{\frac{4}{3}}$, using Eq. 2.39. Then,

  $$M \propto L_{\mathrm{X}}^{\frac{3}{4}} \Delta^{-\frac{7}{8}}(z) E^{-\frac{7}{4}}(z). \tag{2.40}$$

This relation shows that objects of the same mass are more luminous at higher redshifts. The X-ray luminosity can be measured from the flux and redshift of the source (see Eq. 2.6). This scaling relation is very important for high redshift galaxy clusters, which are usually faint in X-rays, and through this relation one can determine their masses. By using Eq. 2.39, the $L-T$ relation can be obtained: $L_X \propto T^2 \Delta^{\frac{1}{2}}(z)E(z)$. Such relation is one of the most widely used since both observables are derived almost independently. However, the power-law has been measured to be steeper than predicted (e.g. Pratt et al. 2009; Reichert et al. 2011).

- ***$M - Y_{\mathrm{X}}$* relation.** Motivated by the SZ observations, Y_{X} is the product of $k_{\mathrm{B}}T$ and M_{gas} (see Eq. 2.12), then $Y_{\mathrm{X}} \propto M_{\mathrm{gas}}T \propto f_{\mathrm{gas}}MM^{\frac{2}{3}} \propto M^{\frac{5}{3}}$. Then,

$$M \propto Y_{\mathrm{X}}^{\frac{3}{5}} \Delta^{-\frac{1}{5}}(z) E^{\frac{2}{5}}(z). \tag{2.41}$$

  This scaling relation has been proved to be very robust, and it has low scatter. From observations it has been measured to follow the self-similar expectation (e.g. Arnaud et al. 2007).

In general, scaling relations have to be calibrated in large samples of well-determined galaxy cluster properties. Moreover, such relations are expected to have an intrinsic scatter, which has to be understood in order to obtain precise scaling relations. Once the calibration has been achieved, scaling relations can serve as *mass proxies* of low mass and/or high redshift galaxy groups and clusters, especially for the objects with low-quality data. This part will be an important tool for upcoming X-ray galaxy cluster surveys (see Chapter 4).

Deviations from the expected self-similar scaling relations are commonly attributed to non-gravitational effects in the ICM. Such processes are complex baryonic physics phenomena like AGN feedback, star formation, supernova explosions, cooling flows, and shocks. Furthermore, merging systems also add scatter to the expected scaling relations.

2.2.5 Cosmological constraints from galaxy groups and clusters

This final section will present a short description of different independent cosmological tests that use galaxy groups and clusters as probes, and which have been used successfully during the last decade and will be of important relevance in the near future with upcoming galaxy cluster surveys and new observatories. As mentioned before, the use of distinct methods allows a cross-check of the current cosmological model with procedures that have a different physical origin. The review from Allen et al. (2011) presents an extensive description of such techniques.

1. **Cluster (Halo) mass function**. This method has been fully described in Section 2.2.3. Briefly, by measuring the number density of galaxy groups and clusters of a given mass and at certain redshift, one can obtain constraints mainly on the matter density, Ω_{m}, and the amplitude of the density fluctuations, σ_8. At the same time, its redshift evolution constrains the linear growth of the density perturbations, which depends also on Ω_{m} and the dark energy density, Ω_Λ. This test requires a precise determination of the masses of the systems, as well as their redshift.

2. **Clustering properties**. The clustering refers to the measurement of the correlation function of the large-scale distribution of galaxy groups and clusters. It provides constraints on the matter and dark energy densities, Ω_{m} and Ω_Λ.

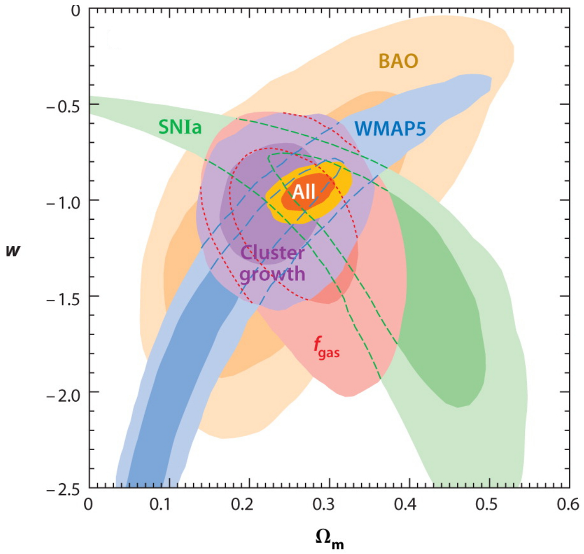

Figure 2.7: Joint 68.3% and 95.4% confidence regions for the dark energy equation of state, w, and the matter density, Ω_m, obtained from galaxy cluster abundance (purple regions) and gas mass fraction measurements, f_gas (red regions). Both methods are derived directly from galaxy clusters, and are compare with other cosmological test: CMB power spectrum (blue regions), supernova light curve measurements (green regions), and baryon acoustic oscillations from galaxy clustering (yellow regions). The combination of all methods gives the confidence regions in orange. Figure adapted from Allen et al. (2011).

3. **Matter power spectrum**. The amplitude and shape of the matter power spectrum (Eq. 2.32) depends also on the matter density, Ω_m, and the amplitude of the density fluctuations, σ_8. This test requires surveys of large area coverage, especially all-sky surveys are suitable for this method. The matter power spectrum and the correlation functions are two different ways of measuring the same properties since they are related by the Fourier transform.

4. **Baryonic acoustic oscillations (BAO)**. BAOs are regular, periodic fluctuations in the density of the visible baryonic matter of the Universe. They were created by reciprocal settlement of baryons and dark matter into each other's potentials. They are measured through the 'baryonic wiggles' of the power spectrum. BAOs can constrain the dark energy density, Ω_Λ, angular diameter distance, D_A, and trace the expansion history of the Universe through $H(z)$. This requires very large samples of galaxy clusters (tens of thousands).

5. **Gas mass fraction**. This test is based on the assumption that galaxy clusters are representative objects of the matter content in the Universe. This is measured through the total baryon fraction $f_\mathrm{b} = f_\mathrm{gas} + f_\mathrm{stars}$, i.e. f_b is the sum of the gas mass and star mass fraction. The former can be measured through X-ray observations and the latter through optical. Therefore, the total baryon fraction in the outskirts of galaxy cluster should approach to the cosmic value. This test is sensitive to the matter density, since $\Omega_\mathrm{m} = \Omega_\mathrm{b}/f_\mathrm{b}$. Furthermore, assuming that $f_\mathrm{gas} \approx$ const at all redshifts, it can be used as a 'standard ruler' to probe the global geometry of the Universe, being also sensitive to the dark energy density, Ω_Λ, angular diameter distance, D_A, and the equation of state, w.

6. **Absolute distance measurements**. By combining X-ray and SZ observations of a galaxy cluster, its absolute distance can be determined, which allows the measurement of the Hubble constant,

H_0. From Eqs. 2.6 and 2.10 one has $S_{\rm X} \propto \int n_{\rm e}^2 D_A {\rm d}\theta$ and $y \propto n_{\rm e} T_{\rm e} {\rm d}l \propto n_{\rm e} T_{\rm e} D_A {\rm d}\theta$, where ${\rm d}l = D_A {\rm d}\theta$, where θ is the line of sight angular size. By eliminating $n_{\rm e}$ from both equations one obtain $D_A \propto \Delta T_{\rm CMB}^2 / S_{\rm X} T_{\rm e}^2 \propto cz/H_0$. The results from this test are compatible with the D_A determination from supernovae Ia studies.

7. **SZ power spectrum**. The thermal SZ effect originates in the ICM of galaxy groups and clusters, which causes a fluctuation in the CMB temperature at small angular scales. Therefore, it is expected that the whole population of galaxy groups and clusters also generate a distortion, which is statistically described by its power spectrum. The distortion signal comes from all galaxy clusters even if they are not individually detected. In this sense, the tSZ power spectrum does not need the measurement of the mass of individual galaxy clusters and is insensitive to observational selection effects. This method is highly sensitive to the matter density, $\Omega_{\rm m}$, and the amplitude of the density fluctuations, σ_8. A number of recent experiments have measured the SZ power spectrum amplitude (e.g. Reichardt et al. 2012), which proved to be lower than model predictions. The constraints on σ_8 obtained from such measurements were in tension with other cosmological probes (e.g. CMB). As a result, the attention has moved to use the SZ power spectrum as a method to investigate the astrophysical uncertainties in the thermal structure of the ICM. This path is the topic of Chapter 7.

The results from all the above cosmological tests should be consistent and complementary, not only among themselves but also when compared to those from other cosmological probes (see Fig. 2.7).

CHAPTER 3

X-ray observations

Since the 1970s, astrophysicists have been studying the Universe in X-ray wavelengths. This has been possible thanks to the technological progress that have allowed the development of X-ray satellite observatories. Today's X-ray missions, such as XMM-Newton and Chandra, are so advanced that they can last for a decade or longer. However, the current generation of X-ray observatories is approaching the end of their lifetimes. Therefore, a new generation of X-ray missions is about to be launched, like the eROSITA mission, or are in preparation, like the ATHENA mission. The technical capabilities, such as imaging and spectroscopy, of both missions will be more powerful than their predecessors.

X-ray sources comprise almost all classes of astronomical objects, from planets and stars out to black holes and galaxy clusters. The ROSAT satellite performed the first X-ray all-sky survey in 1990, detecting thousands of X-ray sources, although mostly bright and low redshift objects. With the advent of more sophisticated X-ray missions, the detection of fainter and more distant sources has become possible. At the same time, the amount of X-ray data has enormously increased during the past 25 years through different and dedicated X-ray surveys. Thus, the sensitivity increment and the huge amount of collected data have led to the development of more complex, reliable, and semi-automatic source detection algorithms. This is of especial importance for X-ray galaxy cluster surveys, where the detection and identification of galaxy groups and clusters must be as complete and pure as possible in order to use such objects as cosmological probes. For a comprehensive knowledge of the detected sample, the systematic effects on galaxy cluster detection must be modelled through extensive X-ray simulations.

This chapter reviews the development of X-ray astronomy during the last 45 years. The X-ray telescopes instrumentation is presented, as well as the current and future generation of X-ray missions. A detailed description of different X-ray surveys, and how X-ray sources are detected and identified is provided. Especial attention is given to galaxy cluster surveys. Finally, different X-ray simulators are discussed.

3.1 X-ray astronomy: a brief overview

Observing the Universe in X-ray is impossible from ground-based observatories since Earth's atmosphere is opaque to X-ray radiation. During the first steps of X-ray astronomy (1960s-1970s), stratospheric balloons and rockets were used to observe the incident X-ray radiation. In this way, for example, the Sun's corona was observed at such wavelengths, as well as the first galactic X-ray source, the X-ray binary Scorpious X-1 (Giacconi et al. 1962), and the first galaxy clusters Virgo (Byram et al. 1966), Perseus (Fritz et al. 1971) and Coma (Meekins et al. 1971).

With the advancement and development of astronomical instrumentation, observational techniques, but especially, of space technology, X-ray astronomy has enormously grown. The main characteristic of X-ray observations is the detection and collection of individual photons one by one. Therefore, X-ray telescopes should be able to determine the arrival direction, energy and time of arrival of the photons. The first X-ray detectors were proportional counters and scintillation counters. The payload of the first X-ray satellite, *Uhuru*, consisted of two sets of proportional counters, which were sensitive in the $[2-20]$ keV energy band. The satellite was launched in 1970 by the National Aeronautics and Space Administration (NASA), and one of its main achievements was the discovery and detailed study of pulsating accretion-powered binary X-ray sources.

The next generation of X-ray observatories introduced focusing and imaging X-ray optics, as well as imaging detectors, providing two-dimensional X-ray images. The first imaging X-ray telescope was the *Einstein Observatory*. It was also a NASA project and it was launched in 1978. Such advancement improved the sensitivity considerably, as well as the resolution of X-ray measurements. The European X-ray Observatory SATellite (*EXOSAT*), launched in 1983 by the European Space Agency (ESA), included two imaging telescopes.

The next major step in X-ray astronomy was provided by the ROentgen SATellit (*ROSAT*) observatory. It was built under international cooperation between Germany, the United Kingdom and the United States. It was launched in 1990 and it was the first imaging telescope to perform an *all-sky survey*. The *ROSAT* mission was able to detect $\sim 125,000$ X-ray sources, thanks to its improved telescopes and technology. The mission ended after eight years. The *Einstein* and *ROSAT* observatories also used proportional counters. Proportional counters presented high background radiation, i.e. photons from diffuse and unresolved X-ray sources and from charged cosmic rays particles, making the X-ray observations a challenging task.

The proportional counters were replaced by Charge-Coupled Devices (CCDs) as X-ray detectors. The Japanese-American Advanced Satellite for Cosmology and Astrophysics (*ASCA*) mission was the first X-ray observatory to use such technology.

There have been around 30 X-ray satellite observatories since *Uhuru* in 1970. Each new mission comes with an improved technology. Thanks to this, current observatories can last for a decade or longer. In general, with the advent of X-ray satellites it was possible to observe and image the emission of extragalactic sources such as the hot gas in galaxy clusters and active galactic nuclei powered by black holes, as well as galactic objects such as supernova remnants, stars, and binary stars containing a white dwarf, neutron star or black hole X-ray binaries.

In the following sections, X-ray telescope characteristics are described, as well as the current and future X-ray observatories. The methodology for conducting X-ray surveys, source detection and identification techniques are also presented. Finally, different X-ray simulations are described.

3.2 X-ray sources

Objects in the Universe can broadly be divided into two types: Galactic and extragalactic sources. The former ones reside within the Milky Way Galaxy, and the latter ones outside it. A short list of both kinds of objects that emit in X-rays is presented. More information on the individual systems can be found in Trümper & Hasinger (2008) and Seward & Charles (2010).

The known Galactic objects that emit or absorb in X-ray are: the Sun and its solar winds, comets, planets, such as Mars, Jupiter and Saturn, stars and their stellar winds, white dwarfs, cataclysmic variable stars, pulsars, neutron stars, black holes, binary systems, supernovae, supernova remnants, and the interstellar medium.

The X-ray extragalactic sources are: galaxies, AGN and galaxy groups and clusters. Galaxies emit in X-ray due to the hot gas trapped in their gravitational potential well. This emission also has a contribution from the galaxy star forming regions, supernova remnants, binary systems, neutron stars and black holes. AGN are powered by supermassive black holes in the centre of galaxies. They accrete material around them, and the friction caused by this process increases the temperature of the material, which starts the X-ray emission. AGN release huge amounts of energy, making some of them the most X-ray luminous objects in the Universe. They have also been observed in the optical and radio wavelengths. The X-ray emission of galaxy groups and clusters has been detailed in Section 2.1.2.

X-ray background

When observing the Universe in X-ray bands, there is a diffuse X-ray emission observed in all directions, which is called X-ray background. This background has two main contributors:

- **Cosmic X-ray background**: it is the result of the integrated emission of unresolved faint extragalactic point sources, mostly AGN. Therefore, its flux depends on the angular resolution of the used X-ray observatory. This component dominates at energies $\gtrsim 1$ keV.
- **Diffuse soft background**: it is the thermal diffuse X-ray emission from the Galactic disk and halo, and the Local Hot Bubble. The latter is a cavity (a region with low Hydrogen density) in the interstellar medium filled with hot, X-ray emitting gas. It surrounds the Sun and other nearby stars. This component dominates at energies $\lesssim 1$ keV.

Both components are constant in time, but the diffuse soft background varies spatially across the sky. A detailed study of the X-ray background can be found in Read & Ponman (2003).

3.3 X-ray telescopes

The design of X-ray telescopes is completely different from conventional optical and radio telescopes. X-ray photons are so energetic that they are absorbed by the mirror of a standard reflector. However, the reflection of low energy (< 20 keV) X-ray photons is possible in the small incidence angle regime. This is known as *grazing incidence*. The reflection efficiency is high as long as the incidence angle of the X-ray radiation remains lower than a critical value, after which the efficiency decreases rapidly. This critical angle value is inversely proportional to the photon energy. Thus, the reflection efficiency is distinct for different photon energies in X-ray telescopes.

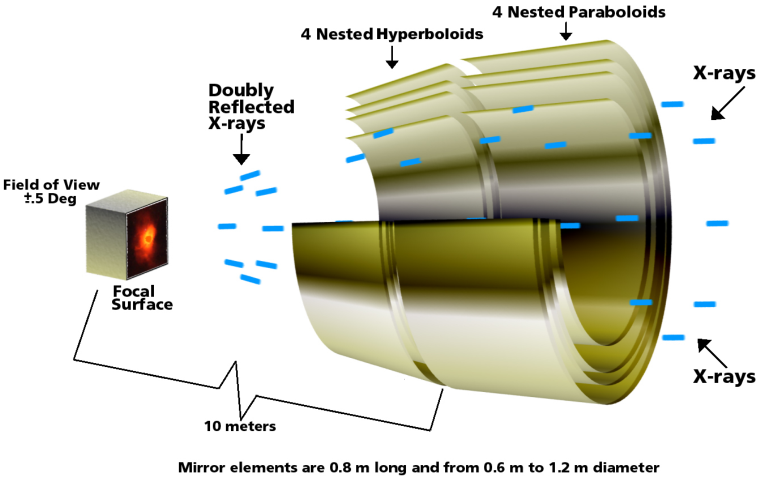

Figure 3.1: Sketch of the X-ray telescope of the *Chandra* X-ray Observatory. The X-ray light is focused on the focal surface thanks to the four nested, co-aligned, confocal, grazing-incidence mirror pairs. Credit: NASA/CXC/D. Berry.

Modern imaging X-ray systems were proposed by Wolter (1952), who was studying optical systems for X-ray microscopy. The *Wolter optics* makes use of the grazing incidence technique in a system of two mirrors in order to focus the X-ray light. Wolter described three configurations of two-mirror systems: both Wolter-I and Wolter-II arrangements consist of a paraboloid as a primary mirror and a confocal and coaxial hyperboloid as the second mirror (see Fig. 3.1), whereas Wolter-III optics is composed of a paraboloid and an ellipsoid as primary and secondary mirrors, respectively. In the Wolter-I configuration, the X-rays strike the paraboloid mirror at the grazing angle and are reflected and strike again the hyperboloid mirror. Then, the X-rays are again reflected and focused on the hyperboloid focus. Wolter-I configurations are designed with segmented mirrors, which results in the constructions of large tubular mirrors (see Fig. 3.1).

In X-ray astronomy, Wolter-I systems are preferred because their mirrors can be *nested*, which allows enlarging the effective collecting area of the telescope. Each mirror pair, or shell, must be co-aligned and confocal (see Fig. 3.1). The confocality property results in individual shells contributing to the different energy bands, i.e. outer shells have steeper incidence angles than the inner mirrors. Therefore, the inner mirrors reflect a larger X-ray bandwidth than the outer shells. Small incidence angles, α_g, give as result large focal lengths, f_l, since $f_l \propto r_f/\alpha_g$, where r_f is the radius of the telescope's aperture entrance. As a consequence, X-ray telescopes are elongated (see Fig. 3.3).

Wolter-I telescopes produce an almost perfect image of a point-source *on-axis*, i.e. at the centre of the field-of-view (FoV). The surface brightness of the source in the detector, i.e. the two-dimensional source intensity, is described by the point spread function[1] (PSF). The PSF is usually characterized by the half energy width (HEW), which is the image radius containing half of the photons in the incident beam. The HEW is usually used to describe the angular resolution of an X-ray telescope.

The source image produced *off-axis* by a Wolter-I telescopes gets degraded by two main reasons. First, as mentioned earlier, each shell possesses different reflection efficiency, this result in a decreasing effect-

---

[1] In optics, the PSF is usually described by an Airy function. However in X-ray telescopes PSF have more complicated shapes due to its dependence on photon energy and off-axis position.

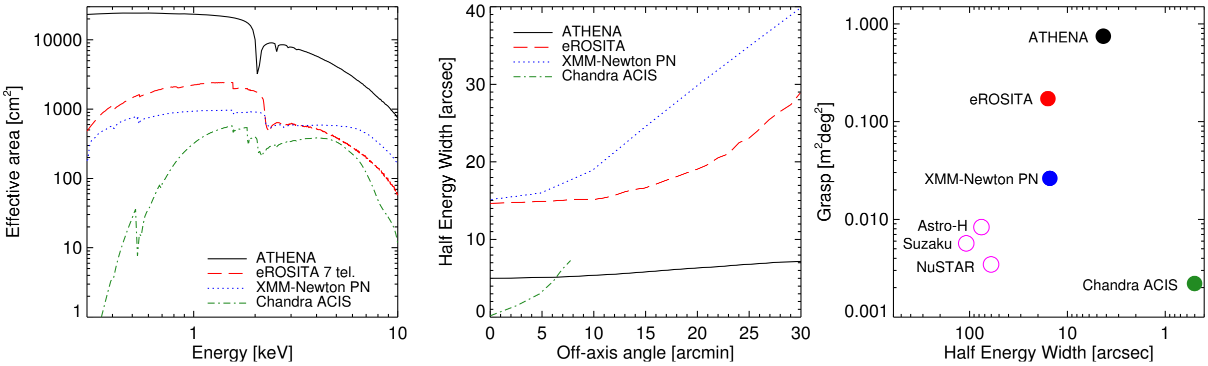

Figure 3.2: Comparison of different X-ray telescope properties for distinct observatories. *XMM-Newton* PN is shown in blue dotted-line, *Chandra* in green dot-dashed line, *eROSITA* in red dashed-line, and *ATHENA* in black solid-line. *Left*: effective area curves as function of energy. The *eROSITA* curve represents the total effective for its seven telescopes. *Middle*: PSF variation across the field of view. *Right*: grasp as function of half energy width.

ive collecting area[2] for a given energy at different off-axis angle (see left panel of Fig. 3.2). Such effect is known as *vignetting*, and can be described as a reduction of an image's brightness at the periphery of the image compared to the centre. Second, the telescope suffers from coma and spherical aberrations, these make the PSF broader as a function of off-axis angle and energy (see the central panel of Fig. 3.2). In this case, the image's brightness gets blurred at the edges in comparison to the middle of the image. Furthermore, mirrors have surface irregularities, which might be of a chemical or physical origin and diminish the performance of the telescope. Such imperfections can also degrade the PSF and reduce the effective collecting area of the telescopes. Hence, the FoV of an X-ray telescope is mainly constrained by the vignetting and the off-axis blurring. Therefore, detector sizes are chosen such that the central part of the FoV has an acceptable vignetting and angular resolution.

Finally, one optimisation criterion for X-ray telescope is the so-called *grasp* value, which is the product of the maximum effective collecting area and the FoV. The right panel of Fig. 3.2 shows the grasp as function of HEW for different X-ray observatories.

X-ray detectors

Although CCDs were developed for optical astronomy, they are also used extensively in X-ray wavebands. In simple terms CCDs act as a camera: when an X-ray photon is absorbed by a silicon pixel, a charge proportional to the photon energy is created there. When the recording interval is finished, the CCD is read out. This read out process is repetitive and takes place at one row at the time: after the edge row is read out, the charge is shifted by one pixel row and the next row is read out. Early and some of the current X-ray CCDs are made of metal-oxide semiconductor (MOS) material, which is modified to make it sensitive to X-rays by increasing its silicon depletion layer thickness. A new generation of X-ray detectors is the so-called PN CCDs, which are more sensitive than MOS detectors. These detectors are denominated PN because they are built from p-n junctions, i.e. from p-type and n-type semiconductor materials.

---

[2] The effective collecting area is given by the product of the mirror geometric area, reflectivity, off-axis vignetting, and detector quantum efficiency. Such properties are a strong function of energy and off-axis angle.

X-ray detectors work in photon-counting mode, i.e. a method for counting individual photons one by one. X-ray detectors record simultaneously the energy, position, and arrival time of each individual photon. In consequence, CCDs are imagers and spectrometers at the same time. Basic X-ray data usually comprise lists of events and their attributes. Furthermore, X-ray datasets are usually photon-limited, i.e. the images, spectra, or lightcurves created from the event lists may have a few or even no photons in many energy bins. Therefore, the data analysis and statistical techniques developed in other wavelengths do not necessarily apply to X-ray astronomy.

X-ray high resolution spectroscopy

The energy resolution of CCD detectors is limited to $\sim$ 100 eV at 1 keV, and their energy *resolving power*, $\Delta E/E$, is highly reduced at low energies. In order to increase the energy resolution (up to few eV), some telescopes have diffraction gratings. They are located in the beam path between the telescope and the focal plane.

3.3.1 Current X-ray observatories

There are currently four major X-ray observatories: *Chandra*, *XMM-Newton*, *Suzaku* and *NuSTAR*. All four telescopes have an improved effective area and angular resolution in comparison with previous observatories. *Suzaku*[3] is a Japanese X-ray satellite launched in 2005. Its major distinction was an on-board X-ray micro-calorimeter, which was expected to provide unprecedented energy resolution compared to other instruments. However, it failed a month after launch. *Suzaku* was switched off on September 2015. The Nuclear Spectroscopic Telescope ARray[4] (*NuSTAR*) is a NASA mission specialized in high energy X-rays (3 − 79 keV). It was launched in 2012. Since *Chandra* and *XMM-Newton* missions have been very successful during the past 15 years, they are described in more detail below.

Chandra

The *Chandra* observatory[5] was named after the astrophysicist Subrahmanyan Chandrasekhar. It is a NASA project and it was launched in 1999. *Chandra* consists of a single X-ray telescope with a focal length of 10 m. It has four pairs of nested, highly-polished mirrors, which allow a resolution of 0.5 arcsec on-axis and a FoV of 30 arcmin. The left panel of Fig. 3.3 shows a schematic illustration of *Chandra*.

Chandra has two major detectors: the Advanced CCD Imaging Spectrometer (ACIS) and the High Resolution Camera (HRC). A mechanism can place any of those instruments at the telescope focus. ACIS is sensitive in the [0.2 − 10] keV energy band, and consists of 10 CCD chips. Due to downlink and read-out issues, only 5 of the 10 chips can be used simultaneously. HRC has two micro-channel plate components and is sensitive in the range of 0.1 − 10 keV. Both of these instruments can be used with the observatory's transmission gratings. *Chandra* carries three sets of gratings, which can be placed if required, in the path of the telescope beam. The High and Low Energy Transmission Grating Spectrometer (LETGS and HETGS, respectively) work over 0.4 − 10 keV and 0.09 − 3 keV with a spectral resolution power of 60 − 1000 and 40 − 2000, respectively.

---

[3] http://global.jaxa.jp/projects/sat/astro_e2/index.html

[4] http://www.nustar.caltech.edu/

[5] http://chandra.si.edu/

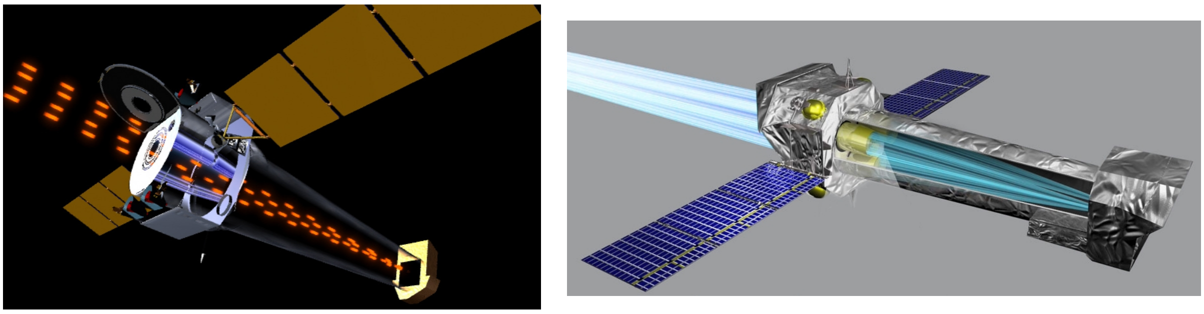

Figure 3.3: Schematic illustrations of the *Chandra* (*left panel*) and *XMM-Newton* (*right panel*) X-ray observatories. X-ray photons enter the telescope and are reflected at grazing angles and focused onto an imaging detector. Credits: XXNASA/CXC/D. Berry & A. Hobart and ESA/AOES Medialab.

This telescope has allowed to observe the X-ray cavities, bubbles rising from the central AGN in galaxy clusters (Fabian et al. 2000). Pressure shock fronts in the ICM and supernovas were possible to study thanks to *Chandra* (e.g. Larsson et al. 2011). Chandra found strong evidence that dark matter exists by observing galaxy cluster collision (Clowe et al. 2006). Also, the first X-ray emission from the supermassive black hole, Sagittarius A*, at the centre of the Milky Way was observed with *Chandra* (Baganoff et al. 2001).

XMM-Newton

The ESA X-ray Multi-Mirror mission[6] was launched in 1999. It is named in honour of Sir Isaac Newton (*XMM-Newton*). The main scientific payload of the observatory consists of three parallel X-ray telescopes of 7.5 m focal length. Each telescope is made of 58 nested mirrors, which combined give an effective collecting area four times larger than the *Chandra* one. However, this impacts its angular resolution: 6 arcsec on-axis. *XMM-Newton* also has a FoV of 30 arcmin. The right panel of Fig. 3.3 show a schematic illustration of this X-ray telescope.

Each X-ray telescope has a CCD at its respective focal plane, which are referred as European Photon Imaging Cameras (EPIC). These cameras are sensitive in the $[0.2 - 12]$ keV energy band. Two EPIC cameras are MOS CCDs and have reflection gratings (RGS), which intercept $\sim$ 50% of the beam. This provides spectroscopy information over the range $0.34 - 2.5$ keV with a spectral resolution of $200 - 800$. Such information is recorded in separate CCDs. The third telescope has a PN CCD, but without reflection gratings.

XMM-Newton was the first X-ray telescope to detect the hot gas in filaments, which connect two galaxy clusters (Werner et al. 2008). Thanks to the *XMM-Newton* large collecting area and spectral resolution it was also possible to detect the first quasi-periodic oscillation from an AGN (Gierliński et al. 2008). Furthermore, it discovered a new class of supernovae of type Ia (Borkowski et al. 2006).

The high-sensitivity of *XMM-Newton* has allowed the detection of faint sources, whose study is complicated due to their low signal-to-noise. Therefore, the development of sophisticated tools to study such sources is necessary. In Chapter 6, two different techniques to study faint X-ray sources are presented: a Bayesian aperture photometry algorithm and a stacking technique. Both procedures are applied to faint and high-z galaxy groups in *XMM-Newton* data.

---

[6] http://xmm.esac.esa.int/

3.3.2 Future X-ray observatories

Currently, there are three major X-ray missions in development: *Astro-H*, *eROSITA* and *ATHENA*. The three of them represent the next generation of X-ray missions. *Astro-H*[7] is the next generation of high-energy X-ray telescopes. It is developed by the Japan Aerospace Exploration Agency (JAXA), and it is expected to be launched in 2016. It will include a micro-calorimeter with an unprecedented energy resolution of $\leq$ 7 eV. The main characteristics and mission objectives of *eROSITA* and *ATHENA* are described in more detail since both observatories are essential to this thesis.

eROSITA

The extended ROentgen Survey with an Imaging Telescope Array[8] (*eROSITA*) is the primary instrument of the Russian/German Spektrum-Roentgen-Gamma (*SRG*) observatory. The secondary instrument is the Astronomical Roentgen Telescope X-ray Concentrator (*ART-XC*). *eROSITA* is mainly developed by the Max-Planck-Institut für Extraterrestrische Physik (MPE) in Germany, while *ART-XC* is being developed by the Russian Space Research Institute (IKI) and the All-Russian Scientific Research Institute for Experimental Physics VNIIEF. *ART-XC* will be more sensitive to higher X-ray energies than *eROSITA* (Pavlinsky et al. 2014). *SRG* is schedule for launch in 2017.

eROSITA consists of seven identical X-ray telescopes of 54 mirror shells each. The telescopes have a focal length of 1.6 m, which gives an angular resolution of 16.3 arcsec on-axis at 1.5 keV and a FoV of 1.03 deg. Each mirror system has a PN CCD camera in its focus, which is sensitive at energies of $\sim 0.2 - 10$ keV. The effective area of *eROSITA* is about twice the one of *XMM-Newton*/PN below 2 keV energies, whereas it is three times less at higher energies (see left panel of Fig. 3.2). Further details can be found in Merloni et al. (2012).

The main scientific goals of *eROSITA* are to:

- detect the hot ICM of $50 - 100$ thousand galaxy groups and clusters and hot gas in filaments between clusters to map out the large-scale structure in the Universe for the study of cosmic structure evolution.
- detect all obscured accreting black holes in nearby galaxies and many new distant active AGN.
- study in detail the physics of galactic X-ray source populations, like pre-main sequence stars, supernova remnants and X-ray binaries.

The first objective is the main driver of the *eROSITA* mission. As explained in Section 2.2.3, a large sample of galaxy groups and clusters can be used as a cosmological probe. In order to detect a huge amount of galaxy clusters, *eROSITA* will scan the entire sky for four years, making it the second imaging X-ray all-sky survey ever made after *ROSAT* (see Section 3.1). The seven *eROSITA* telescopes will provide a sensitivity $\sim$ 20 times larger than the one of *ROSAT*. Furthermore, *eROSITA* will provide the first ever imaging survey of the sky in the hard X-ray band ($2 - 8$ keV).

The X-ray data from a new telescope requires a dedicated software analysis system. Especially if new galaxy clusters will be detected, efficient techniques providing reliable and clean outputs are necessary. Chapter 4 explores different source detection algorithms for future *eROSITA* data. Moreover, by using

---

[7] http://astro-h.isas.jaxa.jp/en/

[8] http://www.mpe.mpg.de/eROSITA

simulated X-ray *eROSITA* observations, the detection efficiency and the selection function of galaxy clusters are studied.

ATHENA

The Advanced Telescope for High ENergy Astrophysics[9] (*ATHENA*) is the next generation of ESA X-ray telescopes. It was selected in 2014 as the second large class mission within the ESA's Cosmic Vision 2015–25 plan, with a launch foreseen in 2028. In Chapter 5 the ESA's long-term science programmes and the selection process that *ATHENA* went through are described in more detail.

The *ATHENA* concept proposes to incorporate important enhancements over current and near future X-ray observatories (see Fig. 3.2). To achieve this, the *ATHENA* observatory will have three key elements[10]. The first component is an X-ray telescope with a focal length of 12 m and an effective area of ~ 2 m^2 at 1 keV [11]. The telescope will use silicon pore optics (SPO), which is a new light, stiff and modular optics (see Beijersbergen et al. 2004; Bavdaz et al. 2010). This technology has been under development by ESA for over a decade and allows to achieve a high angular resolution < 5 arcsec and a wide FoV > 40 arcmin. The second element is an X-ray Integral Field Unit (X-IFU), which is an X-ray micro-calorimeter spectrometer for high-spectral resolution imaging (Barret et al. 2013). It will use transition edge sensors to read out the absorbed X-ray photons. The last component is a Wide Field Imager (WFI), which is a silicon-depleted p-channel field effect transistor active pixel sensor camera (Rau et al. 2013). It will have a large field of view (up to $50'$), high count-rate capability and moderate spectroscopic resolution.

The *ATHENA* mission is expected to have a better performance and scientific results than *XMM-Newton* (~ 10 larger effective area, see Fig. 3.2). The contemplated large effective area combined with the large FoV will make *ATHENA* a major step in the high-energy astrophysics.

The *ATHENA* science objectives will be described in Chapter 5. Briefly, the mission objective is to investigate two key astrophysical questions:

- How does ordinary matter assemble into the large-scale structures we see today?
- How do black holes grow and shape the Universe?

As explained in the previous chapter, galaxy groups and clusters formed by the accretion of baryons intro deep dark matter potential wells. Models for their formation can be tested by determining how these baryons accreted and dynamically evolved in galaxy groups and clusters. One way to constraint such formation models is by finding and detecting the first formed galaxy groups ($z > 2$). *ATHENA* capabilities are suitable for such search. The study of the detection of early galaxy groups through different *ATHENA* instrumental configurations is the objective of Chapter 5.

3.4 X-ray surveys

Telescopes, in general, are not only useful to obtain information of a given object (*target*) through a *pointed* observation, but also are used to perform *surveys* of a given region in the sky. The main goal

---

[9] http://www.the-athena-x-ray-observatory.eu/

[10] As today, *ATHENA* is on study phase, therefore, the characteristics described here can be different in the near future.

[11] http://www.cosmos.esa.int/web/athena/resources-by-esa

Observatory	Survey	Area [deg^2]	Flux limit [erg cm^{-2} s^{-1}]	Type of survey	Reference
ROSAT	RASS	All-sky	3×10^{-13}	WA	Truemper (1993)
	RIXOS	20.2	3×10^{-14}	S	Castander et al. (1995)
	NEP	80.7	3×10^{-14}	D	Henry et al. (2001)
	ROSAT-UDS	0.12	1.2×10^{-15}	D	Lehmann et al. (2001)
	BMW-HRI	742	$10^{-14} - 10^{-12}$	S	Panzera et al. (2003)
XMM-Newton	XCS	800	1.5×10^{-14}	S	Romer et al. (2001)
	HELLAS2XMM	3	5.9×10^{-15}	S	Baldi et al. (2002)
	SXDS	1.14	6×10^{-16}	D	Sekiguchi & et al. (2004)
	XMM-LH	0.43	3.1×10^{-16}	D	Hasinger (2004)
	ELIAS-S1	0.6	5.5×10^{-16}	D	Puccetti et al. (2006)
	COSMOS	2	7.27×10^{-16}	WA	Hasinger et al. (2007)
	XMM-BCS	14	3.7×10^{-15}	WA	Šuhada et al. (2012)
	XXL	50	5×10^{-15}	WA	Pierre et al. (2015)
Chandra	CDF-N	0.125	3×10^{-17}	D	Brandt et al. (2001)
	CDF-S	0.11	5.5×10^{-17}	D	Giacconi et al. (2002)
	ChaMP	14	$10^{-16} - 10^{-13}$	S	Green et al. (2003)
	CLASXC	0.4	5×10^{-16}	WA	Yang et al. (2004)
	ECDF-S	0.3	1.1×10^{-16}	D	Lehmer et al. (2005)
	XBoötes	9.3	4×10^{-15}	WA	Murray et al. (2005)
	C-COSMOS	2	1.9×10^{-16}	WA	Elvis et al. (2009)
	AEGIS-X	0.67	5.3×10^{-17}	S	Laird et al. (2009)

Table 3.1: Compilation of different X-ray surveys conducted by distinct observatories. The flux limit is given by the faintest detected source in the $[0.5 - 2]$ keV band.

of a survey is to obtain useful catalogues of sources for statistical analysis. In X-ray wavebands, there exist three different types of surveys:

- **Wide-angle surveys (WA)**: they are obtained by many contiguous exposures over a large area for a given allocated time. Usually, each pointing has a short exposure time, giving as a result a shallow map, or *mosaic*, of the observed area. Wide-angle surveys can also be obtained by continuously scanning the sky as the telescope slews. X-ray observatories with large FoV, but poor angular resolution, are more suitable for this kind of surveys. However, only the brightest and mostly local X-ray sources are detected, since fainter sources are mixed in the X-ray background. These surveys are useful to build *flux-limited* samples, i.e. samples that include sources only above certain flux limit. Since these surveys cover a large area, the flux-limited samples contain enough sources to do proper statistical studies.

- **Deep surveys (D)**: they are obtained through a smaller number of contiguous observations over a small area for a given allocated time. Each observation has a long exposure time, giving as a result a deep map of the observed area. In comparison with WA surveys, deep surveys allow fainter and higher redshift objects to be detected, where the flux limit is given by the X-ray background. X-ray telescopes with a good angular resolution, where the FoV is usually small, suit better the necessities of this kind of surveys, since long exposure observations can reach the *source confusion limit*. In this case, a good angular resolution allows close by sources to be resolved.

- **Serendipitous surveys (S)**: they are obtained from the existing observations (*archival* data). They

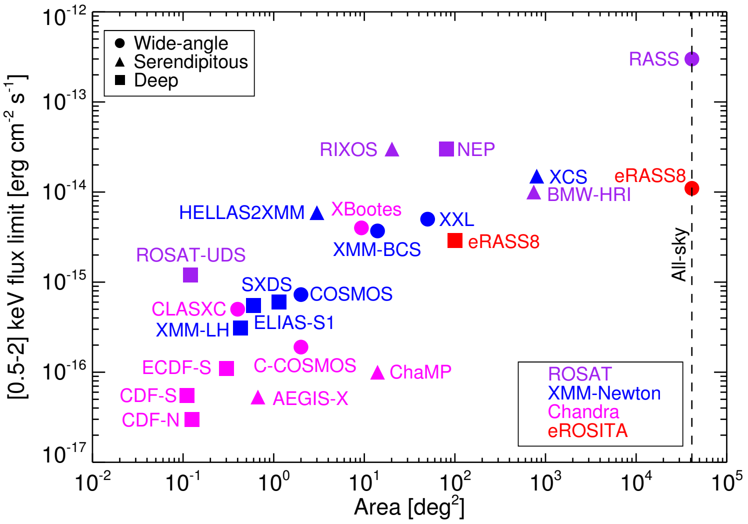

Figure 3.4: Flux limit in the $[0.5-2]$ keV energy band as a function of covered area for several current and future X-ray surveys. Filled circles, triangles and squares represent the surveys classified as wide-angle, serendipitous and deep, respectively. The different colours show the surveys performed by the distinct X-ray observatories: *ROSAT* in purple, *XMM-Newton* in blue, *Chandra* in magenta, and *eROSITA* in red. The flux limit is given by the faintest detected source in the survey.

> are usually used to create *representative* samples, i.e. well-defined samples where the characteristics of the underlying source population are known. Normally, pointed observations are target specific, where only the source of interest is studied and the others sources lying in the FoV are discarded or ignored. Then, serendipitous surveys can detect new sources in this pre-existing data. Since each pointing is observed under different conditions, they have to be treated carefully in order to extract consistent information. The pointings are usually selected in a way that they possess similar exposure times, observational conditions, and X-ray luminosity coverage.

Table 3.1 and Figure 3.4 show a compilation of major X-ray surveys with the *ROSAT*, *XMM-Newton* and *Chandra* observatories over the last 25 years. It is visible how the telescope characteristics influence the type of survey that a given observatory can perform. For instance, *ROSAT* has a very broad PSF and large FoV, which allowed the performance of the first all-sky survey. After this survey was finished, *ROSAT* performed thousands of pointed observations which were used for serendipitous surveys. *XMM-Newton* has an improved PSF and sensitivity over *ROSAT*, with a reasonable FoV, but it can only survey small contiguous areas (< 50 deg^2). On the other hand, *Chandra* has very good angular resolution and very small FoV, which make it suitable for deep X-ray surveys.

3.4.1 X-ray source detection and characterisation

As mentioned in Section 3.3, X-ray images contain very few photons, even for relatively long exposure observations. Moreover, some extended sources could contain only a few tens of photons spread over a large area. In addition, the PSF and vignetting, which change over the FoV, as well as the particle and X-ray background complicate the analysis of X-ray images. Therefore, it is important for a source detection and characterisation algorithm to be able to cope with these complications.

The main goals of X-ray surveys are the discovery and detection of as many objects as possible, especially if there is a research interest on a specific object population. There are two main steps in the source identification process on X-ray observations. The first step is to detect sources by identifying regions with a statistically significant overdensity of photons over the background. The second step is to determine to which kind of object the detected overdensity belongs to. The observed X-ray objects can be divided into two categories: point-like and extended sources. The former objects are unresolved astronomical objects, which are compact and their size is smaller than the telescope PSF, such as AGN. The latter sources have an extended X-ray emission, which can exceed the size of telescope PSF, such as galaxy groups and clusters (see Section 2.1.2). However, due to the complicated shape of the PSF in X-ray telescopes and other instrumental effects (like vignetting, see Section 3.3), point-like sources can appear as extended ones. Determining which sources are point-like or extended can become very difficult.

The discrimination between X-ray point-like and extended sources, or AGN and galaxy groups and clusters, used to be done through optical follow-up or by looking at the spectrum of the sources. The problem is that both methods are time consuming, and with the arrival of large data sets from X-ray surveys, such procedures became rather inefficient. Therefore, having automatic and reliable methods to identify X-ray sources became a necessity. Thus, the classification methods started to compare the measured source extent with that of the PSF in order to distinguish between point-like and extended sources. However, with the advent of better X-ray observatories, i.e. with improved PSF and better sensitivity, the extent alone criteria became obsolete. Nowadays, sophisticated algorithms, mostly maximum likelihood procedures, are used to fit point-like and extended models over the detected sources. In the following some of the most common and successfully applied methods for X-ray source detection and characterisation are described.

Sliding cell

In this method, an X-ray image is scanned by a detection box in small steps. The signal-to-noise (SN) ratio is measured in each step and is compared to the local background or a previously specified threshold value. The signal is measured from the pixel values within the cell, and the noise from nearby pixels. If the SN ratio is greater than the background, then the box position is marked as a source, and the SN is a first approximation of the object flux. The above, are the basics elements of the sliding cell method. There are some improvements to it: successive runs with increasing cell size, adaptive cell size as a function of off-axis angle, a matched filter detection cell, or the addition of a maximum likelihood (ML) algorithm for further source analysis. The latter improvement will be discussed in more detail at the end of this section. The sliding cell method is generally robust in finding isolated point sources, but it can merge close by sources. Moreover, it can fail in detecting extended sources, especially if the cell size is smaller than the source extension. This method has been incorporated into some of the data analysis packages from X-ray missions, like in *XMM-Newton* and *Chandra*.

Voronoi Tessellation and Percolation

In this method, the tessellation is built by each occupied pixel, which defines the centre of a polygon, the Voronoi cell. The surface brightness of each cell is inversely proportional to the Voronoi cell area. In this sense, background pixels have larger Voronoi cells and low photon counts, whereas source pixels have small Voronoi cells and high photon counts. The flux of each cell is compared with the expected

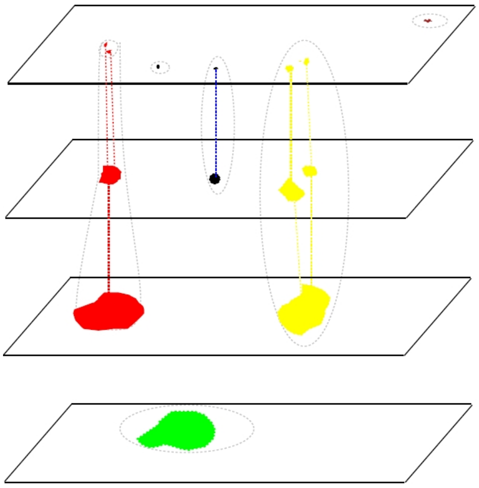

Figure 3.5: Sketch of an image wavelet decomposition, where each level depicts different feature sizes corresponding to a given wavelet scale (from small, top, to large sizes, bottom). Contiguous wavelet images form an object if their features reside within a linking radius. Figure adapted from Starck & Murtagh (2006).

one from a random Poisson distribution. If the flux deviates from this distribution, it is flagged and percolated with the neighbouring cells that also fulfil this requirement to form an object. This method can detect extended sources, even the ones with low surface brightness. However, it tends to merge or blend close by sources. This method has been included in the data analysis package of *Chandra*.

Wavelet transform

The wavelet technique is a multi-scale analysis of an image, where the signal is decomposed through the wavelet transformation. This enables to isolate sources of different sizes from the background signal. Wavelets are scalable, oscillatory functions that deviate from zero within a limited spatial regime. They also have zero normalization, and a full wavelet dictionary can be obtained from a mother wavelet using the simple dilatation equation

$$W(x, y) = \frac{1}{ab} W\left(\frac{x-c}{a}, \frac{y-d}{b}\right), \tag{3.1}$$

where a and b are the dilation parameters, and c and d, the translation parameters.

The wavelet technique convolves an image, $I(x, y)$, with a wavelet function, W:

$$w_{ab}(x, y) = I(x, y) \otimes W\left(\frac{x}{a}, \frac{y}{b}\right). \tag{3.2}$$

w_{ab} are the wavelet coefficients images corresponding to a wavelet scales a, b. By choosing a set of scales, the wavelet transform decomposes the original image into a different number of wavelet coefficient images. In these images, the features with characteristic sizes close to the corresponding wavelet scale are amplified (see Fig. 3.5). Then, the problem lies in the correct identification of the features that are not due to noise but rather to the source signal. Since for X-ray images the Poisson noise dominates, the process of selecting significant features can get complicated. There exist different methods which allow removing the insignificant features. For example, Vikhlinin et al. (1997) assumed local Gaussian noise and defined a significant threshold value; Slezak et al. (1994) transformed an image with Poisson noise into an image with Gaussian noise through the Anscombe transformation; Damiani et al. (1997) uses Monte Carlo simulations to find a convenient source detection threshold; Starck & Pierre

(1998) uses the wavelet function histogram method, which estimates the exact probability distribution function (PDF) of wavelet coefficients originated from Poisson data of locally constant mean.

Once the significant coefficients at each wavelet scale have been identified, the local maximum at all scales are collected and cross-identified to define objects in the data (see Fig. 3.5). This method can separate close by sources, detect sources of different shapes and surface brightness, even with low-surface brightness. One of the most important features is that wavelet transformation does not require previous knowledge of the image background to compute source parameters. However, it can be computationally expensive. Such method has been included in the data analysis packages of *XMM-Newton* and *Chandra*. Furthermore, it has been extensively and successfully used in X-ray surveys, where their main goal is the detection of galaxy groups and clusters (e.g. Rosati et al. 1995; Vikhlinin et al. 1998; Pacaud et al. 2006; Lloyd-Davies et al. 2011).

Combination with a maximum likelihood fitting

The above methods estimate various parameters of the detected sources, such as extent, counts, position, etc. The selection of extended sources used to be based on their spatial extent. However, with the improved PSF of new X-ray observatories, the accuracy of the sizes estimated straight from the detection algorithms is often insufficient to reliably classify sources, especially if the aim is to detect more faint and high redshift objects. A major improvement on such selection has been the addition of a maximum likelihood technique for further analysis of the detected sources.

In this further step, the sources identified by the detection algorithms are analysed by a maximum likelihood fitting. For each source, the fitting code determines a model that maximizes the probability of generating the observed spatial photon distribution. On the one hand, for a point-like source model, the spatial distribution of a detected source is compared to the telescope PSF at the same off-axis position of the source. On the other hand, the extended source can be modelled by the β-profile of galaxy groups and clusters (see Eq. 2.5 in Section 2.1.2). The modelling should be as realistic as possible, therefore, the models are convolved with the telescope PSF and include background. The likelihood ratio that calculates the probability that both distributions are the same is calculated by means of a simplified version of the C-statistic[12], C, (Cash 1979),

$$C = -2 \ln P = -2 \sum_{i=1}^{N} (n_i \ln e_i - e_i), \tag{3.3}$$

where P is the probability, n_i is the number of photons in a pixel i, e_i is the expected model value at pixel i, and N is the total number of pixels. The final model parameter estimation is performed by the maximization of the likelihood fitting. There exist different methods to do this calculation, which require a first guess of the parameters. These starting points are usually taken from the output of the detection methods. Finally, the maximum likelihood fitting provide a series of parameters that can be used to distinguish between point-like and extended sources.

This method has been successfully applied in different galaxy cluster surveys (e.g. Rosati et al. 1995; Vikhlinin et al. 1998; Pacaud et al. 2006; Lloyd-Davies et al. 2011; Pacaud et al. 2015), identifying hundreds of galaxy groups and clusters, which have been optically-confirmed. The methodology varies

---

[12] C-statistic is widely used in photon counting experiments with sparse sampling, which is modelled by a Poisson distribution.

across these different studies, because they are adapted to the features of the data, or simply because the methodology itself has evolved with time.

3.4.2 Selection function and bias

Once X-ray sources have been detected and characterized in a given survey it is important to understand the source sample itself, i.e. understand the characteristics of sources in the sample. Ideally, a sample must fulfil two requeriments: first, the sample should be complete, i.e. all objects which fulfil certain observational criteria should be included in the sample. Second, the sample should be pure, i.e. it should not include objects that do not fulfil those certain criteria (Schneider 2006). In order to understand the detected sample one must determine the survey selection function, taking into account all observational systematics that could affect or bias the detection (the so-called selection bias).

The survey selection function is the probability of detecting an object, like galaxy groups and clusters, which meet given sample selection criteria, i.e. with a certain set of properties and with specific observational parameters. There are two main elements to consider in the selection function. First, the flux limit has to be well determined. It can be given by the faintest detected source in the survey or it can be stated as a flux cut where the survey is considered statistically complete. Second, the surveyed area has to be treated carefully, since the background level, PSF and vignetting vary across the FoV. As a result, the sensitivity to source detection varies across the survey area. Then, these factors must be taken into account in order to quantify the effective sky coverage.

The selection bias of a survey is the systematic effect of astronomical source detection. There are two types: Malmquist bias (Malmquist 1920) is the effect of observing, and, therefore, detecting, brighter sources out to farther distances, i.e. intrinsically bright objects are easier to detect even at higher redshift. This makes luminous objects appear to be more numerous than fainter systems. In this case, a flux-limited sample will detect many bright sources that are spread in a very large volume. The Eddington bias (Eddington 1913) is the effect on the final number of objects due to statistical fluctuations in the flux measurements. Random photometric errors cause some bright sources to be detected with lower flux than they possess, and vice versa, faint sources can be detected with higher flux. In general, there are many more fainter objects than brighter ones. Therefore, the photometric errors cause few bright sources to scatter into the faint source sample, but more faint sources to scatter into the bright sample. In the case of a flux-limited sample, if the statistical scatter spreads above the flux threshold, then the inferred luminosity based only on the detected sources will be overestimated. This last statement is also true for the Malmquist bias.

Understanding the selection function of a detected sample and the incorporation of the selection bias has become a major issue in galaxy cluster surveys. Since galaxy cluster samples can be used as cosmological probes, the properties of the samples have to be well determined. Not all the galaxy cluster samples existing up to now are flux-limited. The XMM-LSS and XXL surveys (see next section) are surface brightness-limited samples (Pacaud et al. 2006, 2015). Their selection function has been determined through extensive simulations and it is based on the count-rates and angular core-radii of galaxy clusters. The XCS survey follows a similar path but includes further parameterisation, such as the temperature and redshift of the galaxy clusters. Additionally, selection bias can have a strong effect on measurements of scaling relations (Mantz et al. 2010b). In Chapters 5 and 4 the determination of the selection function for future X-ray surveys will be discussed.

3.4.3 X-ray galaxy cluster surveys

X-ray galaxy cluster surveys have important advantages over other detection and selection methods of such objects (Rosati et al. 2002):

- X-ray emission from the extended ICM is a proof of the collapse and formation of a galaxy cluster into a deep gravitational potential (see Section 2.1.2).
- The projection effects are minimized since the X-ray emission depends on electron density squared, and therefore, are brighter than less dense regions (see Section 2.1.2).
- The X-ray luminosity is a reliable mass proxy due to its tight correlation with the gravitational mass (see Section 2.2.4).
- The X-ray selection function can be easily determined by a simple flux-cut or can be based only on X-ray parameters, such as surface brightness.

The *ROSAT* All-Sky Survey (RASS) data has led to a great number of galaxy clusters X-ray surveys (for a historical review of X-ray galaxy cluster surveys see Rosati et al. 2002). In the northern hemisphere, the largest and most representative galaxy cluster compilations from contiguous areas of RASS include the Bright Cluster Sample (BCS, Ebeling et al. 1998), its extension (eBCS, Ebeling et al. 2000), and the Northern *ROSAT* All-Sky Survey (NORAS, Böhringer et al. 2000). The southern hemisphere has the *ROSAT*-ESO flux limited X-ray sample (REFLEX, Böhringer et al. 2001). Other important galaxy cluster surveys from contiguous areas in *ROSAT* include: the North Ecliptic Pole survey (NEP, Gioia et al. 2001), the MAssive Cluster Survey (MACS, Ebeling et al. 2001) and the HIghest X-ray FLUx Galaxy Cluster Sample (HiFLUGCS, Reiprich & Böhringer 2002).

Serendipitous *ROSAT* galaxy cluster surveys are numerous, some of the most representative are: *ROSAT* Deep Cluster Survey (RDCS, Rosati et al. 1995), Serendipitous High-redshift Archival *ROSAT* Cluster survey (SHARC, Collins et al. 1997), 160 Square Degree survey (160d, Vikhlinin et al. 1998), Brera Multiscale Wavelet survey (BMW, Campana et al. 1999), *ROSAT* International X-ray/Optical Survey (RIXOS, Mason et al. 2000), Brightest SHARC (Romer et al. 2000), Wide Angle *ROSAT* Pointed Survey (WARPS, Perlman et al. 2002; Horner et al. 2008) and 400 Square Degree survey (400d, Burenin et al. 2007). For a more complete review on galaxy cluster surveys with *ROSAT* see Edge (2004).

The *XMM-Newton* observatory has also led to a number of galaxy cluster surveys: the *XMM-Newton* Large Scale Structure survey (XMM-LSS, Pierre et al. 2004) is one of the largest and deepest galaxy cluster survey to date. The surveyed area covers 11 deg^2 and reaches a flux detection limit of $\sim 5 \times 10^{-15}$ erg cm^{-2} s^{-1}. The survey selection function is one of the best studied and characterized (Pacaud et al. 2006). This survey has been able to detected galaxy clusters with masses $M \sim 10^{14}$ M$_\odot$ above $z > 1$. The XMM-LSS served as a pilot for a larger survey: the Ultimate XMM Extragalactic survey (XXL, Pierre et al. 2015), which cover 50 deg^2. It has a similar depth as XMM-LSS. The first XXL astrophysical and cosmological investigations with galaxy cluster have been just recently published (Pacaud et al. 2015). The XXL field has a multi-wavelength coverage: optical, mid-infrared and radio. The above and following flux limits are quoted in the $[0.5 - 2]$ keV energy band.

The *XMM-Newton* Cluster Survey (XCS, Romer et al. 2001) is an ambitious serendipitous survey which aims to detect all galaxy clusters in all existing *XMM-Newton* archival data (an area $\approx$ 800 deg^2). XCS has found a galaxy clusters at $z \sim 1.5$. The Serendipitous *XMM-Newton* Cluster Athens Survey (SEXCLAS, Kolokotronis et al. 2006) covered an area of ~ 2.1 deg^2 and comprises a total of 21 galaxy clusters with a flux limit of 6×10^{-15} erg cm^{-2} s^{-1}. *XMM-Newton* also surveyed the Cosmic

Evolution Survey (COSMOS, Finoguenov et al. 2007) field, reaching a galaxy cluster flux limit of 3×10^{-15} erg cm^{-2} s^{-1} in 2.1 deg^2. A sample of 72 galaxy clusters was identified. The *Subaru–XMM-Newton* Deep Field (SXDF, Finoguenov et al. 2010) reached a cluster flux limit of 2×10^{-15} erg cm^{-2} s^{-1} over 1.3 deg^2, detecting 57 galaxy clusters. The *XMM-Newton* Distant Cluster Project (XDCP, Fassbender et al. 2011) is a serendipitous X-ray survey dedicated to find and study galaxy cluster at $z > 1$. It covers an area of 76.1 deg^2 with a galaxy cluster flux cut of 1.5×10^{-14} erg cm^{-2} s^{-1}. It has a sample of 22 spectroscopically confirmed galaxy clusters in the range $0.9 < z \lesssim 1.6$. The 2XMMi/SDSS (Takey et al. 2011) is a serendipitous galaxy cluster survey based on the X-ray extended sources in the *XMM-Newton* Serendipitous Source Catalogue (2XMMi-DR3). The survey is constrained to those extended sources that are in the footprint of the Sloan Digital Sky Survey (SDSS). Such overlap area is 210 deg^2. The *XMM-Newton*-Blanco Cosmology Survey (XMM-BCS, Šuhada et al. 2012) is a coordinated X-ray, optical, mid-infrared, and SZ cluster survey in a contiguous area of 14 deg^2. It reaches a median galaxy cluster sensitivity of $\sim 9.3 \times 10^{-15}$ erg cm^{-2} s^{-1}. Finally, Clerc et al. (2012b) processed serendipitous high galactic *XMM-Newton* observations in an area of 90.3 deg^2. The survey is called *XMM-Newton* CLuster Archive Super Survey (X-CLASS), and compiled a catalogue of 850 galaxy clusters, where the sample is not flux limited but rather surface-brightness limited (as the XMM-LSS and XXL surveys).

Due to the limited FoV and lower effective area, *Chandra* has not been used for galaxy cluster surveys (Table 3.1 show some *Chandra* X-ray surveys). The main goal of all these X-ray galaxy cluster surveys has been the study of the cosmological evolution of the number density of galaxy clusters (see Section 2.2.3). Moreover, many of such surveys have a multi-wavelength follow-up of the detected sources, which allows studying the astrophysics of galaxy clusters in bigger samples.

3.5 X-ray image simulators

Extensive X-ray simulations can help to understand and determine the selection function of a given survey. The simulations are created by placing artificial X-ray sources, point-like and extended, in the field, and the selection function is determined by measuring the detection probability for different sources, instrumental and observational parameters. X-ray simulations can also help to plan observations, since the *mock* observations can provide quantitative predictions of what to expect from a given observation. Furthermore, simulations are useful to evaluate possible instrumental configurations that help to optimize the observation of a given source, as well as the necessary allocation time for it.

There are different X-ray simulators available on the market. Some of them have been created for a specific X-ray observatory while others are capable of performing simulations for distinct X-ray telescopes. The level of detail in the simulations depends on the pursued goal of the research, where the created artificial sky can be generated semi-analytically or taken from hydrodynamical simulations. There are different outputs from the simulators: images, spectral files and photon event lists. Again, the output required from a simulator depends on the research for which the simulator is used. In the following a short description of how to obtain a simulated X-ray image is described.

All X-ray simulators follow a similar path when creating mock data. In the semi-analytical simulations galaxy groups and clusters are generally modelled by a β-profile (see Section 2.1.2), where different values for the core radius and β are previously defined. The expected flux, or count-rate, of the source can be calculated with `XSPEC`, which is a very popular and versatile spectral fitting package that offers various spectral models for X-ray emission of sources (Arnaud 1996). Scaling relations (see Section 2.2.4) are used to define the temperature, mass, and r_{500} of the simulated galaxy cluster. The population of point-like sources consist mostly of AGN, whose flux distribution, S, and source density, N, is usually described by an empirical $\log N - \log S$ relation (e.g. Moretti et al. 2003; Gilli et al. 2007). The spatial distribution of both kinds of sources, galaxy clusters and AGN, can be random, as a first approximation, or correlated, to be more realistic.

All X-ray observations have background noise, which also has to be included in a simulation. On the one hand, there exist the Cosmic and the diffuse soft background components (see Section 3.2). The intensity of this background can be calculated through different spectral models with `XSPEC`. Such background is affected by the vignetting of the telescope. On the other hand, there is an internal particle background, which is generated by charged particles travelling through the observatory and releasing their energy inside the detector or its surroundings. Such particles also create swarms of secondary particles, mostly electrons, which can reach the detector as well. The particles have energies comparable to the soft X-ray band, making it difficult to separate them from the cosmic background with similar energies. This particle background is uniform across the FoV. The flux of all sources and the X-ray background is calculated for a chosen energy band and a given exposure time.

The most important instrumental effects that have to be included in the X-ray imaging simulators are: FoV, pixel scale, PSF and vignetting. Point-like and extended sources are convolved with the PSF, which varies across de FoV. The vignetting affects the surface brightness of the sources since the effective area of the telescope is reduced.

Simulations for *XMM-Newton* observations can be generated with a software package called `SciSim`[13]. This software provides a detailed ray-trace simulations of how *XMM-Newton* responds to different astrophysical sources. It allows manual positioning of the sources or generated by the software itself. It includes the PSF, vignetting and detector response, as well as bad pixels, readout effects and the gaps between the CCD chips. `SciSim` can generate the standard Flexible Image Transport System (FITS) event files and images as output. Unfortunately, the development of `Scisim` has been discontinued in 2005, it still exists but is no longer supported and compiled for new machines. The XMM-LSS/XXL survey developed a private software package called `INSTSIMULATION` (Valtchanov et al. 2001). This creates *XMM-Newton* pointing images from a source list and takes into account the main instrumental features: PSF, vignetting, and detector masks.

A recent X-ray simulator is `SIXTE`[14], which can simulate observations from the *XMM-Newton*, *eROSITA* and *ATHENA* observatories. It uses calibration files such as the PSF, Redistribution Matrix Files[15] (RMFs) and Ancillary Response Files[16] (ARFs). The properties of the X-ray sources to be simulated are described in a separate input file, which can be used for simulating observations with different instruments.

Chapter 4 will present how *eROSITA* X-ray simulations can help to find the most suitable and efficient detection algorithm for point-like and extended sources, and to determine a selection function for galaxy clusters detected by *eROSITA*. Chapter 5 will show how X-ray simulations help to find the best *ATHENA* instrumental configuration for detecting the first galaxy groups in the Universe.

---

[13] http://xmm2.esac.esa.int/scisim/

[14] http://www.sternwarte.uni-erlangen.de/research/sixte/

[15] The RMFs files contain information about the energy resolution of the detector, and defines the probability distribution for a given detection in a certain energy channel given the energy of the incident photon.

[16] The ARFs files contain information about the effective area and reflectivity of the mirrors and the quantum efficiency of the detector.

CHAPTER 4

Detection of galaxy clusters with the future *eROSITA* mission

X-ray astronomy will enter a new era with the eROSITA satellite, which is expected to be launched in 2017 *and to perform an all-sky survey. eROSITA will possess unprecedented sensitivity and imaging capabilities for extended emission. Since X-ray imaging is one of the most reliable methods to detect galaxy clusters, eROSITA will detect* $\sim 10^5$ *of such objects. The promising capabilities of eROSITA bring great expectations to constrain dark matter and dark energy models through galaxy cluster science. The instrumental features also bring new challenges, especially on object detection in X-ray images. In this sense, galaxy cluster detection is one of the most important tasks in the eROSITA science.*

The galaxy cluster detection is a complex task that depends on many factors: instrumental and X-ray background, the X-ray morphology of the galaxy clusters, and the source detection algorithm. Nevertheless, the galaxy cluster detection and characterisation can be evaluated by means of extensive Monte Carlo simulations.

The aim of this chapter is two-fold. On one hand, different X-ray source detection procedures, based on wavelet and sliding-cell methods, are tested and applied to simulated eROSITA images. All significant instrumental effects are taken into account, and two kinds of sources are considered: point-like sources, described by the PSF of the telescope, and extended sources, modelled by a β*-profile. Different sets of simulations are constructed, with controlled and realistic source input configurations. The purpose is to compare and analyse the performance and resolving power of the different detection procedures. This allows us to choose the best detection methods and strategies to achieve a high galaxy cluster detectability and characterisation for future eROSITA data.*

On the other hand, the detection pipeline of the eROSITA Science Analysis Software System is used and tested over dedicated eROSITA simulations. The aims are to study the galaxy cluster detection efficiency of this algorithm and to determine a galaxy cluster eROSITA selection function. The selection function is parameterised in terms of flux and source extension, and it is used to forecast the redshift distribution for the expected galaxy cluster sample.

4.1 *eROSITA* all-sky survey and sensitivity

The main instrumental characteristics and goals of the *eROSITA* observatory have been presented in Section 3.3.2. This section will describe the plans for the all-sky survey strategy and the expected performances of the *eROSITA* satellite. For further details see the *eROSITA* Science Book (Merloni et al. 2012).

As mentioned earlier, the main science driver of *eROSITA* is to study the large-scale structure of the Universe and to test and to characterise cosmological models by means of very large samples of galaxy clusters out to redshifts $z \lesssim 1$. In order to achieve these goals, *eROSITA* will be placed at the second Lagrangian point, L2, which is a location in space where the gravitational forces of the Sun and Earth provide the necessary centripetal force to a satellite to orbit with them. L2 is located 1.5 million kilometres away from Earth, and *eROSITA* will take 3 months to get there after its launch. This location has some advantages for a telescope aiming for an all-sky survey: a satellite at L2 does not have to orbit the Earth, a process that can block the FoV of the telescope during Earth occultations, and it is free of the geocoronal X-ray emission from Earth. However, the cosmic radiation at L2 is higher compared with a low Earth orbit, where the satellites are protected by Earth's magnetic field. This results in a higher background and in addition, such radiation can damage the CCD cameras.

eROSITA will continuously scan the entire sky while orbiting the L2 point. The *eROSITA* FoV will trace out approximate great circles on the celestial sphere. These great circles will overlap at the ecliptic poles. The full coverage of the sky will take about 180 days and it will be fairly uniform across the sky with two deeply exposed regions at the ecliptic poles. *eROSITA* will perform a 4-year survey, therefore, the final all-sky survey will consist of eight consecutive passages. The *eROSITA* All-Sky Survey is denoted as eRASS:1-8, where the number represents the data fusion of the first until the eight full sky coverage. Figure 4.1 shows a simulated exposure map of the entire sky expected after the *eROSITA*

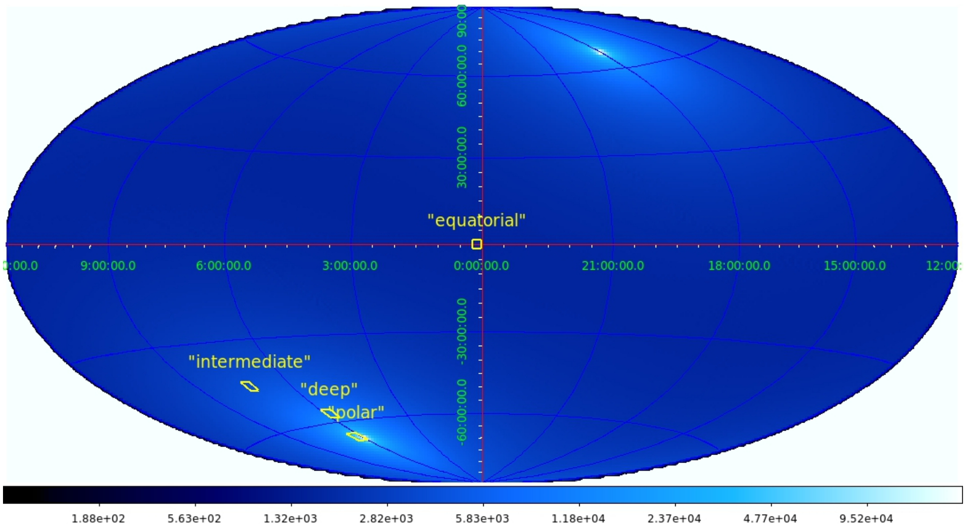

Figure 4.1: 4-year all-sky *eROSITA* exposure map for the soft band ([0.5 – 2] keV). The yellow boxes show regions with different exposure times: "equatorial" has 1.6 ks; "intermediate" has 4 ks; "deep" has 20 ks; and "polar" has 20 – 200 ks. The latter region shows the ecliptic poles where the great circles overlap. Credit: N. Clerc.

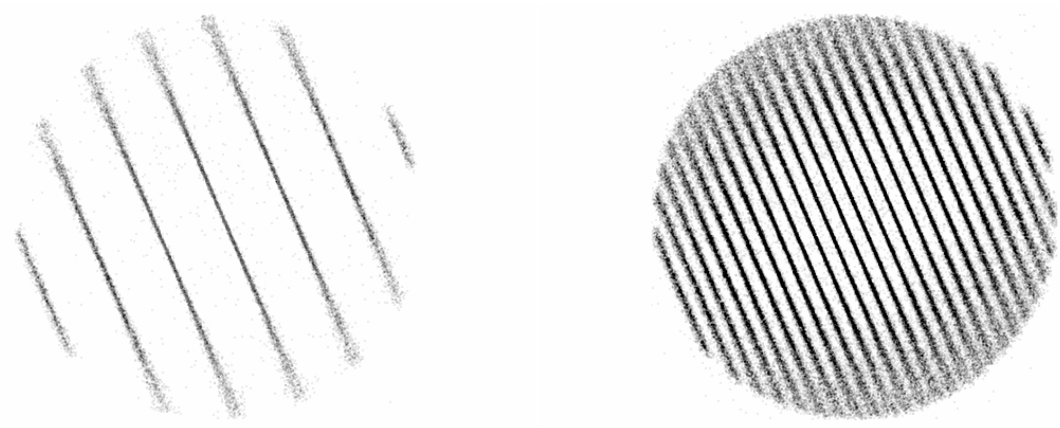

Figure 4.2: Simulated images of a series of *eROSITA* scans over a very bright, point-like source in the soft band ([0.5 – 2] keV). *Left*: During one 6-month all-sky survey, *eROSITA* will scan 6 times the same region of the sky. This panel shows the 6 tracks of the point-like source during this period. *Right*: same as left, but integrated over the 4-years all-sky survey. Credit: N. Clerc.

4-year all-sky survey. The figure shows the lowest exposure of ~ 1.6 ks at the ecliptic equator, and the highest exposure of ~ 200 ks at the ecliptic poles.

During each all-sky survey, each source will be observed up to six times, as the telescope only moves from ~ $1/6^{\mathrm{th}}$ of the FoV in the direction perpendicular to the rotation during the execution of a great circle. Each time the source crosses the FoV, it will follow an approximately linear track in the direction of the rotation. Figure 4.2 shows an example of a simulated bright source as it moves across the detector plane in different scans. The left panel shows the six scans during one 6-months all-sky survey, and the right panel shows all the scans after the 4-years of survey. This figure also shows the spatial broadening of the source towards the edges of the FoV. This is caused by the PSF degradation as a function of off-axis angle. In survey mode, the PSF gets averaged over the FoV. Then, the *eROSITA* PSF in survey mode will have a value of ~ $28''$ in the soft band and ~ $40''$ in the hard band. At the end of the survey, it is expected that *eROSITA* perform pointed observations for at least another 3.5 years.

Figure 3.4 shows the expected coverage and flux limit of eRASS:8 for the average and deep exposed areas. From this figure, it is clear that *eROSITA* will investigate the unexplored region of low flux sources in very large contiguous areas. Moreover, Fig. 3.2 shows that the sensitivity and grasp of *eROSITA*, which compared with other current telescopes, really marks a major breakthrough in the next generation of X-ray observatories.

The flux limit for point and extended sources in eRASS:8 is presented in the *eROSITA* Science Book. For point sources, the flux limit is estimated based on the total net counts needed to securely identify the sources as a function of exposure time. The calculation is based on the Poisson probability of a spurious detection given the number of background and total counts. This results in a signal-to-noise ratio S/N> 5σ for an aperture of 1 arcmin for a secure point source detection. The flux limit for point sources after 4-years all-sky survey is 1.1×10^{-14} erg s^{-1} cm^{-2} for an average of 2 ks exposure time, and 2.9×10^{-15} erg s^{-1} cm^{-2} for 20 ks exposure time at the ecliptic poles in the [0.5 – 2] keV energy band. Given these sensitivities, instrumental effects and survey strategy it is expected that *eROSITA* detect 3×10^{6} extragalactic point-like sources over the full sky.

As already stated in Section 3.4.1, galaxy groups and clusters are extended X-ray sources whose secure detection is closely related to their characterisation as extended. Since the characterisation of extended sources requires extensive and detailed simulations, the *eROSITA* Science Book gives simple flux limit estimates following the same approach as for point sources. In this case, for extended sources being securely identified, a S/N> 7σ is necessary for an aperture of 3 arcmin. Then, the flux limit for extended sources after 4-years of all-sky survey is 3.4×10^{-14} erg s^{-1} cm^{-2} for an average of 2 ks exposure time, and 1.0×10^{-14} erg s^{-1} cm^{-2} for 20 ks exposure time at the ecliptic poles in the $[0.5 - 2]$ keV energy band. The flux limit in the average exposure (2 ks) field corresponds to 70 source photon counts, while in the deep exposure (20 ks) field is 150 source photon counts.

By considering a detection limit of 50 photons counts in the $[0.5 - 2]$ keV energy band with an exposure time of 1.6 ks, Pillepich et al. (2012) predicted that *eROSITA* will detect $\sim 10^5$ galaxy clusters more massive than $M > 5 \times 10^{13}\ h^{-1}$ M$_\odot$ in the entire sky. This will increase the number of known galaxy clusters by at least an order of magnitude, which will help to constrain cosmological parameters with $1 - 2$ orders of magnitude better statistics than current X-ray cluster samples.

In the *ROSAT* all-sky survey, it was possible to identify low-redshift galaxy clusters as extended sources with only 30 counts. This was possible thanks to the low background that *ROSAT* possessed. *eROSITA* will have a better angular resolution than *ROSAT* and a much higher sensitivity. This will lead to the detection of many objects and the characterisation of galaxy clusters as extended sources. However, *eROSITA* will have a higher background than *ROSAT*; and the average survey PSF of ~ 28”, rather large compared to *XMM-Newton* and *Chandra*, will still significantly degrade the images. This can raise the problem of source confusion and source blending. These problems will mostly affect objects at low energy bands (< 5 keV, like galaxy groups and clusters) since few objects show bright emission to be detected at higher energies.

Detailed and realistic simulations can provide a precise detection threshold for the galaxy clusters observed by *eROSITA*, as well as the characterisation of its galaxy cluster selection function. However, these quantities strongly depend on our ability to detect and characterise galaxy clusters as extended sources. Therefore, a deep analysis of detection algorithms which can provide complete and pure samples of galaxy clusters is necessary. This last statement is the main subject of this chapter: to find suitable source detection algorithms for *eROSITA* that allow the construction of pure and complete galaxy cluster samples.

Each X-ray mission has provided an analysis package for its data. For example, *Chandra* Interactive Analysis of Observations (CIAO, Fruscione et al. 2006) for *Chandra*, and *XMM-Newton* Science Analysis System[1] (XMM-SAS) for *XMM-Newton*. These packages also include algorithms for source detection, which use different detection techniques. For example, sliding cell, wavelet transformation and Voronoi Tessellation (see Section 3.4.1). *eROSITA* will have its own data analysis package as well: the *eROSITA* Science Analysis Software System (eSASS). This package currently includes only one detection procedure, which uses the sliding cell method for source detection and a maximum likelihood algorithm for source characterisation.

The first part of this chapter presents an evaluation of the performance of different wavelet-based source detection algorithms. Such algorithms have been successfully applied to previous X-ray surveys (see Section 3.4.1). The performance test is done by means of simulated *eROSITA* images. These simulations take into account all instrumental effects, and controlled and realistic source input configurations are simulated. In the second part of this chapter, the best performing wavelet algorithm is then compared

---

[1] http://xmm.esac.esa.int/sas/

with the eSASS source detection pipeline. This comparison is also done through *eROSITA* image simulations. The idea is to find an alternative to the eSASS source detection pipeline that can give better or comparable results for the detection of galaxy clusters. Finally, the capacity of detecting galaxy clusters by the eSASS detection pipeline is fully tested by extensive and realistic simulated *eROSITA* images. The aim is to test if the available detection algorithms are able to detect the predicted $\sim 10^5$ galaxy clusters by *eROSITA*.

4.2 Comparison of wavelet-based source detection algorithms for *eROSITA* images

The eSASS pipeline has its origins on the XMM-SAS analysis package. Many of the scientists working on the *eROSITA* software system are or used to be responsible for the development and maintenance of XMM-SAS. Therefore, some of the eSASS tasks will be similar to their corresponding XMM-SAS. For example, the eSASS pipeline includes a source detection procedure based in the sliding-cell method of the XMM-SAS task `edetect_chain`. Although sliding-cell algorithms were amply used on the initial X-ray source detection procedures, they present some drawbacks on the detection and characterisation of extended sources (see Section 3.4.1), which are the aim sources of *eROSITA*.

The expectation of *eROSITA* detecting thousands of galaxy clusters strongly depends on the used detection algorithm. Then, it makes sense to investigate the performance of different detection algorithms.

Wavelet-based detection algorithms have some advantages over other detection procedures: they can separate close-by sources and are more effective in detecting sources regardless their shapes, surface brightness and extension. Moreover, wavelets do not require previous knowledge of the image background and can provide reliable estimations on the extent of the detected sources (see Section 3.4.1). Furthermore, wavelet-based detection algorithms have been successfully applied on different X-ray galaxy cluster surveys (e.g. Rosati et al. 1995; Vikhlinin et al. 1998; Pacaud et al. 2006; Lloyd-Davies et al. 2011). Given the impressive results achieved with such surveys, it is worth to test wavelet-based source detection algorithms over *eROSITA* simulated data.

In this section, the performance of different wavelet-based algorithms on simulated *eROSITA* images is estimated and compared. The goal is to find the most appropriate wavelet detection algorithm for *eROSITA* galaxy cluster detection. The comparison is done by using simulated images which take into account all instrumental effect and reproduce controlled source input configurations of two types of objects: point-like and extended sources. In the following, the X-ray image simulations and the wavelet algorithms are described. Then, different tests using only point-like, extended and a combination of both types of sources are discussed.

4.2.1 Simulation of controlled *eROSITA* images

As presented in Section 3.5, simulated data can help to understand and characterise the performance of the different source detection algorithms. With the aim to compare different wavelet-based detection procedures on *eROSITA* simulated data, an X-ray imager simulator was developed.

The simulator takes into account the main instrumental characteristics of *eROSITA* (see Table 4.1 for a summary) and considers two kinds of sources: point-like and extended sources. The simulated *eROSITA*

Parameter	Value
Image scale	4″/pixel
Image size	900×900 pixels
Exposure time	2 ks
Energy band	$[0.5 - 2]$ keV
PSF	25″
Total background	2.16×10^{-3} cts s^{-1} arcmin^{-2}

Table 4.1: Main instrumental characteristics of the simulated *eROSITA* images.

images aim to reproduce observations obtained from the all-sky survey, i.e. with a constant PSF (28″) across the FoV. The PSF for these simulations is modelled as a Gaussian function. The background value is taken from the White Book in the $[0.5 - 2]$ keV energy band.

Point-like sources, i.e. unresolved sources, represent more than 95% of the observed sources at X-ray wavelengths. Most of such sources are extragalactic X-ray objects: AGN. Extended sources are usually low surface brightness at X-ray wavelengths, they can be nearby galaxies or galaxy groups and clusters. For the purposes of this work, extended sources represent galaxy clusters and are modelled with a $\beta-$model profile (see Eq. 2.5).

4.2.2 Wavelet-based detection algorithms

Section 3.4.1 present a brief and concise description of wavelets. In this section, each of the selected wavelet-based source detection algorithms is described. A short summary of the main characteristics of the chosen procedures is given in Table 4.2.

`wavdetect`

`wavdetect`[2] is one of the *Chandra* wavelet-based detection techniques (Freeman et al. 2002). It consists of two parts: `wtransform`, which convolve the data with a wavelet function, and `wrecon`, which analyses the detected sources.

`wtransform` uses the "Mexican" hat wavelet function, which has a positively valued quasi-Gaussian core surrounded by a negatively valued annulus, and an overall zero normalization. The most important control parameters in `wtransform` are the set of scales and the significance threshold. The scale parameter determines the scale length (in pixel units) and the number of scaled transforms that will be computed on the data. The image is convolved with each of the successive larger scale values of the wavelet, obtaining several "correlation maps". In addition, for each scale, a background level is estimated from the negative annulus of the wavelet function. With these background values, several simulated source-free background images are created. For each pixel, a significance probability is calculated. This is obtained by comparing the pixel value distribution with its corresponding background distribution. If the pixel significance value is lower than the provided significance threshold, the pixel is assumed to be associated with a source. For each wavelet scale, `wtransform` creates a list of source pixels or correlation maxima.

---

[2] http://cxc.harvard.edu/ciao/ahelp/wavdetect.html

Procedure	Implementation	Version	Method
`wavdetect`	*Chandra* CIAO	4.2	Wavelet
`ewavelet`	XMM-SAS	6.12	Wavelet
`mr_detect`	MR/1	4.0	Multiscale Vision Model
`mr_filter+SE`	MR/1+`SExtractor`	4.0/2.4.4	Multiresolution filtering followed by SExtractor detection

Table 4.2: Short description of the selected wavelet-based detection algorithms.

For each wavelet scale, `wrecon` creates a "flux image". This image is obtained by smoothing the raw data at the corresponding wavelet scale, and then subtracting the background map created by `wtransform`. The mean value of the flux image is zero, except in the vicinity of a source, where the mean deviates considerably from zero. These regions are flagged as *putative* sources. Source properties are calculated inside the detection cells defined by minimizing the function $|\log_2 r_{\rm PSF} - \log_2 \sigma_F|$, where $r_{\rm PSF}$ is the size of the PSF encircling a given fraction of the total flux and σ_F is the size of the object at the scale closest to the PSF size. To create a final source list, `wrecon` cross-correlates the list of correlation maxima (obtained with `wtransform`) with the list of putative sources in each wavelet scale. If the number of correlation maxima lying inside a detection cell is zero, then the putative source is discarded. Finally, `wrecon` determines different properties for the final list of sources, such as the location, counts, exposure time and count rate.

`ewavelet`

`ewavelet`[3] belongs to the XMM-SAS package of the *XMM-Newton* telescope. `ewavelet` is similar to `wavdetect`: it also uses the "Mexican" hat function as wavelet transformation, the positive part of this function also acts as a source detector and the negative part acts as a measure of background level. The most important control parameters are also a set of scales and a significance threshold.

Unlike `wavdetect`, `ewavelet` assumes that sources have a Gaussian shape, and it uses circular symmetric wavelet functions. This reduces the number of convolutions and makes the task faster. The `ewavelet` algorithm is also simpler than `wavdetect`, it identifies sources by just cross-correlating all the correlation maxima of each wavelet scale. The source properties, like counts and count rate, are determined from the wavelet scale for which the correlation maximum peaks.

Mixed method: `mr_filter+SE`

`mr_filter` belongs to the Multiresolution package `MR/1` (Starck et al. 1998). `mr_filter` uses the *à trous* ("with holes") wavelet algorithm. This algorithm carries out discrete convolutions of the data with a filter of a successively broader kernel. This kernel is a B_3-*spline* scaling function. The wavelet images at different scales are obtained by differencing images at successive filter scales. As a result, the data image is decomposed in a number of wavelet images of growing scales plus a final smoothed image, which correspond to the last filtered array. `mr_filter` identifies the significant coefficients in each wavelet image with an especial treatment for the Poisson noise known as autoconvolution or wavelet histogram method (Starck & Pierre 1998), which estimate the PDF of the noise in the wavelet space assuming a flat distribution. The insignificant signal is then filtered directly in the wavelet space

---

[3] http://xmm.esac.esa.int/sas/current/doc/ewavelet/index.html

using a thresholding algorithm, which consists in setting all wavelet coefficients which have a value lower than a threshold to zero. Based on the significant coefficients, a filtered image can be obtained by an iterative reconstruction algorithm, which recovers the flux and shape of the structures in the data. The control parameters are also a set of scales for the wavelet transformation and a significance threshold for selecting the significant coefficients.

The source detection on the filtered images is performed by the `SExtractor`[4] software (Bertin & Arnouts 1996). Originally, `SExtractor` was developed to detect objects in optical data, but since the multiresolution filtering removes most of the noise in an X-ray image and produces a smooth background, `SExtractor` can also be applied to filtered X-ray images. Roughly speaking, `SExtractor` works as follows: it divides the image into boxes, where the sources are removed and a background is calculated. This process is repeated until the mean value in each box converges to a constant value. By applying median filtering, possible bright boxes are removed. Full background and background-RMS maps are obtained by bicubic-spline interpolation, which smooths the values between boxes. The background-RMS is a map of the background noise. This final background image is subtracted from the original image to obtain a background-free image. The background subtracted image is convolved with a compact support detection filter to bring out faint objects and divided by the background-RMS map to derive a signal-to-noise map used for the detection. Then, `SExtractor` isolates the objects by thresholding. `SExtractor` tries deblending on each isolated source to assure that the object is not composed of several sources. Finally, a detailed analysis of individual sources is delivered: source positions, shapes, photometry, etc.

mr_detect

`mr_detect` also belongs to the Multiresolution package MR/1 (Starck et al. 1998). `mr_detect` also uses the same wavelet algorithm, significant coefficient selection and image filtering methods as `mr_filter`. However, the `mr_detect` includes a source detection and characterisation algorithm, which is described in the following.

`mr_detect` uses the Multiscale Vision Model (MVM) for object identification. In this model, a set of connected significant wavelet coefficients in a given scale is known as a *structure*. Structures within different wavelet scales are connected to form *objects* by means of the "inter-scale relation". This inter-scale process works as follows: a structure $s_{1,j}$ at scale j is connected to a structure $s_{2,j+1}$ at scale $j+1$ if $s_{2,j+1}$ contains the pixel in $s_{1,j}$ with the maximum wavelet coefficient. There are two possible scenarios in this process:

1. If at given scale `mr_detect` detects two objects while in a lower scale it detects only one, then the algorithm reconstructs a single object.
2. If at given scale j `mr_detect` detects two objects which correspond to two objects at scale $j-1$ and one object at scale $j-2$, then the algorithm considers those initial objects as two separate sources.

The advantage of this process is that objects can be identified in wavelet space. The objects are reconstructed iteratively and the counts associated with each object are also computed.

---

[4] http://www.astromatic.net/software/sextractor

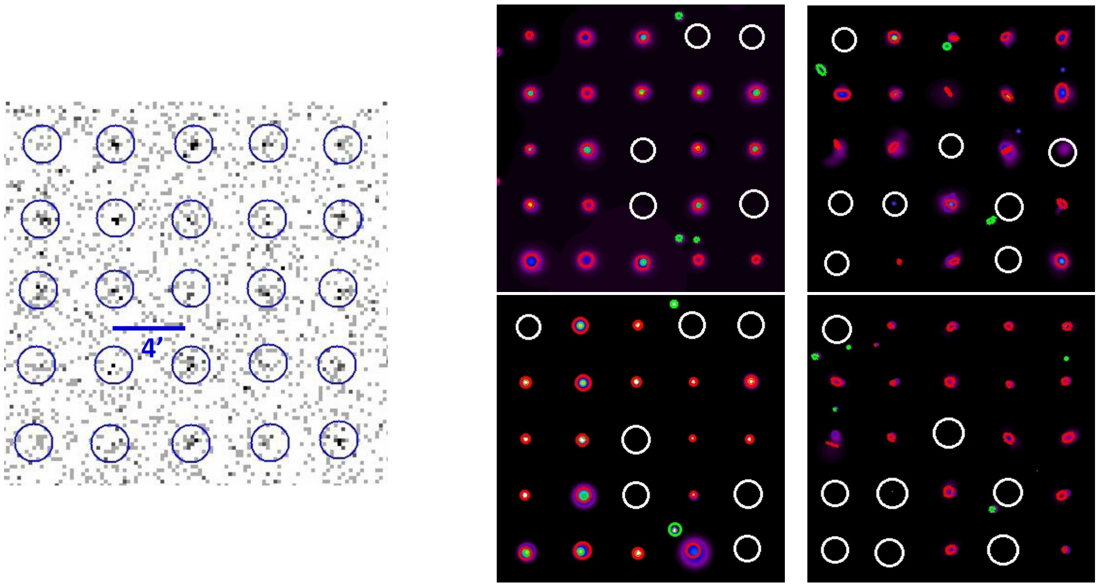

Figure 4.3: *Left*: Cut-out of a simulated X-ray photon image with only point-like sources. The sources have 10 counts and are marked by a blue circle. They are separated by 4′. *Right*: the `mr_filter` filtered image (*upper left*), the `wavdetect` (*upper right*), `ewavelet` (*lower left*) and `mr_detect` (*lower right*) reconstructed images. Overlaid on the images are the detected sources by each procedure (marked by red circles), the spurious sources (green circles) and the non-detected sources (white circles).

4.2.3 Simulations with only point-like sources

To characterise the performance of the different wavelet-based detection algorithms, the problem of point-like sources is first addressed. To do so, *controlled* source input configurations are used. In this way, source overlapping and *false* detections are under control.

A grid of 225 point-like sources is simulated within an image (see Table 4.1 for image characteristics). Each source is convolved with the *eROSITA* PSF, and the sources are separated by 4′ to avoid flux overlapping between them. From now on, 30 simulations constitute a set. Point-like sources have different fluxes in each simulated set: 5, 10, 15, 20, 40, 80 and 200 counts (or photons). An example of a simulated raw image is shown in Fig. 4.3, together with the `wavdetect`, `ewavelet`, and `mr_detect` reconstructed images, and the filtered image produced by `mr_filter`.

The performance of the different wavelet-based detection algorithms is quantified by testing their source detection efficiency, source position recovery and source photometry accuracy.

Source detection efficiency

In this test, the source detection efficiency as a function of false detections is computed for each wavelet-based detection algorithm. The goals are to examine the parameter space defined by these two quantities, and to choose a region within this space where the detection efficiency is maximum and the false detections are minima, i.e. where the detection algorithm detect as many input sources as possible with a low contamination by spurious sources. False or spurious sources are detected objects by the algorithm and are not part of the input source list.

Procedure	`wavdetect`	`ewavelet`	`mr_detect`	`mr_filter`
Minimum threshold	1×10^{-8}	1×10^{-8}	2×10^{-6}	2×10^{-6}
Maximum threshold	8×10^{-4}	2×10^{-4}	4×10^{-4}	8×10^{-2}
Minimum scale	2	2	1	3
Maximum scale	32	32	6	8

Table 4.3: Description of the main control parameters in the wavelet procedures.

Each wavelet algorithm is run over the different sets of point-like simulations. The wavelet scales are fixed and the significance threshold value is varied in each run. Table 4.3 shows the selected range of wavelet scales in each wavelet procedure and the significance thresholds.

The detection efficiency is obtained by cross-identifying the position of the detected sources with the position of the input sources. This cross-checking is performed within a radius of 60″. If more than one source lies within the cross-correlating radius, the closest and brightest source to the input position is taken as the true simulated source. The rest of the detected sources are considered false or spurious.

The detection efficiency of sources of distinct fluxes as a function of false detections for the different wavelet procedures is displayed in Fig. 4.4. Detection efficiency equals 1 means that all simulated sources have been detected by the wavelet algorithm. Each point of the plot is given by a run with different significance threshold. As previously mentioned, the significance threshold determines whether the wavelet transform identifies a given pixel as part of a source. If a given pixel has a lower significance threshold than the specified one, it is then identified as a source pixel. Therefore, the probability of detecting more false detections increases as the value of the significance threshold also increases.

The error displayed in the detection efficiency is given by a binomial law. This distribution is chosen since there are only two events to consider: detection and non-detection of the input sources. The error is given by

$$\sigma(P_s) = \frac{\sqrt{N_d(1-P_s)+1/4}}{N_s N_i + 1}, \tag{4.1}$$

where N_i is the number of simulated images, N_s the number of simulated sources, and N_d the number of detected sources. P_s is the detection rate of one source ($P_s = N_d/N_i N_s$). The error in the false detection rate is given by

$$\sigma_{\rm mean} = \frac{\sigma}{\sqrt{N_i}}, \tag{4.2}$$

where σ is the standard deviation of the false detection per simulation set, and $\sigma_{\rm mean}$ gives the standard deviation of the sampled mean.

Figure 4.4 shows that the overall performance of `mr_filter`+SE and `mr_detect` is better than `ewavelet` and `wavdetect`, especially when detecting faint point-like sources. One of the reasons for this is because `mr_filter`+SE and `mr_detect` are background independent algorithms, whereas `ewavelet` and `wavdetect` require an exposure map as an input to calculate a background map. As expected, by increasing the value of the significance threshold the detection probability and the false detection rate get larger. In general, 10 source counts are required to assure a point-like detection efficiency $\gtrsim$ 50%.

As mentioned previously, the goal of this exercise is to select parameters of the wavelet algorithms that allow detecting a maximum number of input sources with a minimum contamination by spurious sources. An acceptable contamination level on the simulations can be determined from the expected

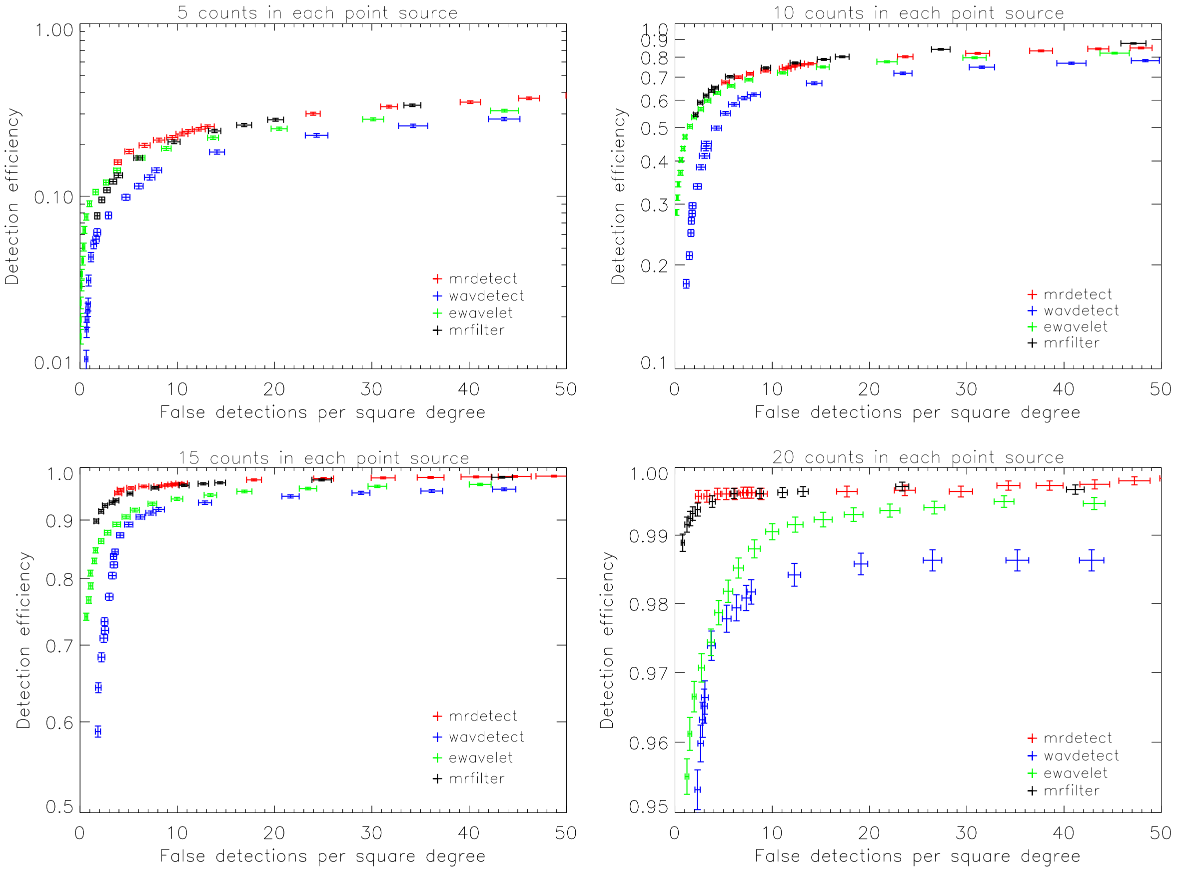

Figure 4.4: Detection efficiency as a function of false detections for point-like sources. Each colour represents a different wavelet procedure, and each point a different significant threshold (from left to right and in ascending order): red represent `mr_detect` with significance thresholds from 2×10^{-6} to 4×10^{-4}, blue shows `wavdetect` with significance thresholds from 1×10^{-8} to 8×10^{-4}, green stands for `ewavelet` with significance thresholds from 1×10^{-8} to 2×10^{-4}, and black is for `mr_filter+SE` with significance thresholds from 2×10^{-6} to 8×10^{-2}. Each plot corresponds to one set of simulations, which have different input flux for the point sources: 5 counts (*upper left*), 10 counts (*upper right*), 15 counts (*bottom left*), and 20 counts (*bottom right*). The detection efficiency is displayed in logarithmic scale and it changes from plot to plot.

source density on real *eROSITA* data. This is computed using the $\log N - \log S$ relation[5] from Moretti et al. (2003) down to a flux of 1.0×10^{-16} erg s^{-1} cm^{-2}. The background values are obtained from the *eROSITA* Science Boon (Merloni et al. 2012).

Assuming that all the point-like sources above 15 counts are detected, the count-rate in the average 2 ks survey will be 0.0075 cts/s for a flux of 1.065×10^{-14} erg s^{-1} cm^{-2}. This corresponds to a source density of 117.5 sources per square degree; so a false detection rate of about $1 - 2$ per square degree ($\gtrsim 1\%$) seems a good aim for the final catalogue. If one assumes that the wavelet-based detection algorithms would be followed by some cleaning (e.g. maximum likelihood fitting), then one can go as high as 20% contamination, which corresponds to $\sim 20-23$ false detections per square degree. At this contamination level, the wavelet algorithms detect most of the 15 counts sources, and nearly $> 70\%$ of the 10 counts sources. This contamination rate corresponds to a significance threshold in each wavelet algorithm: for

---

[5] The $\log N - \log S$ relation gives the number of sources, N, at a given flux, S.

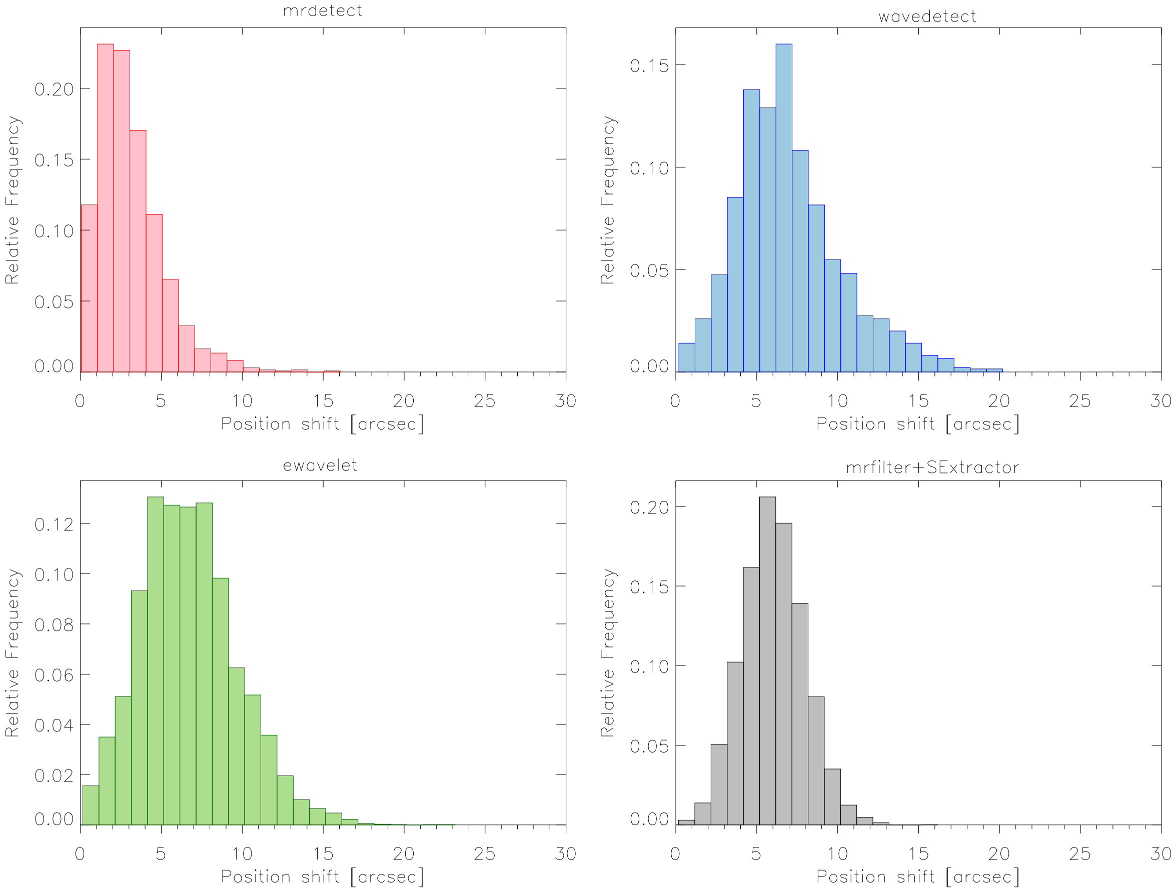

Figure 4.5: Histograms showing the positional accuracy on point-like sources for the different wavelet procedures. The position shift represents the distance between the input positions of the simulated sources and the positions of their corresponding closest detected sources.

`wavdetect`, 6×10^{-5}; for `ewavelet`, 3×10^{-5}; for `mr_detect`, 3×10^{-5}; and for `mr_filter`, 2×10^{-4}. The following tests are performed using just the set of simulations with these thresholds.

Positional accuracy

The convolution of the simulated sources with the PSF can lead to a displacement of the input source position, especially given the broad *eROSITA* PSF (28″). To estimate this positional shift, the distance between the input positions of the sources and the positions of their corresponding closest detected sources is measured. This information is obtained from the simulations with brightest sources (20 counts) since these sources have a high detection efficiency.

The results for each wavelet-based detection algorithm are shown in Fig. 4.5. It is clear that all the wavelet procedures detect the simulated sources within 20″ of their original position, which is lower than the *eROSITA* PSF, 28″. Except for `mr_detect`, the wavelet procedures have a peak of $\gtrsim 1$ pixel (6″) in the positional shift. This test shows that it is secure to assume that point-like sources are detected within a radius of 20″.

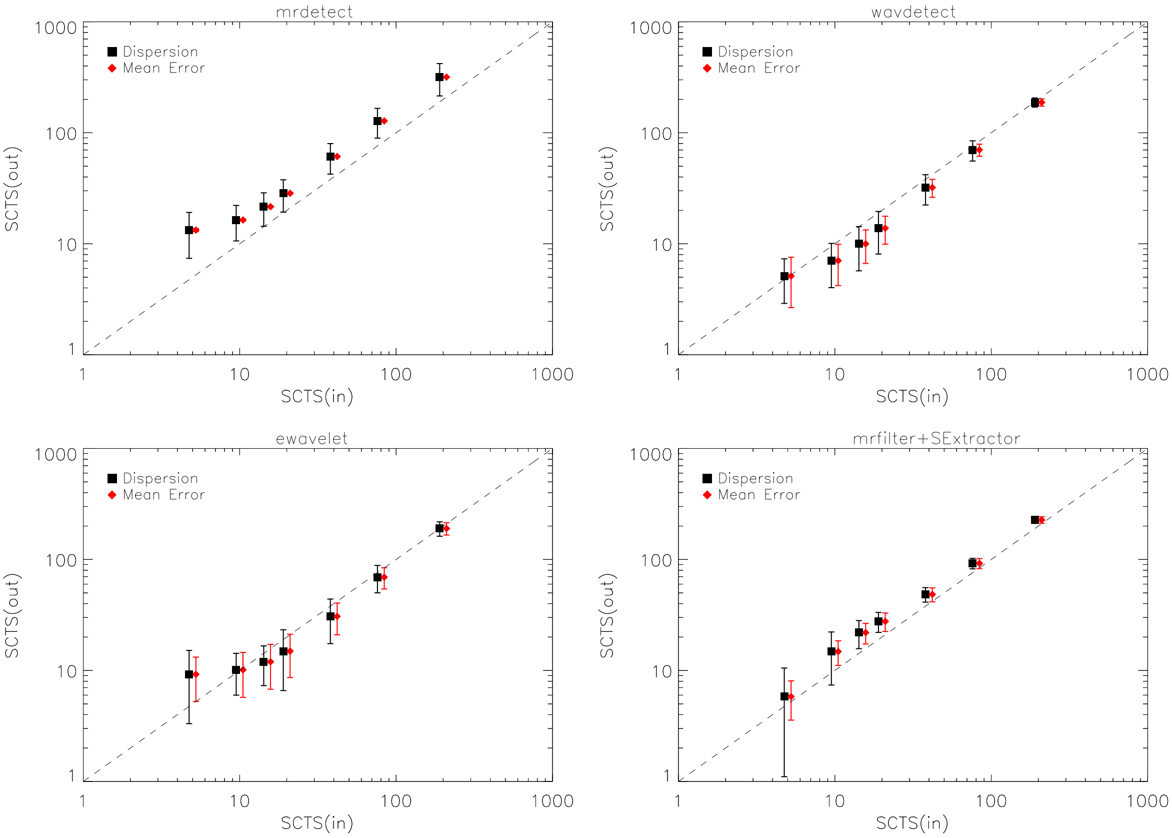

Figure 4.6: The plots show the results of inferred counts, SCTS(out), as a function of their corresponding input counts, SCTS(in), for the four wavelet-based detection algorithms. The black error lines show the standard deviation of the estimated flux over all detected sources, whereas the red error lines show the mean of the determined flux errors.

Photometric accuracy

The photometry recovery of the wavelet-based detection algorithms is tested. This is done by comparing the determined source counts, $\mathrm{SCTS}_i(\mathrm{out})$, by the algorithms with the input source counts, $\mathrm{SCTS}_i(\mathrm{in})$. Each wavelet algorithm not only estimates the number of source counts, but also its corresponding error ($\sigma_i(\mathrm{out})$). The results are shown in Fig. 4.6.

In Fig. 4.6 both types of data points represent the mean number of counts ($\overline{\mathrm{SCTS(out)}}$) over all sources in a given set of simulations. The black error bars display the standard deviation over the measured number of counts. The red right-side vertical bars are given by the mean of the individual determined errors: $\sigma_{\mathrm{mean}} = \overline{\sigma_i(out)}$. This analysis is performed in order to detect possible biases in the photometric errors: for instance, if the mean of the errors is larger than the standard deviation of the measured number of counts, the wavelet algorithm overestimate the measurement uncertainties.

`mr_detect` and `ewavelet` have trouble reconstructing the flux of very faint sources (5 counts). For `mr_filter+SE` and `ewavelet` the dispersion of SCTS(out) is larger for the faintest sources. `mr_detect` and `mr_filter+SE` overestimate the flux at any input by $\gtrsim 50\%$ and $20 - 40\%$, respectively. On the contrary, `ewavelet` and `wavdetect` underestimate the source flux by $10-30\%$. The general flux

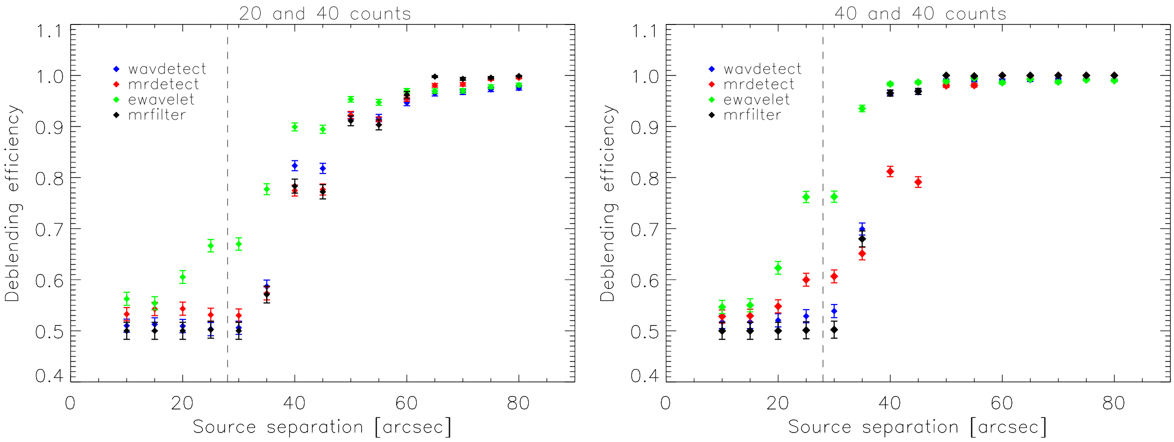

Figure 4.7: Deblending efficiency of the wavelet procedures as a function of source separation for close-by point sources. Deblending efficiency equal 1 means that both sources in the simulated pair are recovered and detected, while an efficiency equal to 0.5 means that the simulated pair is detected as a single source. The sources in the simulated pair have fluxes of: 20 and 40 counts (*left panel*), and 40 counts (in both sources *right panel*). The dashed line shows the *eROSITA* PSF, 28″.

error reconstruction is lower for brighter sources than for fainter sources, where the flux determination is more difficult.

Deblending capabilities

The source deblending capabilities of each wavelet-based detection algorithm are also tested. This test is important because blended sources affect the source photometry and the source detection efficiency.

For this particular test, other kinds of controlled simulations were created. In these simulations, pairs of point-like sources are placed in a grid, and the sources are separated by different distances: from 10″ to 80″, in steps of 5″. Moreover, the pair of sources has different flux ratios: $20-40$ and $40-40$ counts.

The deblending efficiency as a function of source separation of each wavelet algorithm is shown in Fig. 4.7. Three different cases can be distinguished in the deblending efficiency plot: detection of both sources (deblending efficiency equal 1), detection of a single source because both sources have been merged (deblending efficiency equal 0.5), and non-detection of the pair of sources (deblending efficiency equal 0). The deblending efficiency error is given by Eq. 4.1.

Figure 4.7 shows that below 40″ all the wavelet procedures identify the simulated pair of sources as a single source. This is expected, since the *eROSITA* PSF is rather broad, 28″, making impossible to disentangle both sources below this value. When the pair of sources are separated by 40″ or more, all wavelet-base detection algorithms can mostly ($> 80\%$) identify the individual sources.

Discussion

The overall performance of the wavelet-based detection algorithms over point-like sources is acceptable. The four wavelet procedures have similar results in the source detection efficiency, photometric reconstruction and deblending capabilities.

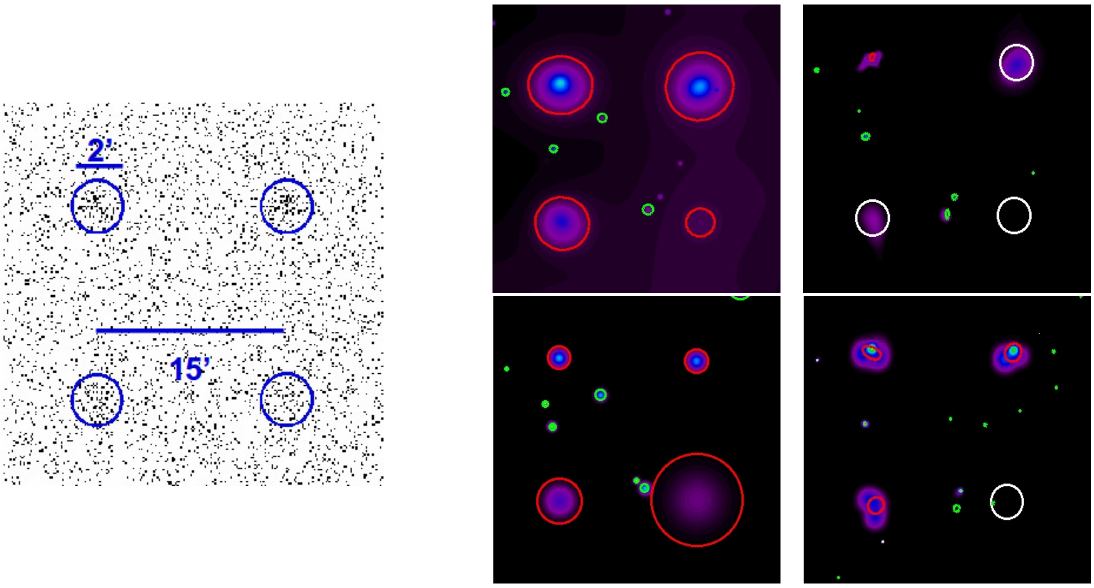

Figure 4.8: *Left*: Cut-out of a simulated X-ray photon image with only extended sources. The sources have 80 counts and are marked by a blue circle. They are separated by 15′. *Right*: the `mr_filter` filtered image (*upper left*), the `wavdetect` (*upper right*), `ewavelet` (*lower left*) and `mr_detect` (*lower right*) reconstructed images. Overlaid on the images are the detected sources by each procedure (marked by red circles), the spurious sources (green circles) and the non-detected sources (white circles).

`wavdetect` and `ewavelet` show a slightly lower detection efficiency than `mr_filter`+SE and `mr_detect`. This can be explained by a possible background overestimation by `wavdetect` and `ewavelet`. This will overshadow the source emission, and, therefore, the algorithm misses the detection of the source. On the contrary, `mr_detect` and `mr_filter`+SE do not need a background estimation for source detection, since the source analysis is performed in the wavelet space. This gives a better performance in the source detection efficiency.

A general conclusion for all wavelet-based detection algorithms is that sources with at least 10 counts have $\geq$ 80% of probability to be detected, and its position recovery is within 20″. The photometry is well recovered within the errors, `wavdetect` and `ewavelet` underestimate the flux of the sources by $\lesssim$ 10%, and `mr_detect` and `mr_filter`+SE overestimate the flux by $\lesssim$ 20%.

4.2.4 Simulations with extended sources

The analysis performed in Section 4.2.3 is repeated over simulations with extended sources. These objects are modelled with a β–profile (see Section 2.1.2), with $\beta = 2/3$ and a fixed core radius of value $r_c = 1'$. The controlled source input configuration consists of a square grid of 16 extended sources, which are separated by 15′ to avoid source overlap. Each simulated source is convolved with the *eROSITA* PSF. 30 different sets of simulations were created and each set has a different input source fluxes: 40, 60, 80, 100, 200, and 500 counts. An example of a raw photon image and the filtered/reconstructed images from the wavelet-based detection algorithms are shown in Fig. 4.8. In this figure one can see the circular shape of the detected extended sources on the reconstructed image by `ewavelet`, the reason being the used symmetrical wavelet function.

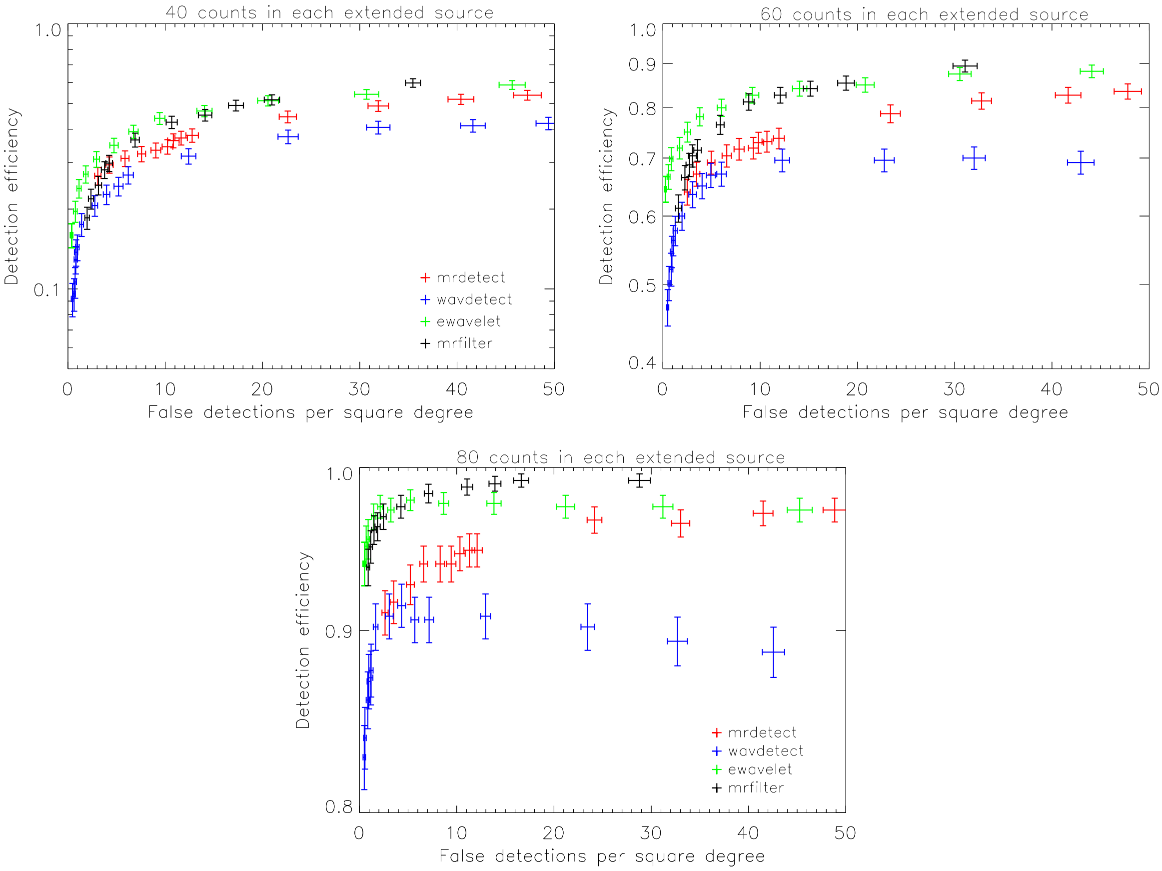

Figure 4.9: Detection probability as a function of false detections for extended sources. Each colour represent a different wavelet procedure, and each point a different significant threshold (from left to right and in ascending order): red represent `mr_detect` with significance thresholds from 2×10^{-6} to 4×10^{-4}, blue shows `wavdetect` with significance thresholds from 1×10^{-8} to 8×10^{-4}, green stands for `ewavelet` with significance thresholds from 1×10^{-8} to 2×10^{-4}, and black is for `mr_filter`+SE with significance thresholds from 2×10^{-6} to 8×10^{-2}. Each plot corresponds to one set of simulations, which have different input flux for the extended sources: 40 counts (*upper left*), 60 counts (*upper right*), and 80 counts (*bottom*). The detection efficiency is in logarithmic scale and it changes from plot to plot to show the differences more clearly.

In the following, the same performance test as in Section 4.2.3 are applied to the wavelet-based detection algorithms but using the extended source simulations. To avoid repetition, details on error calculation and plot description are omitted.

Source detection efficiency

The detection efficiency as a function of false detections for each wavelet algorithm is shown in Fig. 4.9. The cross-correlation radius is set to 90″. If more than one source lies within the search radius, the most extended objects is taken as the true simulated source.

Figure 4.9 shows that the best detection performance is achieved with `mr_filter`+SE. Although `ewavelet` shows a slightly higher detection efficiency for low significance thresholds, for high-flux sources its detection efficiency decreases with the significant threshold. This last erratic behaviour is also presented

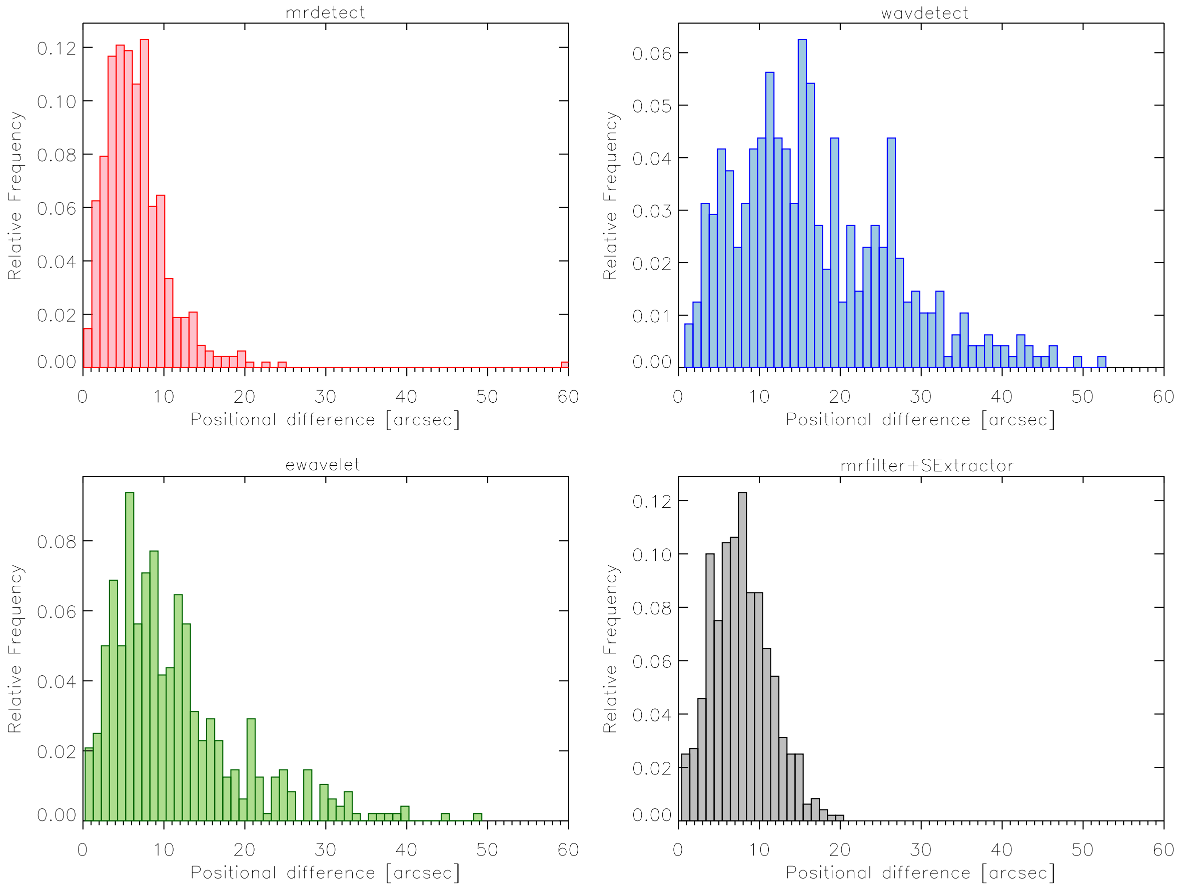

Figure 4.10: Histograms showing the positional accuracy on extended sources for the different wavelet algorithms. The position shift is estimated from the distance between the source input positions and the positions of their closest detected sources.

by `wavdetect`, which also shows the poorest efficiency in the detection of extended sources. This can be explained by the form that `wavdetect` defines its source detection cell (see Section 4.2.2). Extended sources may have more than one local maximum at a given wavelet scale, which can lead to multiple detections. And this seems to be the reason for `wavdetect` not detecting the extended sources. One way to overcome this issue is by increasing the detection cell size, however, this would also increase the probability that other close-by sources will be blended with the extended source.

It is worth to mention that the significance thresholds of the four wavelet algorithms produce a very similar number of false detections as in the simulations with only point-like sources. Therefore, the selected significance thresholds in the previous section are valid for the following tests.

Positional accuracy

As mentioned previously extended sources may have more than one local maximum at a given wavelet scale, leading to multiple source detections. Or when the source reconstruction is taking place, the source centroid can be affected given the extension of the source and the PSF of the telescope.

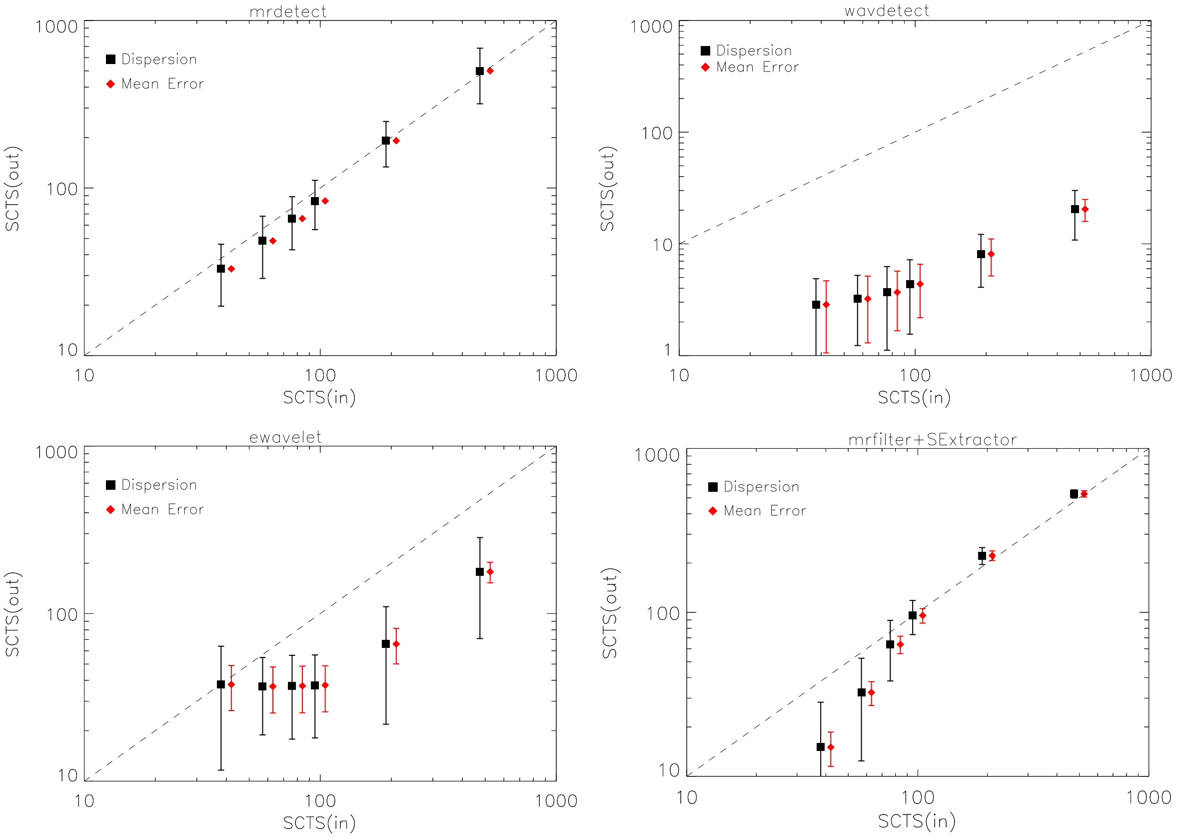

Figure 4.11: The plots show the results of inferred counts, SCTS(out), as a function of their corresponding input counts, SCTS(in), the four wavelet detection procedures. The black error lines show the standard deviation of the estimated flux over all detected sources, whereas the red error lines show the mean of the flux error determination.

Figure 4.10 shows the distance between the source input positions and the positions of their corresponding closest detected sources for the four wavelet algorithms. `mr_detect` and `mr_filter+SE` show a similar positional recovery as with the point-like sources (within $\lesssim 20''$). On the contrary, the positional shift distribution of `ewavelet` and `wavdetect` gets wider ($\lesssim 50''$), meaning that the recovered position of the simulated source is shifted or that the source gets split in various sources around the input position. In any case, a correlation radius of $60''$ seems to secure the detection of the simulated extended sources.

Photometric accuracy

The results of the photometric reconstruction for the four wavelet algorithms over extended sources are shown in Fig. 4.11.

`wavdetect` underestimates the flux of the extended sources by almost an order of magnitude. This could be improved by increasing its detection cell size, but if close-by sources are blended during this process, the new estimated flux will not be properly determined again. `ewavelet` also shows a bad performance in the photometric estimation. This can be explained by the fact that `ewavelet` uses only the wavelet scale of the maximum of the convolved source for count-rate estimation. Therefore, if the

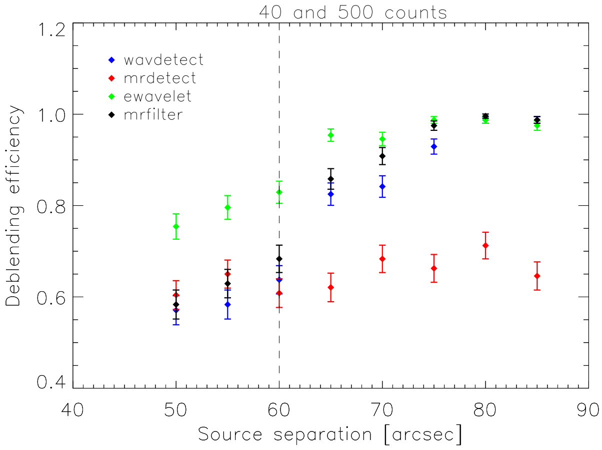

Figure 4.12: Deblending efficiency of the wavelets algorithms as a function of source separation for close-by sources. The sources have fluxes of 40 counts for the point-like source and 500 counts for the extended source. The dashed line shows the core radius value (60″) of the simulated extended sources.

maximum occurs at the largest scales, the information in the lower scales is lost and is not used in the photometric estimations.

`mr_detect` shows good flux estimation, i.e. within the dispersion of the flux distribution the simulated flux is recovered. However, the error in the flux measurements is strongly underestimated. `mr_filter+SE` shows problems in recovering the flux of the faintest extended sources, with $\lesssim$ 60 counts. However, above this flux, the photometric recovery is very precise.

Point-like plus extended sources

For this exercise, a new kind of controlled simulations was produced. These simulations include pairs of sources, formed by an extended and a point-like source, arranged into a grid. The sources are separated by different distances, from 50″ to 85″, in steps of 5″, and have different fluxes: 40 counts in each point-like source and 500 counts in each extended source.

The deblending efficiency as a function of source separation for the four wavelet algorithms is shown in Fig. 4.12. `wavdetect`, `ewavelet`, and `mr_filter+SE` show a smooth increment of the deblending efficiency as the distance between the pair of sources increases. The dashed line shows the core radius value of the simulated extended sources, and even within this distance separation, the wavelet algorithms are capable of detecting both sources, although with a small probability. `ewavelet` is the wavelet procedure that deblends close-by sources more efficiently. `mr_detect` shows a constant and low deblending efficiency, $\sim 65\%$, through all source separations.

Discussion

The detection and characterisation of extended sources are a challenging job for the wavelet-based detection algorithms. From the analysis presented above, `mr_filter+SE` seems to be the best detection algorithm for extended sources. The same conclusion was reached by Valtchanov et al. (2001), who tested different detection algorithms with simulated *XMM-Newton* images. Although `mr_detect` is similar to `mr_filter` the detection and deblending efficiency is lower, meaning that the source reconstruction method, the Multiscale Vision Model, is not fully recovering the simulated sources. `wavdetect` and `ewavelet` have problems detecting and restoring the fluxes of the extended sources. The flux estimation for both procedures is similar in the sense that the characterisation cell size, within which the flux is computed, is taken from the wavelet scale where the size of the detected object is similar to the wavelet scale or PSF. Therefore, if the characteristic size of an object is larger the procedures will tend to underestimate the flux.

4.2.5 Conclusions I

Various wavelet-based detection algorithms for detecting and characterising point-like and extended X-ray sources were tested on simulated *eROSITA* X-ray images. The goal was to find a suitable wavelet detection algorithm for *eROSITA*. The detection efficiency and the recovery of different characteristics of the input objects, such as flux, positional accuracy and deblending capabilities were tested.

From the four tested wavelet algorithms, `wavedetect` shows the lowest detection efficiency for point-like and extended sources and the poorest characterisation of extended sources. This algorithm is well known for being efficient in detecting point-like sources on *Chandra* observations. However, *Chandra* and *eROSITA* have very different imaging features, making difficult the source characterisation by `wavedetect` on simulated *eROSITA* data.

`ewavelet` shows a good performance in the detection and deblending of point-like and faint extended sources. However, the photometric reconstruction, as well as the detection of bright extended sources, is unreliable. `mr_detect` shows good results for most of the tests, it has high detection efficiency for point-like and extended sources and the photometric recovery is precise, although, it underestimates the error on the measured flux. The main drawback of `mr_detect` is that cannot properly deblend point-like sources that are close to extended one. It seems that the algorithm assumes that point-like sources are just local minima at small wavelet scales, and, therefore, it merges both sources.

The `mr_filter+SE` procedure seems to be the best performer of the four wavedetect procedures, even though this method is a mixed approach consisting of two distinct steps. `mr_filter+SE` has good detection efficiency for both, point-like and extended sources. The position recovery is very similar for both types of sources as well. Although, it tends to slightly overestimate the flux of the sources, it performs well in the photometric recovery of point-like and extended sources. The same applies to the deblending efficiency of both types of sources.

Source classification

Until now, the problem of classifying sources as point-like or extended, i.e. unresolved or resolved, has not been addressed. This is an important step for the detection of galaxy clusters by *eROSITA*, since there is not multi-wavelength follow-up of the whole sky to confirm the nature of all its detections. The ideal case is when the detection algorithm, extensively tested by simulations, builds reliable samples of extended sources and point-like sources, and if required, only the extended sources can be observed in other wavelengths to confirm the source nature.

The tested wavelet-based procedures are "just source detection algorithms", and they estimate in a simple way different source parameters, like the extension and count-rate. The exception is the `SExtractor` software, which offers a parameter for source classification, the stellarity index (see Bertin & Arnouts 1996, for details). This parameter is often used to distinguish between stars (point-like sources) and galaxies (extended sources) in optical images. Although it can give good results in combination with `mr_filter` for X-ray images (Valtchanov et al. 2001), it presents a high misclassification rate, i.e. many point-like sources are classified as extended.

One can establish criteria for source characterisation by exploring and looking for indicators in the output parameter space of the wavelet detection algorithms. For example, by looking at the estimated source extent, the ratio between the estimated semi-minor and semi-major axis of the source, the estimated area of the source, etc. These indicators depend on the output parameters that each algorithm offers. The right combination of parameters can be a robust source discriminator, and additional parameters can be added for ambiguous cases.

As presented in Section 3.4.1, the source classification can be achieved by means of a maximum likelihood fitting method. This approach calculates the probability and models the observed spatial photon distribution. In this way, point-like and extended source probabilities can be assigned to each detected source. In the following sections, such method will be used with the eSASS detection algorithm. Chapter 5 presents an application of the `mr_filter+SE` detection algorithm together with a maximum likelihood fitting method for source classification.

4.3 Comparison of source detection algorithms for *eROSITA* images

The next step in the characterisation of source detection algorithms is to test the detection procedures in more realistic simulations, where source confusion and source blending effects are important. For this purpose, simulated extragalactic fields which include point-like and extended sources are used. These simulations also take into account all the *eROSITA* instrumental effects.

As mentioned in Section 4.1, the eSASS package includes a source detection algorithm based on the sliding cell method. Since one of the aims of this thesis is to find a suitable source detection algorithm for *eROSITA*, it is natural to also test the eSASS source detection pipeline.

It is important to stress that during the development of this work there have been several changes, updates and developments on the realistic simulations and the eSASS pipeline. Therefore, in the following sections, different versions of simulations and the eSASS pipeline are used. Moreover, details of the distinct releases of the synthetic simulations and the general eSASS source detection pipeline are described.

4.3.1 Simulations of realistic *eROSITA* images

The synthetic *eROSITA* simulations were produced by Dr. Nicolas Clerc at the Max-Planck Institute for Extraterrestrial Physics (MPE) in Garching, Germany. The simulations represent a 4-year all-sky survey, and were created with the SIXTE simulator (see Section 3.5). The simulated fields contain AGN (point-like sources), galaxy clusters (extended sources), galactic background and particle background. The simulations include all instrumental effects: PSF, vignetting, detector masks, etc. The adopted cosmological parameters are: $\Omega_\mathrm{m} = 0.3$, $\Omega_\Lambda = 0.7$, $h = 0.72$. The main purpose of these simulations is to provide support to different *eROSITA* preparatory tasks, such as source detection and characterisation, testing detection algorithms, stacking analysis, selection function calculation, etc.

In these simulations, the sources have been simulated with realistic spectra and flux distributions. Galaxy clusters are modelled by a β-profile (Cavaliere & Fusco-Femiano 1976) with $\beta = 2/3$ and for different core radii and fluxes. Their spectra are generated with the `XSPEC` spectral fitting package (Arnaud 1996) using an `APEC` model and a galactic hydrogen absorbing column density, $n_{\rm H}$, adapted to the simulated field. The number of simulated galaxy clusters per field is not realistic (~ 2 per deg^2) and they are randomly distributed in the FoV (overlaps can happen). The AGN population is sampled from the $[0.5 - 2]$ keV Hasinger et al. (2005) luminosity function, and it is constructed following the Gilli et al. (2007) model. The AGN positions are also randomly distributed in the field.

There have been two releases of the synthetic simulations, which are briefly described in the following. Further information can be found in the *eROSITA* internal web pages under the section: Synthetic Simulations.

Release January 2013

The synthetic simulations of this release were created with SIXTE (version December 2012). Three different sky regions (or fields, shown in Fig. 4.1) of size 3.6×3.6 deg^2 were simulated. Such fields have an exposure time that is representative of the future *eROSITA* all-sky survey. The constructed AGN $\log N - \log S$ in each field contains many objects with fluxes well below the detection limit. Therefore, a lower flux threshold has to be determined. The source spectra below this threshold are stacked and considered as an uniform background over the simulated field. The characteristics of each field are:

- Equatorial, with ~ 1.6 ks, $n_{\rm H} = 3.0 \times 10^{20}$ cm^{-2} and flux limit of 3.0×10^{-15} erg s^{-1} cm^{-2}.
- Intermediate, with ~ 4 ks, $n_{\rm H} = 8.8 \times 10^{20}$ cm^{-2} and flux limit of 1.0×10^{-15} erg s^{-1} cm^{-2}.
- Polar, with $\sim 20 - 200$ ks, $n_{\rm H} = 4.4 \times 10^{20}$ cm^{-2} and flux limit of 2.0×10^{-16} erg s^{-1} cm^{-2}.

For each field and for all the 7 *eROSITA* CCDs, which are considered as identical, two types of simulations were produced: an "AGN+background" and a "cluster only" simulation. As the name indicates, "AGN+background" simulations contain the AGN population and the galactic and particle background, whereas "cluster only" simulations contain only a population of galaxy clusters. In order to save computing time, only one "AGN+background" simulation per field is produced. This "AGN+background" simulation is merged with a "cluster only" simulation to obtain a complete and realistic simulated *eROSITA* observation.

Each "cluster only" simulation contains galaxy clusters with the same flux and core radius. In this way, there is enough statistics for the analysis of each type of cluster. The galactic absorbed fluxes of the simulated clusters are: 1×10^{-14}, 5×10^{-14}, 1×10^{-13} and 5×10^{-13} erg s^{-1} cm^{-2}. These fluxes are simulated at two different redshifts: $z = 0.3, 0.8$; and for two galaxy cluster temperatures: $T = 1.0, 5.0$ keV. Moreover, galaxy clusters were simulated with nine distinct core radius ($r_{\rm c}$) values: $20''$, $25''$, $30''$, $35''$, $40''$, $50''$, $70''$, $90''$, $120''$. The combination of all these characteristics gives a total of 144 "cluster only" simulations per field.

The simulation release includes event files, images, exposure maps and region files. The images and exposure maps were created in the $[0.5 - 2]$ keV energy band with $4''$/pixel binning.

Release July 2014

The simulations in this release are very similar to the ones in the Release January 2013. In the following, only the major changes are briefly mentioned. A newer version of the SIXTE simulator (July 2014) was used, as well as newer models of PSF and vignetting (June 2014). The simulations also include a shift of 0.4 mm in the focus of the telescope. G. Lamer, S. Thater, C. Schmid and P. Friedrich shown that the defocusing of telescopes improves the eRASS sensitivity and the off-axis PSF. Although, the on-axis PSF gets slightly wider.

A finer grid of core radius values and fluxes for the "cluster only" simulations was implemented. The new galaxy cluster fluxes are: 2×10^{-15}, 5×10^{-15}, 1×10^{-14}, 2×10^{-14}, 3×10^{-14}, 5×10^{-14}, 1×10^{-13} and 5×10^{-13} erg s^{-1} cm^{-2}. And the values of the core radius are: $20'', 25''$, $30''$, $35''$, $40''$, $50''$, $80''$, $120''$. This gives a total of 256 simulations per field.

A new sky region was also simulated: Deep, with $\sim$ 20 ks in exposure time and $n_{\mathrm{H}} = 6.3 \times 10^{20}$ cm^{-2}. Moreover, 15 "AGN+background" simulations per field were created by randomizing the positions of the original AGN list.

Contrary to the Release January 2013 set, the Release July 2014 only offers the 7 CCD event files of each simulation. It is up to the user to merge the "AGN+background" and "cluster only" simulations and to produce final products. In Section 4.4.1 the process of producing images from these event files will be described.

4.3.2 eSASS source detection pipeline

The eSASS source detection pipeline follows the "*XMM*-style" for source detection, i.e. it is based on the sliding cell method and maximum likelihood fitting (see Section 3.4.1). The detection routine has been developed by Dr. Georg Lamer (Leibniz Institute for Astrophysics Potsdam, AIP) and forms the source detection chain within the eSASS data reduction pipeline (maintained by Dr. Hermann Brunner at the MPE).

The eSASS source detection pipeline calls different eSASS tasks that can run simultaneously over several instruments and energy bands and over different observing modes (pointed mode, survey mode and raster scans). In the following, a brief description of each task and the important input parameters is presented:

- `ermask` creates a detector mask (with values equal to 1) based on the exposure map. The detection task uses the mask to limit the detection to areas where the mask equals to 1.

- `erbox` (in local background mode) uses a $n \times n$ pixel box (user-specified `boxsize` parameter) and a surrounding (2 pixels) background area to search for significant sources. It also offers an optional β-profile kernel to smooth the images before the detection stage by setting `boxsize`= 4 (9×9 pixel box). The kernel is chosen to match the HEW of the survey PSF in the pixel box. The detection of extended sources is possible thanks to subsequent runs, where the box size is doubled (`nruns` parameter). The detection likelihood is calculated from the likelihood of the best fit and the likelihood of a null model, i.e. a model of a source with zero count rate, in a circular source aperture. If the detection likelihood value exceeds the user-specified threshold, set by `likemin`, the source is written to the final source list.

- `erbackmap` uses the source list from `erbox` (in local background mode) to remove sources from the input images and creates smooth background map by fitting a 2D spline to the source free image. The source cut-out radii is calculated from the `erbox` extent information. The parameter `nsplinenodes` determines the number of spline nodes/spatial bins per dimension.

- `erbox` (in map mode) estimates the background from the output of `erbackmap`, and then performs the same source detection as in local background mode.

- `ermldet` uses the source list from `erbox` (in map mode) and determines parameters for each input source by means of a maximum likelihood fit to the input image. The source parameters are calculated by fitting the PSF convolved with a source extent model (β-profile) to the distribution of counts of the sources detected by `erbox`. Several source parameters can be set to define the source model:

  - `likemin` is the minimum detection likelihood. It is recommended to use a higher detection threshold than for `erbox`, in this sense `ermldet` makes the final choice on what is a source.
  - `extlikemin` is the minimum extension likelihood.
  - `extmin` is the minimum source extent in pixels.
  - `extmax` is the maximum source extent in pixels.
  - `nmulsou` determines the maximum number of input sources used to fit one input source.
  - `nmaxfit` is the maximum number of input sources which can be fitted simultaneously.

  The detection likelihood is calculated using the likelihood ratio described by Cash (1979, see Section 3.4.1). Furthermore, `ermldet` offers the possibility to fit two or more point sources, where an extended source is detected, and if the likelihood of the multi-point source fit is larger the source is split and the source parameters are re-calculated. In the output list, only sources with likelihood values above the user-specified ones are kept.

`ermldet` assigns to each detected source a set of parameters characterising its properties. For example, position, sky coordinates and count-rates. For this work, three output `ermldet` parameters are the most relevant: *i*) *detection likelihood* gives the significance of the detection; *ii*) angular *extent* is the apparent extension of the best fitting β-model; and *iii*) *extension likelihood* compares the significance of the extended model and the point-like model. This last parameter basically classifies the detected sources as point-like (value equal zero) or as extended-like (value greater than zero).

4.3.3 Comparison of sliding-cell and wavelet source detection methods

In this section, different tests are carried out to compare the performance of the eSASS source detection pipeline with the best wavelet-based source detection algorithm found in Section 4.2, `mr_filter`+SE. For this analysis, the simulated images of the Intermediate field ($\sim$ 4 ks in exposure time) of the January 2013 release are used. The eSASS version used for this exercise is `fits_090304`, which has the following task versions: `ermask` version 1.1, `erbox` version 1.4, `erbackmap` version 1.4, `ermldet` version 1.6. The version of the joint procedure `mr_filter`+SE is the same as stated in Section 4.2.2. A list of the most relevant parameters used in each procedure is shown in Tables 4.4 and 4.5.

eSASS (`fits_090304`)			
Parameter	Value	Parameter	Value
`erbox` (local mode)		`ermldet`	
`emin`	500	`emin`	500
`emax`	2000	`emax`	2000
`ecf`	1.0	`ecf`	1.0
`nruns`	1	`likemin`	15.0
`likemin`	10.0	`extlikemin`	0.0
`boxsize`	2	`cutrad`	14.0
		`multrad`	14.0
`erbox` (map mode)		`extmin`	1.5
`nruns`	2	`extmax`	30.0
		`extentmodel`	beta
`erbackmap`		`thres_col`	like
`nsplinenodes`	8	`thres_val`	30.0
		`nmaxfit`	1
		`nmulsou`	1

Table 4.4: Relevant parameters of the eSASS detection pipeline (version `fits_090304`).

`mr_filter+SE`	
Parameter	Value
`mr_filter`	
Threshold	10^{-3}
Minimum scale	1
Maximum scale	9
`SExtractor`	
Detection threshold	3σ
Minimum detection area	32
Deblending subthresholds	64
Min. deblending contrast	0.001

Table 4.5: Relevant parameters of the `mr_filter+SE` detection algorithm.

Synthetic simulations with only point-like sources

In this section, different performance tests are carried out on the simulations that include only point-like sources, i.e. on the "AGN+background" simulation. As a reminder, sources detected by the eSASS detection pipeline are considered as point-like sources if they have an extension likelihood value equals zero. For `mr_filter+SE` it is still assumed that the detected sources correspond to the simulated ones.

The positional accuracy was first determined. The images obtained from the survey mode have a final averaged PSF across the entire image. Then, it is expected that all the sources are affected by the same positional shift. Given the broad *eROSITA* PSF in survey mode ($28''$), the initial searching radius is set to $40''$ for both detection algorithms. For each simulated object, the nearest detected source inside this radius is searched and cross-correlated with the source input list. The results show that more than $\sim 97\%$ of the cross-identified point-like sources lie within $30''$. Then, this value is adopted as search radius of point-like sources.

The point-like source detection efficiency as function of input flux is shown in Fig. 4.13. The plot shows that both detection algorithms, eSASS and `mr_filter+SE`, have a similar performance. Both procedures detect more than 90% of the sources above 2.0×10^{-14} erg s^{-1} cm^{-2}. Figure 4.13 does not display any error bars because the Release January 2013 only offers a single "AGN+background" simulation per field.

Another issue that has to be taken into account is the number of *missed* (non-detected) and *false* (spurious) sources detected by each algorithm. As mention earlier, a good source detection algorithm identifies as many as possible *true* sources with a low or null contamination by false detections. Valtchanov et al. (2001) have presented a number of issues that can originate false detections and lower the source detection efficiency:

1. False detections represent non-simulated objects or two or more simulated sources that are blended into a single detected object. In this latter case, the blended object becomes a false detection

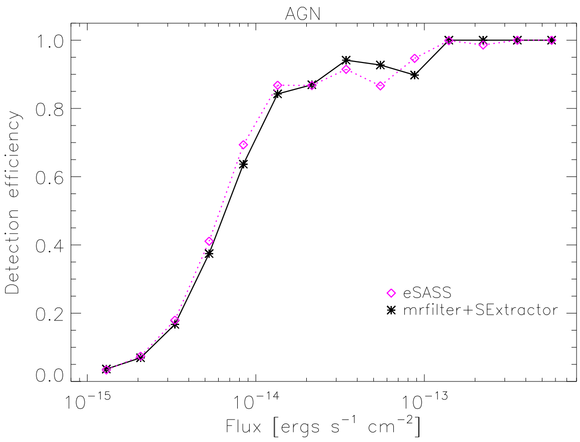

Figure 4.13: Detection efficiency as a function of input flux for point-sources for eSASS and `mr_filter+SE` pipelines in ~ 4 ks exposure (Intermediate field). It is not possible to add error bars since the analysis has been done over only one simulation (see text for more details).

if it is not in the input list or if its determined centroid has shifted beyond the searching radius.

2. It can happen that in the source cross-identification process the closest detected source to the input source position is not the simulated source.
3. Simulated objects can be missed by the detection algorithm because they are located in regions with high noise properties.

It is not easy to disentangle all the above issues, especially for faint sources which tend to be confused with the background and, therefore, missed. Moreover, these kinds of sources are more prone to blending effects if they are close to each other. Taking all these into account, the closest detected source to the input source will be considered as the *true* match, and the rest of detected sources as spurious detections.

The results on the false detection rate are: ~ 13 false detections per square degree for eSASS, and ~ 15 false detections per square degree for `mr_filter+SE`. These false detection rates represent a high level of contamination. For an all-sky survey, like the *eROSITA* one, the number of false detections would be too large, making very difficult and unreliable the use of such samples for any scientific purpose. In order to overcome this problem one can further explore the output parameter space of `ermldet`, to look for parameters that can help to distinguish between true and false detected sources, and, therefore, obtain cleaner samples. In the case of `mr_filter+SE` a further implementation of a maximum likelihood fitting method can reduce the contamination rate.

Synthetic simulations with point-like and extended sources

In this second exercise, simulations with point-like and extended sources are used. The images are created by merging the "AGN+background" with the "cluster only" simulations. As explained in Section 4.3.1, each "cluster only" simulation contains the same kind of galaxy cluster, i.e. with the same flux and core radius. In this way, one can obtain enough statistics on the detection efficiency of each type of galaxy cluster. The objective of this exercise is to estimate the capabilities of the eSASS and `mr_filter+SE` algorithms to detect and identify extended objects embedded in a point-like field. The point-like sources can change the local and global background properties and, therefore, lead to source

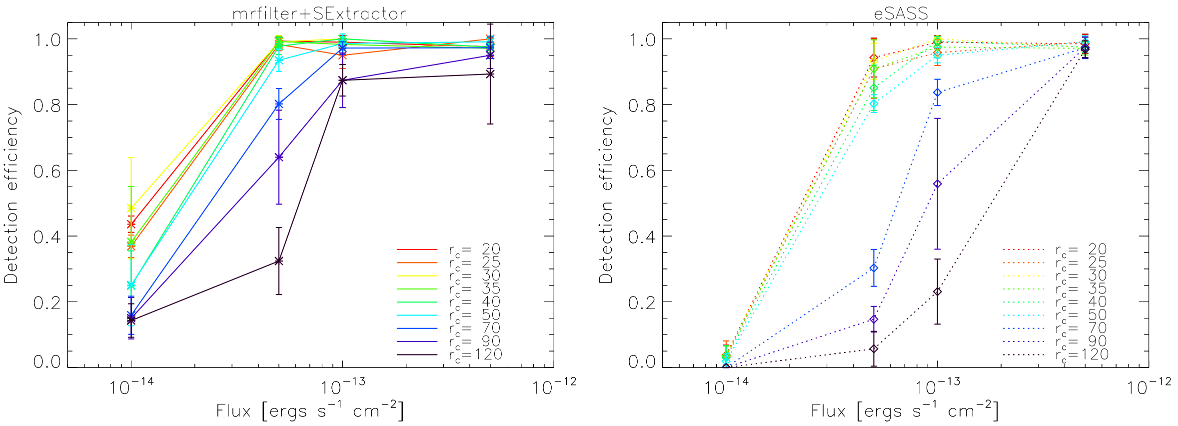

Figure 4.14: Detection efficiency as a function of input flux for extended sources by `mr_filter+SE` (*left*) and eSASS (*right*) with maximal contamination in ∼ 4 ks exposures (Intermediate field). Each colour represents a different galaxy cluster core radius (in arcsec).

confusion effects. Moreover, the presence of a point-like source near to an extended one can lead to source confusion, to a non-source detection or to a source misclassification. This can affect faint extended sources, even when the nearby point-like source is also faint.

As shown in Section 4.2.4, the recovered position of extended sources is usually more displaced from the simulated position than the determined position of point-like sources. Moreover, the fainter the extended source the larger is the displacement from the simulated position. This issue will become clear in the next section. For this exercise, a search radius of 60″ is chosen in both detection algorithms.

The extended source detection efficiency as a function of input flux for both algorithms is shown in Fig. 4.14. There are just four different fluxes for galaxy clusters in the Release January 2013 simulations, hence the only four points in the plot. The error bars display the standard deviation. Again, for `mr_filter+SE` the closest detected source to the input position is assumed to be the true match, while for eSASS only sources with extension likelihood greater than zero are considered as extended sources. Both algorithms show a good performance in detecting bright galaxy clusters ($> 5{\times}10^{-14}$ erg s^{-1} cm^{-2}), especially the ones that are more concentrated, i.e. with small core radius ($< 70''$). However, fainter (10^{-14} erg s^{-1} cm^{-2}) or larger ($r_c \leq 70''$) extended sources are more difficult to detect with the eSASS pipeline. `mr_filter+SE` shows a better performance at this flux, but the lack of an extended source classifier in this detection procedure makes difficult to conclude if such results really reflect the true extended source detection efficiency.

4.3.4 Conclusions II

The eSASS and `mr_filter+SE` detection procedures were tested using realistic *eROSITA* simulations. The position recovery, the number of false detections and the detection efficiency were analysed. Both algorithms show similar characteristics when detecting point-like sources, they even produce a similar number of spurious detections.

For extended sources, both algorithms show a similar performance in detecting extended sources, especially the brightest and more concentrated sources have a high detection efficiency. For fainter extended sources, `mr_filter+SE` seems to perform better than the eSASS pipeline. However, the results are complicated to decipher for `mr_filter+SE` since it lacks a source classifier. As mentioned in Section 4.2, `mr_filter+SE` is just a detection algorithm that need an extra procedure to perform further source characterisation. The eSASS pipeline has the advantage that it possesses a maximum likelihood fitting method, which allows the classification of the source, i.e. if it is a point-like or extended source. Therefore, it is easier to characterise the properties of the detected sources.

4.4 Towards a galaxy cluster selection function for *eROSITA*

As mentioned in Section 4.1, it is expected that *eROSITA* detect $\sim 10^5$ galaxy clusters with fluxes $> 1.0 \times 10^{-14}$ erg s^{-1} cm^{-2} in the $[0.5 - 2]$ keV energy band. However, as it has been shown in Sections 4.2 and 4.3, the discovery and characterisation of such a number of galaxy clusters through X-ray imaging largely depends on the selected source detection algorithm. A desirable source detection algorithm has to be able to reach the predicted source sensitivity limit as well as to obtain high source detection efficiency with a low contamination.

In this section, a deeper analysis of the source detection efficiency and characterisation is carried out. The first goal is to study and define the source population that *eROSITA* will be able to identify with the available source detection tools. The second goal is to determine a galaxy cluster selection function and calculate the number of galaxy clusters that *eROSITA* will detect.

As mentioned in Section 3.4.2, an X-ray selected sample can be defined by a flux limit (a so-called flux-limited sample). However, the approach to define the future *eROSITA* cluster sample in this work is based on the method first proposed by Rosati et al. (1995) and Vikhlinin et al. (1998), and successfully implemented in recent years on different X-ray surveys (Pacaud et al. 2006 in the XMM-LSS, Lloyd-Davies et al. 2011 in the XCS, Pacaud et al. 2015 in the XXL survey). The method consists in defining the galaxy cluster sample based only on X-ray properties, in this case on the flux and extension of the sources. This method is preferred over a flux-limited approach because it has been shown that the galaxy cluster selection function is not a simple function of flux (Pacaud et al. 2006). The method gives as a result a brightness-limited sample rather than a flux-limited one.

The selected method basically consists in determining the detection efficiency of galaxy clusters through extensive Monte Carlo simulations. In the following, this method, the used simulations and detection pipeline are described.

4.4.1 Simulations and pipeline description

The forecast of the *eROSITA* galaxy cluster selection function is by using the synthetic simulations of the July 2014 release. Since the *eROSITA* all-sky survey will have different exposures time throughout the sky (see Fig. 4.1) two simulated fields are tested: the Equatorial and the Intermediate sky regions, which have ~ 1.6 and ~ 4 ks exposure time, respectively. These regions are chosen because most of the *eROSITA* survey will have exposure times similar to them.

As described in Section 4.3.1, the synthetic simulations of the Release July 2014 only include event files for the 7 *eROSITA* telescopes. Therefore, the X-ray images have to be created. It is important to recall that this release includes “cluster only” and “AGN+background” simulations. To obtain realistic simulations in a given sky region an “AGN+background” and a “cluster only” simulations must be

<table>
<tr><th colspan="5">eSASS (eSASSusers_140905)
Equatorial/Intermediate sky regions</th></tr>
<tr><th rowspan="2">Parameter</th><th rowspan="2">Value</th><th rowspan="2">Parameter</th><th colspan="2">Value</th></tr>
<tr><th>Non-optimal</th><th>Optimal</th></tr>
<tr><td colspan="2">erbox (local mode)</td><td colspan="3">ermldet</td></tr>
<tr><td>emin</td><td>500</td><td>emin</td><td>500</td><td>-</td></tr>
<tr><td>emax</td><td>2000</td><td>emax</td><td>2000</td><td>-</td></tr>
<tr><td>ecf</td><td>1.0</td><td>ecf</td><td>1.0</td><td>-</td></tr>
<tr><td>nruns</td><td>3</td><td>likemin</td><td>4.0</td><td>10.0/20.0</td></tr>
<tr><td>likemin</td><td>6.0</td><td>extlikemin</td><td>6.0</td><td>6.0/7.0</td></tr>
<tr><td>boxsize</td><td>4</td><td>cutrad</td><td>15.0</td><td>-</td></tr>
<tr><td></td><td></td><td>multrad</td><td>15.0</td><td>-</td></tr>
<tr><td colspan="2">erbox (map mode)</td><td>extmin</td><td>1.5</td><td>1.5/3.5</td></tr>
<tr><td>nruns</td><td>1</td><td>extmax</td><td>30.0</td><td>-</td></tr>
<tr><td>likemin</td><td>3.5</td><td>extentmodel</td><td>beta</td><td>-</td></tr>
<tr><td></td><td></td><td>thres_col</td><td>like</td><td>-</td></tr>
<tr><td colspan="2">erbackmap</td><td>thres_val</td><td>15.0</td><td>-</td></tr>
<tr><td>nsplinenodes</td><td>6</td><td>nmaxfit</td><td>3</td><td>-</td></tr>
<tr><td></td><td></td><td>nmulsou</td><td>2</td><td>-</td></tr>
</table>

Table 4.6: Relevant parameters of the eSASS detection pipeline (version `eSASSusers_140905`).

merged. The simulated images are produced using the eSASS pipeline (version `eSASSusers_140905`) and `ftools` following the next steps:

1. Merging the 7 CCD event lists; only "AGN+background" or "AGN+background" plus "cluster only". This is performed with the eSASS task `evmerge` (version 1.1).
2. Selection of events in the energy band of interest. This is done through the eSASS task `evselect` (version 1.3) in the [0.5 – 2] keV energy band.
3. Selection of events within the sky map area (3.6×3.6 deg^2). As described on the Synthetic simulations *eROSITA* web page, in order to avoid border effects, the simulated event lists contain more events that the *observed* sky area. Such events must be discarded. This is done by using an event filter algorithm from `ftools`[6]: `fselect`. Such algorithm has to be used since eSASS does not support selection expressions in detector coordinates, which are the only reference provided to remove these extra events (Dr. N. Clerc, priv. comm.).
4. Separation of event files in on- and off-axis photons. The eSASS detection pipeline can simultaneously run over two images. From the same simulation, two images are produced with photons chosen according to their position on the FoV. The photons are split on inner photons ($< 16.5'$) and outer photons ($> 16.5'$). The PSF fitting of `ermldet` is more sensitive to the core of the PSF when on- and off-axis photons are separated and runs simultaneously on both images. The photon separation is also done with `fselect`. Fig. 4.15 shows a cut-out example of raw on- and off-axis images of the same region.
5. Image creation. This is done with the `evselect` task. Two images of 3.6×3.6 deg^2 with a pixel scale of $4''$/pixel are then created.
6. Exposure map creation. The eSASS task `expmap` (version 1.7) creates exposure maps for the on- and off-axis photon images.

---

[6] https://heasarc.gsfc.nasa.gov/ftools/ftools_menu.html

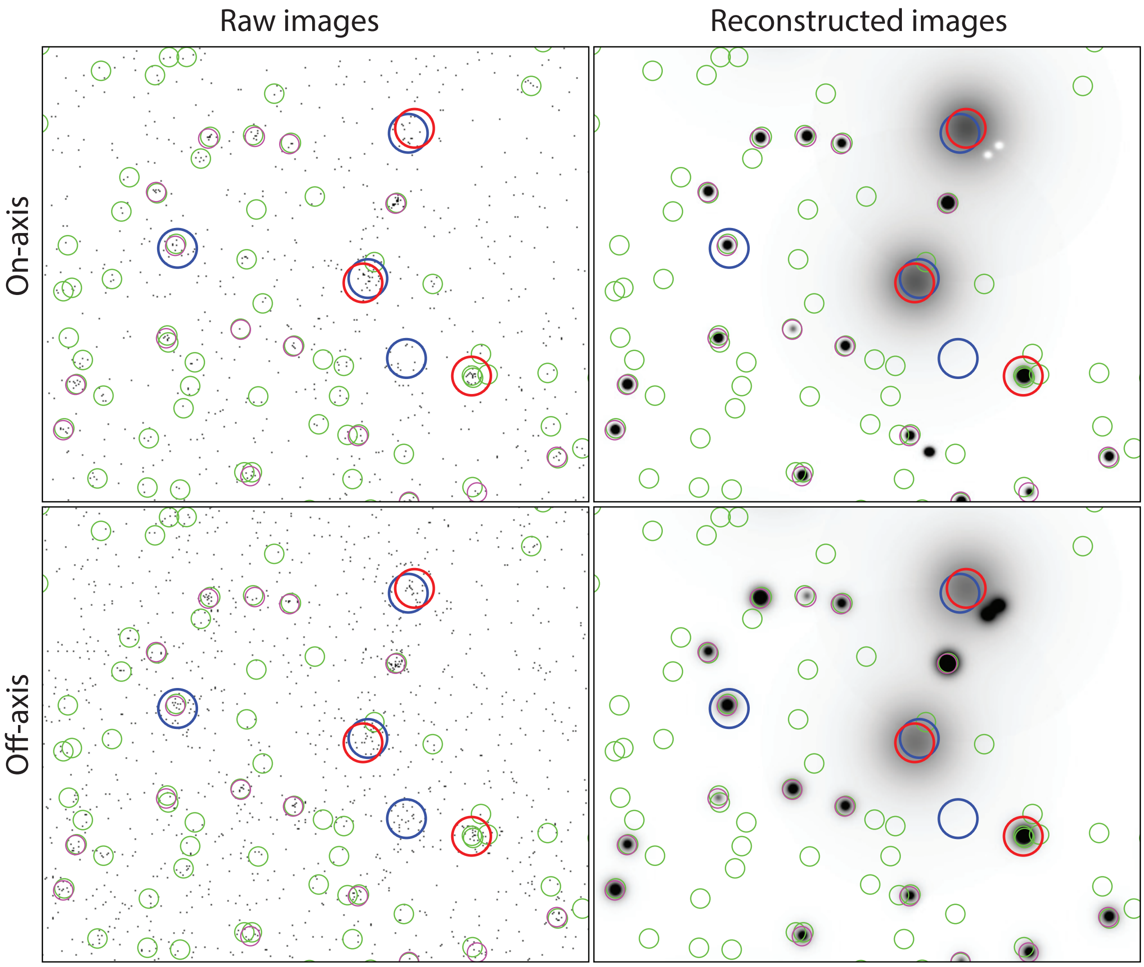

Figure 4.15: Cut-outs (30′ × 30′) of simulated *eROSITA* images for the Equatorial region (~ 1.6 ks, the co-addition of the 7 CCD cameras). *Left panels*: raw photon images. *Right panels*: `ermldet` reconstructed images. *Top panels*: images from on-axis photons (< 16.5′). *Bottom panels*: images from off-axis photons (> 16.5′). Green and blue circles indicate input position of point-like and extended sources, respectively. Magenta and red circles show the `ermldet` detected point-like and extended sources, respectively. The simulated galaxy clusters have a flux of 5×10^{-14} erg s^{-1} cm^{-2} in the [0.5 – 2] keV energy band.

The final images consist of two kinds of simulations per sky region: *i*) 15 simulations containing only point-like sources ("AGN+Background" fields), and *ii*) 256 simulations with extended sources embedded in the point-like simulations ("AGN+Background+Clusters" fields, see Section 4.3.1 for more details).

All simulated images were analysed with the eSASS detection pipeline (version `eSASSusers_140905`, see Section 4.3.2). Table 4.6 summarizes the selected values of the main input parameters in the different eSASS detection tasks. Initially, the source detection and analysis are performed with exactly the same parameters for all simulations in the two simulated sky regions.

Cut-outs of Equatorial field simulated images and their respective eSASS reconstructed images are shown in Fig. 4.15. The two images (top and bottom) in this figure are the on- and off-axis images of the same region. There is a number of features that stand out in Fig. 4.15 and are important to mention:

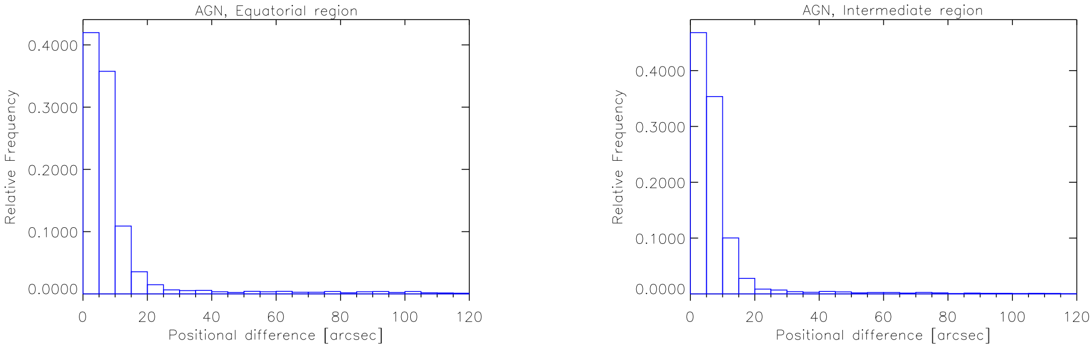

Figure 4.16: Histograms showing the distance from the input AGN positions to the closest detected point-like sources for the simulated Equatorial (*left*) and Intermediate regions (*right*).

- As expected from the AGN $\log N - \log S$ relation, there are more faint point-like sources than bright ones. The brightest AGNs are easily detected by the pipeline while the fainter sources are more difficult to identify.
- The position recovery of the detected point-like sources is very precise.
- Close-by point-sources can be misidentified as a single point-like or extended source.
- Poisson noise can lead to false detection of point-like and extended sources.
- The position recovery of simulated extended sources is usually displaced.
- Point-like sources located nearby extended ones are merged with the extended source.

In the following, the above items and other features will be quantitatively discussed.

First, the source position recovery is measured for point-like and extended sources. Using the “AGN+Background” simulations, the distance to closest detected point-like sources to the input AGN positions is determined for both simulated fields. The results are shown in Fig. 4.16. It is clear from the plots that most of the point-like sources are identified within 30″ (7.5 pixels) in both fields. Thus, this value will be used as the search radius to cross-correlate and identify point-like sources.

A similar methodology is used for extended sources, but using the “AGN+Background+Clusters” simulations. Only the results for the Intermediate field are shown in Fig. 4.17. This figure displays the results

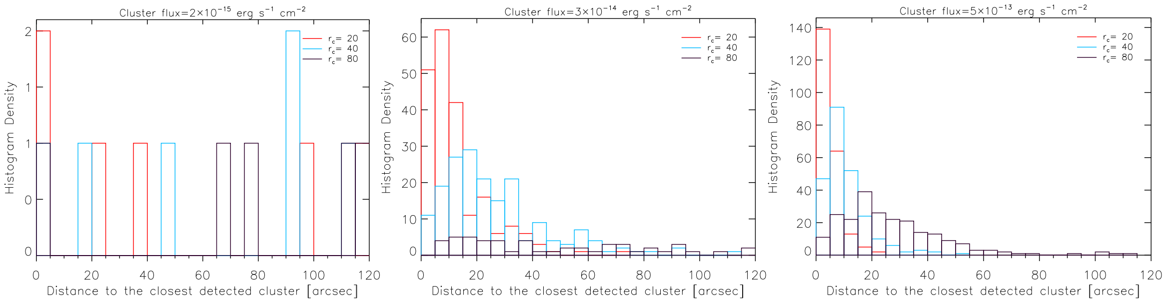

Figure 4.17: Histograms showing the distance from the input cluster positions to the closest detected extended sources in the simulations of the Intermediate field. The panels show the results for three cluster fluxes: 2×10^{-15} erg s^{-1} cm^{-2} (*left*), 3×10^{-14} erg s^{-1} cm^{-2} (*middle*), 5×10^{-13} erg s^{-1} cm^{-2} (*right*). Each panel also shows the results for three different cluster core radius values: 20″, 40″, and 80″.

	Equatorial region with non-optimal / optimal parameters		Intermediate region with non-optimal / optimal parameters	
Field	False clusters per deg^2	False AGN per deg^2	False clusters per deg^2	False AGN per deg^2
AGN+Bkg	0.7 ± 0.3 / 0.7 ± 0.3	17 ± 1 / 0.1 ± 0.1	3.0 ± 0.5 / 0.8 ± 0.3	18 ± 2 /1.5 ± 0.4
AGN+Bkg+Clusters	0.6 ± 0.2 / 0.5 ± 0.1	18 ± 4 / 0.7 ± 0.7	2.0 ± 0.3 / 0.4 ± 0.2	20 ± 2 / 1.7 ± 0.3

Table 4.7. Number of false (spurious and misclassified) galaxy clusters (extended) and AGN (point-like) in the "AGN+Background" and "AGN+Background+Clusters" simulations on the Equatorial and Intermediate fields.

for three different simulated galaxy cluster flux values (2×10^{-15}, 3×10^{-14} and 5×10^{-13} erg s^{-1} cm^{-2}) and three distinct core radius values (20″, 40″, and 80″). The results clearly show that the estimated position of fainter and extended (with large core radius) galaxy clusters tend to be more shifted from the input positions than the recovered position of brighter and compact galaxy clusters. The results of the Equatorial field simulations are very similar. After this analysis one can safely assume a searching radius of 80″ (20 pixels) for extended sources.

As in previous sections, the detected sources that cannot be cross-identified with any input source within the search radii will be considered and referred to as *spurious* detections.

4.4.2 Source classification, completeness and contamination

The estimation of the cluster selection function in X-ray surveys requires a careful source classification and an accurate determination of the sample completeness and contamination. To estimate these quantities for *eROSITA* the methodology from Pacaud et al. (2006) is adopted in this work. This approach basically consists in exploring the output parameter space of the maximum likelihood fitting to set point-like and extended source selection criteria, determining the source detection efficiency and estimating the contamination by spurious or misclassified sources.

Point-like sources

AGNs represent the dominant extragalactic population in X-ray wavelengths. Although the goal of this study is to determine the galaxy cluster selection function, the estimation of the point-like detection efficiency and its contamination helps to control the systematics in the detection and characterisation of the extended source population.

When running the eSASS detection pipeline over the "AGN+Background" simulations of both sky regions, a high spurious detection rate is found: 17 ± 1 and 18 ± 2 spurious point-like detections per square degree for Equatorial and Intermediate fields, respectively (see "AGN+Background" fields in Table 4.7). This contamination level is too high and a different strategy has to be followed in order to reduce it. Moreover, these simulations are contaminated by some spurious sources classified as extended: 0.7 ± 0.3 and 3.0 ± 0.5 spurious extended detections per square degree for Equatorial and Intermediate fields, respectively.

By exploring the `ermldet` output parameter space of the "AGN+Background" simulations, one can see that a simple threshold of 10 in the minimum detection likelihood parameter removes most of the spurious point-like sources in the Equatorial field (dashed line in the left panel of Fig. 4.18). However,

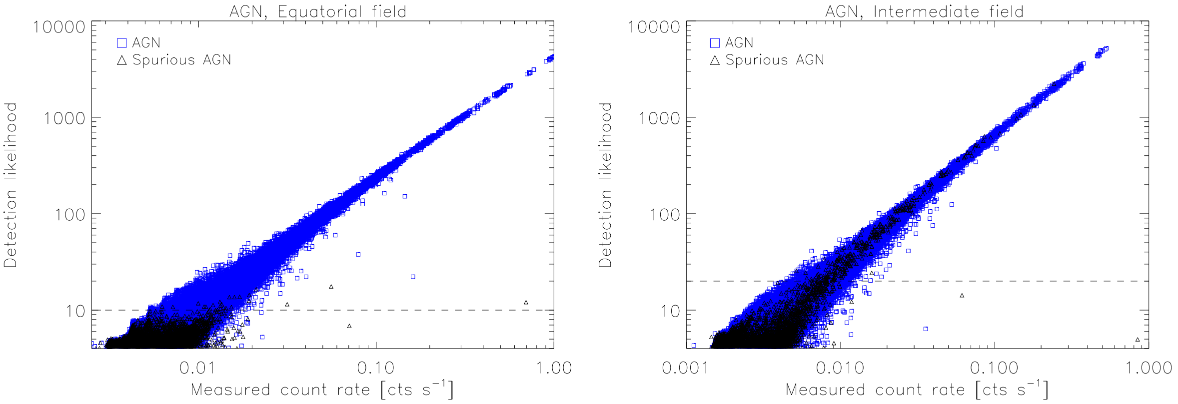

Figure 4.18: Determination of the eSASS pipeline selection criteria for point-like sources. The selection is performed in the count rate−minimum detection likelihood plane for both simulated sky regions: Equatorial (*left*) and Intermediate (*right*) of the point-like simulations ("AGN+Background"). Simulated AGN are displayed as blue squares and spurious point-like detections as black triangles. The dashed line at *minimum likelihood* defines the point-like source sample.

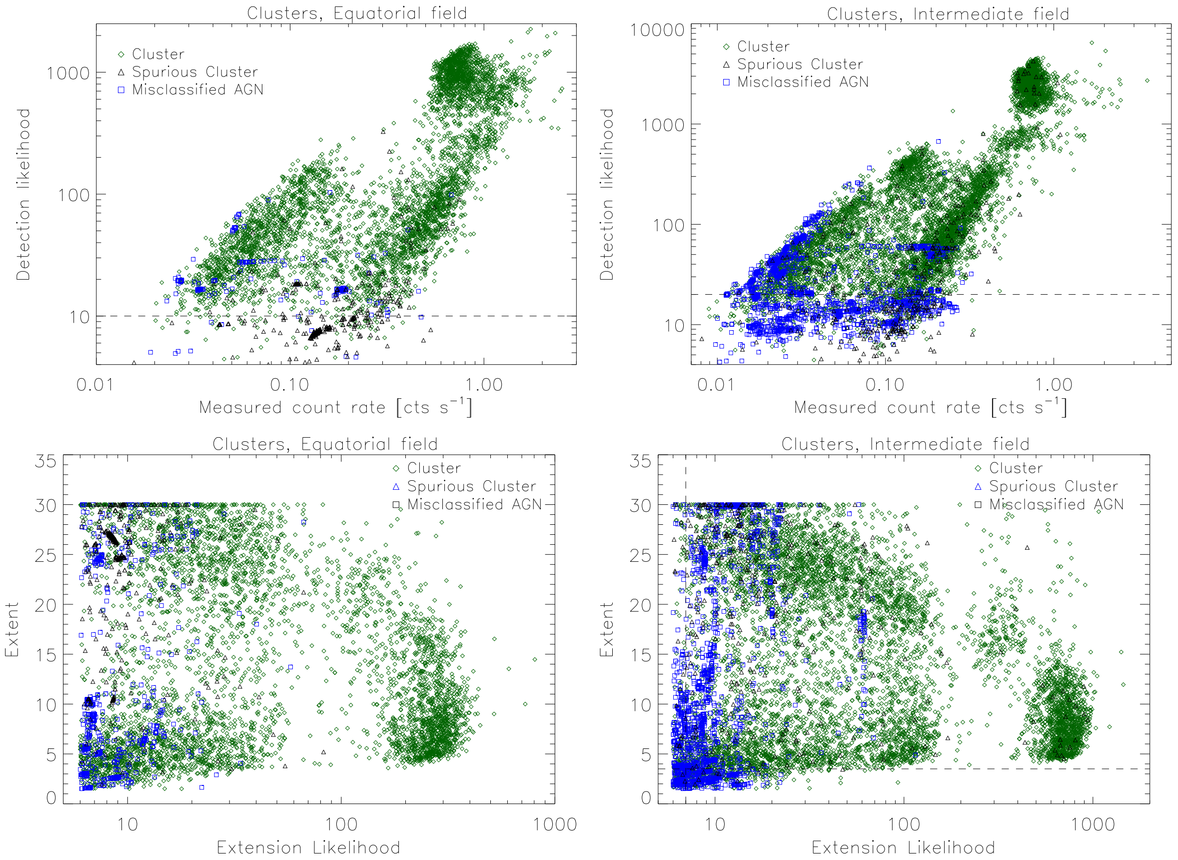

Figure 4.19: Determination of the eSASS pipeline selection criteria for extended sources. The selection is performed in the count rate−minimum detection likelihood plane and in the extent - extension likelihood plane for both simulated sky regions: Equatorial (*left*) and Intermediate (*right*). Simulated AGN are displayed as green diamonds, spurious extended detections as black triangles, and misclassified AGN as blue squares. The dashed lines define the optimal parameters for the extended source samples.

choosing a similar threshold seems more complicated for the Intermediate field, where many spurious sources are detected and are difficult to disentangle from the *true* sources. In this case, the output parameter space of the “AGN+Background+Clusters” simulations is investigated. This is a valid move since the goal is to find low-contaminated samples of extended sources. Extended sources are less affected by spurious sources with a threshold of 20 in the minimum detection likelihood parameter (dashed line in the top-right panel of Fig. 4.19). This value also applies for the point-like sources only simulations (right panel of Fig. 4.18). The parameters that remove most of the spurious detections are considered as optimal values.

The eSASS task `ermldet` was run again over the `erbox` output (in map mode) of the “AGN+Background” simulations, but using the optimized parameters (see optimal parameters in Table 4.6). The new results give spurious detection rates of 0.1 ± 0.1 and 1.5 ± 0.4 spurious point-like detections per square degree, and 0.7 ± 0.3 and 0.8 ± 0.3 spurious extended detections per square degree for Equatorial and Intermediate fields, respectively (see “AGN+Background” fields with optimal parameters in Table 4.7). These contamination levels are more reasonable than before.

The resulting AGN, i.e. point-like sources, detection efficiency as a function of input flux is shown in the top panels of Fig. 4.20. This efficiency is obtained by calculating the ratio of the cross-identified objects to the input sources. The displayed error is given by the standard deviation over the 15 simulations of each sky region. For the Equatorial field, the point-like sources have a 90% completeness at a flux limit of $\sim 1.5\times10^{-14}$ erg s^{-1} cm^{-2}, while for the Intermediate field this flux limit is $\sim 1.2\times10^{-14}$ erg s^{-1} cm^{-2}. The large error bars in bright sources reflects mainly their lower density number, which is given by the AGN $\log N - \log S$ distribution.

The dashed lines in the top panels of Fig. 4.20 show the predicted point-source flux limit presented in the *eROSITA* Science Book (Merloni et al. 2012) for the corresponding exposure times. However, such predictions are based in an AGN model completely different from the one used in the synthetic simulations. Moreover, as presented in Section 4.1, the predicted flux limit represent the 5σ probability detection over an aperture of $60''$ diameter. Therefore, a direct comparison is difficult.

The differential flux distributions for the Equatorial and Intermediate fields are shown in the middle panels of Fig. 4.20. This representation allows putting a conservative point source flux limit of $\sim 2\times10^{-14}$ erg s^{-1} cm^{-2} and $\sim 1.5\times10^{-14}$ erg s^{-1} cm^{-2} for the Equatorial and Intermediate fields, respectively. Below such fluxes, the sample incompleteness becomes important. Such limiting fluxes and incompleteness are confirmed by the $\log N - \log S$ functions shown in the bottom panels of Fig. 4.20.

Extended sources

The extended source selection is a complicated task since it has to deal with spurious detections characterised as extended sources and with misclassified point-like detections. Extended sources are usually lower and extended surface brightness objects, which also makes their detection a difficult process. As with point-like sources, the aim is to find a location in the `ermldet` output parameter space where the majority of the simulated extended sources are recovered while keeping the contamination level at a reasonable rate. This is important to keep in mind since the goal of *eROSITA* is to use galaxy cluster counts to constrain the dark energy. Therefore, obtaining a pure and complete galaxy cluster sample is necessary.

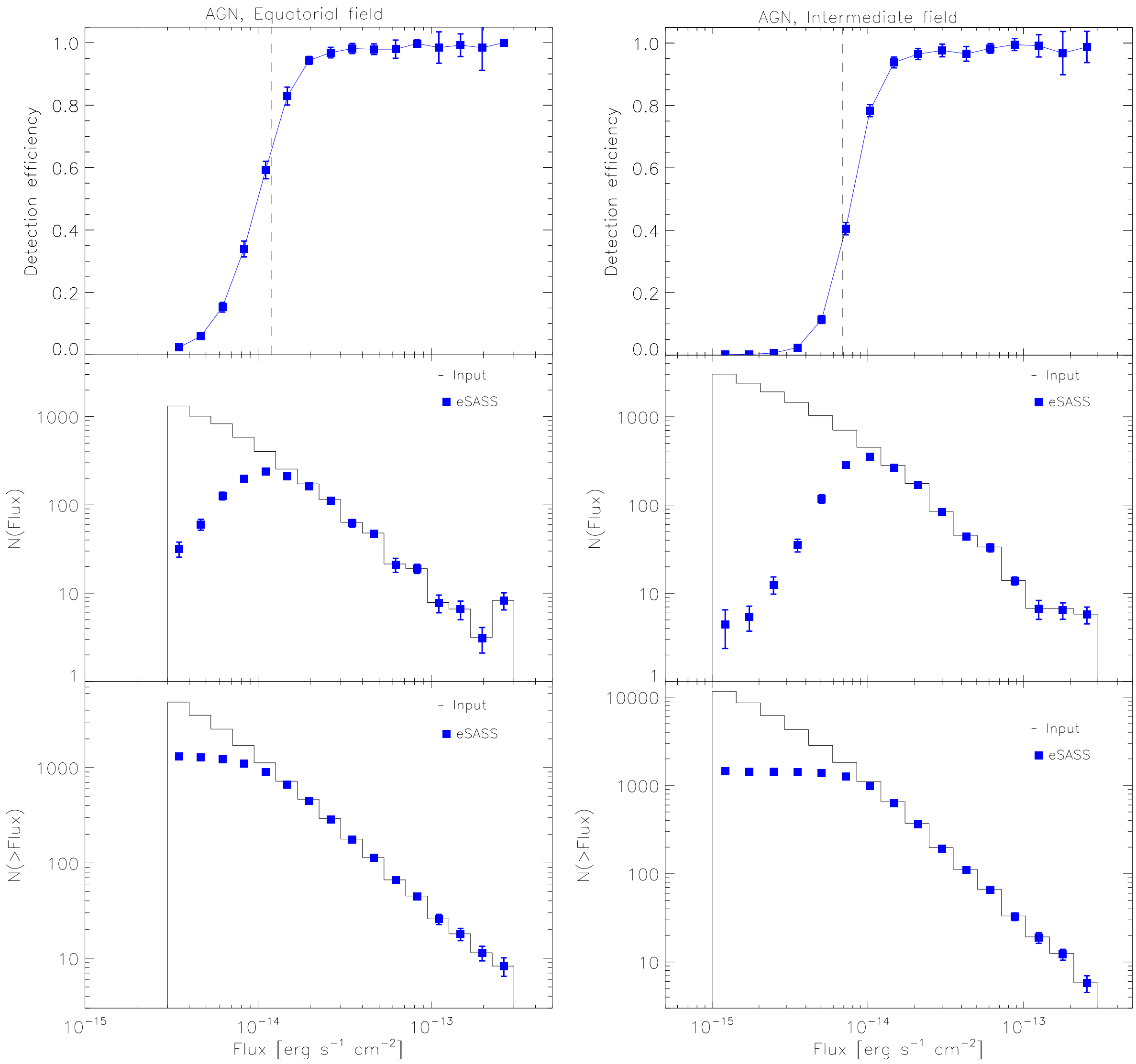

Figure 4.20: Point-like source completeness analysis for both simulated sky regions: Equatorial (*left*) and Intermediate (*right*). *Top panels*: Point-like detection efficiency as function of input flux. The dashed line indicates the Merloni et al. (2012) flux prediction for a secure point-like detection. *Middle panels*: Differential number counts as a function of input flux. *Bottom panels*: Integral number of point-like sources as a function of input flux. In the *middle and bottom panels* the continuous histogram shows the input distribution and the blue squares show the eSASS detected distribution. The error is given by the standard deviation over the 15 simulations.

As a first step, the source contamination rate over the "AGN+Background+Clusters" simulations, for the Equatorial and Intermediate fields, are analysed. The results show the following spurious detection rate: 0.6 ± 0.2 and 2.0 ± 0.3 false extended sources per square degree, and 18 ± 4 and 20 ± 2 false point-like sources per square degree for the Equatorial and Intermediate sky regions, respectively (see "AGN+Background+Clusters" field in Table 4.7). There are two main things to highlight from these results. First, the number of spurious extended sources in the Intermediate field is rather high. Such contamination cannot be allowed in a galaxy cluster survey. Reliable cluster output samples are a necessary condition for cosmological tests. Second, the number of spurious point-like sources is slightly higher than the one obtained in the "AGN+Background" simulations. The reason is that some galaxy clusters, especially the ones with a low surface or very extended, are more easily split in more than one source, which are misclassified as point-like by the detection algorithm. This, of course, increases the number of false point-like sources.

By looking at the `ermldet` output parameter space of the "AGN+Background+Clusters" simulations, shown in Fig. 4.19, one realizes that the adopted threshold in the minimum detection likelihood parameter (equal 10) for point sources also reduces the contamination rate in the extended sources in the Equatorial field. Although such threshold excludes a number of extended sources, a trade-off between sample completeness and contamination has to be made. For the simulated Intermediate field, in addition to the threshold in the minimum detection likelihood parameter (equal to 20), thresholds of on the extent (equal to 3.5) and extension likelihood (equal to 7) parameters can lower the spurious and misclassified sources. By using these optimized parameters on `ermldet`, one obtains a spurious detection rate of 0.5 ± 0.1 and 0.4 ± 0.2 false extended sources per square degree, and 0.7 ± 0.7 and 1.7 ± 0.3 false point-like sources per square degree for the Equatorial and Intermediate sky regions, respectively (see "AGN+Background+Clusters" field in Table 4.7).

Figure 4.21 shows the extent - extension likelihood plane of the "AGN+Background+Clusters" simulations. The left panels of Fig. 4.21 show *all* the extended-like sources detected by `ermldet`: *true*, spurious and misclassified sources. In the Equatorial field simulations, an uncontaminated sample can be determined by choosing only extended sources with extension likelihood values greater than 170. This kind of sample cannot be defined for the Intermediate field simulations since there are spurious detections all over the extent - extension likelihood plane.

The middle panels of Fig. 4.21 show only the *true* detected galaxy clusters, which are colour coded according to their core radius. Although the core radius values are spread all over the extent - extension likelihood plane, there is a tendency of galaxy clusters with low core radius values to have a smaller extension, while galaxy clusters with large core radius values have a larger extension. The right panels of Fig. 4.21 show also the *true* detected galaxy clusters colour coded according to their input flux. From these plots one can see that mostly bright galaxy clusters are detected and correctly identify ($> 2 \times 10^{-14}$ erg s^{-1} cm^{-2}). Although fainter clusters do not appear in these plots, it does not mean they are not detected. It can be that they have been just misclassified, and they can be recovered by changing the input parameters in `ermldet`. However, changing the parameters has consequences, for example, a higher contamination level.

The detection efficiency of extended sources is shown in Fig. 4.22 for the Equatorial and Intermediate field simulations. The top panels display the detection efficiency as a function of input flux for each simulated value of core radius. The dashed lines show the predicted 7σ flux limit over a $3'$ diameter for a secure detection of extended sources (*eROSITA* Science Book; Merloni et al. 2012). This theoretical flux represents a source detection limit, rather than a threshold for classifying the source as extended. The extended source detection efficiency obtained in this work is obtained after applying two thresholds, on source detection and extension. Therefore, a comparison between the predicted flux limit and the measured one is not straightforward. Galaxy clusters with fluxes $> 5 \times 10^{-14}$ erg s^{-1} cm^{-2} and core radii $> 80''$ have more than 50% probability of being detected in both simulated sky fields. At lower fluxes and core radius values, the detection efficiency decreases rapidly.

The bottom panels of Fig. 4.22 show the galaxy cluster detection probability as a function of input flux and core radius for both simulated sky regions. In general, the detection and characterisation of extended sources with fluxes below 1×10^{-14} erg s^{-1} cm^{-2} seems rather difficult for the two simulated

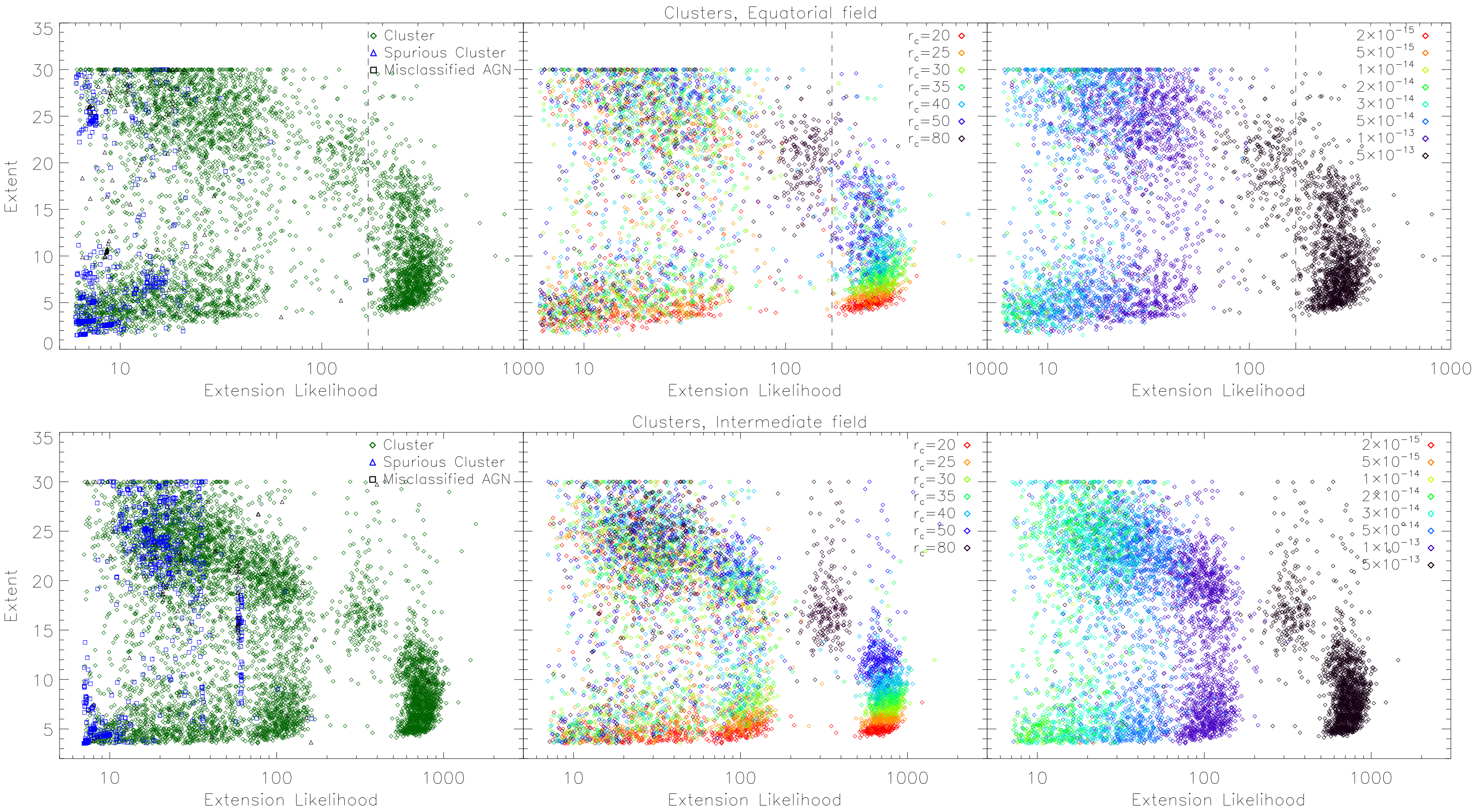

Figure 4.21: Determination of the eSASS pipeline selection criteria for extended sources with optimal (low-contamination) `ermldet` parameters. The extent - extension likelihood plane is shown for both simulated sky regions: Equatorial (*top*) and Intermediate (*bottom*). *Left panels*: simulated AGN are displayed as green diamonds, spurious extended detections as black triangles, and misclassified AGN as blue squares. *Middle panels*: Only input detected galaxy clusters are displayed (green diamonds in the *left panels*). The distinct colours show the different simulated core radii (in arcsec). *Right panels*: Only input detected galaxy clusters are displayed. The different colours show the distinct simulated input fluxes (in units of erg s^{-1} cm^{-2}). The dashed line in the top panels defines the criteria for an uncontaminated sample.

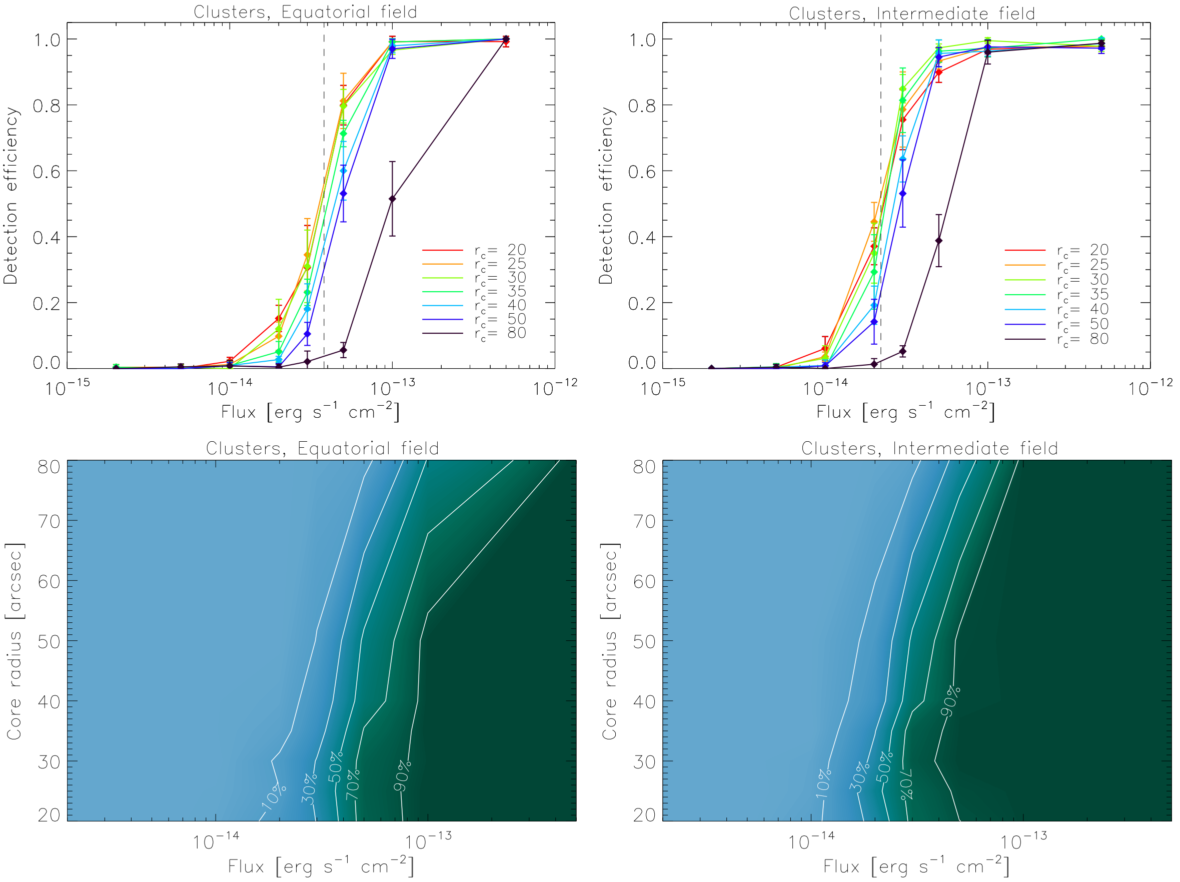

Figure 4.22: Extended source detection efficiency of the eSASS pipeline in the Equatorial (~ 1.6 ks exposure, *left*) and Intermediate (~ 4 ks, *right*) simulated fields. *Top panels*: As a function of input flux and for each simulated core radius value. *Bottom panels*: As a function of input flux and core radius.

fields. This does not necessarily signify that such galaxy clusters are not detected at all, it mainly implies that such objects do not satisfy the chosen extended source criteria. In Equatorial simulations, which have the lowest exposure time (~ 1.6 k), `ermldet` has problems in detecting and characterising low surface ($< 5\times10^{-14}$ erg s^{-1} cm^{-2}) and very extended sources ($r_c > 70''$). The extended source detection efficiency for the Intermediate field simulations is moderately higher than for the Equatorial field due to the higher exposure time. The improvement is mostly noticed for sources with large core radius, at least for the brightest galaxy clusters.

As stated in Pacaud et al. (2006), and confirmed by the results of this work, the galaxy cluster detection efficiency is not a simple function of cluster flux. It highly depends on the galaxy cluster flux and size (or morphology). According to these results, flux-limited samples can be incomplete given the cluster detection dependence on the cluster size. The probability efficiency of the Intermediate field somewhat resembles a flux-limited sample for bright sources, but as going to fainter fluxes, the picture gets as complex as for the Equatorial field. Next section presents a comparison between a flux-limited sample and a sample described by the results obtained here.

4.4.3 The *eROSITA* cluster selection function

As described in Chapter 2, by assuming a set of scaling relations one can obtain the luminosity, the gas temperature and physical extent of a galaxy cluster of a given mass at a given redshift. From these quantities, different galaxy cluster characteristics can be determined, such as the angular core radius and the X-ray flux. By knowing these two quantities, the detection probability of a galaxy cluster of any mass at any redshift can be predicted by using the detection efficiency curves displayed in Fig. 4.22. This information is essential for the calculation of the *eROSITA* cluster selection function.

Dr. Nicolas Clerc (MPE) has used the cluster detection efficiency curves obtained in this work (Fig. 4.22) to compute the expected redshift distribution of the galaxy clusters that *eROSITA* will detect. In the following, this work is briefly presented as an illustration of the application of the obtained cluster detection efficiency.

Cosmological model and scaling relations

A ΛCDM cosmological model is assumed, together with a flat Universe and a non-evolving dark energy. The cosmological parameters are set to the 5-year *Wilkinson Microwave Anisotropy Probe (WMAP5)* cosmology: $h = 0.72$, $\Omega_\mathrm{m} = 0.25$, $\Omega_\mathrm{b} = 0.043$, $\Omega_\Lambda = 0.75$, $n_s = 0.96$, and $\sigma_8 = 0.79$ (Dunkley et al. 2009). The Tinker et al. (2008) fit is used to describe the comoving halo number density as a function of mass, $\mathrm{d}n(M,z)/\mathrm{d}M$, i.e. the halo mass function (see Section 2.2.3). This fit calculates the halo masses within $r_{200\mathrm{b}}$, i.e. the mass within a radius that encloses an overdensity 200 times the mean density of the Universe at a given redshift. However, the mass function is needed in terms of a mass defined with respect to the critical density of the Universe, since this is the mass definition that is used by the scaling relations. The conversion is performed using the approximate inversion equation from Hu & Kravtsov (2003) assuming an NFW mass profile (see Section 2.2.2) and the concentration parameter model from Bullock et al. (2001).

As stated previously, at a given redshift a galaxy cluster can be described by its gas temperature and its bolometric luminosity. However, from the halo mass function, only the mass and redshift of the galaxy clusters are known. By using cluster scaling relations, the temperature and luminosity of the galaxy clusters can be obtained from the mass and redshift information. The cluster gas temperature is calculated using the $M - T$ relation from Arnaud et al. (2005), and its bolometric luminosity using the $L_\mathrm{X} - T$ relation from Pratt et al. (2009). Both relations include a self-similar redshift evolution. The intrinsic scatter of such relations was also taken into account to model the final cluster population.

The β-model (see Section 2.1.2) is used to describe the emission profile of galaxy clusters. The chosen values for this model are: $\beta = 2/3$ and the core radius, r_c, is parameterised in terms of r_{500}: $x_\mathrm{c} = r_\mathrm{c}/r_{500}$, where r_{500} is the radius that encloses an overdensity 500 times the critical density of the Universe at a given redshift. x_c is taken constant at all redshifts and masses, with value $x_\mathrm{c} = 0.15$ (Böhringer et al. 2014). The core radius is an important parameter in this process since the derived cluster detection efficiency depends on it (see Fig. 4.22).

The next step is to convert the galaxy cluster quantities (r_c, T and L_X) into observable ones. The core radius is transformed into angular scale by means of the angular diameter distance (see Section 2.1.2). The total cluster count-rate or flux in the $[0.5-2]$ keV energy band is calculated with the `XSPEC` spectral fitting package (Arnaud 1996) by using an `APEC` thermal plasma emission model with a metallicity of

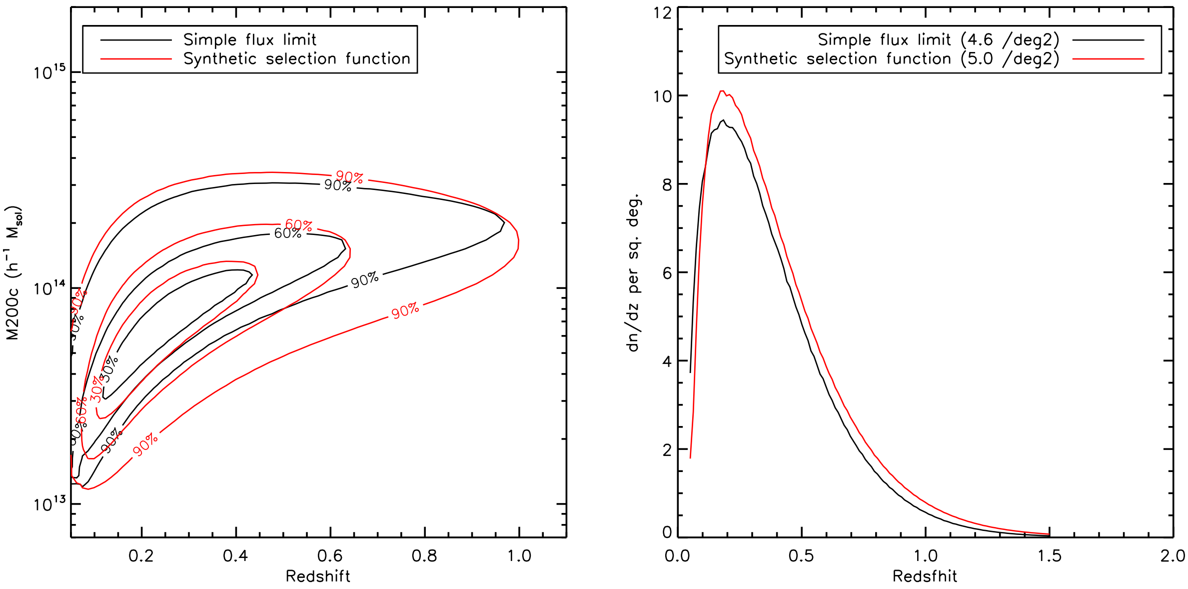

Figure 4.23: Comparison of the cosmological expectations between a flux-limited cluster sample (black solid line) and sample folded with a source selection function (from the synthetic sample of the simulated Equatorial sky region, red solid line). *Left*: Expected cluster selection function in the mass-redshift plane for the synthetic sample compared with the flux-limited one. The contours enclose the 30%, 60% and 90% of the total expected number of clusters. *Right*: Expected dn/dz for the synthetic sample compared with the flux-limited survey. Image provided by N. Clerc.

0.3 $Z_\odot$ and a Hydrogen column density corresponding to the used simulated field (see Section 4.3.1) folded through the *eROSITA* response matrices.

Model for the mass and redshift distributions

By using the above quantities, the expected galaxy cluster distribution, $\mathrm{d}n/\mathrm{d}M/\mathrm{d}z/\mathrm{d}T/\mathrm{d}L_\mathrm{X}$, can be computed. First, the scaling relations are used to turn the halo mass function, $\mathrm{d}n/\mathrm{d}M/\mathrm{d}z$, into $\mathrm{d}n/\mathrm{d}M/\mathrm{d}z/\mathrm{d}L_\mathrm{X}/\mathrm{d}T$ at a given redshift. The count-rate is estimated from each luminosity - temperature pair, and the core radius from each mass, M. The $\mathrm{d}n/\mathrm{d}M/\mathrm{d}z/\mathrm{d}L_\mathrm{X}/\mathrm{d}T$ distribution is ultimately based on the total count-rate and extent (core radius) of the galaxy clusters[7]. In this way, the cluster detection efficiency is applied in the $M - L_\mathrm{X} - T$ plane. By marginalizing over L_X and T, one is able to recover $\mathrm{d}n/\mathrm{d}M/\mathrm{d}z$ with the selection function included. Finally, by integrating over all masses the $\mathrm{d}n/\mathrm{d}z$ distribution is obtained.

The above method is applied to the simulated galaxy clusters that pass the selection of Fig. 4.22. This will be referred as the *eROSITA* synthetic selection function. Figure 4.23 shows an example of the shape of $\mathrm{d}n/\mathrm{d}z/\mathrm{d}M$ and the redshift distribution of $\mathrm{d}n/\mathrm{d}z$ for the simulated Equatorial field selection (left bottom panel of Fig. 4.22). The results are compared with a flux-limited sample, which is assumed to have flux limit of 3.4×10^{-14} erg s^{-1} cm^{-2}. This flux limit is taken from the *eROSITA* predictions

---

[7] The $\mathrm{d}n/\mathrm{d}M/\mathrm{d}z/\mathrm{d}L_\mathrm{X}/\mathrm{d}T$ distribution depends on the assumption that galaxy cluster temperatures can be measured from their collected X-ray photons, whose error depends mainly on the number of collected photons and the precision of the cluster redshift

(see Merloni et al. 2012). Both samples show very similar redshift distributions, with a peak at $z = 0.2$. Most of the expected clusters have masses between $3 \times 10^{13}\ h^{-1}\ \mathrm{M}_{\odot}$ and $1.5 \times 10^{14}\ h^{-1}\ \mathrm{M}_{\odot}$.

From the synthetic cluster selection it is expected to detect 5 clusters per $\deg^2$, whereas from the flux-limited sample only 4.6 clusters per $\deg^2$ are expected. The synthetic cluster density gives more than 2×10^5 galaxy clusters in the whole sky while the flux-limited cluster density gives less than 1.9×10^5. By taking as a reference a total sky coverage of $27,145\ \deg^2$ (excising $\pm 20°$ around the Galactic plane) the final number of expected clusters for the synthetic selection is $\sim 1.36 \times 10^5$, and $\sim 1.25 \times 10^5$ for the flux-limited selection. However, the cluster selection function of the Equatorial field has a contamination level of 10%, i.e. 0.5 spurious clusters per $\deg^2$, increasing the number of clusters extended detections to $\sim 1.49 \times 10^5$. This additional contamination needs to be accounted for, either using an accurate determination of their distribution in the flux-extent plane, which can be included it in the cosmological modelling, or by establishing other strategies to clean the sample (e.g. via optical follow-up, when available).

X-ray observations are usually contaminated by background flares, which only impact the particle background and have to be removed from the data. In the calculation of the total number of clusters the area covered by the Galactic plane was removed. Then, the remaining sky area has a larger exposure time than 1.6 ks. However, assuming that the data has to be cleaned from flares, the total exposure time is reduced. Therefore, as a first approximation, the calculation remains acceptable.

The 8% difference in the number of clusters between the synthetic cluster sample and the flux-limited sample can make a huge difference when using large samples of galaxy clusters to constrain cosmological parameters. Pillepich et al. (2012) has found that the constraints on the cosmological parameters can be improved up to 30% when they increase their sample from 9.32×10^4 to 1.37×10^5 clusters, i.e. in $\sim 4.5 \times 10^4$ clusters.

4.4.4 Discussion and conclusions III

As presented in Section 4.1, Pillepich et al. (2012) predicted that *eROSITA* will detect $\sim 9.3 \times 10^4$ galaxy clusters with a median redshift of $z \simeq 0.35$ for an exposure time of 1.6 ks in the $[0.5 - 2]$ keV energy band. These results assume a detection limit of 50 photons and take into account only clusters with masses above $5 \times 10^{13}\ h^{-1}\ \mathrm{M}_{\odot}$. Although the approach followed in this work is very different from the one by Pillepich et al. (2012), the results are quite similar. Pillepich et al. (2012) also use WMAP5 cosmology and the Tinker et al. (2008) halo mass function.

The expected number of clusters in this work ($\sim 1.36 \times 10^5$, without contamination) agree more with the results of Pillepich et al. (2012) when the mass limit is $1 \times 10^{13}\ h^{-1}\ \mathrm{M}_{\odot}$, obtaining $\sim 1.37 \times 10^5$ clusters. This is clearly seen in the left panel of Fig. 4.23 which shows that galaxy clusters with masses $\sim 1 \times 10^{13}\ h^{-1}\ \mathrm{M}_{\odot}$ can be detected by the pipeline. Although the match between this work and the results of Pillepich et al. (2012) is good, it is important to emphasize their relative differences and the impact that they have on the obtained results.

First of all, the *eROSITA* calibration files are different. In this work the latest files are used while Pillepich et al. (2012) use an older version. The metal abundance and sky coverage is the same in both approaches. The set of scaling relations is also different in both methods. As mention earlier the $M - T$ relation from Arnaud et al. (2005) and the $L_X - T$ relation from Pratt et al. (2009) are used here, whereas Pillepich et al. (2012) use the relations from Vikhlinin et al. (2009a). These different relations and their errors can also contribute to a discrepancy between the methods. Pillepich et al. (2012) applied a lower mass limit in their calculations, $5{\times}10^{13}\ h^{-1}\ \mathrm{M}_{\odot}$. The reason is because the scatter in the scaling relations increases for low halo masses, i.e. in the galaxy group regime (e.g. Sun et al. 2009; Eckmiller et al. 2011; Lovisari et al. 2015). Galaxy group properties are more affected by non-gravitational processes due to their shallower gravitational potential. Moreover, the used scaling relations were obtained from clusters with masses above $5 \times 10^{13}\ h^{-1}\ \mathrm{M}_{\odot}$.

Although the above reasoning also applies to the calculations presented in this work, it is important to keep in mind that the results presented in Section 4.4.3 clearly show that the cluster selection function is not a simple function of flux, it highly depends on the cluster extend (morphology) and flux. Then, even with a cut of 50 photons and $5 \times 10^{13}\ h^{-1}\ \mathrm{M}_{\odot}$, if the extent of the cluster is too large, for example, the detection pipeline will miss it and, therefore, the sample defined by Pillepich et al. (2012) will be incomplete. Moreover, in practice, it will not be possible to apply such mass cut since the cluster masses will not be available. Thus, it is not clear how such selection could be reproduced on real data.

As presented in Section 4.4.2, one could define an uncontaminated sample from Fig. 4.22 in the simulated Equatorial field. In this way, the contamination problem is overcome and the obtained sample can be assumed pure and used straightforwardly for cosmological analysis. This approach is followed by Pacaud et al. (2006) in the XMM-LSS survey. Moreover, Fig. 4.22 also shows that the uncontaminated sample is formed by only high flux clusters, giving the impression that a complete flux-limited sample can only be achieved by setting a very high flux limit. The main consequence of such conservative criteria is the exclusion of a number of extended sources. Estimation of the selection function in surveys is a complicated task since one has a trade-off between completeness and contamination.

A final remark on the source detection procedure. Although the eSASS detection pipeline performs well and it can give important results on the cluster detection, one should keep in mind that there are other detection algorithms that can give the same or maybe better results. One of such algorithms is the wavelet-based methods discussed in Section 4.2. The best strategy is to repeat the exercise with different detection algorithm(s) and see which perform the best, keeping in mind all the advantages and disadvantages of each method.

4.5 Summary and outlook

The main goal of the *eROSITA* mission is to obtain a large sample of galaxy clusters to constrain dark energy by means of cluster counts. However, *eROSITA* will possess a large PSF (28″) and the cluster detection task will be further complicated by the presence of significant Poisson fluctuations of the X-ray background on cluster scales. In this regard, the main purpose of the work presented here was to show different methods and strategies to achieve a high detectability and characterisation of galaxy cluster for *eROSITA*.

In the first part of this chapter, various wavelet-based source detection algorithms were tested by means of simulated *eROSITA* images. For this purpose, a simulator code was developed. It generates X-ray images for a given exposure time with controlled configurations of point-like and extended sources, and it takes into account the main instrumental characteristics of *eROSITA*. The detection efficiency and contamination level, as well as the recovery of source characteristics, such as the count-rate and positional accuracy, were analysed. The results show that some wavelet-based source detection algorithms perform well on the detection of point-like and extended sources on the simulated *eROSITA* images.

In the second part of the chapter, a more profound comparison of different source detection methods was made. For this exercise, realistic simulations of the sky and a two distinct detection algorithms, a wavelet-based and a sliding cell algorithm, were used. Both methods show a good performance in the detection of point-like and extended sources. Although both methods give similar results, the main conclusion is that any source detected by the algorithms must be further characterised via a maximum likelihood fitting. This allows performing source classification, separating point-like from extended sources, and to derive more precise source properties.

The obtained results show that wavelet-based detection algorithms represent an excellent alternative to the current *eROSITA* detection tools, in particular regarding the detection of extended sources.

In the last part of the chapter, the galaxy cluster population that *eROSITA* will be able to identify by means of the available source detection tools was studied. For this purpose, the eSASS source detection pipeline was run over extensive and dedicated realistic *eROSITA* image simulations. In this way, the capabilities of eSASS detection algorithm were investigated. The output space parameter of the eSASS detection pipeline provides the necessary means to understand the detected sources and to assemble a sample of galaxy clusters with controlled selection effects. In this way, the sample can be used for cosmological studies. The results show that the *eROSITA* cluster selection is characterised by a 2D selection function, based on cluster extension and flux, rather than a flux-limit characterisation.

The distribution of galaxy clusters of a given mass and redshift that passed the obtained selection function was calculated. The results show that current detection algorithms will allow the detection of more than $\sim 10^5$ galaxy clusters on the *eROSITA* data, thus confirming the theoretical predictions. This will allow a tight constraint on the cosmological parameters using galaxy cluster counts. The results show that the use of suitable source detection and characterisation algorithms and a careful construction of a cluster selection function are the key points for obtaining a complete sample of galaxy clusters.

4.5.1 Future work

As mentioned before, two of the main factors that influence the cluster selection function are the used detection algorithm and the X-ray morphology of the galaxy clusters. Regarding the first aspect, there are many available X-source detection techniques that can be used for the determination of the *eROSITA* cluster selection function. Different detection approaches should be tested since each method helps to investigate different source properties. As mention earlier, wavelet-based detection algorithms promise a good performance on the cluster detection efficiency. Therefore, a future work consists in obtaining the cluster selection function by means of other detection algorithms and comparing it with the eSASS results.

So far, galaxy clusters have been simulated as symmetrical β-models. However, the distribution of the morphological characteristics of clusters as a function of redshift is not known. Therefore, a further characterisation of the cluster selection function with more simulations that cover a broader range of cluster properties is necessary. For example, galaxy clusters can be broadly classified as disturbed and non-disturbed. Both samples must be simulated and the selection function must be quantified.

On the other hand, the simulations used up-to-now distribute randomly the position of the sources. However, both objects, AGN and clusters, have their own measured correlation functions. Such correlations must be taken into account in the image simulation since it can introduce spurious sources affecting the purity of the sample. In particular, the AGN auto-correlation function tends to increase the number of close-by AGN pairs and would make the impact of confusion even more important for the selection of extended sources.

Finally, it is well known that AGNs lie in galaxy clusters. Their X-ray emission contaminates the clusters, making it difficult to disentangle both objects. Due to the lack of high-resolution imaging in *eROSITA*, the cluster detection efficiency and the source classification scheme can be altered due to the presence of X-ray bright AGN in (or projected onto) the cluster. On the one hand, the unresolved AGN emission can boost the surface brightness of a cluster and, therefore, enhance the detection probability. On the other hand, the AGN emission can dominate over the extended emission and then the cluster will be rejected. Therefore, it is necessary to estimate the effects of AGN on the cluster detection efficiency.

CHAPTER 5

Detection of high-redshift galaxy groups with the future *ATHENA* mission

ATHENA (Advanced Telescope for High Energy Astrophysics) is the next generation of X-ray observatories, and it has been selected as the second L-class mission in ESA's Cosmic Vision 2015-25 plan. Its launch is foreseen in 2028, and it will address some fundamental questions in modern astrophysics and cosmology by investigating black holes, matter under extreme conditions, the formation and evolution of galaxy groups, galaxy clusters and the large-scale structure, and the lifecycles of matter and energy.

By 2028, it is expected that our cosmological model, which describes the evolution of the Universe, will be tightly constrained from projects such as the eROSITA and Euclid satellite missions. However, major astrophysical questions related to the formation and evolution of the largest collapsed structures, namely galaxy groups and clusters, will remain open. ATHENA will help to answer the questions of how and when the first galaxy groups in the Universe, massive enough to bind more than 10^7 *K gas, formed. In this chapter, the capabilities of detecting early galaxy groups (*$z > 2$*) by ATHENA are studied. Since little is known about the thermo-dynamical state of such objects, different physically motivated models are simulated and tested. Moreover, distinct performance parameters for the ATHENA instrumental setup (effective area, PSF, spatial resolution, etc.) are examined in order to define the ATHENA science requirements for finding high-redshift galaxy groups. Detailed simulations show that such galaxy groups can be detected as extended sources by ATHENA and that the key instrumental parameters are a large effective area and a good spatial resolution over the full FoV.*

Note: This chapter is adapted from the *Athena+ supporting paper: The evolution of galaxy groups and clusters*, to which I am a contributor (Pointecouteau et al. 2013). The paper was part of the prospective work to prepare and support the White Paper presenting the science theme of the *Athena+* mission to ESA (Nandra et al. 2013). The content of the paper was adapted for this part of the thesis, in order to better highlight my contribution.

5.1 ESA's long-term science programmes

The science programme is the main mandatory activity of the European Space Agency[1] (ESA). It focuses on scientific research from space, primarily in the areas of the exploration of the solar system, the Universe and fundamental physics. Given the cost of space missions and the limited available funds, defining the programme demands an extensive long-term planning. This requires the development of broad and competitive study processes, in which the scientific community takes a very active role, all with the aim to provide the best possible selection of scientific goals and projects that fulfil them.

In 1985, ESA approved the first long-term programme (1985-2000) of scientific research in space: Horizon 2000. It consisted of four cornerstone missions, which were related to previously selected science themes: the Solar observatory (*SOHO*), the X-Ray Multi-Mirror Mission (*XMM-Newton*), the *Rosetta* mission, and the *Herschel* Space Observatory. The second long-term programme, Horizon 2000 Plus, was approved in 1995 for the 2007-2016 time frame. This programme included the successful *Gaia* mission. It was also decided to refer to the Horizon 2000 and the Horizon 2000 Plus programmes as the Horizons 2000 plan. The Horizons 2000 plan also contains a large number of medium and smaller missions, like the *Cassini-Huygens* mission and the *Planck* satellite. ESA classifies the missions in three categories: small (S-class), medium (M-class) and large (L-class). This classification is based on the assigned budget, with L-class missions being the most expensive ones. All missions cover many of the frontier space science fields and typically take over two decades to go from initial concept to the production of scientific results.

5.1.1 Cosmic Vision

Created in 2005, Cosmic Vision[2] (2015–2025) is ESA's current long-term plan for space science missions, and it is the continuation into the next decade of the ESA science planning cycle. Its programme theme is based on the following key questions:

1. What are the conditions for planet formation and the emergence of life?
2. How does the Solar System work?
3. What are the fundamental physical laws of the Universe?
4. How did the Universe originate and what is it made of?

Any proposed mission should address one or more of the above questions. There has already been four ESA calls for mission ideas. So far, the approved missions are: the CHaracterizing ExOPlanet Satellite (*CHEOPS*) a S-class mission for launch in 2017; three M-class missions to be launched at the end of this decade and at the beginning of the next one, the Solar Orbiter, the *Euclid* satellite, and the PLAnetary Transits and Oscillations of stars (*PLATO*) mission; and three L-class missions for launch in the 2020s, the Jupiter Icy Moons Explorer (*JUICE*), the Advanced Telescope for High-ENergy Astrophysics (*ATHENA*), and the evolved Laser Interferometer Space Antenna (*eLISA*).

---

[1] http://www.esa.int/ESA

[2] http://sci.esa.int/cosmic-vision/

5.1.2 The selection of a science mission

Whenever appropriate, ESA issues a call for proposals for new science missions to fulfil the purposes of its science programme. The call includes descriptions of the scientific programme goals, size, the cost of the mission, development time required, among other details. Such calls are addressed to the scientific community, and can generate up to 100 responses from different academic groups.

The selection process of a science mission, which can take up to 1 year, can be summarised as follow:

- ESA calls for mission ideas.
- Deadline for submission of a letter of intent.
- Deadline for proposal submission.
- Peer review by the Space Science Advisory Committee (SSAC), such process leads to a recommendation of 3-4 selected mission candidates.
- Second peer review by the SSAC recommendation, leaving 2 selected mission candidates.
- Decision by the Science Program Committee (SPC).
- Final peer review by the SSAC.
- Final SPC decision.

5.2 Towards a real mission

In March 2013, ESA issued a call[3] for White Papers (proposals), where the scientific community was asked to propose science themes and associated questions that could be addressed by the next two L-class missions, L2 and L3, within the Cosmic Vision programme. Such missions are currently planned for launch in 2028 and 2034, respectively.

The European X-ray community met to pursue and conceive a single theme/mission concept, which could satisfy the ESA call. The general consensus was that the proposed science theme will be called *The Hot and Energetic Universe*. This science theme will address primarily two questions:

1. How do black holes grow and shape the Universe?
2. How does ordinary matter assemble into the large-scale structures that we see today?

With such goals, the Cosmic Vision themes 3 and 4 (see Section 5.1.1) could be covered. Following ESA's call rules, the X-ray community decided that the proposed White Paper would be based on supporting science papers prepared by different science working groups.

5.2.1 The Hot and Energetic Universe

The White Paper submitted by the X-ray community presented the science theme motivating the *Athena+* mission (Nandra et al. 2013). The *Athena+* mission supersedes the International X-ray Observatory *(IXO)* and the *ATHENA* mission concepts. The *IXO* mission was a former ESA-NASA collaboration selected for an Assessment Phase study during the first L-class mission call in ESA's Cosmic Vision plan. In 2011, the rules of this international cooperation changed, and ESA decided to redefine the L-class mission candidates. During the reformulation *IXO* became *ATHENA*. *Athena+* is the successor

---

[3] http://sci.esa.int/cosmic-vision/51454-call-for-white-papers-for-definition-of-l2-and-l3-missions/

of *ATHENA*, but with enhanced capabilities in terms of angular and spectral resolution, effective area, therefore, better detection sensitivity, and instrument FoV. In this section, a brief description of the two main elements of the science theme *The Hot and Energetic Universe* is presented. More details can be found in Nandra et al. (2013).

The first key question is *how black holes grow and shape the Universe*. A complete understanding of galaxies requires the comprehension of the growth of their central supermassive black hole through cosmic history. A key goal is to increase the understanding of black hole evolution out to early cosmic times where the first galaxies were formed. Black holes in galaxies emit primarily in X-rays thanks to accretion processes. However, current facilities do not allow to study the evolution of black holes out to high redshifts ($z = 6 - 10$) due to a lack of high sensitivity and good angular resolution. These instrumental features are necessary to study in detail the X-ray spectrum of accreting black holes at the peak of galaxy growth at $z = 1 - 4$. These measurements can help to understand the interaction between black holes and their host galaxies in a wide redshift range.

The second key question addresses *how ordinary matter assembles into the large-scale structures that we see today*. This question can be answered by studying the physical evolution through cosmic time of the most massive structures in the Universe, namely galaxy groups and clusters. As explained in Section 2.1.2, these massive structures have formed by accreting gas from the intergalactic medium. By falling into the deep dark matter potential, the accreted gas heats up and emits in X-rays. This can lead to studies of the astrophysical origin of the large-scale structure. In order to quantify the effect of astrophysical processes in the structure formation, it is necessary to study the thermodynamical and chemical composition of the gas. This can be achieved by performing spectroscopic observations of groups and clusters at high redshift ($z > 1$). However, current X-ray observatories do not possess the necessary collecting area and spectral resolution to study the origin of galaxy groups and clusters.

The *Hot and Energetic Universe* does not only comprise the study of black holes and galaxy groups and clusters. The desirable mission will have unprecedented observational capabilities, enabling the observation of a wide range of objects of interest to the astronomical community. This includes solar system bodies and exoplanets, stars, compact objects, supernova remnants, the interstellar medium, and luminous extragalactic transients, such as gamma-ray bursts (see Fig. 5.1).

As mentioned above, the White Paper that motivates the *Athena*+ mission is based on more detailed supporting papers. Different science working groups[4] were assembled to advocate how the *Athena*+ mission could address various science questions in the following areas:

- The evolution of galaxy groups and clusters (Pointecouteau et al. 2013).
- The astrophysics of galaxy groups and clusters (Ettori et al. 2013).
- AGN feedback in galaxy clusters and groups (Croston et al. 2013).
- The missing baryons and the warm-hot intergalactic medium (Kaastra et al. 2013).
- The formation and growth of the earliest supermassive black holes (Aird et al. 2013).
- Understanding the build-up of supermassive black holes and galaxies (Georgakakis et al. 2013).
- Astrophysics of feedback in local AGN (Cappi et al. 2013).
- The close environments of supermassive black holes (Dovciak et al. 2013).
- Solar system and exoplanets (Branduardi-Raymont et al. 2013).
- Star formation and evolution (Sciortino et al. 2013).
- End points of stellar evolution (Motch et al. 2013).

---

[4] For more detailed information: http://athena2.irap.omp.eu/spip.php?rubrique7

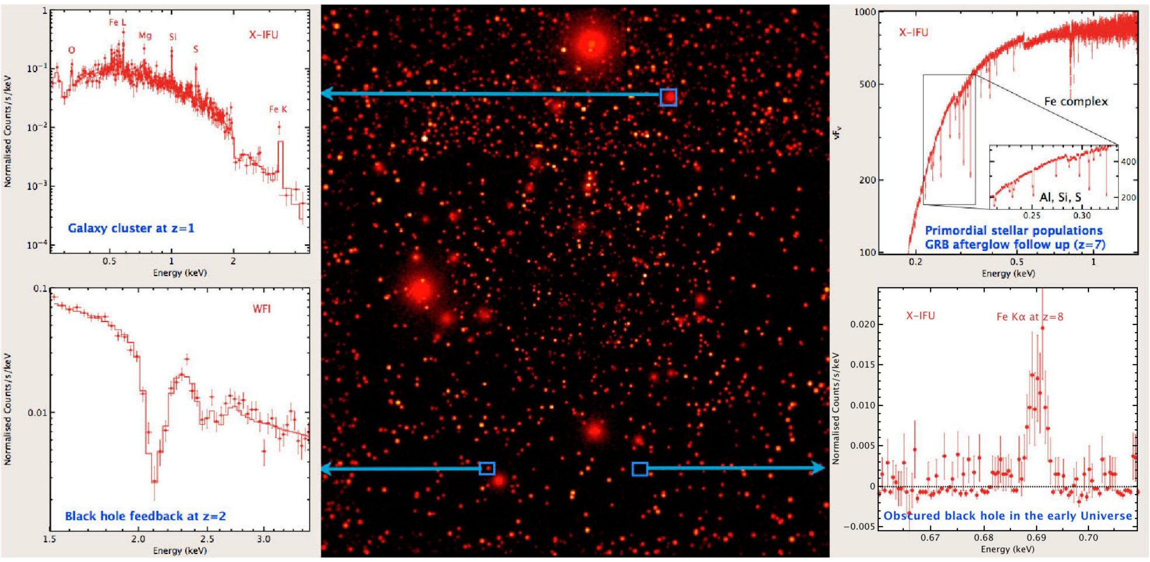

Figure 5.1: The central panel is a simulated deep *Athena+* observation, while the four surrounding spectra illustrate advances in different science areas, none of which are possible with current facilities. *Top left*: Simulated X-IFU X-ray spectrum of a high-redshift ($z = 1$) galaxy cluster. *Top right*: Simulated X-IFU X-ray spectrum of an afterglow from primordial stellar populations ($z = 7$). *Bottom left*: Simulated WFI spectrum from a QSO feedback at $z = 2$. *Bottom right*: Simulated X-IFU X-ray spectrum of an early AGN at $z = 9$. Figure adapted from Nandra et al. (2013).

- The astrophysics of supernova remnants and the interstellar medium (Decourchelle et al. 2013).
- Luminous extragalactic transients (Jonker et al. 2013).

In the next section I briefly describe the proposed *Athena+* mission, and then, I fully detail my work on the detection of high-redshift groups with *Athena+*. This work is included in Pointecouteau et al. (2013).

5.2.2 The *Athena+* Observatory

The main instruments and performance characteristics of *Athena+* have been described in detail in Section 3.3.2. Compared with *IXO*/*ATHENA*, the *Athena+* concept proposes to incorporate important enhancements: doubling of the effective area, an improvement by a factor ~ 2 in the angular resolution ($5''$ on axis), and quadrupling of the FoV. Fig. 3.2 shows that *Athena+* will have an order of magnitude greater photon grasp and 3 times better optical resolution than *XMM-Newton*. Then, *Athena+* will have a better performance and scientific results than *XMM-Newton*. Moreover, the targeted large effective area combined with the large instrumental FoV will make *Athena+* a major step in the high-energy observational capabilities (see left panel of Fig. 3.2).

5.3 Galaxy groups and clusters at high redshift with *Athena+*

Current instruments, like *XMM-Newton* and *SPT*, have detected galaxy clusters up to $z \sim 1.5 - 2$ (e.g. Bayliss et al. 2014; Mantz et al. 2014). By the end of the next decade, it is expected that the *eROSITA*

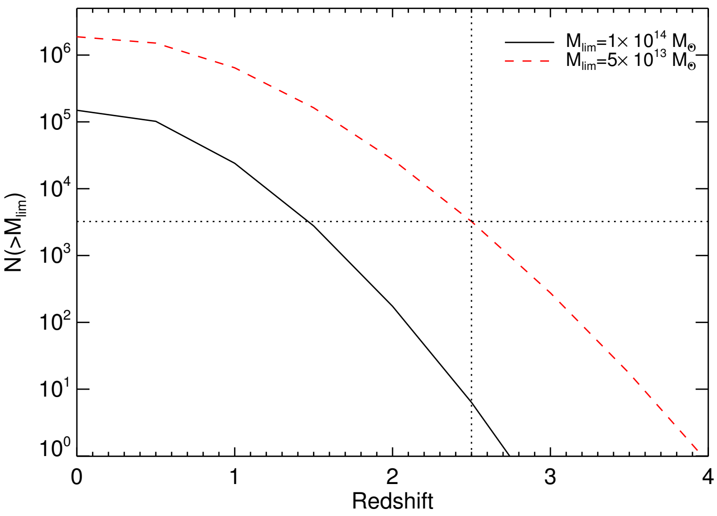

Figure 5.2: Expected number of halos above a given redshift with a masses greater than 1×10^{14} $M_\odot$ (black-solid line) and 5×10^{13} $M_\odot$ (red-dashed line). This halo mass function has been calculated by assuming a WMAP9 cosmology (Hinshaw et al. 2013) and a Tinker et al. (2008) mass function.

and *Euclid* missions would have identified all galaxy clusters and a large fraction of galaxy groups out to $z \sim 2$ (Refregier et al. 2010; Merloni et al. 2012). However, there will be plenty of open questions regarding the physical processes and the state of matter in the collapsing structures at high redshift.

At high redshifts ($0.5 < z < 2.5$), massive star-forming galaxies start to assemble galaxy groups and clusters in the dark matter potentials. Around the same redshift range, the star formation activity in galaxies is at its maximum (e.g. Bouwens et al. 2009). Moreover, some studies show that central supermassive black hole outbursts are taking place at the same redshifts (e.g. Merloni et al. 2004). It is expected that the trapped gas in the forming galaxy groups is heated not only by gravitational in-fall but also by non-gravitational feedback processes taking place in the infalling galaxies. However, the relation between the halo properties and the physical processes involved in their formation and evolution is still not understood. Observing and understanding these relations and processes are one of the main goals of *Athena+* (Pointecouteau et al. 2013).

As discussed in Section 3.4.3, the presence of an extended X-ray emitting ICM is a proof of the collapse and formation of a galaxy group in a gravitational potential well. At higher redshifts ($z > 2.5$), the detection and study of such small and faint galaxy groups are possible only through powerful X-ray telescopes like *Athena+*. By the end of the 2020s, it is expected that *Athena+* will discover the first galaxy groups ($z > 2.5$), and it will be also used to follow-up on galaxy groups and clusters detected by other surveys, like *eROSITA* and *Euclid*.

5.3.1 Number of galaxy groups at high redshift

If one calls objects with $M < 1 \times 10^{14}$ $M_\odot$ a galaxy group, one expects to find quite a number of galaxy groups through all redshifts. In the case of galaxy clusters ($M > 1 \times 10^{14}$ $M_\odot$), more than 99% are formed below $z \leq 2$, whereas above $z = 2$ there are about 27,000 groups with $M \geq 5 \times 10^{13}$ $M_\odot$ all over the sky. This can be clearly seen through the halo mass function (see Section 2.2.3) shown in Fig. 5.2. This figure shows the number of galaxy clusters and groups in the Universe above certain redshift and above two different limiting masses: 1×10^{14} M$_\odot$ and 5×10^{13} M$_\odot$. This halo mass function has been calculated by assuming a WMAP9 cosmology (Hinshaw et al. 2013) and a Tinker et al. (2008) mass function.

Above $z \geq 2.5$, around 3,200 galaxy groups with $M \geq 5\times10^{13}$ M$_\odot$ are expected to exist in the Universe. Assuming that these galaxy groups are uniformly distributed in the sky, *Athena*+ needs to survey a minimum area of ~ 41253 deg$^2/3,200 \approx 13$ deg^2 to detect at least one high-redshift ($z \geq 2.5$) galaxy group. The goal FoV value for *Athena*+ is $50'$, which corresponds to an observing area of ~ 0.55 deg^2 per pointing. By assuming that *Athena*+ will observe with an 80% of efficiency, and only 40% of those observations will have acceptable conditions for extragalactic studies (e.g. with large exposure time), then $\sim 10,000$ ks can be used to look for galaxy groups at high redshift per year. Dividing this time into 100 observations of 100 ks each, one obtains a survey area of ~ 55 deg^2. Therefore, it is expected that more than four galaxy groups with $M \geq 5 \times 10^{13}$ M$_\odot$ at $z \geq 2.5$ can be discovered by *Athena*+ per year.

One could think that such galaxy groups (with $M = 5 \times 10^{13}$ M$_\odot$ at $z = 2.5$) are too faint and too small to actually be detected by *Athena*+, but in reality they are expected to have a radius (r_{500}) of around $30''$, which is six times larger than the *Athena*+ PSF. Moreover, for such galaxy groups, *Athena*+ will collect about 900 source photons and 3100 background photons within r_{500} in the $[0.2 - 2]$ keV energy band. These values correspond to a signal-to-noise ratio larger than 14. These values are calculated by assuming on-axis response files, an `APEC` model with an abundance of 0.3 and a Hydrogen absorption of 2×10^{20} cm^{-2}, and local cluster scaling relations (Reichert et al. 2011).

To assess the detection of high-redshift groups more quantitatively, controlled source detection tests are performed. In this work, simulated *Athena*+/WFI pointed observations have been produced. These simulations take into account the expected X-ray and particle background, and the different instrumental effects, such as vignetting and off-axis PSF degradation. The simulations are analysed through a source detection and characterisation algorithm to quantify the detection efficiency of high-redshift galaxy groups. The methodology is detailed explained in the following.

5.3.2 Simulation of X-ray images

As discussed in Section 3.5, simulations are helpful to identify key instrumental parameters that are necessary to detect galaxy groups at high redshift with *Athena*+. A simulation code was developed in order to generate X-ray images for a given exposure time with extended sources and a realistic population of point-like sources. The code takes into account the main instrumental characteristics of *Athena*+, and it is flexible enough to allow testing for different instrumental configurations.

Due to the effect of the redshifted bremsstrahlung exponential cut-off, the simulations are performed in the $[0.2 - 2]$ keV energy band where one expects most of the galaxy group emission (see Section 2.1.2). The extended sources (galaxy groups) are modelled by a $\beta-$profile. The core radius has a fixed value of $r_c = 0.2 r_{500}$ and $\beta = 0.55$ (Clerc et al. 2012a). The expected count-rate is calculated with the `XSPEC` spectral fitting package (Arnaud 1996) by using an `APEC` model, with an abundance of 0.3 and a Hydrogen column density $n_H = 2 \times 10^{20}$ cm^{-2}; and the cluster mass-temperature and mass-luminosity scaling relations of Reichert et al. (2011). The spatial distribution of the extended sources is fixed at different off-axis angles ($0'$, $12.7'$, and $18.6'$) in order to test the effect of vignetting on their detection.

The population of point-like sources is assumed to consist of AGNs. The flux distribution and source density of AGNs is described by the $\log N - \log S$ relation of Moretti et al. (2003), down to a flux of 1.15×10^{-15} erg s^{-1} cm^{-2} in the [0.5 – 2] keV energy band. The conversion factor between the flux given by the $\log N - \log S$ relation and the source count-rate in the [0.2 – 2] keV energy band is calculated assuming a power law model in `XSPEC` and using the *Athena*+/WFI on-axis response files. This power law model uses an index equal to -1.42 and a n_H column density of 2×10^{20} cm^{-2}. The AGNs are randomly distributed in space.

The *Athena*+/WFI pointings are simulated using a circular FoV of $50'$ with a resolution of $1''$ per pixel. The source count-rates are based on the on-axis response convolved with the corresponding PSF and vignetting. These effects are applied on a source by source basis. As shown in Section 3.3, the vignetting effect causes the loss of some photos, since the effective area of the telescope at a given off-axis angle depends on the energy of the photon (see left panel in Fig. 3.2 and left top panel in Fig. 5.3). The PSF is modelled using a King model (as parameterised by Ghizzardi 2001). The PSF shape parameter is rescaled to match the energy and off-axis range of *Athena*+. Then, the PSF core radius is estimated in order to match the half energy width (HEW, see Section 3.3), which is provided by the mirror calibration files as a function of energy and off-axis. This modelling does not account for the asymmetry at large off-axis angle and high energy. The PSF is recomputed for each source depending on its off-axis angle.

The X-ray background is also included in the simulations (see Sections 3.2 and 3.5). The induced instrumental and cosmic X-ray background are modelled using the software `XSPEC` according to the *Athena*+ specifications (Rau 2013). The particle background has a flux of 5.07×10^{-4} cts s^{-1} arcmin^{-2} in the [0.2 – 2] keV energy band, the cosmic X-ray background flux value is 2.16×10^{-2} cts s^{-1} arcmin^{-2}, and the diffuse soft background flux is 3.64×10^{-4} cts s^{-1} arcmin^{-2}.

An example of a *Athena*+/WFI simulated image is shown in the right top panel of Fig. 5.3.

5.3.3 Detection procedure

A proper analysis of the detection of high-redshift groups with *Athena*+ should report on the probability of identifying such objects as extended sources, and not simply on detecting them. As described in Section 3.4.1, in the absence of multi-wavelength surveys[5], some techniques have been developed to detect and identify galaxy groups and clusters in X-ray surveys.

In order to quantify the detection probability of high-redshift groups, an approach similar to the one used in Pacaud et al. (2006) is applied to simulated *Athena*+ observations. The method consists of three main steps:

1. The raw photon images are manipulated with a multiresolution filtering.
2. The filtered images are scanned by a source detection algorithm, resulting in a preliminary source list.
3. Each detected source is fitted and characterised by a maximum likelihood procedure.

The wavelet-based `mr_filter` algorithm is used for image filtering. The source detection is performed by the `SExtractor` software. Section 4.2 gives a complete description of such algorithms. The source characterisation is done by means of a maximum likelihood procedure. In the following a brief description of each step is presented (see Section 3.4.1 for general remarks on source detection algorithms).

---

[5] By cross-correlating multi-wavelength data, galaxy groups and clusters can be identified in X-rays.

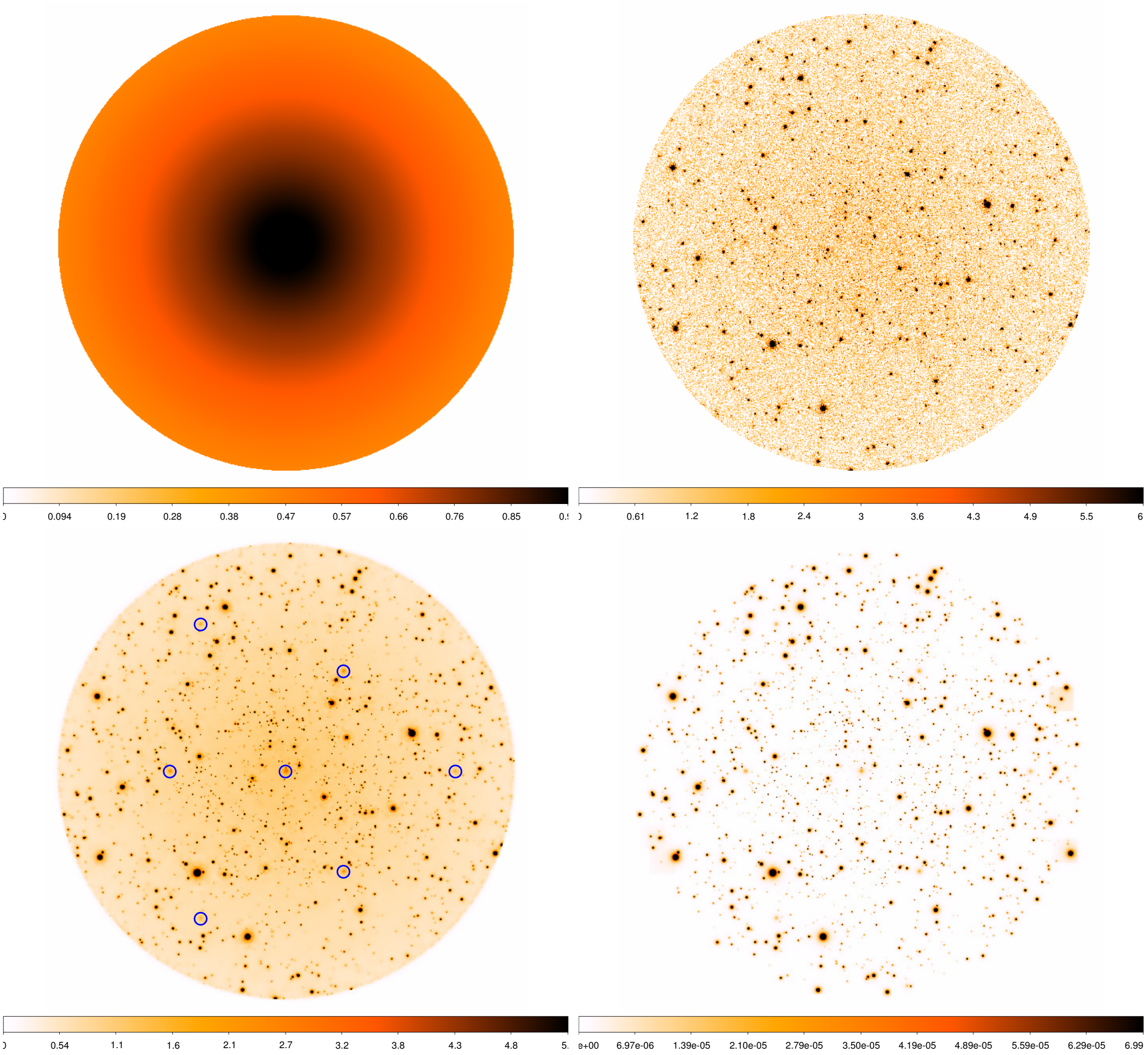

Figure 5.3: *Top left*: *Athena*+/WFI vignetting. The colour bar indicates the decrement of the effective area as a function of off-axis angle. *Top right*: *Athena*+/WFI raw X-ray photon image. The observation is simulated for 100 ks, and it has 50′ diameter in FoV. It includes a realistic population of AGNs and some galaxy groups. Particle and cosmic X-ray background are included. The effect of the vignetting and PSF degradation can be observed with off-axis angle. *Bottom left*: Filtered image obtained with `MR_FILTER`. The blue circles indicate the position of the simulated galaxy groups. *Bottom right*: Reconstructed image (counts per second) by the maximum likelihood fitting.

The simulated *Athena*+ images are filtered using the wavelet task `mr_filter` from the multiresolution package `MR/1` (Starck et al. 1998). `mr_filter` uses the "à trous" ("with holes") wavelet method and has a rigorous treatment of the Poisson noise (known as autoconvolution or wavelet function histogram method, Starck & Pierre 1998), which allows removing the insignificant features directly in the wavelet space using a thresholding algorithm.

The source detection on the filtered images is performed by the `SExtractor`[6] software (Bertin & Arnouts 1996). Originally, `SExtractor` was developed to detect objects in optical data, but since

---

[6] http://www.astromatic.net/software/sextractor

the multiresolution filtering removes most of the noise in an X-ray image and produces a smooth background, it can also be applied to filtered X-ray images (see left bottom panel of Fig. 5.3).

In the final step of the detection procedure, the sources identified by `SExtractor` are analysed by a maximum likelihood profile fitting procedure. The source fitting algorithm uses some `SExtractor` output parameter values as an input for source characterisation. For each source, the fitting code determines a model that maximizes the probability of generating the observed spatial photon distribution. Two source models are tested: a point-like model and a point plus extended model. The extended source model is given by a β-profile (see Eq. 2.5 in Section 2.1.2). Both models are convolved with the *Athena*+ PSF, include background, and all the significant *Athena*+ instrumental effects, such as exposure time and vignetting (see Pacaud et al. 2006 for further details).

The source model parameter estimation is calculated through the likelihood ratio, which uses the C-statistic (see Eq. 3.3), and it is minimized using the simplex method `AMOEBA` (Press et al. 1992). In this work, the most relevant best-fit output parameters are: extension likelihood, detection likelihood, source extent, and best-fitting position in pixel coordinates. The bottom right panel of Fig. 5.3 shows an example of a reconstructed image from the best fit model parameters.

5.3.4 Source classification

To assess the detection of high-redshift galaxy groups with *Athena*+, extensive Monte Carlo simulations are performed (see Section 5.3.2). Each simulation contains a population of AGNs and 7 identical galaxy groups of $M_{500} = 5\times10^{13}$ $\mathrm{M}_{\odot}$. The simulated galaxy groups are located at different off-axis angles: one is located on-axis, three at $12.7'$ off-axis angle, and three at $18.6'$ (see the bottom left panel in Fig. 5.3). The galaxy groups properties are simulated at seven different redshifts $z = 1$, 1.5, 2, 2.5, 3, 3.5, 4, having 15 simulated pointings per redshift. A total of 105 *Athena*+ pointings of 100 ks are simulated. These simulations are analysed with the detection procedure described in Section 5.3.3. All the detected sources are cross-identified with the input parameters using a correlation radius of $10''$. In principle, any detected source which cannot be cross-identified with any input source is considered a *spurious* detection. In this analysis, they are not quantified since the goal is only to measure the detection probability of high-redshift groups as extended sources. However, spurious detection must be taken into account for a deeper analysis (see Pacaud et al. 2006).

For the detection and identification of high-redshift groups as extended sources, the output best-fitting parameter space is explored. This examination has the purpose of establishing a source classification criterion, and to estimate the contamination by misclassified/spurious sources. Following a similar approach as Pacaud et al. (2006), the extent−extension likelihood space is examined (see Fig. 5.4). The distinction between point and extended-like sources is clearly visible. By choosing the location of $4 <$ extent < 150 and extension likelihood > 20 (solid lines in Fig. 5.4) the majority of the galaxy groups are recovered and the level of contamination is kept as low as possible.

Figure 5.5 (blue-shaded histograms) shows the detection probability of galaxy groups of being detected as extended sources. In such histograms, detection probability equals 1 means that all simulated galaxy groups, at a given redshift and off-axis angle, have been detected as extended sources. The error in the detection probability is given by a binomial law since there are only two events to consider: detection or

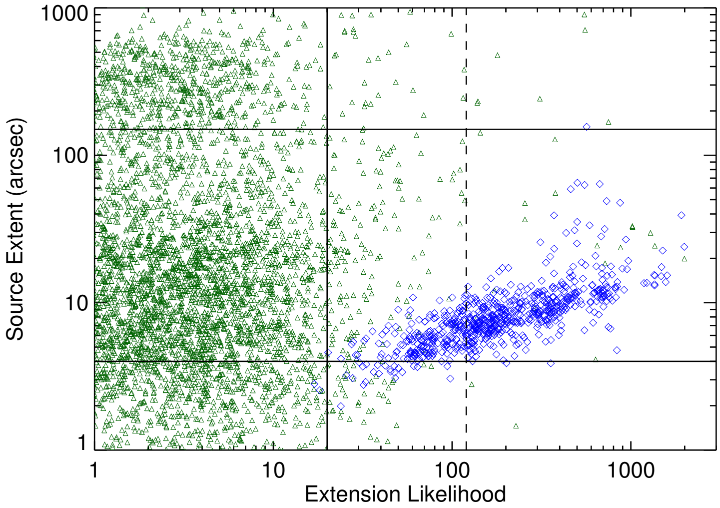

Figure 5.4: Best-fitting values in the extent−extension likelihood plane. Point-like sources (AGN) are displayed as green triangles, while the simulated extended sources (galaxy groups) as blue diamonds. The solid lines at extent = 4, 150 and extension likelihood = 20 determine the selection criteria for extended-like sources.

non-detection of the input sources. The error is calculated through the Wilson interval approximation:

$$\sigma(P_s) = \frac{\sqrt{N_d(1 - P_s) + 1/4}}{N_s N_i + 1}, \tag{5.1}$$

where N_i is the number of simulated images, N_s the number of simulated sources, and N_d the number of detected sources. P_s is the detection rate of one source ($P_s = N_d/N_i N_s$). One can observe that even at large off-axis angles, a 100 ks simulation allows detecting almost all simulated galaxy groups.

Above $z > 1$, around $\sim 6.5 \times 10^5$ galaxy groups of $M_{500} = 5 \times 10^{13}$ $\mathrm{M}_\odot$ are expected to exist in the Universe (see Fig. 5.2). Assuming that such groups are uniformly distributed in the sky, it is expected that *Athena*+ detects $\sim 6.5 \times 10^5/41,253$ deg^2/0.55 deg^2 ~ 9 galaxy groups per pointing. The contamination level, i.e. misclassified sources located at the chosen parameter space, is $\sim$ 11 false extended sources per pointing. This gives 55% contamination in the extended source detection. On the one hand, to maintain the contamination to a reasonable level, one can choose a more conservative criterion. For example, an extension likelihood = 120 (dashed line in Fig. 5.4). This gives a false detection value of $\sim$ 1 source per simulation. However, this selection excludes a number of extended sources, and the detection probability decreases (see blue-filled pattern histograms in Fig. 5.5). This decrement increases with off-axis angles, showing the effect of the PSF degradation and vignetting on extended sources: the maximum likelihood fitting gives a lower extent and extension likelihood values to sources located closer to the edges of the pointing because they get fainter and broader. On the other hand, by 2028 such high contamination levels can be handled by cross-identifying the data with other multi-wavelength measurements, e.g. from *Euclid*, and the Large Synoptic Survey Telescope (*LSST*).

Figure 5.5 also shows a fairly flat detection probability with redshift. This result is explained by different properties of the self-similar evolution model of galaxy groups and clusters (see Section 2.2.4):

1. The X-ray cluster luminosity increases with redshift, by consequence more X-ray photons are emitted. In this work, the expected luminosity is calculated by using a non-self similar paramet-

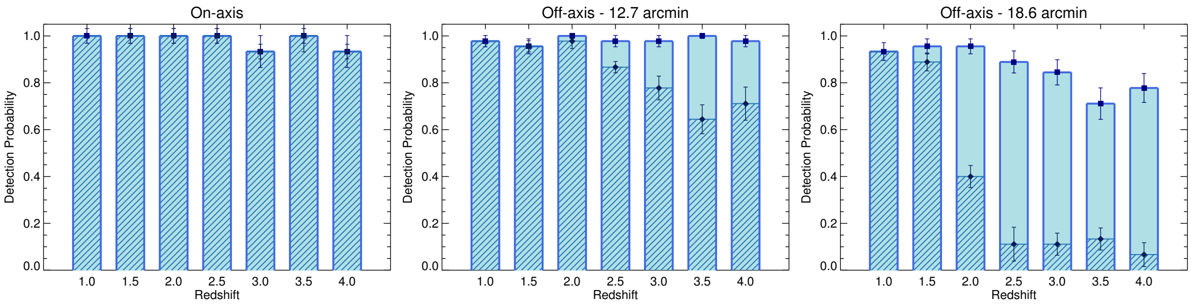

Figure 5.5: The histograms show the source detection probability of $M_{500} = 5 \times 10^{13}$ $\mathrm{M}_{\odot}$ galaxy groups as function of redshift in 100 ks simulations. Each panel shows a different off-axis angle where the galaxy groups are placed in the simulations (on-axis, 12.7′, 18.6′). The blue-shaded histograms display a less conservative criteria ($4 <$ extent < 150 and extension likelihood > 20 in Fig. 5.4) for selecting galaxy groups as extended sources than the blue-filled pattern ones (extension likelihood > 120).

erisation (Reichert et al. 2011), which predicts a lower luminosity than the self-similar one but it also increases with redshift (see Fig. 5.6).

2. The cluster temperature also increases with redshift, giving an enhancement of photons in the detection band.
3. The cluster intrinsic size (r_{500}) decreases with redshift since the density of the Universe rises as a function of redshift (see Section 2.2.4). Despite this lowering, the size of the simulated galaxy groups is always larger than the *Athena*+ PSF ($> 10''$). This also results in fewer number of background photons within the source area.

In summary, galaxy groups with masses $M_{500} = 5 \times 10^{13}$ $\mathrm{M}_{\odot}$ can be detected with high probability as extended sources by *Athena*+, at any off-axis angle and out to high redshift.

5.3.5 Different scenarios at high redshift

The feasibility of galaxy group detection at high redshift ($z > 2$) can be questioned since little is known about the physical processes and the state of the collapsing structures at that time. As mention in Section 5.3, the current knowledge on galaxy clusters is limited to redshifts below $z \lesssim 2$. In the following, different physically motivated scenarios at high redshifts are tested. Such models mainly modify the shape and count-rate of the surface brightness of galaxy groups.

Central AGN contamination

From low redshift observations it is known that there exists a correlation between supermassive black hole masses and the global properties of their host galaxies (e.g. mass, velocity dispersion; Ferrarese & Merritt 2000; Marconi & Hunt 2003). This suggests that the formation and evolution of galaxies are tightly coupled to their central supermassive black hole. It is also known from X-ray observations that AGN feedback in central galaxies of galaxy groups and clusters has a major effect on the thermodynamics and heavy element distribution in the ICM (e.g. Giacintucci et al. 2011; Gitti et al. 2012).

Merloni et al. 2004 has shown that the supermassive black hole accretion rate has a peak activity at $z > 2$, implying that AGN feedback could be playing an important role in galaxy groups at high redshift.

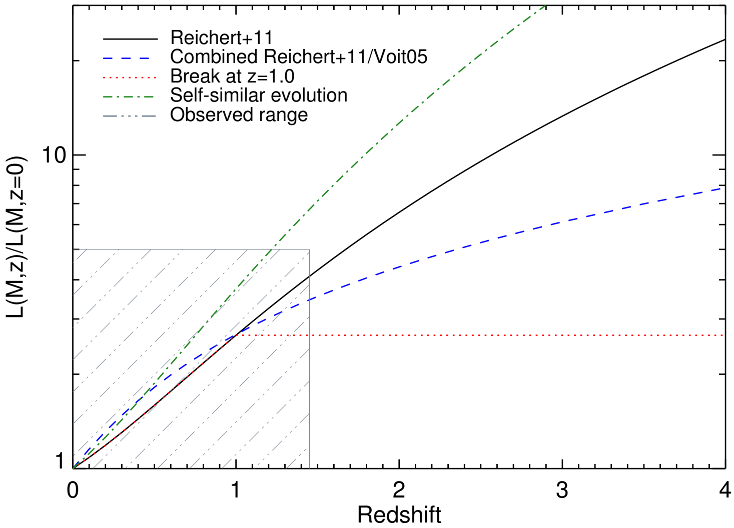

Figure 5.6: Redshift evolution of the Luminosity−Mass, $L_X - M$, scaling relation. The self-similar redshift evolution is shown by the green dot-dashed line. The default relation in this work is displayed by the black-solid line, which was measured by Reichert et al. (2011). Two other non-self similar models are displayed: the blue-dashed line shows a mixed model between Reichert et al. (2011) and Voit (2005), and the red-dotted line represents a model where the luminosity does not evolve above $z = 1$. The region marked by the triple-dot-dashed lines indicates the redshift range over which the luminosity of galaxy groups and clusters have been observed.

Furthermore, it has been shown that the density of X-ray bright AGN in galaxy clusters is larger than the field density (Ruderman & Ebeling 2005; Gilmour et al. 2009), and even more, such density appears to be significantly larger for clusters at $z > 1$ (Galametz et al. 2009; Martini et al. 2013). Several of the known galaxy groups and clusters at high redshift show the presence of a central X-ray AGN (e.g. Gobat et al. 2011; Erfanianfar et al. 2013). Therefore, the presence of a central AGN could be a limiting factor for the *Athena*+ detection of high-redshift galaxy groups as extended sources.

The presence of X-ray bright AGN in (or projected onto) a galaxy group or cluster can have two different consequences on their detection probability: unresolved AGN emission can boost the X-ray flux and surface brightness of a galaxy cluster, which will enhance the detection probability; or the extended emission can be overlooked, and then the galaxy cluster will be rejected. In order to quantify the impact of AGN on the detection probability of high-redshift groups, a central AGN is included on top of the galaxy groups in the *Athena*+/WFI simulations.

Recent cosmological hydrodynamical simulations (Magneticum Pathfinder simulation, Dolag et al., in prep.) indicate that the X-ray emission from AGN in clusters contributes a significant fraction to the total X-ray emission at high redshift (Fig. 5.7). On the contrary, at low redshift the AGN X-ray emission is negligible, consistent with observations. Furthermore, such simulations show that at high redshift one may typically expect a factor of ∼ 5 times fewer X-ray photons from AGN than from the hot gas and that typically only 1 or 2 AGN contribute 95% of the total AGN X-ray luminosity. Finally, the simulations also show that the ICM X-ray luminosity increases with redshift, as expected (see Fig. 5.6).

From the results of the Magneticum simulations, the X-ray flux of the simulated central AGN is taken as five times lower than its corresponding galaxy group X-ray flux. Figure 5.8 shows the detection probability of high-redshift groups with a central AGN (lila-shaded histograms). At on-axis and at intermediate off-axis angles, the detection probability at any redshift is not significantly affected by the

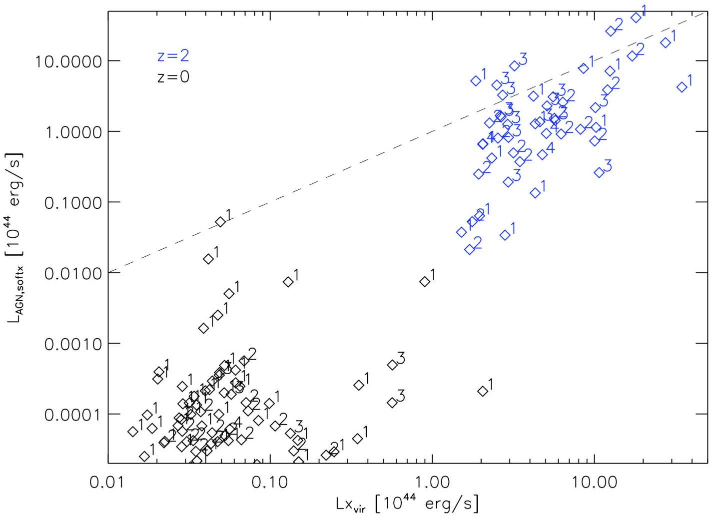

Figure 5.7: Soft band X-ray luminosities of AGN and ICM in massive galaxy groups at $z = 0$ (black diamonds) and $z = 2$ (blue diamonds). The number of AGNs in each cluster is indicated on top of the corresponding diamond. In estimating this number, the faintest AGNs that together make up less than 5% of the total point-source luminosity were ignored. Figure provided by K. Dolag.

presence of a central AGN (see blue-shaded histograms in Fig. 5.5 for comparison). However, at higher off-axis ($\gtrsim 18'$), the detection probability starts to decrease above $z > 2$. At such off-axis angles the PSF gets broader ($\gtrsim 10''$), which affects the characterisation of contaminated extended sources.

It is important to stress that the detection probability of galaxy groups containing a central AGN is also well determined due to the maximum likelihood fitting, which includes an extended source profile plus a point-like model (see Section 5.3.3). If such fitting would not include a point-like model, the detection probability would be lower since the AGN emission would overshadow the extended emission from the galaxy group.

So far, it has been assumed a 100 ks *Athena*+/WFI observation time for the simulations. However, the availability of such long exposures remains uncertain. Thus, a more conservative exposure time value is

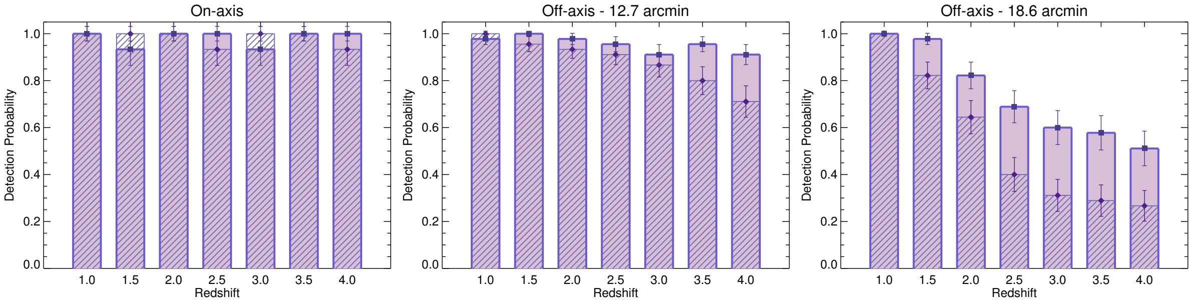

Figure 5.8: The histograms show the source detection probability of $M_{500} = 5 \times 10^{13}$ $M_\odot$ galaxy groups with a central X-ray AGN as function of redshift in 100 ks simulations (lila-shaded histograms). The AGN have five times lower flux than the total galaxy group flux. Each panel shows a different off-axis angle where the galaxy groups are placed in the simulations (on-axis, 12.7′, 18.6′). The lila-filled pattern histograms display the detection probability for simulations with a lower exposure time, 30 ks.

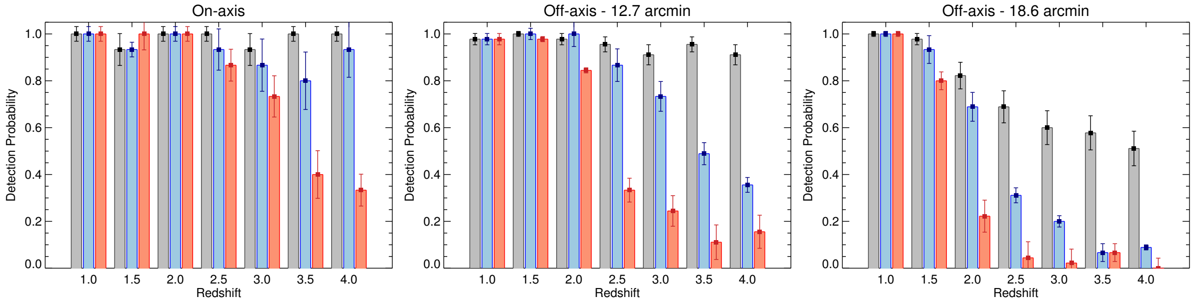

Figure 5.9: The histograms show the source detection probability of $M_{500} = 5 \times 10^{13}$ $\mathrm{M}_\odot$ galaxy groups with a central X-ray AGN as function of redshift for different luminosity evolution models in 100 ks simulations. The AGN have five times lower flux than the total galaxy group flux. Each panel shows a different off-axis angle where the galaxy groups are placed in the simulations (on-axis, 12.7′, 18.6′). The gray-shaded histograms represent the galaxy groups with a luminosity given by Reichert et al. (2011, same histograms as in Fig. 5.8). The blue-shaded histograms have galaxy groups with a strong feedback impact in the luminosity evolution, and the red-shaded histograms have no luminosity evolution beyond $z > 1$.

also tested: 30 ks. The detection probability for such simulations is also presented in Fig. 5.8 (lila-filled pattern histograms). At on-axis angles, the probability of detecting high-redshift groups with a central AGN is high, while at intermediate off-axis and beyond, the detection probability starts to decrease, especially for the high-redshift objects. For example, at higher off-axis angles the detection probability of galaxy groups at $z > 3$ in the 30 ks simulations drops by 50% in comparison to the 100 ks ones.

In summary, a central AGN will not significantly affect the *Athena*+ detection of high-redshift galaxy groups at intermediate off-axis and below. The most affected detection probability is only at large off-axis for the highest redshifted galaxy groups, where it drops to 50%.

Luminosity evolution

As mentioned in Section 5.3.4, the luminosity of high-redshift galaxy groups has been calculated from the extrapolation of the $L_X - M$ relation measured by Reichert et al. (2011). This relation exhibits a flatter redshift evolution than the self-similar evolution (see Fig. 5.6), and it has been determined using clusters below $z = 1.46$. Beyond this redshift, very little is known about the evolution of the $L_X - M$ scaling relation.

Thanks to the good sensitivity and angular resolution, *Athena*+ could increase the observed number of massive galaxy groups and galaxy clusters out to $z = 2$, and the measurement of the cluster $L_X - M$ scaling relation beyond this redshift would be feasible. At present, only simple tests can be performed by artificially modelling a weaker redshift evolution. Similar tests as above are carried out, but employing two more conservative evolution scenarios of the $L_X - M$ scaling relation: a strong feedback model (Voit 2005), where L_X evolves as $E^{\frac{1}{2}}(z)$, combined with the Mass-Temperature, $M - T$, relation from Reichert et al. (2011, which is close to self-similar); and a very conservative case, where no evolution above $z = 1$ is assumed (see blue-dashed and red-dotted lines, respectively, in Fig. 5.6). The impact of such strong redshift evolution criteria on the detection probability of high-redshift groups is displayed in Fig. 5.9.

As expected, sources with lower surface brightness have less probability to be detected as extended sources. The extended emission is too shallow in comparison with the one from the central AGN, mak-

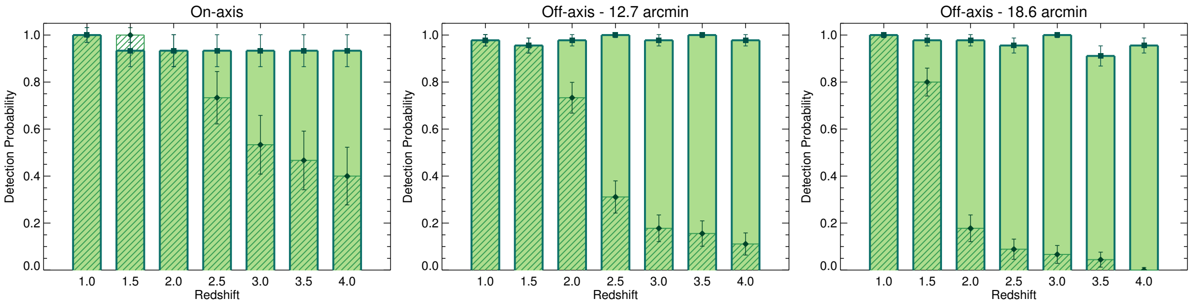

Figure 5.10: The histograms show the source detection probability of $M_{500} = 5 \times 10^{13}$ $M_\odot$ galaxy groups with a central X-ray AGN as function of redshift for two different redshift luminosity evolution models in 100 ks simulations. The green-shaded histograms represent the galaxy groups with a luminosity given by Reichert et al. (2011), and the green pattern-filled histograms are without luminosity evolution beyond $z > 1$. The AGN have five times lower flux than the total galaxy group flux, and the core radius has been increased from $0.2r_{500}$ to $0.6r_{500}$ in comparison with the previous histograms. Each panel shows a different off-axis angle where the galaxy groups are placed in the simulations (on-axis, 12.7′, 18.6′).

ing the source characterisation more difficult. Thus, *Athena*+ can contribute in constraining evolution models by the number of detected galaxy groups and clusters at $z > 1$, as well as from direct spectral analysis for the brightest sources. However, if *Athena*+ is not able to detect high-redshift groups, it does not necessarily mean that the redshift evolution of the luminosity is flatter. The non-detection of high-redshift galaxy groups can also be attributed to a combination of different physical processes happening at that redshift, for which there is no complete understanding or knowledge. In the next section, this possible scenario is explained in more detail.

Flatter surface brightness profile

AGN feedback, star formation and supernova explosions are well-known processes that release a significant amount of energy into the surrounding interstellar and intra-cluster media. Such feedback processes can redistribute the ICM in galaxy groups and clusters, causing a less concentrated surface brightness (e.g. Eckert et al. 2012). In consequence, galaxy groups do not appear self-similar anymore and their detection probability is affected. In a similar way as with the different redshift luminosity evolution models, *Athena*+ can constrain feedback models by detecting a different number of galaxy groups at $z > 2$ than expected. Moreover, *Athena*+ can contribute to feedback model constraints by observing the flatter surface brightness profiles in low-redshift groups, since such objects will be well-resolved.

To test the impact of feedback on the detection probability of high-redshift groups, the core radius of the surface brightness was increased from $0.2r_{500}$ to $0.6r_{500}$ in the simulated galaxy groups. Such a change results in a flatter $\beta-$profile. The tests were redone for two different luminosity evolution models: the default by Reichert et al. (2011) and the extreme case, where there is no luminosity evolution beyond $z > 1$. The results are displayed in Fig. 5.10.

Increasing the core radius makes the galaxy groups appear more *extended*. This can be seen when comparing Fig. 5.8 (blue-shaded histograms) to Fig. 5.10 (green-shaded histograms), where the only difference is the increment in the core radius. The maximum likelihood fit tends to give a higher extension likelihood value for such sources, increasing their detection probabilities. However, if the luminosity evolution is flatter, the maximum likelihood fitting does not find the simulated galaxy groups as extended sources, and therefore, their detection probabilities are lower (green pattern-filled histogram in Fig. 5.10). If the luminosity decreases with redshift and the surface brightness is flatter, then the central AGN emission dominates the source characterisation. The combination of a lower luminosity redshift evolution with a flatter surface brightness profile can be disentangled, but the wings of extended emission have to be well characterised to break up the $r_c - \beta$ degeneracy.

5.4 Mission acceptance

On November 28 2013, ESA's SPC announced the decision on the science themes for the large missions L2 and L3 in 2028 and 2034, respectively. ESA received thirty-two proposals, out of which *The Hot and Energetic Universe* and *The search for Elusive Gravitational Waves* were chosen as the focus of ESA's next two large science missions within the Cosmic Vision science programme.

In January 2014, ESA announced a call for mission concepts for the large L2 mission opportunity within its science programme. Again, this proposal was open to the broad scientific community. For the European X-ray community it was evident that the *Athena*+ mission would be recommended since it was an essential part of the proposed and accepted ESA's science theme. The preparatory tasks for submission of such a proposal started, and it was decided that the mission would be referred to as *ATHENA* once more (see Section 5.2.1).

The different assembled science working groups were asked to provide quantified science requirements for different performance parameters which will define the mission instrumental setup (effective area, PSF, spatial resolution, etc.), and will allow carrying out the ESA's science programme at the same time. All working groups delivered science requirement details to fulfil their goals. The information was gathered in a mission proposal with the title: *ATHENA*, The Advanced Telescope for High ENergy Astrophysics, a mission addressing *The Hot and Energetic Universe* science theme; and submitted to ESA. In June 2014, ESA selected the *ATHENA* telescope as its second Large-class science mission.

I have contributed to constraining distinct performance parameters which allow the detection of high-redshift galaxy groups as extended sources. The methodology is the same as the one described in the previous section. In the following a brief summary of the approach is given.

5.4.1 Science requirements for finding high-redshift galaxy groups

A baseline *ATHENA* mission setup was defined, and a set of calibration files were distributed to study the scientific capabilities (response files, PSF and vignetting dependence on off-axis angle, background model, etc.). In order to justify such science requirements and assess the impact of deviations from the baseline setup, additional instrumental configurations files were provided. In the following the baseline model and setup, as well as the most important instrumental parameters that can affect the detection of high-redshift groups, are presented.

Baseline mission setup

In the baseline model mission setup, the *ATHENA* mirror module has an Iridium (Ir) coating and an effective area of ~ 2.1 m^2 at 1 keV and ~ 0.26 m^2 at 6.5 keV. The mirror has a conical-curved shape, which gives an optimum performance at on- and off-axis. The considered outer aperture radius for the telescope is 1500 mm, and the inner aperture is 250 mm. There is an optical blocking filter to reduce the contamination by optical light. The HEW on-axis has a value of $\sim 5''$, and $\sim 7''$ at $25'$ off-axis angle, both at 1 keV. The WFI/FoV has $40'$ diameter.

For the present analysis on-axis response files are used, since the PSF and vignetting effect are applied on a source by source basis (see Section 5.3.2). The *ATHENA*/WFI particle background has a value of $\sim 5.1 \times 10^{-4}$ cts s^{-1} arcmin^{-2} in the $[0.2 - 2]$ keV energy band, the AGN background is $\sim 5.0 \times 10^{-3}$ cts s^{-1} arcmin^{-2}, and the Galactic background value is $\sim 2.9 \times 10^{-2}$ cts s^{-1} arcmin^{-2} (see `XSPEC` model parameters in Rau 2014).

Default *ATHENA*/WFI simulation

The science goal is to detect and characterise high-redshift ($2 < z < 3$) galaxy groups with masses of 5×10^{13} M$_\odot$ to constrain formation models of such objects. The galaxy group surface brightness is predicted from local scaling relations (Reichert et al. 2011). All simulated groups are contaminated by a central AGN, which has five times lower flux than the total galaxy group flux (see Section 5.3.2 for details). Two different exposure times are simulated, 100 and 30 ks. There is no need to test for different models (e.g. no AGN contamination, distinct luminosity evolution, etc.) since the results presented in Section 5.3.5 can easily be scaled to other configuration setups.

To detect and characterise the high-redshift groups as extended sources, the parameters obtained from the maximum likelihood fitting are fixed again (see Section 5.3.4). The extension likelihood parameter is fixed to a value of ≥ 50 for the 100 ks simulations, and ≥ 30 for the 30 ks simulations. For both set of simulated observations, a source extent of $\geq 3.5''$ and $\leq 40''$ is set. Such boundaries give a ~ 1.5 misclassified sources per pointing in the 100 ks simulations, and ~ 4.5 in the 30 ks ones.

For practical reasons, the discussion will be centred on the results of galaxy groups at $z = 2.5$. The averaged FoV-detection efficiency and the number of misclassified sources per pointing in the baseline setup are given in Table 5.1 for the 100 and 30 ks simulations. In this case, the detection efficiency is almost 100% across the entire FoV for the 100 ks simulations, but not for the 30 ks case, where 30 % of the simulated sources remain undetected.

Relevant performance parameters

In the following the relevant instrumental parameters within different setup configurations, which directly affect the detection of high-redshift galaxy groups, are presented in more detail. The description includes the changes in the instrumental parameters with respect to the baseline model and the consequences on the detection of high-redshift galaxy groups. A summary is presented in Table 5.1.

- **Effective area**: Two alternative mirror setups were tested,
    1. A smaller mirror (fewer outer mirror shells) with an effective area of ~ 1.5 m^2 at 1 keV. Such effective area reduces the detection efficiency by 10% in the 100 ks simulations, and by $> 20\%$ in the 30 ks ones. The number of misclassified sources remains similar to the baseline model setup.

Performance parameters	Simulated exposure time							
	100 ks				30 ks			
	FoV detection efficiency				FoV detection efficiency			
	< 15′	< 20′	< 25′	False detections	< 15′	< 20′	< 25′	False detections
Baseline setup	100%	98%	97%	1.5	95%	85%	72%	4.5
Smaller effective area	90%	90%	90%	2.5	76%	61%	44%	4.5
Ir + B_4C coating	95%	94%	94%	4.0	95%	94%	93%	8.0
4×Particle background	100%	95%	93%	3.0	96%	89%	81%	6.0
Worse PSF	92%	91%	90%	3.5	83%	76%	69%	8.5
No optical filter	98%	97%	96%	3.0	94%	93%	92%	7.0

Table 5.1: Different instrumental parameters which have the most impact on the detection of high-redshift galaxy groups are shown. Two types of simulated observations are tested, 100 and 30 ks. For both sets, the FoV-averaged detection efficiency for the different parameters is presented. Such efficiency is given within distinct off-axis angles. The number of misclassified sources per pointing is also given.

2. Same geometry mirror as the baseline setup, but with an Iridium plus Boron Carbide (B_4C) coating. Such change increases the effective area by ~ 20%, i.e. to ~ 2.5 m^2 at 1 keV. The detection efficiency of the 100 ks simulations is a bit lower than the baseline model. The reason being that the background increases, which can affect the source characterisation. This is confirmed by the increment of false extended sources. The greater effective area has a positive result on the detection efficiency in the 30 ks simulations, but again, the number of misclassified sources increase by a factor of two in comparison with the default setup.

- **Charged particle background**: The normalisation of the default charged particle background is increased by a factor of four. Such increment does not significantly affect the detection efficiency in either set of simulations. The only negative consequence is the boost on the misclassified extended sources.
- **Point-spread function**: On-axis the HEW has a value of ~ 7″, and ~ 10″ at 25′ off-axis angle. The detection efficiency is affected by less than 10% in the 100 and 30 ks simulations. The reason is that the considered objects still have an angular size larger than the PSF.
- **No optical filter**: If no optical filter is considered, the detection efficiency of the 100 ks simulations remains similar to the default setup. For the 30 ks simulations the efficiency increases.

In summary, the default setup will allow detecting high-redshift galaxy groups with good efficiency. An effective area larger than 2 m^2 is necessary to have an efficiency above 50% for shallow observations. Because it is not currently clear whether deep observations will be possible, keeping a large effective area is important to detect high-redshift galaxy groups. The PSF should not exceed a HEW value of 8″ on-axis and 10″ at 25′ off-axis angle, otherwise the detection of early galaxy groups would not be reached. The rest of the tested instrumental parameters do not have a high impact on the detection efficiency of high-redshift galaxy groups.

5.4.2 Final remarks on the *ATHENA* mission

Once the *ATHENA* mission was accepted, the selection process moved into a study phase. In this phase, the initial mission design and costs are investigated in detail.

In the first study done by ESA's Concurrent Design Facility (CDF), it was suggested that the outer radius of the telescope should be reduced, yielding an on-axis effective area of 1.56 m^2 at 1 keV (lower than the proposed setup with $\sim$ 2.1 m^2 at 1 keV). Furthermore, a possible reduction in the rib spacing from 3 to 1 mm was also considered by the CDF. This rib spacing is the width of the different azimuthal cells that constitute one mirror in the pore optics design. This change would reduce the effective area at all energies by 12%, giving $\sim$ 1.37 m^2 at 1 keV. Once more, the *ATHENA* working groups were asked to assess the impact of such an effective area decrement on the science programme.

Impact of the effective area decrement

To quantify the impact of effective area reduction on the detection of high-redshift groups, similar tests as previously were performed. Briefly, in comparison with the baseline proposed setup, the averaged-FoV detection efficiency of galaxy groups at $z = 2.5$ decreases by $\sim$ 5% and $\sim$ 10% for the 1.56 m^2 and $\sim$ 1.37 m^2 cases, respectively, in the 100 ks simulations. Such decrement gets worse for the 30 ks simulations, where the detection efficiency is $\sim$ 30% and $\sim$ 40% lower than the default model for the 1.56 m^2 and $\sim$ 1.37 m^2 cases, respectively. Given the low detection efficiency in shallow observations, it is necessary to keep the proposed $\sim$ 2.1 m^2 effective area at 1 keV in order to secure the detection of high-redshift groups.

New calibration files have been released[7], and ESA is now comparing two main configuration setups: a proposed mission with an effective area $\sim$ 2.1 m^2 at 1 keV, and a CDF model with $\sim$ 1.4 m^2 at 1 keV. The new proposed model is slightly different from the baseline model described above. In the new proposed model, the detection efficiency of high-redshift groups increases to 100% for the 100 ks simulations, and up to 20% for the 30 ks ones, in comparison with the previous baseline configuration. Comparing these new numbers with the CDF model, in the 100 ks simulations the efficiency decreases only by 2% while in the 30 ks ones is 25% lower. Again, showing the importance to keep a large effective for the detection of high-redshift groups.

5.5 Summary and conclusions

In 2014, the Advanced Telescope for High Energy Astrophysics (*ATHENA*) was selected by ESA as the next generation of L-class mission within the Cosmic Vision programme. This X-ray observatory will study the *the hot and energetic processes in the Universe*. *ATHENA* aims to answer to fundamental questions: *i)* How do black holes grow and shape the Universe?, and *ii)* How does ordinary matter assemble into the large-scale structures that we see today?.

By the time *ATHENA* is launched in 2028, it is expected that the parameters of our cosmological model will be tightly constrained by other missions, such as *eROSITA* and *Euclid*. However, major astrophysical questions related to the formation and evolution of the largest collapsed structures, namely galaxy groups and clusters, will remain. A large X-ray observatory like *ATHENA* will allow observing and studying the earliest galaxy groups ($z > 2$) thanks to its combination of high sensitivity, large effective area, and good spatial and spectral resolution. This will contribute to our understanding of how and when the first galaxy groups in the Universe were formed.

---

[7] http://www.cosmos.esa.int/web/athena/resources-by-esa

In this work, the *ATHENA* capabilities on the detection of high-redshift galaxy groups were evaluated through extensive and dedicated image simulations. These simulations take into account the main instrumental features of *ATHENA*: X-ray and particle background, vignetting and PSF degradation with off-axis angle. Galaxy groups are simulated with realistic surface brightness profiles. The simulations also contain a realistic AGN population. The source detection process was done by a wavelet-based algorithm combined with the `SExtractor` software, and the source classification was performed through a maximum likelihood fitting.

The main results showed that high-redshift galaxy groups with masses of $M_{500} = 5 \times 10^{13}$ $\mathrm{M}_{\odot}$ at $z > 1$ will be detected with high probability ($> 80\%$) as extended sources by *ATHENA* in 100 and 30 ks simulated observations.

Since the hot gas properties in galaxy groups at redshift larger than 2 are unknown, several models were tested. These models are physically motivated from known local galaxy group properties. For example, central AGN contamination, different X-ray luminosity evolution models, and distinct surface brightness profiles. The general outcome of the simulations is that *ATHENA* will help to constrain structure formation and evolution models as well as feedback models by the number of detected galaxy groups at high redshift.

Distinct performance parameters for the *ATHENA* instrumental setup were also tested in order to define the science requirements for finding the earliest galaxy groups. The examined performance parameter were different effective area, PSF degradation with off-axis angle, spatial resolution, and instrumental background. The results show that galaxy groups at high redshift can be detected as extended sources by *ATHENA* when the key instrumental parameters are a large effective area (~ 2.1 m^2 at 1 keV) and a good spatial resolution ($< 10''$) over the full FoV.

The capacity of *ATHENA* in detecting high-redshift groups is promising due to its high sensitivity and good angular resolution. It is worth to stress that state-of-the-art source detection and characterisation algorithms also play an important role in the detection. From the obtained results, one can see that wavelet-based detection algorithms are efficient in detecting faint extended sources, and that maximum-likelihood fitting algorithms are key for source classification.

CHAPTER 6

Study of faint X-ray sources

Progress in our understanding of galaxy clusters and their use as precision cosmological probes requires a deeper multi-wavelength analysis of clusters. Galaxy clusters are identified by various observational techniques. These methods are sensitive to distinct physical components of the galaxy clusters. For example, X-ray techniques are sensitive to the extended bremsstrahlung emission arising from the hot intra-cluster medium, while optical and infrared observations identify the light coming from the cluster galaxy members. Then, multi-wavelength observations of galaxy clusters are necessary because they allow to understand the different physical states occupied by galaxy clusters at any cosmic epoch. This is important since the ultimate goal is to obtain an accurate census of clusters which leads towards a more accurate constraints on our cosmological model.

In this chapter, a comparison of two samples of high-redshift ($z > 0.8$) galaxy clusters, selected in the mid-infrared and X-ray bands, is presented. The aim is to study the physical differences between these galaxy cluster samples. Since some mid-infrared selected clusters are not detected in the X-ray bands, new and sophisticated tools are developed to study them.

The two techniques to study faint X-ray sources are: a Bayesian aperture photometry method and a stacking procedure. The former method uses Bayesian inference and takes into account the Poisson nature of the X-ray data. This allows to extract as much information as possible for a given source. The second technique allows to study the mean properties of a given sample by stacking their X-ray data. Both methods are developed in the framework of data obtained by the XMM-Newton observatory.

Note: Section 6.4 of this chapter is adapted from a paper of the same title. This manuscript will be submitted to the Monthly Notices of the Royal Astronomical Society (MNRAS) Journal. Since I am a co-author of the paper, I have adapted the manuscript for this thesis. The first two sections of this chapter correspond to Sections 4.1 and 5.5 of such manuscript and describe in detail the methods I have developed for the study of faint X-ray sources. The reference is Willis, J., Ramos-Ceja, M. E., Pacud, F., and Muzzin, A., 2016, MNRAS, to be submitted.

6.1 Studying faint X-ray sources

Current X-ray missions have been able to detect faint sources due to their high sensitivity and long exposure observations. Such sources are of great interest since they have never been observed before. Given the low flux of such sources, it is important to develop careful methods that allow extracting as much information as possible from the available data. For instance, such methods must take into account the Poisson nature of X-ray data, i.e. the low number counts of photons in X-ray images, in order to obtain useful quantities that describe faint X-ray sources.

In this chapter, two different techniques for studying faint X-ray sources are described. First, a Bayesian aperture photometry method is presented. This approach takes into account the Poisson aspect of the X-ray data and models the background noise. Second, a stacking method is described. It basically consists in adding together X-ray image cut-outs of sources. The aim is to enhance the information and to study the collective properties of a given sample.

In the final section of this chapter, an application of the above methods is presented. The techniques are applied to a mid-infrared selected sample of high redshift ($z > 0.8$) galaxy clusters. Most of these objects are not individually detected in X-rays. Hence, the necessity of using the Bayesian aperture photometry and stacking methods to investigate their X-ray emission. The aim of this study is to understand how the physical properties of galaxy cluster samples differ depending upon the observational technique used to identify them.

6.2 Aperture photometry

Photometry is the measurement of the source brightness in a given wavelength range. The simplest form of photometry is aperture photometry, where the flux is measured inside a particular region of the sky. Originally this was done in optical telescopes by using a physical aperture (e.g. a hole in a piece of metal). But nowadays, with imaging instruments, it is possible to use software to define an aperture.

The aperture contains photon counts not just from the source, but also from nearby sources and the background. The X-ray background is a diffuse emission observed in all directions (see Section 3.2). To reduce the contamination by background on the source photons, the aperture can be made smaller. However, this also reduces the number of photons from the source. And vice versa, if the aperture is larger to increase the photons from the source, the background also increases. A general trend is to choose an aperture that maximizes the signal-to-noise-ratio[1] (S/N) of the source in question.

An important difference between optical and X-ray is typical lower number of photons counts in X-ray astronomy. In the X-ray regime, sources with a few hundred photon counts are considered as bright objects. In fact, this has an impact on the X-ray photometry determination, since one has to use a broad energy band in order to collect a significant number of photon counts.

In the classical aperture photometry, the net source counts are obtained by directly subtracting the estimated background value from the data. However, in the low-count regime, such method is not optimal, especially for faint sources or for significant background values. Instead, more sophisticated approaches are necessary. One of such techniques is given by a Bayesian method, which allows the inclusion of the

---

[1] The signal to noise ratio is calculated as: $S/N = S/(S+B)^{1/2}$, where S and B are the source and background photons, respectively.

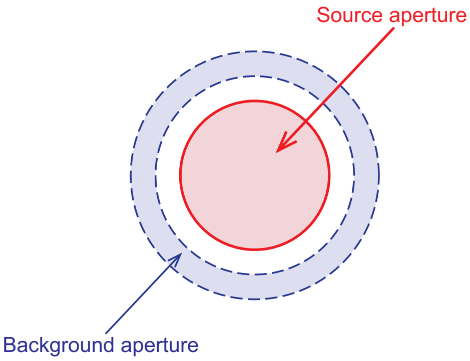

Figure 6.1: Aperture photometry sketch for an isolated source. In general, apertures can be of any shape.

background information, as well as the differences in effective areas and exposure times between the source and background regions. In the following, both the classical and the Bayesian approaches are described, along with the application of the Bayesian method to *XMM-Newton* observations.

6.2.1 The classical method

As previously mentioned, the source aperture is contaminated by background photons, and such contamination must be taken into account in order to estimate the net source counts. The background value is usually measured from an independent annular region located around the source (see Fig. 6.1). This region must be free of other sources to avoid further contamination. The above can be described mathematically as follows. The observed counts in a source aperture, C, of area A_S, and the observed counts in a background aperture, B, of area A_B are given by

$$C = s + b, \tag{6.1a}$$
$$B = rb. \tag{6.1b}$$

C is given by the sum of counts due to the source, s, and the background, b. The parameter $r = A_B/A_S$ accounts for differences in source and background areas. By solving these equations, the net source counts, s, can be obtained as

$$s = C - \frac{B}{r}. \tag{6.2}$$

One can observe that the net source counts are obtained by a direct subtraction of the background value from the source aperture.

As mention previously, current X-ray missions have been able to detect very faint sources due to their high sensitivity in long exposure observations. However, these objects usually have a handful of photon counts, making their detection and analysis difficult tasks. Furthermore, in long exposure observations, the background value also increases, overshadowing the source emission. In these cases, the source aperture photometry calculation given by Eq. 6.2 fails. This can result in the problem of negative source photon counts. Therefore, for faint X-ray sources, a different aperture photometry method is necessary.

6.2.2 Bayesian analysis

The advantage of a Bayesian approach for aperture photometry over a classical one is that Bayesian inference describes the different quantities in terms of probability distributions. This is suitable for X-ray observations, where the data has a Poisson nature. In the following, the core of Bayesian analysis, the Bayes' Theorem, is described, and then its application to the aperture photometry calculation.

Bayes' Theorem

Bayesian probability analysis is based on Bayes' Theorem, which calculates the *probability distribution* of an event based on data that might be related to the event. More specifically, Bayes' theorem describes how a given prior knowledge is updated based on information contained in observed data. Mathematically, the Bayes' theorem is described by

$$p(\theta|A, B) = \frac{p(A|\theta, B)p(\theta|B)}{p(A|B)}, \tag{6.3}$$

where A is the observed data, θ is the model parameter, and B represents any initial information known before A is observed. $p(\theta|B)$ is known as the *prior distribution*, and represents the previous knowledge before observing A. $p(A|\theta, B)$ represents the *sampling distribution* or *likelihood* of the data given the model parameters. $p(\theta|A, B)$ is called the *posterior probability* and is the updated knowledge regarding θ after observing A. Finally, $p(A|B)$ is the unconditional distribution of A and normalizes the posterior probability.

Bayesian aperture photometry

The Bayesian method for X-ray aperture photometry described here is based on the works by van Dyk et al. (2001) and Park et al. (2006).

As mention previously, in X-ray observations the observed source and background counts in a given aperture are generated via Poisson process. Thus, the source and background aperture photons can be described by Poisson distributions

$$C \sim \text{Poisson}(f(s+b)), \tag{6.4a}$$

$$B \sim \text{Poisson}(grb). \tag{6.4b}$$

Here, the factors f and g convert photon counts into a desired photometric quantity. For example, if $f \propto 1/T_S$ and $g \propto 1/T_B$, i.e. the inverse of the average exposure times in A_S and A_B, the resulting photometric quantity is the count rate in units of counts per second (cts s^{-1}).

In terms of Bayesian inference, the net source counts, s, in an given aperture are described by the posterior probability of s, marginalized over the background,

$$p(s|CB) = \int p(sb|CB)\mathrm{d}b. \tag{6.5}$$

This equation can be solved by using the Bayes' theorem. This is described in the following.

The joint posterior probability of s and b, $p(sb|CB)$, can be written in terms of the prior probability distributions for the source and background apertures, $p(s)$ and $p(b)$; and in combination with the data likelihood, $p(C|sb)$ and $p(B|b)$, for both apertures,

$$p(sb|CB) = \frac{p(s)p(b)p(C|sb)p(B|b)}{\int\int p(s)p(b)p(C|sb)p(B|b)\mathrm{d}b\mathrm{d}s}. \tag{6.6}$$

As previously mentioned, the data likelihood is described by a Poisson distribution in the source and background apertures,

$$p(C|sb) = \frac{f^C (s+b)^C e^{-f(s+b)}}{\Gamma(C+1)}, \tag{6.7a}$$

$$p(B|b) = \frac{(rgb)^B e^{-rgb}}{\Gamma(B+1)}. \tag{6.7b}$$

The corresponding prior probability distributions of the data likelihoods are the so-called $\gamma-$priors,

$$p(s) = \frac{\beta_S^{\alpha_S} (fs)^{\alpha_S - 1} e^{-f\beta_S s}}{\Gamma(\alpha_S)}, \tag{6.8a}$$

$$p(b) = \frac{\beta_B^{\alpha_B} (gb)^{\alpha_B - 1} e^{-g\beta_B b}}{\Gamma(\alpha_B)}. \tag{6.8b}$$

Here, α_S, α_B, β_S and β_B are parameters that define the shape of the functions, and take values from the prior knowledge on the data (see van Dyk et al. 2001 for further details).

Having all this information, Eq. 6.6 can be written as

$$p(sb|CB) = \frac{(s+b)^C s^{\alpha_S - 1} b^{B+\alpha_B-1} e^{-fs(1+\beta_S)} e^{-b(g\beta_B + f + rg)}}{\int_0^\infty \int_0^\infty (s+b)^C s^{\alpha_S - 1} b^{B+\alpha_B-1} e^{-fs(1+\beta_S)} e^{-b(g\beta_B + f + rg)} \mathrm{d}s\mathrm{d}b}. \tag{6.9}$$

By using the binomial expansion of $(s+b)^C$,

$$(s+b)^C = \sum_{j=0}^{C} \frac{\Gamma(C+1)}{\Gamma(j+1)\Gamma(C-j+1)} s^j b^{C-j}, \tag{6.10}$$

one can analytically solve the denominator in Eq. 6.9. For this, one first has to marginalize over s, and then integrate over b,

$$\int_0^\infty s^{\alpha_S + j - 1} e^{-s(f + f\beta_S)} \mathrm{d}s = \frac{\Gamma(\alpha_S + j)}{(f + f\beta_S)^{\alpha_S + j}}, \tag{6.11a}$$

$$\int_0^\infty b^{C+B-j+\alpha_B-1} e^{-b(g\beta_B + f + rg)} \mathrm{d}b = \frac{\Gamma(C + B - j + \alpha_B)}{(g\beta_B + f + rg)^{C+B-j+\alpha_B}}. \tag{6.11b}$$

The above results allows to solve analytically Eq. 6.5,

$$
\begin{aligned}
p(s|CB) = & \left[\sum_{j=0}^{C} \frac{1}{\Gamma(j+1)\Gamma(C-j+1)} \frac{\Gamma(C+B+\alpha_B-j)}{(f+gr+g\beta_B)^{C+B+\alpha_B-j}} \frac{\Gamma(\alpha_S+j)}{(f+f\beta_S)^{\alpha_S+j}} \right]^{-1} \\
& \times \sum_{j=0}^{C} \frac{1}{\Gamma(j+1)\Gamma(C-j+1)} \frac{\Gamma(C+B+\alpha_B-j)}{(f+gr+g\beta_B)^{C+B+\alpha_B-j}} s^{\alpha_S+j-1} e^{-fs(1+\beta_S)}.
\end{aligned}
\tag{6.12}
$$

The posterior probability distribution of s is described only in terms of observable quantities, like the source aperture, C, and background aperture, B, counts.

Until now, a priori knowledge has been included through the prior probability distribution. However, such information is not always available. Especially in X-ray observations, where the source data is limited to a single observation most of the time. In this case non-informative priors can be used. Such priors are usually flat and have no influence in the final result. Using non-informative priors, i.e. $p(s) = p(b) = 1$ in Eq. 6.6, is equivalent to set $\alpha_S = \alpha_B = 1$ and $\beta_S = \beta_B = 0$ in Eq. 6.12. The obtained posterior distribution for s is

$$
\begin{aligned}
p(s|CB) = & \left[\sum_{j=0}^{C} \frac{1}{\Gamma(j+1)\Gamma(C-j+1)} \frac{\Gamma(C+B+1-j)}{(f+gr)^{C+B+1-j}} \frac{\Gamma(1+j)}{f^{1+j}} \right]^{-1} \\
& \times \sum_{j=0}^{C} \frac{1}{\Gamma(j+1)\Gamma(C-j+1)} \frac{\Gamma(C+B+1-j)}{(f+gr)^{C+B+1-j}} s^{j} e^{-fs}.
\end{aligned}
\tag{6.13}
$$

As previously mentioned, in Bayesian inference, the final parameter information is contained in the posterior probability distribution. However, it is common to present the parameter in terms of a point estimator and credibility regions. For example, the mode of the posterior probability distribution is usually used as the point estimator. The mode corresponds to the maximum value in the posterior distribution and represents the most likely value of the parameter given the data. The credibility interval is determined by summing values of the posterior probability distribution alternately above and below the mode until the chosen credibility interval is reached. In case the mode results equal to zero, only the upper credibility bound is evaluated, and it is considered as an upper limit.

Figure 6.2 shows the performance of Eq. 6.13 in recovering the net source counts. This exercise assumes a constant background value equals 40 over the source and background apertures. The total number of counts in the source aperture is constantly increased, i.e. more counts are added to the 40 background counts. These extra counts represent the input source counts that Eq. 6.13 should recover. The top panel of Fig. 6.2 shows that Eq. 6.13 is indeed able to recover the input source counts. The points represent the mode of the posterior distribution, and the error bars show the 68% credibility interval. The bottom panels show the full posterior distribution obtained from Eq. 6.13 for some input source values.

There are two main points to highlight from the above Bayesian aperture photometry derivation. First, when C is large enough, the posterior probability distribution can be accurately approximated by a Gaussian distribution (see the bottom right panel of Fig. 6.2). In this case, it is expected that the classical and the Bayesian aperture photometry methods give very similar results. Second, in the case of very low source counts, the prior information truncates the posterior probability distribution at $s = 0$ (see top panel of Fig. 6.2). This avoids obtaining negative results for the net source counts. This represents an advantage of the Bayesian aperture photometry method over the classical approach.

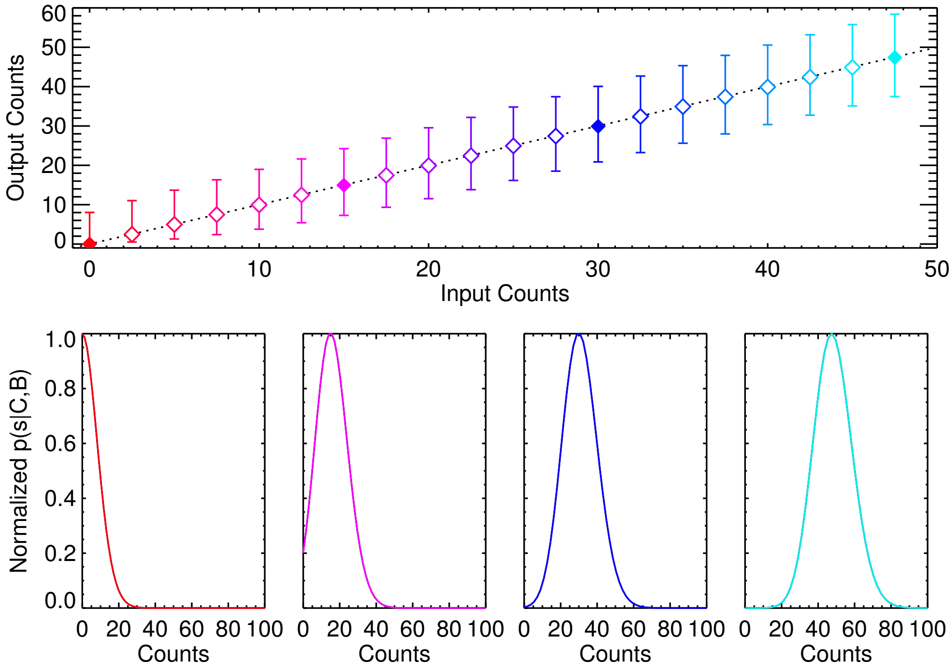

Figure 6.2: *Top:* Inferred counts from Eq. 6.13 as a function of input counts. The points represent the mode and error bar are given by the 68% credibility interval of the posterior probability distribution. The dotted line shows the expected 1 to 1 relation. For low number of counts, the credibility errors are asymmetric, avoiding negative counts as a result. *Bottom:* Normalized posterior probability distributions $p(s|C,B)$ for different input counts s (corresponding to the filled diamonds in the top panel). For high number of counts, $p(s|C,B)$ can be approximated by a Gaussian distribution.

6.2.3 Application to *XMM-Newton* observations

The Bayesian aperture photometry approach can be applied to any source in a given X-ray observation. In this section, the analysis is focused on observations made with the *XMM-Newton* telescope. In principle, the source and background apertures can be of any shape and size. In this work, the source aperture is taken as a circle and the background aperture as an annulus.

The background estimation is determined from local backgrounds, i.e. regions close to the source which share the same observational features. Since the X-ray background varies as a function of off-axis on the *XMM-Newton* detectors, the background can measure in two different ways:

1. If the source is located close ($< 2'$) to the pointing centre, the background aperture is an annulus centred on the source position. This annulus has a width of $1'$ and it is detached from the source aperture by $1'$. This minimizes the scatter of source counts into the background aperture.
2. If the source position is far ($> 2'$) from the pointing centre, the background aperture is an annulus that encompasses the source aperture and is located at a similar off-axis angle as the source. A quadrant of 45° centred on the source position is excluded to avoid residual source contamination.

Such background apertures help to reduce the systematic uncertainties due to the radial dependence of the background. Fig. 6.3 shows an example of both local background apertures.

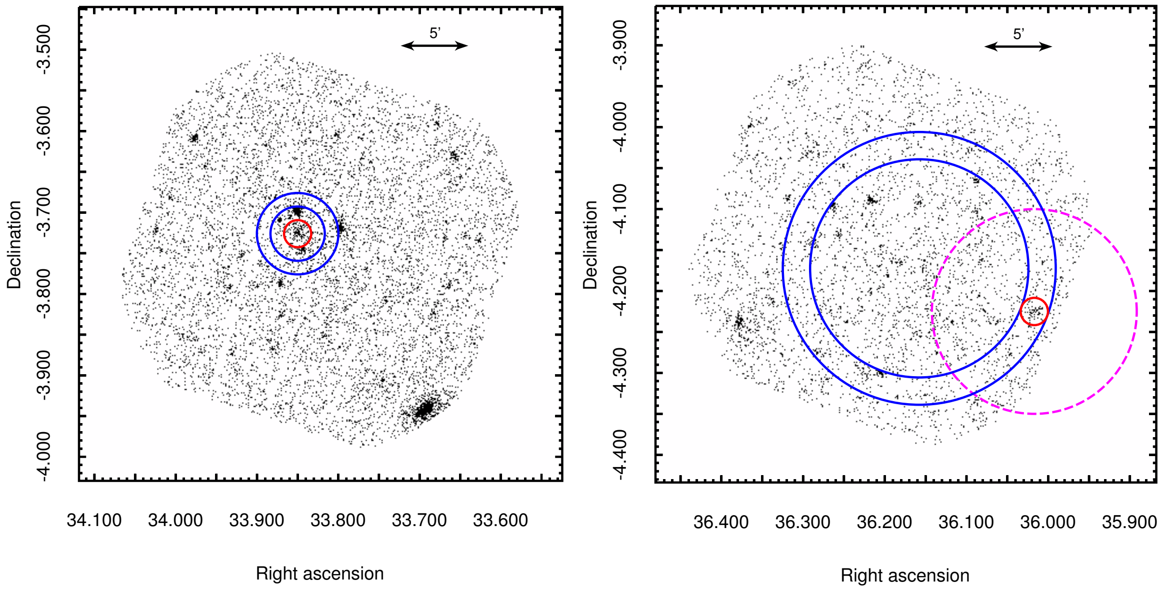

Figure 6.3. Examples of the background estimation method used in the Bayesian aperture photometry. Both examples show the PN detector of *XMM-Newton*. The photometry of the source is measured within the red circle, and the background within the blue annulus. *Left*: If a source is located close to the pointing centre, the background annulus surrounds the source aperture. *Right*: If a source is located far enough (> 2′) from the centre of the pointing, the background annulus encompass the source aperture and is located at the same similar off-axis angle as the source. The dashed magenta circle shows an excluded region from the background in order to avoid contamination from the source of interest.

As mentioned in Section 3.3.1, *XMM-Newton* has three cameras on board, MOS1, MOS2 and PN. The Bayesian aperture photometry method is applied individually to the three EPIC detectors, obtaining three different posterior probability distributions for each source. The goal is to measure the aperture counts of a given source, then, the different posterior distributions must be combined to obtain a single estimation of the net source count. Since the three measurements are independent, the joint posterior probability distribution is given by the product of the individual distributions

$$\begin{aligned} p(s_{\mathrm{MOS1}}, s_{\mathrm{MOS2}}, s_{\mathrm{PN}}|C_{\mathrm{MOS1}}, C_{\mathrm{MOS2}}, C_{\mathrm{PN}}, B_{\mathrm{MOS1}}, B_{\mathrm{MOS2}}, B_{\mathrm{PN}}) =& p(s_{\mathrm{MOS1}}|C_{\mathrm{MOS1}}B_{\mathrm{MOS1}}) \\ &\times p(s_{\mathrm{MOS2}}|C_{\mathrm{MOS2}}B_{\mathrm{MOS2}}) \\ &\times p(s_{\mathrm{PN}}|C_{\mathrm{PN}}B_{\mathrm{PN}}). \end{aligned} \tag{6.14}$$

This relation must be evaluated carefully, since the MOS and PN detectors have different sensitivities. Before applying Eq. 6.14, the sensitivity of the MOS (or PN) detectors must be scaled according to the MOS/PN (or PN/MOS) response ratio. Fig. 6.4 illustrates the posterior distributions obtained from the three *XMM-Newton* cameras for a given source, and the process of combining them to obtain a joint posterior distribution.

In X-rays, the usual photometric quantity is the flux. The Bayesian aperture photometry method can calculate the count-rate posterior probability distribution (see the f and g parameters in Eq. 6.4b). The left panel of Fig. 6.4 illustrates the count-rate posterior distributions obtained from the three *XMM-Newton* cameras for a given source. By multiplying the count-rate distribution by an energy conversion factor (ECF), one can obtain a flux posterior probability distribution (see right panel of Fig. 6.4). The

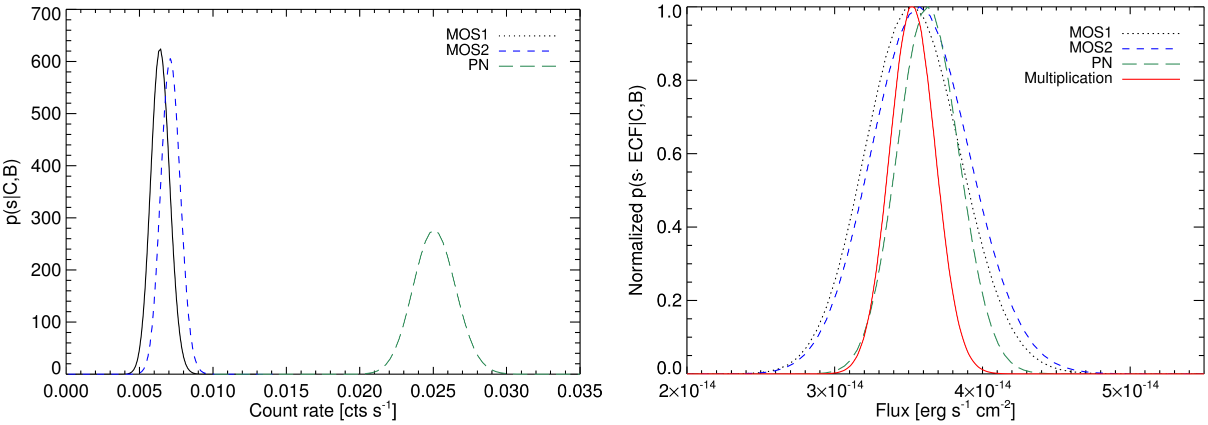

Figure 6.4. *Left*: Posterior probability distributions $p(s|C,B)$ for the count-rate in the three different detectors of *XMM-Newton*. The difference on the detection sensitivity between the MOS and PN cameras is clearly seen by the shift of the distributions. *Right*: Normalized posterior probability distributions, where the detector sensitivity corrections have been applied through the energy conversion factor (see text for details), which also translates the count-rate into a flux. The red line represents the multiplication of the three posterior probability distributions, i.e. the joint distribution (see Eq. 6.14).

ECF factor can be calculated using the `XSPEC` spectral fitting package (Arnaud 1996) for a given model together with the standard on-axis EPIC response matrices. The `XSPEC` model depends on the source in question.

For point-like sources, a final correction in the Bayesian aperture photometry is made by the encircled energy fraction (EEF). This is the fraction of the total light from a point source that is contained within a circular aperture. The EEF adjustment can be modelled using the King model (Ghizzardi 2001).

6.3 Stacking X-ray images

Stacking is a known statistical tool which adds data from a given set of objects to study their average emission. In most cases, the sources of interest are too faint to be individually detected, but they are known from other data sets. In this case, stacking provides an average detection, i.e. an upper limit of the characterisation of the sample properties. The stacking is usually done using images or source fluxes, and its astrophysical interpretation depends on the selection criteria of the input sources. This technique is used and applied on data from X-rays to radio wavelengths.

Given the large data sets from X-ray surveys, the stacking technique is becoming an important tool to study the mean properties of fainter X-ray sources, whether they are point-like (e.g. Nandra et al. 2002; Lehmer et al. 2007; Zinn et al. 2012) or extended (e.g. Dai et al. 2007; Rykoff et al. 2008; Anderson et al. 2013, 2015). The goal of adding together X-ray photons is the characterisation of the X-ray properties of a well-defined sample. To achieve this, bright X-ray sources, which are detected in the vicinity of sources in the sample, must be removed in order to avoid a bias in the results. Nonetheless, it is necessary to check whether any of the objects in the sample is individually detected in X-rays, which might give hints on the origin of the X-ray emission in the population of interest.

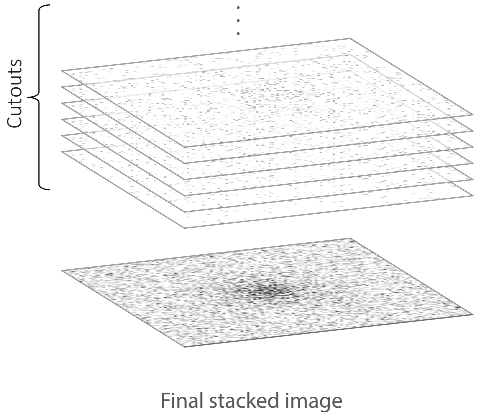

Figure 6.5: Representation of the X-ray stacking procedure: individual cut-outs, centred at the source positions, are added together to obtain a final stacked image. This example highlight that X-ray images have few photon in general.

6.3.1 Stacking procedure

In this work, a stacking method is developed within the framework of studying extended sources, namely galaxy groups and clusters. Although the stacking of point-like sources is very similar, some differences remain. The stacking algorithm is implemented to work in the image plane, with data from the *XMM-Newton* telescope. If necessary, the stacking procedure can be adapted to data from a different X-ray observatory.

Given a sample of objects, the stacking procedure works as follows:

1. Extract a cut-out from the EPIC images of each object for a given size and energy band, as well as cut-outs of the corresponding exposure maps. The size of the cut-out depends on the sources in question. On the one hand, the physical scale for sources at high redshift ($z > 0.8$, assuming a ΛCDM cosmology) is almost constant, i.e. the angular diameter distance does not change by more than 5%. Therefore, it is reasonable to fix a size for the cut-outs. On the other hand, the angular size coverage for sources at lower redshifts ($z < 0.8$) is different, consequently, it is necessary to rescale each cut-out to the same angular size in a given redshift. In this case, the photon count must be preserved.

2. Create a corresponding background map for each object. The background maps are produced by fitting a two component model to free-sources EPIC images. The background is modelled as: $B = A_1 \cdot \mathrm{M} + A_2 \cdot \mathrm{E} \cdot \mathrm{M} + \mathrm{OTT}$, where B is the background, A_1 and A_2 are the parameters to be fitted, M is the mask of the map, i.e. the fitted image is source-free, E is the exposure map, and OTT is the out-of-time events data file. Starting from the result of linear fit as a first guess, A_1 and A_2 are found by minimizing B. For this, the `AMOEBA` (Press et al. 1992) minimization method is used, together with C-statistics for parameter estimation. In this way, the effects of radial dependence of the background are taken into account.

3. Mask out all detected point sources in each image, exposure and background cut-outs. Such point sources can be obtained from other catalogues in X-rays.

4. Add together each of the EPIC cut-outs to produce a stacked image (see Fig. 6.5). Also, add together each of the individual exposure and background cut-outs. In this step, the MOS (or PN) exposure maps are corrected according to the MOS/PN (or PN/MOS) response ratio. The relative sensitivity of the MOS and PN detectors can be calculated with `XSPEC` using standard on-axis PN and MOS response matrices. Furthermore, if the cut-outs have been rescaled, the exposure

maps are also individually weighted by a factor $w(z) = [d_L(z)/d_L(\tilde{z})]^2$, where d_L is the luminosity distance to the source, and $d_L(\tilde{z})$ is the luminosity distance to the chosen redshift of the sample, which is usually defined by the average redshift of the sample. In this way, it is avoided that the final stacked image will be biased by that the nearest objects since they cut-outs are the largest and, therefore, enclose the most photons.

The final product is a count-rate image which obtained by subtracting the stacked background map from the stacked photon image and divided by the stacked exposure map.

It is important to mention that stacking algorithms in other wavelength ranges usually provide as a final result the mean or median of the stacking, due to the Gaussian noise distribution they present. However, in X-ray, where the noise is Poisson distributed, the mean will be biased towards low flux and the median will be always zero because most of the stacked pixel values are zero. This is the reason for providing the stacked images without further adjustments.

The effect of the telescope PSF must be also considered in the stacking analysis. For example, the PSF can affect the photometric measurements on the stacked images. When studying extended sources, one must check that the final stacked image shows a real extended emission, i.e. a broader emission than the FWHM of the PSF. However, as seen in Section 3.3, the PSF of X-ray telescopes varies across the FOV, and the stacking of sources at different off-axis positions complicates the analysis.

A simple way to measure the PSF in the stacking is by constructing empirical PSFs to match the one in the final stacked image. This can be achieved by stacking known X-ray point sources, and analysing them in the same way as the sources of interest. For example, in case the sources have been rescaled to a given angular scale, one can assign the same rescaling to the point sources, and, therefore, obtain an average PSF. One may think that the PSF measured in this way can be unrepresentative of the PSF at the source positions, since the total exposure time at the point-like sources positions, the instrumental efficiency, and the vignetting are different. However, since the number of stacked sources is usually a large number, on average the point-like positions should represent similar instrumental characteristics to the source positions.

As a test for the stacking procedure, one can stack randomly selected positions from the X-ray observation in question, and analyse them in an identical way as the real sources. In principle, no significant excess of emission should be detected at the centre of the image.

6.4 Wavelength bias in distant galaxy cluster samples: A case study using the XMM-LSS and SpARCS cluster samples

Note: This section is adapted from a paper with the same title. In this paper I am only a co-author, therefore I have adapted some parts of the paper for this thesis. I mostly keep the sections that are essential to understanding the flow of the work and the ones mostly influenced by my contributions. For the rest, I will reference for the paper. The reference is Willis, J., Ramos-Ceja, M. E., Pacud, F., and Muzzin, A. 2016, to be submitted to MNRAS.

As described in Section 2.1, galaxy clusters can be identified by various observational techniques: galaxy overdensity searches identify the statistical excess of projected cluster member galaxies in relation to the “background” of non-cluster galaxies along the line-of-sight; X-ray searches identify the integrated emission from thin bremsstrahlung emission arising from the hot ICM; weak lensing searches identify the integrated shear signal introduced into the shapes of background galaxies by the effect of the cluster mass on local space-time; and SZ searches identify the apparent decrement in the brightness of the CMB caused by the inverse Compton scattering of CMB photons by energetic electrons in the ICM.

Each of these principal observational techniques is sensitive to a distinct physical component of each galaxy cluster: overdensity searches are sensitive to the integrated star formation history of the cluster; X-ray searches to the projection of the square of the free electron density in the ICM (with a weak dependence upon the ICM temperature); weak lensing searches to the total projected cluster mass; and SZ searches to the projected ICM free electron density plus a term which depends upon the ICM temperature.

The question which concerns this work is how the physical properties of cluster samples differ depend upon the observational technique used to identify them. Such knowledge is important because it a) permits a consistent comparison between results generated for different cluster samples and b) provides a means to relate the results generated for a particular cluster sample to the "true" cluster population.

At low redshifts ($z < 0.3$) some comparisons between cluster catalogues compiled using different wavebands have been published (e.g. Rozo et al. 2014). There are also comparisons using cluster catalogues compiled over common sky areas on the basis of individual detections (e.g. Bergé et al. 2008; Starikova et al. 2014). Although to date such comparisons have been limited to small sky areas (4 square degrees or less) and consequently small sample sizes, the conclusions are that clusters that are detected in one waveband but are absent in another can generally be explained by measurement uncertainty and scatter in the relationships between observables and mass.

Two studies which attempt to account for unmatched as well as matched clusters between catalogues have been conducted by Donahue et al. (2002) and Sadibekova et al. (2014). Each compares an optical and X-ray selected cluster sample typically sensitive to clusters at $z < 1$. Donahue et al. (2002) noted that the relative fraction of optical clusters lacking an X-ray counterpart could be explained by a steep scaling relationship between X-ray and optical cluster luminosity, i.e. $L_X \propto L_{\mathrm{opt}}^{3-4}$. In addition, both studies concluded that the majority of the X-ray clusters lacking an optical counterpart could be attributed to the maximum and minimum effective redshift limitations of the optical cluster selection criteria.

This work is motivated by the interest in applying a similar comparison to samples of distant galaxy clusters, in part due to the increased potential for cluster-scale astrophysics, e.g. recent star formation (Hayashi et al. 2011; Bayliss et al. 2014), mergers (Nastasi et al. 2011), or AGN activity (Wylezalek et al. 2013), to influence the observed properties of such clusters. However, because such distant clusters are typically identified at low significance in survey quality data (and thus might be prone to considerable scattering effects on mass-observable relations) cluster catalogues compiled at different wavebands via their scaling relations are not compared. Instead, in this work multiple techniques are applied to determine the extent to which each sample exhibits different physical properties and relate those properties to cluster evolutionary state (e.g. star formation and merger histories).

In the following sections, the distant cluster samples are described, as well as the available data common to each sample. The section ends with the presentation of main results and conclusions of this work. In this work a ΛCDM cosmological model described by parameters consistent with WMAP9 (Hinshaw et al. 2013) is assumed.

6.4.1 Distant galaxy cluster samples

X-ray sample: XMM-LSS

The distant X-ray selected galaxy clusters studied in this work are taken from Willis et al. (2013). This paper presented a sample of 21 confirmed and candidate galaxy clusters at $z > 0.8$ selected from an approximate 9 deg^2 area of the *XMM-Newton* Large Scale Structure survey (XMM-LSS, Pierre et al. 2004). The studied area corresponds to the common footprint of the XMM-LSS, Canada France Hawaii Telescope Legacy Survey W1 (CFHTLS-W1, Gwyn 2012) field, and the Spitzer Wide Area Infrared Extragalactic (SWIRE, Lonsdale et al. 2003) survey.

Clusters were selected as C1/C2 extended sources (Pacaud et al. 2006) in the XMM imaging data as either possessing a known spectroscopic redshift $z > 0.8$ or displaying a line of sight overdensity of galaxies unlikely to be located at $z < 0.8$. Ten band photometry ($u, g, r, i, z, Y, J, K,$ 3.6μm and 4.5μm) for these latter systems was compiled and employed to derive photometric redshifts for bright galaxies deemed to be associated with each extended X-ray source. Candidate clusters were retained in the distant sample if they displayed an overdensity of galaxies consistent with a single location in photometric redshift space at $z_{\rm phot} > 0.8$.

Mid-infrared sample: SpARCS

The mid-infrared (MIR) selected distant clusters studied in this work are taken from the Spitzer Adaptation of the Red Sequence Cluster survey (SpARCS, Muzzin 2008). Candidate clusters were identified with significant overdensities in the multiple dimensional space defined by sky positions, $R-3.6\mu$m colour, and 3.6μm brightness. In addition to the candidate cluster sky position, the catalogue also includes the cluster photometric redshift estimate based upon the estimated location of the cluster red sequence in $R - 3.6\mu$m colour, and 3.6μm brightness. Two centroid estimates are provided for each cluster: the first is the sky position of the brightest cluster galaxy (BCG) determined from its location on the cluster red sequence. The second estimate is referred to as the barycentre position and is based upon the mean sky position of all candidate cluster members identified by the red sequence method. Throughout this work the barycentre position is employed for each SpARCS cluster as, in the all but one case, the choice of barycentre versus BCG position makes little quantitative difference to the reported results. Finally, in addition to the candidate cluster sky position, we also retain the cluster photometric redshift estimate based upon the location of the cluster red sequence in R-3.6μm colour.

The final SpARCS catalogue located within the SWIRE field contains 218 candidate galaxy clusters within the redshift interval $0.1 < z < 1.7$. From this sample, a further 98 clusters located within the combined XMM-LSS/SWIRE/CFHTLS-W1 footprint and with $z > 0.8$ were selected for comparison with XMM-LSS.

6.4.2 X-ray, MIR and optical data

X-ray data: XMM-LSS

X-ray data were obtained from the XMM-LSS survey. The survey has imaged a 11.1 deg^2 area centred on R.A.= $2^{\rm h}22^{\rm m}$, Dec.= $-4^\circ30'$ with a mosaic of 98 overlapping *XMM-Newton* pointings. Each pointing displays a typical exposure time of 10 ks and corresponds to a single observation with the EPIC detectors (MOS1, MOS2 and PN) in full frame imaging mode, spanning a field of view of roughly 30′ diameter. The effective flux limit for extended sources identified by the C1/C2 surface brightness selection threshold is $\sim 1 \times 10^{-14}$ ergs s^{-1} cm^{-2}.

MIR data: SpARCS

Approximately 9 deg^2 of the XMM-LSS region was imaged by the Spitzer space telescope as part of the SWIRE extragalactic survey. The Spitzer/SWIRE data used in this work are described in Chiappetti et al. (2013). In particular, the IRAC channel 1 data corresponding to a photometric bandpass located at 3.6μm is used.

Optical data: CFHTLS

In addition to the X-ray and MIR data described above, optical *ugriz* photometry obtained from the CFHTLS-W1 field is also used. Photometry is computed within an aperture based upon the Kron (1980) radius and quoted on the AB magnitude system. Optical photometry is extracted for all sources which appear in the Spitzer MIR catalogue. Optical sources are matched to MIR sources if they lie within a positional tolerance of $< 2''$ with the brightest optical source selected in the case of multiple matches.

6.4.3 Fixed aperture brightness measures

Given the two cluster samples described above and a common X-ray, optical and MIR data set, it is possible to measure X-ray and MIR brightness values for all clusters employing a simple, consistent approach.

The cluster signal in each waveband was measured in a circular aperture of 1′ centred on the X-ray position for XMM-LSS clusters or the galaxy barycentre position for SpARCS clusters. The SpARCS catalogue also contains the brightest cluster galaxy (BCG) position. The results presented in this work generally do not depend strongly upon which cluster centroid measure is used. The one exception is for the case of the stacked X-ray images and this will be commented further in the relevant section.

A fixed aperture approach was selected to measure the cluster signal in as robust a manner as possible and using the fewest assumptions regarding the properties of individual clusters. For example, this approach requires only the sky position of each cluster and thus lends itself well to comparing cluster samples drawn from a variety of selection approaches.

Application of a circular aperture is the simplest response to the lack of data on the shapes of distant clusters. Furthermore, application of a fixed angular radius offers a number of advantages: the background applied to correct the line-of-sight signal from each cluster is uniform across the sample. As the line-of-sight signal from each cluster is often background dominated, this generates consistent and comparable uncertainties across the sample of measurements.

In addition, although one could choose to apply an aperture of fixed physical radius in the rest frame of each cluster (i.e. using the redshift, angular diameter distance and assumed cosmological model), one cannot be certain that the redshift of each candidate cluster represents the true redshift of a unique, gravitationally bound structure. Candidate clusters which turn out to be spurious will potentially generate confusing results. This same consideration motivates the comparison using cluster fluxes rather than luminosities.

Finally, it should be noted that, over the redshift interval $0.8 < z < 2$ and within the assumed cosmological model, the angular diameter distance (required to convert from angular to physical radius) varies by approximately ±5% about the fiducial redshift $z = 1$. Therefore the application of an aperture of fixed angular radius differs only slightly from an aperture of fixed physical radius.

X-ray aperture photometry

As mentioned earlier, the X-ray brightness measurement from a galaxy cluster is sensitive to the emission from gravitationally confined gas at the virial temperature of the cluster dark matter halo[2]. The X-ray brightness of a cluster is primarily a measure of the (square of) the baryonic gas mass with a slowly varying dependence upon the cluster gas temperature.

The Bayesian approach for calculating X-ray aperture photometry described in Section 6.2.2, is used to extract information on the SpARCS sample. The extracted information was a count-rate posterior probability in an aperture of $1'$ radius in the $[0.5-2]$ keV energy band. Each count-rate distribution was converted into a flux posterior probability density using an `APEC` emission model with $z = 1$, $T = 4$ keV, $N_{\rm H} = 2.6 \times 10^{20}$ cm^2, $Ab = 0.3$, and standard on-axis EPIC response matrices. The final flux is given in terms of the mode of the distribution together with the 68% credibility interval.

Spitzer MIR aperture photometry

The Spitzer MIR brightness measurement for a galaxy cluster is sensitive to the summed, observed-frame stellar 3.6μm luminosity of individual galaxies identified as cluster members. All MIR sources within the measurement aperture displaying colours $r - 3.6\mu$m> 3.38 are selected as candidate $z > 0.8$ galaxies. The 3.6μm flux values of all galaxies satisfying this threshold are summed to generate a cluster 3.6μm flux measurement. See Willis et al. (in preparation) for further details on the determination of MIR background aperture flux measurements.

6.4.4 Results

X-ray versus MIR flux measures

Figure 6.6 compares the cluster 3.6μm aperture flux to the X-ray aperture flux measured for all XMM-LSS and SpARCS $z > 0.8$ clusters. A total of 18 XMM-LSS and 95 SpARCS clusters were ultimately measured. The remaining clusters (2 XMM-LSS and 3 SpARCS) were located sufficiently close to the survey data footprint that their aperture measurements were compromised.

Two initial impressions are apparent from this comparison. Firstly, there is a broad correlation defined by X-ray faint, MIR faint ranging to X-ray bright, MIR bright clusters. This work does not attempt to quantify this trend in the current study as the adopted measurement approach is deliberately simple and

---

[2] The virial temperature of a dark matter halo is a measure of the binding energy of the halo material, i.e. the halo can only trap baryonic gas with temperatures $T_{\rm gas} \lesssim T_{\rm vir}$. The virial temperature of a halo depends on its mass and assembly redshift.

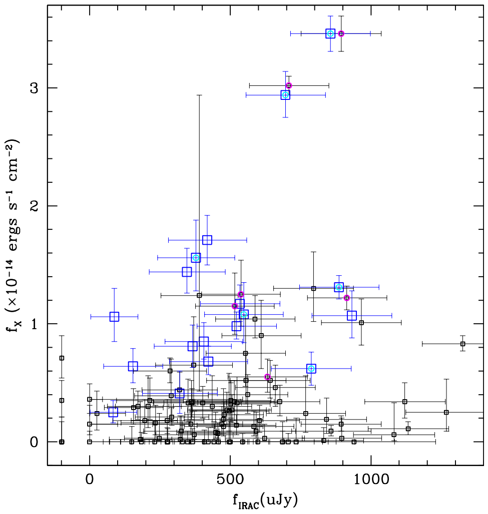

Figure 6.6: A comparison of X-ray and MIR 1′ aperture brightness values for XMM-LSS (blue squares) and SpARCS (black squares) clusters. XMM-LSS and SpARCS clusters which are located within 3′ on the sky (and thus potentially represent the same source) are indicated with an additional cyan or magenta circle, respectively. Error bars indicate the 68% interval of the posterior background subtracted flux distribution for each source.

is designed to provide a robust comparison between clusters of widely different properties. In contrast to this broadly defined correlation between X-ray gas emission and stellar emission within both cluster samples, there is a population of MIR selected clusters which can be described as X-ray faint (effectively consistent with zero emission) and MIR bright.

Based upon the distribution of the SpARCS clusters on the X-ray/MIR plane displayed in Fig. 6.6, three sub-samples can be defined - the aim being to determine if the visually apparent sub-samples display recognisable physical differences with the XMM-LSS sample. An X-ray bright MIR selected clusters sample is defined by those galaxy clusters displaying $f_X \geq 0.6 \times 10^{-14}$ ergs s^{-1} cm^{-2}. A further split of the X-ray faint ($f_X < 0.6 \times 10^{-14}$ ergs s^{-1} cm^{-2}) MIR selected clusters is done. These X-ray faint clusters are divided into those that are MIR bright ($f_{3.6\mu m} \geq 650\mu$Jy) and those that are MIR faint ($f_{3.6\mu m} < 650\mu$Jy). The final numbers of clusters present in each sample are as follows: XMM-LSS, 18, SpARCS X-ray-bright, 15, SpARCS X-ray-faint+MIR-bright, 17, SpARCS X-ray-faint+MIR-faint, 63. Despite these differences, each sub-sample presents statistically identical distributions of observables such as redshift and off-axis angle in XMM-Newton pointings.

MIR properties

The angular surface brightness distribution was evaluated, and a visual assessment of the clusters in each subsample was performed (see Willis et al., in preparation, for further details). The main findings are summarized here:

- The X-ray selected galaxy clusters display a more compact distribution of stellar light. This indicates that X-ray selection is biased towards compact high surface brightness systems. This is confirmed by the visual check, where these objects appear as centrally concentrated systems of galaxies.

- X-ray-faint+MIR-faint objects and X-ray-bright+MIR-bright systems have similar surface brightness distributions. The visual inspection reveals that the X-ray-bright+MIR-bright galaxy clusters also appear as centrally concentrated systems of galaxies, while the X-ray-faint+MIR-faint clusters objects show a range of appearances: from concentrated systems to sparce objects.

- X-ray-faint+MIR-bright galaxy clusters have a decrement in the central surface brightness, this results indicates that such systems are physically different from the other subsamples. This is confirmed by the visual assessment, which reveals that X-ray-faint+MIR-bright systems have a lack of concentrated systems of galaxies.

Stacked X-ray images

The creation of stacked X-ray images for each cluster sub-sample permits the average X-ray emission properties of each to be discussed. Furthermore, the low noise properties of stacked images allow a sensitive test of the average emission from the SpARCS X-ray faint sub-samples to be investigated.

Stacked images of the cluster sub-samples were created using the data from the XMM-LSS survey. The stacking method is described in Section 6.3. The cut-outs have a radius of $2'$ and were extracted in the $[0.5-2]$ keV energy band. Figure 6.7 shows the final stacked images for each sub-sample. As a simple test of our stacking procedure, a set of randomly selected positions from the XMM-LSS region was also analysed in an identical way.

Highly significant X-ray emission is seen in both the XMM-LSS and X-ray-bright+MIR-bright sub-samples when compared to the image created by combining 100 random locations. Weaker emission is also detected in the stacked image corresponding to the X-ray-faint+MIR-faint sub-sample. There is some evidence from the stacked images that X-ray emission in the SpARCS sub-samples is associated more closely with the cluster BCG position compared to the barycentre position. This is indicated visually in the stacks for the X-ray bright and X-ray-faint+MIR-faint sub-samples where more compact, centrally-peaked X-ray emission is generated when stacking on the BCG position. In contrast to this, the stacked image for the X-ray-faint+MIR-bright SpARCS sub-sample displays no centrally concentrated X-ray emission when stacking on either the BCG or barycentre position. Some peripheral X-ray emission is noted in the stacked image yet is only marginally significant when compared to the stacked random location image.

The visual trends noted in the stacked images are reinforced by inspection of the angular X-ray surface brightness distribution in each cluster sub-sample shown in Fig. 6.8. The angular surface brightness was computed using the relation

$$f_{\mathrm{X,cum}} = \frac{\sum_i^N f_{\mathrm{X},i}}{r_i^2}, \tag{6.15}$$

where $f_{\mathrm{X},i}$ is the X-ray flux summed as a function of increasing radius r_i. The X-ray centroid is used as the reference position for XMM-LSS clusters and the barycentre of the galaxy light is used for SpARCS. The results confirm that the X-ray flux in the SpARCS sub-samples is centred on the BCG instead of the barycentre position and that the X-ray faint, MIR bright sub-sample is devoid of central X-ray emission.

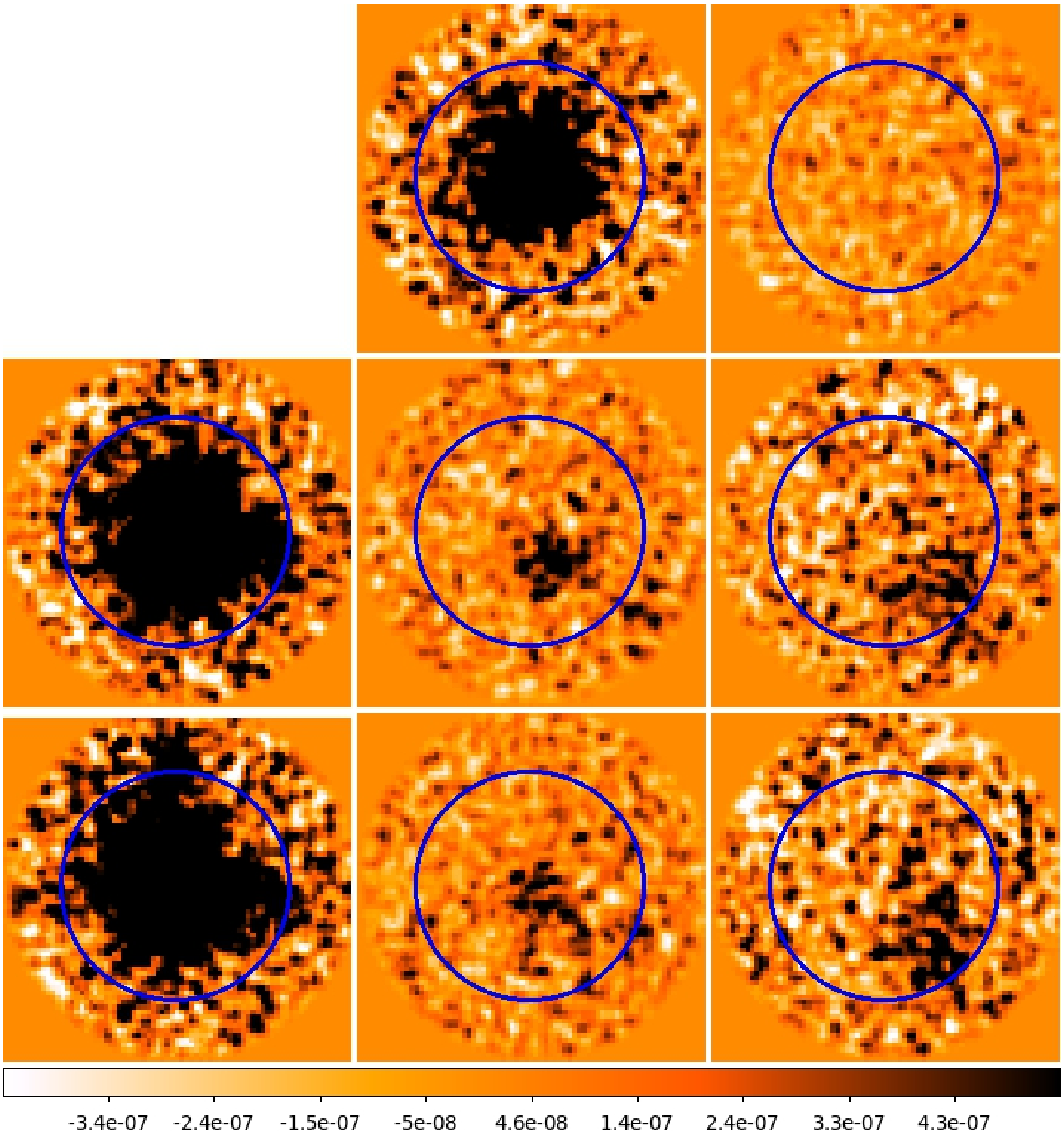

Figure 6.7: Stacked X-ray images for each cluster sub-sample. Each image is smoothed with a Gaussian kernel of sigma equal to two pixels. The scale bar indicates photon count rate per second. *Top row*: *middle*: XMM-LSS clusters; *right*: Stack of 100 random positions. *Middle row*: SpARCS clusters stacked on the catalogue barycentre position: *left*: X-ray-bright; *middle*: X-ray-faint+MIR-faint; *right*: X-ray-faint+MIR-bright. *Bottom panel*: SpARCS clusters stacked on the catalogue BCG position. The order follows the middle row. The blue circle in each panel represents the $1'$ radius aperture used to measure individual cluster X-ray fluxes.

6.4.5 Conclusions

The comparison of the properties of the XMM-LSS and SpARCS distant cluster samples has revealed a number of physical differences between the two cluster samples.

Firstly, it appears that X-ray selected galaxy clusters represent a dynamically relaxed subset of the

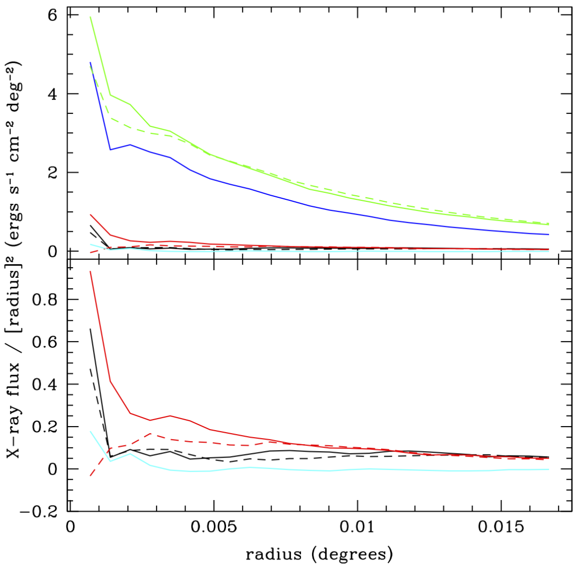

Figure 6.8: The cumulative angular X-ray surface brightness distribution of each cluster sub-sample: XMM-LSS (blue), X-ray-bright SpARCS (green), X-ray-faint+MIR-faint SpARCS (red), X-ray-faint+MIR-bright (black). For the SpARCS sub-samples solid coloured lines indicate the measurements applying the BCG position of each cluster whereas dashed lines indicate barycentre positions. The cyan line indicates the average cumulative surface brightness distribution computed from 100 randomly placed apertures. The upper panel shows all cluster sub-samples, the lower panel presents a zoomed view of the low surface brightness sub-samples.

massive cluster population. This is primarily evident from the comparison of the MIR surface brightness distribution of the XMM-LSS and X-ray-bright SpARCS clusters. This result can be understood in terms of X-ray selection in the following manner. X-ray selection of extended sources is biased to those of higher surface brightness which, in turn, is proportional to the square of the projected electron density in galaxy clusters. At fixed cluster mass, a relaxed cluster will display a more concentrated mass distribution than a cluster which is more dynamically disturbed. This statement applies equally to the gas of the intra cluster medium (ICM) which loses energy via collisional cooling as to the bright (i.e. massive) galaxy distribution which loses energy via dynamical friction with the fainter (less massive) galaxies within each cluster[3].

A second conclusion regarding X-ray selection is that it identifies clusters equivalent in mass yet possessing a wider range of optical-MIR properties than identified by optical-MIR searches alone. Evidence for this statement is drawn from the comparison of the red sequence properties of the XMM-LSS and X-ray bright SpARCS samples (Figure 7 of Willis et al. in preparation). At comparable X-ray brightness (and therefore approximately comparable mass) the X-ray selected clusters display a lower average red sequence normalisation compared to X-ray bright optical-MIR red sequence selected clusters. X-ray selection therefore identifies clusters displaying a broader range of star formation histories than methods which rely upon the presence of the red sequence – a conclusion previously noted by Donahue et al. (2002).

A third conclusion is that colour-overdensity searches, such as SpARCS, identify a broader range of

---

[3] Note that these considerations ignore two secondary physical considerations: at fixed mass a relaxed cluster will display a marginally lower X-ray temperature than a disturbed cluster - with a consequently slightly lower surface brightness as a result (however, the changes in the square of the gas density dominate). Secondly, if clusters are indeed described by the distribution of collisionless cold dark matter, then one should also compare the properties at fixed mass and collapse epoch.

cluster dynamical states (at fixed mass) than X-ray selected samples. This statement is not simply the converse of the first conclusion as it also concerns the nature of the X-ray-faint+MIR-bright subsample of SpARCS clusters. The lack of detectable X-ray emission in the stacked image of the X-ray-faint+MIR-bright clusters provides a strong indication that the majority of these systems are not collapsed structures in virial equilibrium.

Two possibilities present themselves: firstly these systems could be projected large-scale structures along the line-of-sight which mimic the signal associated with bona-fide clusters in the Spitzer-adapted red sequence cluster finding method. The evidence for this conclusion is the similarity between the projected MIR surface brightness in such systems and the distribution measured for the stacked random apertures. However, the average red sequence for the X-ray-faint+MIR-bright SpARCS clusters is marginally different from the random line-of-sight distribution. Whether this is a bias associated with the application of the red sequence criterion to line-of-sight large-scale structure variations is not clear.

A second possibility is that X-ray-faint+MIR-bright clusters represent gravitationally bound, collapsing structures which have not yet reached virial equilibrium. Although this explanation is consistent with the majority of the measurements of these systems, it does rely on fortuitous timing in the sense that the majority of these systems must be being observed early in the collapse phase, i.e. before the formation of a virialised core which might be detected via weak X-ray emission or central galaxy concentration.

6.5 Summary and outlook

The Poisson nature of the X-ray data demands a careful treatment and the development of sophisticated tools to extract useful information from it. In this regard, Bayesian statistics plays an important role in the low-counts regime, where the Gaussian statistics is not longer valid. This chapter presents two techniques to analyse faint X-ray sources: a Bayesian aperture photometry method and a source stacking procedure.

The Bayesian aperture photometry method basically computes values and confidence regions of the source intensity (count-rates, flux, luminosity) by using counts and exposure data obtained in source and background apertures. The approach consists in calculating the background marginalized posterior probability distribution function of the source counts assuming Poisson likelihoods for the source and background components. The mode of this distribution is determined, and the lower and upper bounds of the confidence region are calculated by summing values of the distribution alternately above and below the mode until the desired confidence level is reached. This approach works fine in the low-counts regime, where the classical aperture photometry method fails and reproduces the results of the classical approach in the high-counts regime, where the Gaussian statistics works appropriately.

In principle, this method can be used by any imaged X-ray data from any instrument, but in this work it is shown its application to *XMM-Newton* data. Since this X-ray telescope has two different types of CCD cameras, the source posterior probability distributions of each CCD are corrected by the different camera sensitivities, and the final source aperture photometry is obtained from the multiplication of the three corrected distributions.

The stacking technique creates stacked X-ray images of a given source population. In this way, the average X-ray emission properties of a given sample can be investigated, especially if the sources of interest are X-ray faint. The stacking technique is particularly complex to implement on *XMM-Newton* data since one has to combine data from two different types of CCD cameras and the *XMM-Newton* PSF and background varies considerably across the field-of-view.

In this regard, a novel stacking technique has been developed. Basically, the stacking procedure adds together cut-outs of source images and their corresponding exposure maps. It also creates corresponding background maps, which are carefully modelled. The final count-rate image is obtained by subtracting the stacked background map from the stacked photon image and dividing by the stacked exposure map. Moreover, this technique has been optimized to stack objects in physical radius, i.e. in the rest frame of each cluster.

The two techniques have been used in the study of wavelength bias in high-redshift galaxy cluster samples. The goals of this research are to consistently study different wavelength-selected cluster samples and to provide evidence of the astrophysics that influences the cluster observed waveband-dependent properties. For this research, $z > 0.8$ mid-infrared (MIR) and X-ray selected galaxy cluster samples have been used. Then, the Bayesian aperture photometry method and the source stacking procedure are used in the study of the MIR-selected clusters in X-rays.

The X-ray (18 systems) and MIR (95 systems) selected galaxy clusters were taken from a common area (~ 9 deg^2) between the *XMM-Newton* Large Scale Structure Survey (XMM-LSS, ~ 11 deg^2) and the Spitzer Adaptation of the Red Sequence Cluster Survey (SpARCS), respectively. Only 33% of the X-ray selected clusters can be related to one of the MIR selected clusters. The comparison of the properties of both distant cluster samples reveals a number of physical differences:

- X-ray surveys identify a dynamically relaxed subset of the massive cluster population at high redshift, where the intra-cluster gas has settled and started to emit in X-ray. This is confirmed by the compact MIR surface brightness of such clusters, meaning that these systems have a concentrated mass distribution.
- In contrast to the above, MIR surveys identify clusters exhibiting a broader range of dynamical states and, therefore, offer a useful complement to X-ray studies. However, our comparisons also identify a population of low X-ray emission MIR clusters (e.g. some bright MIR systems have a lack of X-ray emission) which may well represent non-virialised large-scale structure.

This successful pilot study indicates that multi-wavelength studies of galaxy cluster populations are an effective method of revealing physical bias in such samples.

6.5.1 On-going and future work

There are a quite number of additional applications of the Bayesian aperture photometry method and the source stacking procedure. In the following two of the most relevant are mentioned.

Wavelength bias in galaxy cluster samples. The next step in the research of wavelength bias in large galaxy cluster samples is to extend the study to larger samples. The XXL survey is the largest and deepest *XMM-Newton* project approved so far, covering two extragalactic areas of 25 deg^2 (Pierre et al. 2015). The XMM-LSS survey was a pilot survey for XXL. The XXL has detected ~ 315 galaxy clusters at $z < 1$ with a flux limit of $\sim 10^{-14}$ erg s^{-1} cm^{-2}. For all these clusters there exists redshift information (photometric or spectroscopic). The XXL survey also has a well-defined selection function in terms of flux and source extension. However, the influence of cluster astrophysics on X-ray observability is not well understood.

XXL has ∼ 30 associated follow-up programmes, which allow joint and diverse studies on cluster and AGN physics and cosmology. Within these programmes there are two optical spectroscopic surveys covering the XXL northern field that their own galaxy cluster searching programme. Then, both surveys can be used in the wavelength bias comparison of galaxy cluster samples. Such surveys are:

- VIMOS Public Extragalactic Redshift Survey (VIPERS; Guzzo & The Vipers Team 2013) is a spectroscopic on-going Large Programme to map in detail the large-scale distribution of $\sim 10^5$ galaxies at $0.5 < z < 1.2$, and overlaps by 16 deg^2 with XXL. Its galaxy colour selection was based on 5-bands of the CFHTLS. So far, VIPERS has detected ∼ 1400 groups, out of which 560 possess 5 or more members, in the redshift range of $0.5 < z < 1.2$ within the overlap region with XXL (A. Iovino, priv. comm.)
- Galaxy And Mass Assembly (GAMA; Driver et al. 2011) is a completed spectroscopic survey of $\sim 2 \times 10^5$ galaxies at $z < 0.5$, and overlaps with XXL by ∼ 20 deg^2. In this region, GAMA has ∼ 95% redshift completeness (Liske et al. 2015). The target galaxies were also selected from the CFHTLS. So far, GAMA has detected ∼ 1380 groups in redshift range of $0 < z < 0.5$ in ∼ 20 deg^2 of the sky with an approximate mass limit of $\gtrsim 10^{13}$ M$_\odot$.

These larger galaxy samples will be analysed in the same way as in Section 6.4.3 to perform a comprehensive comparison of cluster catalogues. The goal is to understand how each waveband-dependent detection technique generates cluster samples of different physical properties.

Gas mass fraction in low-mass haloes. Recent studies (Planck Collaboration et al. 2013b; Anderson et al. 2015) have used a sample of locally brightest galaxies (LBGs) to compare the properties of dark matter haloes in optical, X-ray, SZ and lensing. The LBGs are selected from the Sloan Digitized Sky Survey[4] and are assumed to be central galaxies within their respective dark matter haloes. The LBGs were stacked in the SZ using data from the *Planck* satellite, and in X-rays using data from the ROSAT All-Sky Survey (RASS). Their results showed that unified SZ and X-ray scaling relations apply for galaxies, galaxy groups and galaxy clusters, i.e. from halo masses of $\sim 10^{12.5}$ M$_\odot$ (similar to the Milky Way) to $\sim 10^{15}$ M$_\odot$.

Lead by Dr. Jean Coupon at the Astronomical Observatory of the University of Geneva, a similar approach has been implemented in XXL north field. The main goal is to probe the gas- and stellar-mass content of dark-matter halos down to low masses. Although the XXL volume is much smaller, the XXL data is much deeper and has a better PSF than RASS.

Using optical/IR data from CFHTLS and WIRCAM, a preliminary sample of $\sim 3,000$ LBGs galaxies with $M \gtrsim 10^{11}$ M$_\odot$ at $0.2 < z < 1.0$ has been set. The LBGs sample has been divided into four stellar mass bins and in two redshift bins, and for each mass bin, a luminosity stacked map has been produced using the stacking method described in Section 6.3. Preliminary results show that a strong and extended X-ray signal is detected in all four mass bins in the low redshift bin ($0.2 < z < 0.5$). Null stacked tests performed on random positions confirm the high signal-to-noise ratio of the stacked maps.

---

[4] http://www.sdss.org/

CHAPTER 7

Constraining the intra-cluster pressure profile from the thermal SZ power spectrum

The angular power spectrum of the thermal Sunyaev-Zel'dovich (tSZ) effect is highly sensitive to cosmological parameters such as σ_8 and Ω_m, but its use as a precision cosmological probe is hindered by the astrophysical uncertainties in modeling the gas pressure profile in galaxy groups and clusters. In this paper we assume that the relevant cosmological parameters are accurately known and explore the ability of current and future tSZ power spectrum measurements to constrain the intracluster gas pressure or the evolution of the gas mass fraction, $f_{\rm gas}$. We use the CMB bandpower measurements from the South Pole Telescope and a Bayesian Markov Chain Monte Carlo (MCMC) method to quantify deviations from the standard, universal gas pressure model. We explore analytical model extensions that bring the predictions for the tSZ power into agreement with experimental data. We find that a steeper pressure profile in the cluster outskirts or an evolving $f_{\rm gas}$ have mild-to-severe conflicts with experimental data or simulations. Varying more than one parameter in the pressure model leads to strong degeneracies that cannot be broken with current observational constraints. We use simulated bandpowers from future tSZ survey experiments, in particular a possible 2000 deg^2 CCAT survey, to show that future observations can provide almost an order of magnitude better precision on the same model parameters. This will allow us to break the current parameter degeneracies and place simultaneous constraints on the gas pressure profile and its redshift evolution, for example.

Note: This chapter is a reproduction of a paper of the same title, published in the Astronomy & Astrophysics Journal. The reference is Ramos-Ceja, M. E., Basu, K., Pacaud, F., and Bertoldi, F. 2015, A&A, 583, A111. The manuscript is reproduced here under the non-exclusive right of re-publication granted by ESO to the author(s) of the paper.

7.1 Introduction

The scattering imprint of the cosmic microwave background (CMB) radiation from the hot, thermalized electrons in the intracluster medium (ICM) is known as the Sunyaev-Zel'dovich (SZ) effect (Sunyaev & Zel'dovich 1972, 1980), which is playing an increasingly important role in the cosmological and astrophysical research using galaxy clusters. The SZ effect is generally divided into two distinct processes: the kinetic SZ (kSZ) effect describes the anisotropic scattering due to the cluster bulk motion, while the thermal SZ (tSZ) effect describes the inverse Compton scattering of the CMB photons by the thermal distribution of hot electrons in the ICM, which is proportional to the line-of-sight integral of the electron pressure. For the tSZ effect, the energy gain by the CMB photons gives rise to a specific spectral dependence of the tSZ signal, such that below roughly 217 GHz, clusters appear as a decrement and above as an increment in the CMB surface brightness. Because the tSZ surface brightness is independent of the redshift of the scattering source, it provides a powerful means to study the structure and dynamics of the hot intracluster gas throughout cosmic history.

Apart from observing individual clusters, the tSZ effect can also be detected in a statistical sense through the excess power over the primordial CMB anisotropies, coming from all the resolved and unresolved galaxy groups and clusters in a CMB map. Unlike the optical and X-ray observables, the redshift independence of the tSZ signal makes this "confusion noise" a significant source of temperature anisotropies at millimeter/submillimeter wavelengths in the arcmin scale regime, where the primordial CMB anisotropies are damped exponentially. Similar to the cluster number counts, the tSZ anisotropy signal is sensitive to the same set of cosmological parameters because its contribution comes primarily from the hot ($\gtrsim 1$ keV), ionized ICM bound to groups and clusters (e.g., Hernández-Monteagudo et al. 2006). The amplitude of the tSZ power spectrum depends roughly on the eighth power of σ_8, the rms amplitude of the matter density fluctuations and on the third power of Ω_m (Komatsu & Seljak 2002; Trac et al. 2011). However, the tSZ power receives significant contribution from the low mass, high redshifts objects. This seriously hinders its use as a precision cosmological probe, since the thermodynamic properties of these systems are not well constrained from direct observations. Thus, the astrophysical uncertainties in modeling the tSZ power spectrum are too large to place significant constraints on cosmological parameters. Consequently, attention has moved to measuring the higher order statistics of the correlation function, such as the tSZ bispectrum, which arises mostly from massive systems at intermediate redshifts and is therefore less prone to astrophysical systematics (e.g., Rubiño-Martín & Sunyaev 2003; Bhattacharya et al. 2012; Wilson et al. 2012).

As the measurement precision of the cosmological parameters improves from other methods, the use of the tSZ power spectrum in cosmology can be reversed. The tSZ power can then be used as a probe for measuring the distribution and evolution of the intracluster gas, down to low cluster masses and up to high redshifts, where direct observations are difficult. Similar arguments have been presented by several authors (e.g., Shaw et al. 2010; Battaglia et al. 2012a), although a quantitative comparison between the results of analytical cluster pressure models and the observations of the tSZ power spectrum has been lacking. It is also of great interest to know how the future ground-based SZ surveys may constrain the intracluster gas models because their resolutions are better suited to constraining the shape of the tSZ power spectrum.

The amplitude of the tSZ power spectrum was predicted analytically by Komatsu & Seljak (2002), with an expected value of $8-10\ \mu\mathrm{K}^2$ around $\ell = 3000$. Later semi-analytic modeling predicted similar values (Sehgal et al. 2010), but experimental results have confirmed these early predictions to be too high. The first conclusive measurement of the combined tSZ+kSZ power spectrum came from the South

Pole Telescope (SPT; Lueker et al. 2010). Successive data releases from the SPT and ACT (Atacama Cosmology Telescope) have provided increasingly sensitive and consistent measurements of the tSZ power on arcminute scales ($\ell \sim$ few $\times$ 1000) where the contributions from galaxy groups and clusters are expected to peak (Shirokoff et al. 2011; Dunkley et al. 2011; Reichardt et al. 2012; Sievers et al. 2013; George et al. 2014). Recent results from the *Planck* spacecraft are also consistent with the SPT value within 2σ (Planck Collaboration et al. 2014c), although the *Planck* resolution cannot resolve the position of the peak of the tSZ power, and is more sensitive on roughly degree angular scales. At these low multipoles, the two-halo correlation term might be important, or the contribution from the warm-hot intergalactic medium (WHIM) might dominate (e.g., Suárez-Velásquez et al. 2013).

In this work we adopt the SPT measurement of CMB bandpowers from Reichardt et al. (2012), which constrained the peak amplitude of the tSZ power spectrum at 150 GHz at $3.65 \pm 0.69\,\mu\mathrm{K}^2$. This value is less than half of what was predicted from early semi-analytic cluster models. The source of this discrepancy has been investigated in several works, following analytic and semi-analytic modeling (Shaw et al. 2010; Trac et al. 2011), as well as full hydrodynamical simulations (Battaglia et al. 2012a; McCarthy et al. 2014). These authors identify several physical processes that can produce a lower amplitude of the tSZ power, namely the turbulent bulk motions of the intracluster gas, feedback from supernovae and AGN – plus the redshift evolution of these quantities – that cause cluster properties to deviate from a simple self-similar scaling. The uncertainties in the implementation of various astrophysical processes in these semi-analytical or numerical models remain sufficiently high ($\sim 30\%$, e.g., Shaw et al. 2010), such that cosmological constraints using template models for the tSZ power spectrum are generally not the most competitive.

We aim to make a detailed comparison between analytical models for the intracluster pressure and the latest tSZ power spectrum data, such that errors on the model parameters can be derived directly from observations. This contrasts with earlier analytic or semi-analytic works that were compared against simulation predictions. We set up a Markov Chain Monte Carlo (MCMC) based method to explore the range of possible values in the selected pressure model from a set of CMB bandpower measurements, obtaining the full covariance between these parameters. This also allows us to use simulated bandpowers from the future CMB/SZ experiments (e.g., CCAT and SPT-3G) to predict their ability to break the parameter degeneracies and constrain cluster physics.

This paper is organized as follows. In Section 7.2 we describe the "halo model" for computing the tSZ power spectrum, followed-by its measurement technique, and outline our procedure to constrain cluster model parameters from the SPT data. Section 7.3 summarizes the current knowledge on the cluster pressure structure which will provide the baseline of our work. Section 7.4 presents our attempts to reconcile the tSZ power spectrum model predictions and available measurements, using altered pressure models. In Section 7.5 we extend our analysis to future SZ cluster survey experiments, and discuss the impact of cosmological parameter uncertainties on the results. We summarize our work in Section 7.6 and present conclusions. Throughout this work we assume a ΛCDM cosmology with $h = 0.71$, $\Omega_\mathrm{m} = 0.264$, $\Omega_\mathrm{b} = 0.044$, $\Omega_\Lambda = 0.736$, $n_s = 0.96$, and $\sigma_8 = 0.81$ (Komatsu et al. 2011).

7.2 Method

In this Section we describe the halo formalism for computing the tSZ power spectrum, and the observation and modeling of the microwave sky that we use in a Bayesian MCMC formalism to constrain cluster pressure model parameters.

7.2.1 Analytical estimate of the tSZ power spectrum

From the halo model to the power spectrum

The tSZ power spectrum consists of one-halo and two-halo contributions. The one-halo term results from the Comptonization profile of individual halos in a Poisson distributed population, while the two-halo term accounts for the two-point correlation function between individual halos. For intermediate to small angular scales ($\ell \gtrsim 1000$), which correspond to the angular size of individual galaxy clusters ($\theta \lesssim 10'$), Komatsu & Kitayama (1999) showed that the one-halo Poisson term is by far the dominant contribution. Following their prescription, the analytical expression of the tSZ power reduces to the formula

$$C_\ell = f_\nu^2(x) \int_0^{z_{\max}} dz \frac{dV}{dz} \int_{M_{\min}}^{M_{\max}} dM \frac{dn(M,z)}{dM} |\tilde{y}_\ell(M,z)|^2. \tag{7.1}$$

Here dV/dz is the co-moving volume of the Universe per unit redshift z, $\tilde{y}_\ell$ is the spherical harmonics decomposition of the sky-projected Compton $y-$parameter, $dn(M,z)/dM$ is the dark matter halo mass function, $f_\nu(x)$ is the spectral function of the tSZ effect given by

$$f_\nu(x) = \left(x\frac{e^x+1}{e^x-1} - 4 \right)[1 + \delta_{\mathrm{SZ}}(x)], \tag{7.2}$$

where $x \equiv 2\pi\hbar\nu/k_{\mathrm{B}}T_{\mathrm{CMB}}$, and $\delta_{\mathrm{SZ}}(x)$ is the relativistic correction to the frequency dependence. The reduced Planck constant is $\hbar$, k_{B} is the Boltzmann constant, and T_{CMB} is the CMB temperature. We do not include relativistic corrections to $f_\nu(x)$ as they have a negligible effect at the temperatures of groups and low-mass clusters which dominate the tSZ power spectrum.

The integral in Eq. 7.1 is insensitive to $z \gtrsim 4$ due to the absence of sufficiently massive halos. In our calculations, we thus set the upper redshift boundary to $z_{\max} = 6$. Similarly, to cover a maximum critical mass range for galaxy groups and clusters, we set $M_{\min} = 10^{12}\ h^{-1}\ \mathrm{M}_\odot$ and $M_{\max} = 10^{16}\ h^{-1}\ \mathrm{M}_\odot$. We use the mass function obtained by Tinker et al. (2008).

From Komatsu & Seljak (2002), the spherical harmonics contribution of a given Compton $y-$parameter profile on angular scale ℓ is given by

$$\tilde{y}_\ell(M,z) = \frac{4\pi r_{500}}{l_c^2} \int dr' r'^2 y_{3\mathrm{D}}(M,z,r') \frac{\sin(\ell r'/l_c)}{\ell r'/l_c}, \tag{7.3}$$

where $r' \equiv r/r_{500}$ is a scaled, non-dimensional radius, $l_c \equiv D_{\mathrm{A}}/r_{500}$ is the corresponding angular wavenumber, and $y_{3\mathrm{D}}$ is the 3D radial profile of the Compton $y-$parameter. This last parameter is given by a thermal gas pressure profile, P_{gas}, through

$$\begin{aligned} y_{3\mathrm{D}}(M,z,r') &\equiv \frac{\sigma_T}{m_e c^2} P_e(M,z,r') = \frac{\sigma_{\mathrm{T}}}{m_e c^2}\left(\frac{2+2X}{3+5X}\right) P_{\mathrm{gas}}(M,z,r') \\ &= 1.04 \times 10^4\ \mathrm{Mpc}^{-1}\left[\frac{P_{\mathrm{gas}}(M,z,r')}{50\ \mathrm{eV\ cm}^{-3}}\right], \end{aligned} \tag{7.4}$$

where P_e is an electron-pressure profile, $X = 0.76$ is the Hydrogen mass fraction, σ_{T} is the Thomson cross-section, m_e is the electron mass, and c is the speed of light.

Effect of the intrinsic pressure scatter

Despite the tight correlation between the tSZ signal and cluster mass, several works have shown that the dispersion of individual cluster pressure profiles $P_e(r')$ at a given mass is far from negligible (~30% according to Planck Collaboration et al. 2013a and Sayers et al. 2013b). So far the contribution of this scatter has not been considered in analytical treatments of the tSZ power spectrum. Modeling this effect would indeed require a detailed knowledge of the diversity of cluster Comptonization morphologies. Observationally this is not yet well-constrained as tSZ experiments still aim at improving our estimate of the average cluster pressure profiles.

In our modeling of the tSZ power, we try to capture the bulk contribution of the intrinsic scatter. To do so, we make the assumption that the dispersion in the pressure structure can be encapsulated in a simple scatter on the normalization of the pressure profile, leaving the shape unchanged. In this case, marginalizing over the distribution of profile normalization results in a straightforward scaling of the tSZ power spectrum amplitude as follows:

$$C_\ell^s = (1 + \sigma_s^2) C_\ell, \tag{7.5}$$

where σ_s is the intrinsic scatter on the $P_e(r')$ normalization. With this approximation, the 30% intrinsic scatter on the pressure amplitude increases the tSZ power amplitude by roughly 10%. We include this additional contribution in all subsequent results. More details on the adopted pressure profile and the measurement of intrinsic scatter are given in Section 7.3.

7.2.2 Microwave sky model

Our analysis relies on the microwave extragalactic power spectra published by Reichardt et al. (2012, hereafter R12) for three different frequency bands. Those observations were extracted from 800 deg^2 maps obtained within the SPT survey and cover angular scales of $2000 < \ell < 10000$.

Such observations are a combination of signals from primary CMB anisotropy, foregrounds, and secondary SZ anisotropies. The power spectrum from each of these components has different frequency dependence, so detailed multifrequency observations can in principle distinguish their relative contributions in the maps (see e.g., Planck Collaboration et al. 2014a). Unfortunately, three frequencies are not sufficient to perform this kind of analysis. Instead, we have to rely on a model for the microwave sky power, calibrated using external information wherever possible. The problem then reduces to a decomposition of the observed signal into a set of templates, for which mostly the normalization has to be quantified.

In this purpose, we use the same model as in R12 where the total microwave sky power, D_ℓ^{mod}, breaks down into the following components:

$$D_\ell^{\mathrm{mod}} = D_\ell^{\mathrm{CMB}} + D_\ell^{\mathrm{tSZ}} + D_\ell^{\mathrm{kSZ}} + D_\ell^{\mathrm{P}} + D_\ell^{\mathrm{C}} + D_\ell^{\mathrm{R}} + D_\ell^{\mathrm{cir}}. \tag{7.6}$$

Here, D_ℓ^{CMB} is the lensed primary CMB anisotropy power at multipole ℓ. On scales $\ell > 3000$, D_ℓ^{CMB} is strongly damped, and other components start to dominate. The population of dusty star-forming galaxies (DSFGs) have a significant microwave emission (specially at high frequencies), which contributes with Poisson (D_ℓ^{P}) and clustered (D_ℓ^{C}) power components. Likewise, mainly at low frequencies, the population of radio sources contributes prominently with a Poisson term, D_ℓ^{R}. A small contribution from the

Galactic cirrus emission, $D_\ell^{\rm cir}$, is also taken into account. Finally, the power of the tSZ and kSZ signals are given by $D_\ell^{\rm tSZ}$ and $D_\ell^{\rm kSZ}$, respectively.

Our work can therefore be considered as an astrophysical extension of the analysis presented by R12, where we allow for more freedom in the tSZ power spectrum by tieing it to a range of empirical models of the ICM. The other components of our baseline model are treated as nuisance parameters and described in detail in Appendix 7.7.

7.2.3 Parameter estimation

The SPT measurements as described in R12 comprise three auto-spectra (95×95, 150×150, 220×220 GHz), and three cross-spectra (95×150, 95×220, 150×220 GHz), in 15 spectral bands b_ℓ, each covering a narrow range in ℓ. In our work, we seek to match the parameters of intracluster pressure models with those observations. This is achieved by minimization of the χ^2 statistic,

$$\chi^2 = \sum_{b_\ell} \sum_{\nu_1,\nu_2} (D^{\rm obs}_{b_\ell,\nu_1,\nu_2} - D^{\rm mod}_{b_\ell,\nu_1,\nu_2})\, \mathbb{N}^{-1}_{b_\ell,\nu_1,\nu_2} (D^{\rm obs}_{b_\ell,\nu_1,\nu_2} - D^{\rm mod}_{b_\ell,\nu_1,\nu_2})^{T}, \tag{7.7}$$

where $D^{\rm obs}_{b_\ell,\nu_1,\nu_2}$ and $D^{\rm mod}_{b_\ell,\nu_1,\nu_2}$ are respectively the observed and modeled powers in band b_ℓ, and $\mathbb{N}^{-1}_{b_\ell,\nu_1,\nu_2}$ is the bandpower noise covariance matrix (obtained from R12), for the cross-spectra at frequencies ν_1 and ν_2.

The modeled bandpowers are estimated from the full-resolution power spectra of Eq. 7.6 and the band window functions w_{ℓ,b_ℓ} (also obtained from R12) as:

$$D^{\rm mod}_{b_\ell} = \sum_\ell w_{\ell,b_\ell} \times D^{\rm mod}_\ell. \tag{7.8}$$

The best fit parameters and their errors are obtained by sampling the likelihood function over the whole parameter space using a MCMC Metropolis algorithm.

In order to validate our modeling of the SPT data and our fitting procedure, we first replaced our analytical tSZ model with the template provided by Shaw et al. (2010) - as done in R12 - and jointly fitted the amplitudes of the tSZ template ($D^{\rm tSZ}_{3000}$), Poisson ($D^{\rm P}_{3000}$) and clustered ($D^{\rm C}_{3000}$) CIB components, fixing all other parameters to the R12 values. The results of this three-parameter samplings are displayed in Table 7.1 and Fig. 7.1, and are in agreement with R12. As expected, the errors in our result are smaller, since we held fixed the cosmological parameters and several of the foreground components. However, the difference is not large, reflecting the fact that the three fitted components are the leading contributors to the microwave background anisotropies on the considered wavelengths and angular scales.

In the following, we always fit the amplitudes of the Poisson and clustered CIB components together with our cluster pressure model parameters. Given the small impact they have on the final measurements, the additional components (lensed CMB, kSZ effect, radio and Galactic cirrus) are kept fixed for simplicity, and so are the cosmological parameters. The cosmological constraint is discussed in more detail in Section 7.5.3.

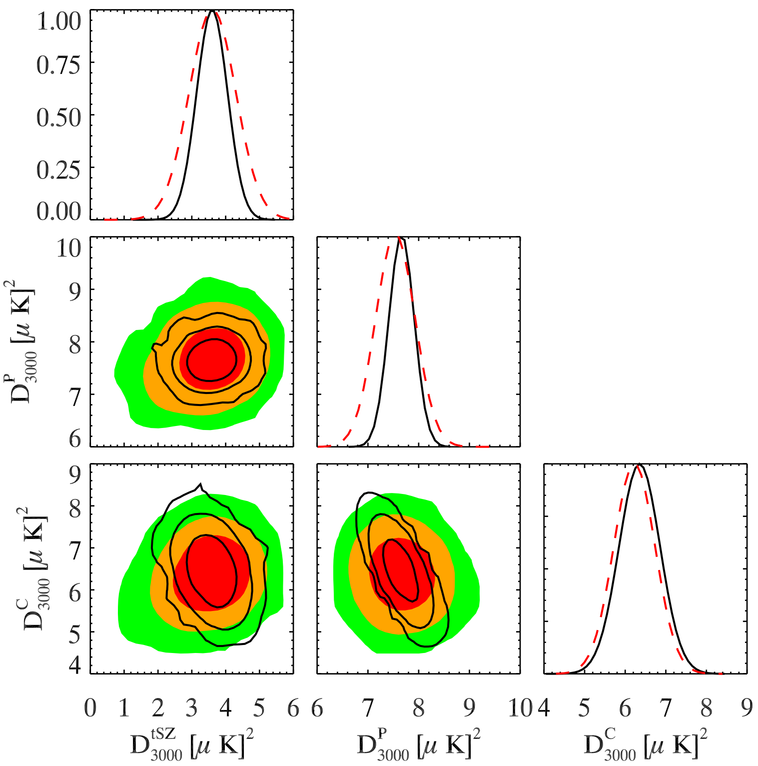

Figure 7.1: 2D likelihoods for the power spectra amplitudes at $\ell = 3000$ using our MCMC algorithm, compared to the results from R12. The plot shows the tSZ power spectrum ($D^{\rm tSZ}_{3000}$) using the template of Shaw et al. (2010), and the two CIB components, its Poisson contribution ($D^{\rm P}_{3000}$) and the clustered component ($D^{\rm C}_{3000}$). The filled colored contours show the 1, 2, and 3σ constraints from the SPT analysis. The black solid contours show the constraints from our MCMC sampling, where the other foregrounds are held fixed together with the cosmological parameters.

7.3 Pressure model

In this Section we introduce briefly the self-similar theory that describes the properties of galaxy groups and clusters. We also explain in detail the latest measurements of the pressure profile in galaxy clusters, and show the inconsistency between the SPT measurements and the theoretical predictions for the tSZ bandpowers based on such pressure profiles.

7.3.1 Self-similar models

In a hierarchical structure formation scenario on a CDM cosmology, groups and clusters are the end products of gravitational collapse of a small population of highly over-dense regions in the early universe. The term “self-similar” points to the scale-free nature of gravitational collapse in such a universe (Kaiser 1986). This implies that if clusters were strictly self-similar, we would expect the same evolution of their global properties on any scale and time. In the context of self-similar evolution, the redshift dependence of cluster observables can be expressed as a combination of different powers of $E(z)$ and $\Delta(z)$, where $E(z) = \sqrt{\Omega_{\rm m}(1+z)^3 + \Omega_\Lambda}$ is the Hubble ratio in flat ΛCDM universe, and $\Delta(z)$ is the dens-

Amplitude	SPT	This work	CCAT
$D_{3000}^{\rm tSZ}$	3.65 ± 0.69	3.61 ± 0.46	3.65 ± 0.09
$D_{3000}^{\rm P}$	7.54 ± 0.38	7.66 ± 0.25	7.54 ± 0.02
$D_{3000}^{\rm C}$	6.25 ± 0.52	6.35 ± 0.51	6.24 ± 0.05

Table 7.1: Comparison between the tSZ and CIB power amplitudes for our MCMC modeling and R12 results.

ity ratio between the mean (or critical) density of the universe at redshift z and that inside a fiducial radius of the cluster.

Furthermore, a self-similar formation model implies that gravitational collapse is the only source of energy input into the ICM. Since we assume cluster formation process is governed by gravity alone, we can derive simple scaling relations for the global observables properties as a function of cluster mass. These relations have been extensively studied in the literature (see Böhringer et al. 2012, and references therein). Particularly in the nearby Universe, they have been studied and determined with high precision. In the following section we describe the current state of knowledge on the self-similar redshift evolution and mass scaling of the ICM pressure profile.

7.3.2 The “universal” pressure profile

One of the most successful application of the self-similar model is the dark matter halo mass profile measured from N-body simulations by Navarro et al. (1995), known as the NFW profile. Following this model a more generalized version was proposed by Nagai et al. (2007) to describe the gas distribution in galaxy clusters, which contains additional shape parameters besides the normalization and the scale radius (generalized NFW, or GNFW profile). Arnaud et al. (2010, hereafter A10) measured these parameters for the GNFW model, as well as the mass scaling of the overall normalization, combining X-ray data and numerical simulations. This was the first demonstration of a scale-free, universal shape of the cluster pressure profile with a mass scaling very close to self-similar. The parametrization of the GNFW pressure model found by A10 is now commonly known as the “universal” pressure profile, and forms the basis of our analytical modeling.

A10 measured the GNFW profile parameters from a sample of 33 local clusters ($z < 0.2$), selected from the REFLEX catalogue and observed with *XMM-Newton*. The sample covers a mass range $7 \times 10^{13} \lesssim M_{500} h/{\rm M}_\odot \lesssim 6 \times 10^{14}$, where M_{500} is the mass enclosed within r_{500}, in which the mean density is 500 times the critical density of the Universe. The pressure profile is given by

$$P_{\rm e}(r') = 1.65\left(\frac{h}{0.7}\right)^2 {\rm eV\ cm^{-3}}\ E^{\frac{8}{3}}(z)\left[\frac{M_{500}}{3\times 10^{14}(0.7/h)\ {\rm M}_\odot}\right]^{\frac{2}{3}+\alpha_p} p(r'). \tag{7.9}$$

The function $p(r')$ describes the scale-invariant shape of the pressure profile,

$$p(r') \equiv \frac{P_0(0.7/h)^{\frac{3}{2}}}{(c_{500}r')^{\gamma}[1+(c_{500}r')^{\alpha}]^{(\beta-\gamma)/\alpha}}, \tag{7.10}$$

where $P_0 = 8.403$, $c_{500} = 1.177$ is a gas concentration parameter, the parameter $\gamma = 0.3081$ represents the central slope ($r' << 1$), $\alpha = 1.051$ is the intermediate slope ($r' \sim 1$), and $\beta = 5.4905$ is the outer slope ($r' >> 1$) of the pressure profile. The A10 profile was constrained from X-ray observations out to radii $r \sim r_{500}$. Beyond this radius, an extrapolation was made to fit the results from numerical simulations of clusters (Borgani et al. 2004; Nagai et al. 2007; Piffaretti & Valdarnini 2008). A small deviation from the self-similar scaling with cluster mass is given by $\alpha_p = 0.12$. We incorporate this additional mass dependence in all our calculations, which has a small effect on the amplitude of the tSZ power ($\sim 9\%$ at $\ell = 3000$). We ignore the extra smaller shape-dependent term of the mass scaling, described by the $\alpha'_p(x)$ term (see Eq. 10 in A10), because it has a negligible contribution ($\sim 2\%$ at $\ell = 3000$). Finally, the derived average A10 pressure profile has a dispersion around it, which is less than 30% beyond the core ($r > 0.2r_{500}$), and increases towards the center. This deviation around the mean is mainly due to the dynamical state of the clusters. Following 7.2.1 we assume this scatter only affects the pressure shape normalization (P_0), and incorporate its contribution into our power spectrum calculations accordingly.

The nearly self-similar mass scaling of the universal pressure profile has been verified down to the low mass end (galaxy groups) in the local universe. Sun et al. (2011) extended the measurements of A10 to lower masses, from a study of 43 galaxy groups at $z = 0.01 - 0.12$, within a mass range of roughly $M_{500} = 10^{13} - 10^{14}\ h\ \mathrm{M}_\odot$. All the ICM properties of these groups were derived at least out to r_{2500} from observations made with *Chandra*, and 23 galaxy groups have in addition masses measured up to $\sim r_{500}$. As with the original data set used by A10, the X-ray comparison by Sun et al. (2011) does not reveal the state of the gas pressure in groups at higher redshift, or at radii beyond r_{500}. Nevertheless, this rules out the possibility of a highly non-self-similar mass scaling for the ICM pressure, at least in the low redshifts, in a mass range spanning nearly two decades. Recent results by McDonald et al. (2014), using X-ray follow-up observation of SZ selected clusters, also confirm the validity of the universal pressure profile in a wide redshift range, down to a mass limit $M_{500} \sim 3 \times 10^{14}\ \mathrm{M}_\odot$. These are strong constraints while finding modifications for the universal pressure model to match the tSZ power spectrum observation.

Direct tSZ observations of individual clusters have now verified the validity of the universal pressure model at the high mass end, even though measurement errors remain high. In contrast to the X-ray measurement of the GNFW profile, tSZ observations are more sensitive to the cluster outskirts ($r > r_{500}$). Planck Collaboration et al. (2013a) measured the pressure profile of a sample of high mass and low redshift galaxy clusters. Their mean profile shows a slightly lower pressure in the inner parts when compared with the A10 profile, although there are strong degeneracies between the derived model parameters. It is possible that the lower pressure in the core region detected by *Planck* is a consequence of detecting more morphologically disturbed clusters than other samples. Outside the core region the *Planck*-derived pressure profile show good agreement with the extrapolated A10 pressure model, out to a radius $\sim 3r_{500}$. It should be noted that the poor angular resolution of *Planck* restricts its sensitivity for the pressure profile shape measurement mostly to a handful of nearby, massive clusters detected with high S/N.

A higher-resolution tSZ observation of individual cluster pressure profiles became available from the *Bolocam* experiment (Sayers et al. 2013b), which has 1 arcminute resolution at 150 GHz. The *Bolocam* team observed 45 massive galaxy clusters, with a median mass of $M_{500} = 9 \times 10^{14}\ \mathrm{M}_\odot$, and spanning a large range in redshift: $0.15 < z < 0.89$. They fitted a GNFW profile between $0.07r_{500}$ and $3.5r_{500}$. Despite the strong covariance between the model parameters, the overall shape is fairly well constrained. The mean profile shows good agreement with the A10 model, although there is an indication of a shallower pressure outer slope ($r \gtrsim r_{500}$). Furthermore, both *Planck* and *Bolocam* teams have measured the intrinsic scatter for the pressure profile in their samples, finding it to be roughly 30% as was also noted by A10. In the absence of more accurate measurements, we use $\sigma_s = 0.3$ (see Eq. 7.5) as a fiducial value in the rest of the paper.

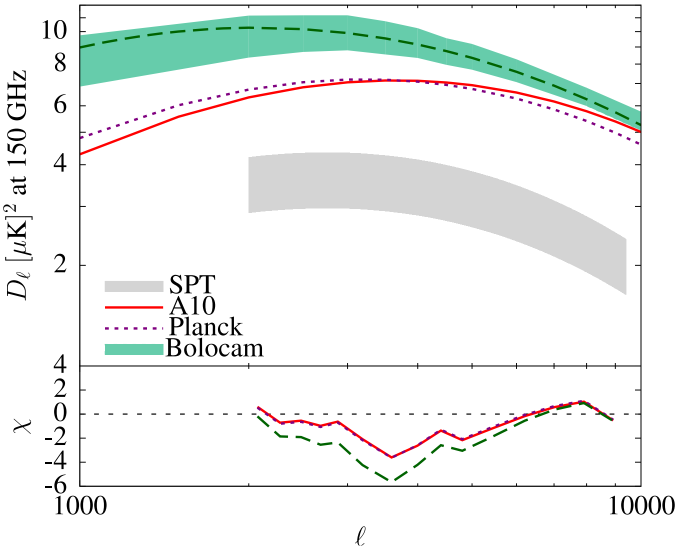

Figure 7.2: Discrepancy between the semi-analytic model predictions for the tSZ power and the SPT measurements. The red solid line is the tSZ power spectrum given by the A10 pressure profile (Eq. 7.9). The shaded gray region represent the 1σ constraints from the SPT, which is restricted by the shape of the Shaw model (see text for details). The purple dot-dashed line gives the result for the mean GNFW profile as measured by *Planck* (Planck Collaboration et al. 2013a). The green band marks the corresponding *Bolocam* measurement (Sayers et al. 2013b) with the 68% confidence interval on their model fit parameters. The bottom panel shows the value of χ at each point for these models with respect to the SPT bandpower measurements, in units of the measurement errors in each ℓ-band.

An important point to note here is that neither the *Planck* not the *Bolocam* analysis is based on a representative sample of galaxy clusters. Therefore, although these two data sets serve to constrain the alterations to the A10 pressure model in Section 7.4, none can yet be considered compelling.

7.3.3 Discrepancy between theoretical prediction and observation of the SZ power spectrum

The discrepancy between the theoretical model predictions for the tSZ power spectrum and its experimental measurement were shown early on, following pure analytical modeling (Komatsu & Seljak 2002; Bode et al. 2009) and simulations (Sehgal et al. 2010). The tSZ power based on the A10 universal pressure model is not the exception, as is shown in Fig. 7.2. The red solid curve is the prediction based on the A10 model, using Equations 7.1 and 7.9, which has a factor of ~ 2 higher amplitude than the SPT measurement (marked by the gray-shaded region). Similar results were also shown by Efstathiou & Migliaccio (2012).

We point up that despite its high sensitivity, the SPT data is unable to constrain simultaneously both the amplitude and shape of the tSZ power spectrum. For this reason R12 used the Shaw et al. (2010) tSZ template to quote the amplitude at $\ell = 3000$, which is $3.65 \pm 0.69\,\mu\text{K}^2$. In Fig. 7.2 and subsequent plots, we show the SPT 68% confidence region derived from the Shaw et al. (2010) model in gray bands, to provide a visual comparison with our best fit results. The plots are in terms of $D_\ell = \ell(\ell+1)C_\ell^s/2\pi$ with units of $[\mu\text{K}]^2$ at 150 GHz. For quantifying the goodness of fit between a model prediction and the SPT data, we compute the probability to exceed (PTE, or the p-value) for the model using the actual CMB bandpower measurements from SPT, and not with the Shaw et al. (2010) model template. The PTE for the A10 model prediction is 0.0006, suggesting a very poor fit.

It is now possible to check the compatibility of the *Planck* and *Bolocam* measurements of the pressure profile with the SPT result following the procedure outlined in Section 7.2. These are shown in Fig. 7.2 with the dotted and dashed lines, respectively. The prediction based on the mean *Planck* profile is very similar to the A10 model, whereas the mean *Bolocam* profile predicts higher amplitude for the tSZ power and returns further lower PTE value. This is primarily because of the shallower outer slope of the pressure profile as reported in the *Bolocam* paper, giving excess power al $\ell \lesssim 3000$. We take note of the fact that making a comparison with only the mean pressure profile, using the maximum likelihood values of the GNFW model parameters, is not correct since there is a large covariance between these parameters which will produce a range of equally likely pressure profiles. The *Planck* parameter covariance is not published, but we obtained the parameter chains for the GNFW model fit for *Bolocam* (J. Sayers, priv. comm.), which allow us to draw a 68% credibility region of the tSZ power spectrum based on the *Bolocam* result. This is shown by the green shaded region in Fig. 7.2, which is small compared to the roughly 5 $\mu\mathrm{K}^2$ difference between the predicted power and the SPT measured value. Based on similar parameter errors on the GNFW model fit by Planck Collaboration et al. (2013a), it can be assumed that the measured errors on the mean *Planck* profile cannot explain the mismatch with data either.

It can be argued that the source of the discrepancy between the predicted amplitude of the tSZ power spectrum and its measurement comes from the assumed cosmological model. The tSZ power spectrum relies on the correct modeling of the halo mass function, but it has been proven that the halo mass function is known to an accuracy of about 5% (Tinker et al. 2008; Bhattacharya et al. 2011). However, the values of the key cosmological parameters differ significantly between the measurements made by different probes, like WMAP and *Planck* , which will result in large systematic changes in the tSZ power spectrum. In Section 7.5.3 we address this issue in more detail, and show if we ignore the large systematic difference between the WMAP and *Planck* cosmology, then the measurement uncertainties in any of the adopted set of parameters is not an issue. Moreover, use of the *Planck* cosmology increases the predicted tSZ power amplitude by roughly factor 2, thereby making the tension between theory and observation more severe. Since we observe a reduced amplitude of the tSZ power, the most likely explanation for that lower amplitude must be astrophysical, and our use of WMAP cosmology amounts to a more conservative modification of the ICM pressure distribution to match theory and observation.

7.3.4 Radial, mass and redshift contribution to the power spectrum

We split the tSZ power into mass, redshift and radial bins to identify where the main contributions to the tSZ power come from. The results in this Section are similar to those already presented in Komatsu & Seljak (2002), Battaglia et al. (2012b) and McCarthy et al. (2014), although we use the universal pressure model of A10 for our analysis.

First, we radially truncate the pressure profile to investigate which regions of the galaxy clusters contribute more to the total tSZ power spectrum. The differential contributions from three radial bins are shown in Fig. 7.3 (top panel). Earlier works have shown the results for radial contributions in cumulative plots, which automatically include the cross-correlation of the tSZ power between different bins. We make a differential plot for ease of comparison and take the cross-correlation terms into account. When considering all clusters at all redshifts, most of the power ($\sim 85\%$) on small angular scales ($\ell > 3000$) comes from $r < r_{500}$, since bulk of the cluster tSZ signal comes from this central region. Outskirts of

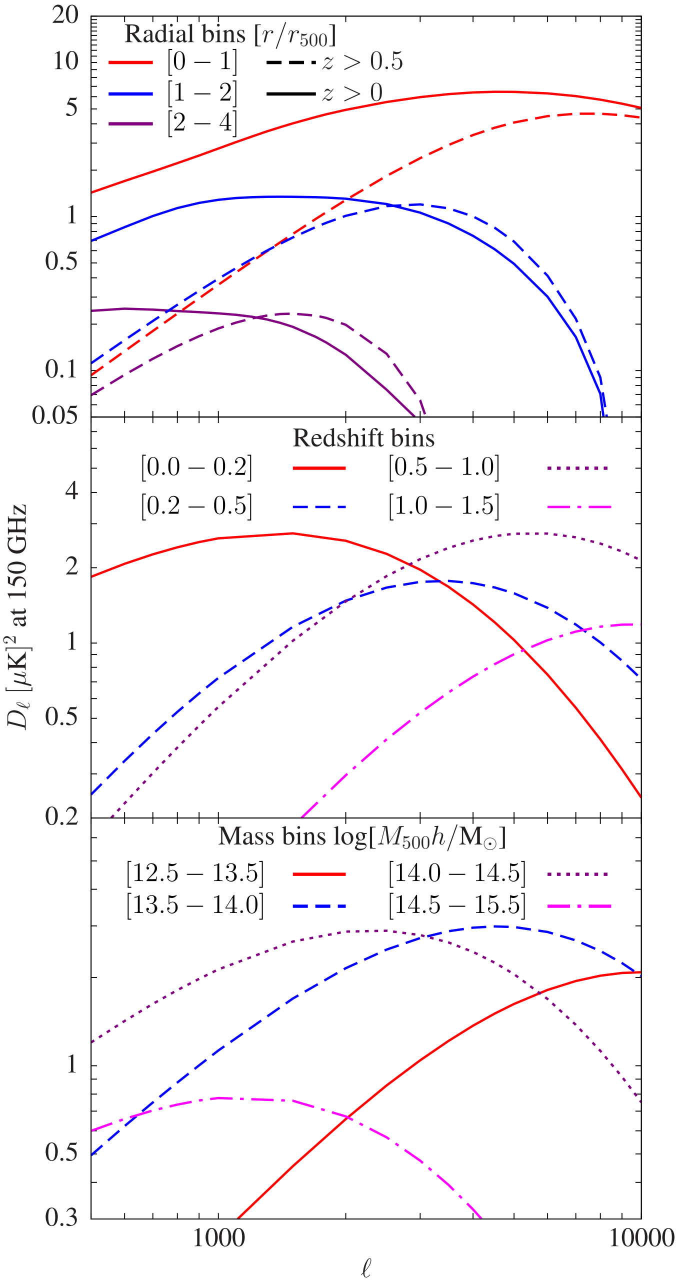

Figure 7.3: Contribution of the tSZ power spectrum in different cluster radial, mass and redshift bins. The plot is in terms of $D_\ell = \ell(\ell+1)C^s_\ell/2\pi$ with units of $[\mu\mathrm{K}]^2$ at 150 GHz. For these illustrative plots we have used the A10 pressure profile without modifications, and factored in the contribution from intrinsic scatter. The numbers in the square brackets mark the radial, redshift and mass bins for the individual curves. In the upper panel, the dashed lines only show the contribution from high-redshift ($z > 0.5$) clusters. The anisotropy power from cluster outskirts ($r > r_{500}$) becomes increasingly important at $\ell \lesssim 3000$.

galaxy clusters play an important role at lower ℓ. The tSZ power increases by $\sim 50\%$ at $\ell = 500$ when the upper limit of the radial integration is increased to $2r_{500}$. Thereafter, the tSZ amplitude does not vary much if the integration limit is extended to radii $r > 4r_{500}$. If we only consider clusters at high redshifts ($z > 0.5$), the power contribution from the outskirts will be roughly equal to that coming from the inner region for $\ell \lesssim 2000$ (dashed-lines in the upper panel of Fig. 7.3).

In a similar way, we calculate the tSZ power spectrum in mass and redshift bins, which are shown in the middle and bottom panels of Fig. 7.3, respectively. On large angular scales ($\ell < 2000$) the largest contribution to the tSZ power comes from high mass ($14 < \log[M_{500}h/\ \mathrm{M}_\odot] < 14.5$) and low redshift objects ($z < 0.2$). Above $\ell \sim 3000$, the tSZ power is dominated by low mass ($13.5 < \log[M_{500}h/\ \mathrm{M}_\odot] < 14$) and high redshift ($z > 0.5$) galaxy groups/clusters. The very massive objects ($\log[M_{500}h/\,\mathrm{M}_\odot] > 14.5$) have a negligible contribution on small angular scales. Therefore the clusters that are currently constrained from direct tSZ observation by *Planck* and *Bolocam* are not representative in terms of the measurement of the tSZ power spectrum. Objects with very low mass, or redshift $z > 1$ dominate the tSZ power only at multipoles larger than $\ell \sim 15000$, assuming the extrapolation of the A10 pressure model is correct in such extreme cases.

From the illustrations above it can be seen that the tSZ power near the angular scales of its expected peak is dominated by contributions from the low mass clusters or groups at intermediate redshifts, for which there are little observational constraints on their ICM properties. Thus, using the fiducial values for the A10 pressure model on high redshift galaxy groups and clusters could be the source of the over-estimation of the tSZ power. Likewise, the A10 pressure profile beyond r_{500} was constrained from hydrodynamical simulations, which could also be overestimating the thermal pressure component in the outskirts, giving more tSZ power. Thus, two obvious choices for modifying the A10 pressure profile would be *i)* decreasing the pressure amplitude with redshift that offsets the self-similar evolution, or *ii)* decreasing the thermal pressure support in the outskirts.

The mass dependence of the pressure normalization (or the outer pressure slope), as discussed in Section 7.4, are generally better constrained from observation (or simulations) and are not the main focus of the current paper.

7.3.5 Effect of cluster morphology

Before proceeding to modify the universal pressure profile, it is natural to ask whether an over-abundance of merging systems at high redshifts can be responsible for the lower measured tSZ power. This follows from the result of A10 who found, with high significance based on X-ray data, that disturbed clusters have lower pressure near the core region compared to the mean. In the standard ΛCDM scenario the number of mergers within a time interval is a slowly increasing function of halo redshift and mass (e.g., Fakhouri et al. 2010), and there is some evidence of this increased merger fraction from X-ray selected clusters (Maughan et al. 2012; Mann & Ebeling 2012). The resulting change in the cool-core (CC) to non cool-core (NCC) cluster ratio with redshift might be causing the lower amplitude of the tSZ power spectrum in the SPT data.

A10 divided their cluster sample into CC and NCC clusters and provided parametric fits for the respective populations (see Appendix C of A10). The CC clusters have more peaked profile at the center, the region that produces bulk of the emissivity in X-rays. However, from Fig. 7.4 we can conclude that the core region ($r < 0.2r_{500}$) contributes a negligible fraction of the tSZ power on scales larger than ~ 1 arcmin: the contribution is only 5% at $\ell = 3000$, and rises up to nearly 17% at $\ell = 10000$. A10 found the pressure profiles of the CC and NCC cluster samples nearly self-similar in the intermediate ($r \sim r_{500}$) to outer regions, and currently there are no direct evidence for a systematic difference between the CC and NCC cluster pressure distribution from tSZ data. Given that restriction, the CC and NCC clusters produce roughly the same result for tSZ power (Fig. 7.4). We thus conclude that an increased occurrence of NCC clusters at high-z cannot be the explanation of the low measured value of the tSZ power, if those NCC clusters follow the same mass and redshift scaling as given for the universal pressure profile by A10.

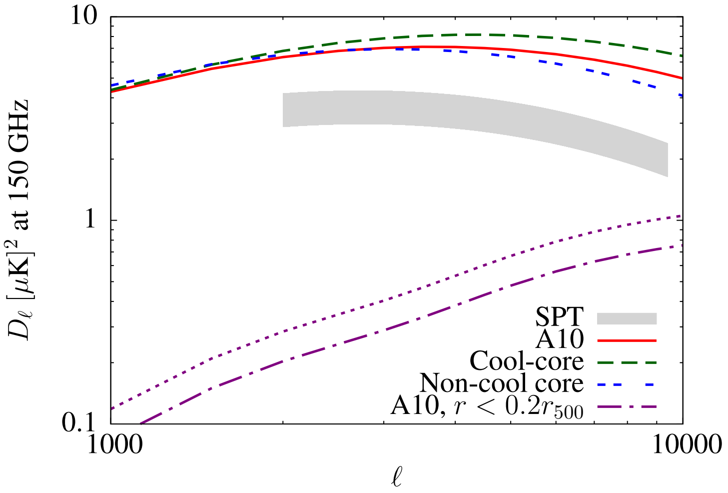

Figure 7.4: Predictions for the tSZ power spectrum for cluster morphological evolution. The red-solid line is given by the mean A10 pressure profile, the green-dashed line for cool-core clusters, and the blue short-dashed line for non-cool clusters. The purple dot-dashed line shows the relative contribution from the core regions of galaxy clusters ($r < 0.2r_{500}$) to the total tSZ power, and the dotted line above it factors in an additional scatter contribution (40%) for the core region. This plot shows that, unlike the X-ray luminosity, the core region contributes very little to the tSZ anisotropy power.

7.4 Results

This Section presents our main results, following various attempts at modifying the universal pressure model. We group these model changes according to their deviations from a simple self-similar scaling.

7.4.1 Modification following strictly self-similar evolution

In the classical self-similar scenario of cluster evolution, the baryon distribution will have the same shape and amplitude once they are scaled to the cluster mass and redshift with the standard scaling powers (e.g., Böhringer et al. 2012). In context of the A10 pressure profile, this means that clusters at all mass and redshift will have the same set of amplitude and shape parameters: $\{P_0, c_{500}, \alpha, \beta, \gamma\}$, and the total pressure amplitude will scale with redshift as $E(z)^{8/3}$. In a first attempt to keep the redshift evolution unchanged, we try to find a suitable set of shape parameters that will remove the tension between the model predictions and SPT data.

Constraints on the outer slope of the pressure profile

As mentioned previously, the "universal" pressure profile was constrained from X-ray observations out to radii $r \sim r_{500}$, and extrapolated beyond r_{500} to match hydrodynamical simulation results. The outer slope parameter is denoted by β, whose value is fixed at $\beta = 5.49$ in the A10 paper. A significant amount of the tSZ signal comes from $r > r_{500}$, more than 50% if we neglect the few nearby, high-mass clusters (that are generally resolved in deep tSZ surveys), therefore the impact of β on the tSZ power amplitude is pivotal. A higher value of β would imply less thermal pressure. Physical reason for

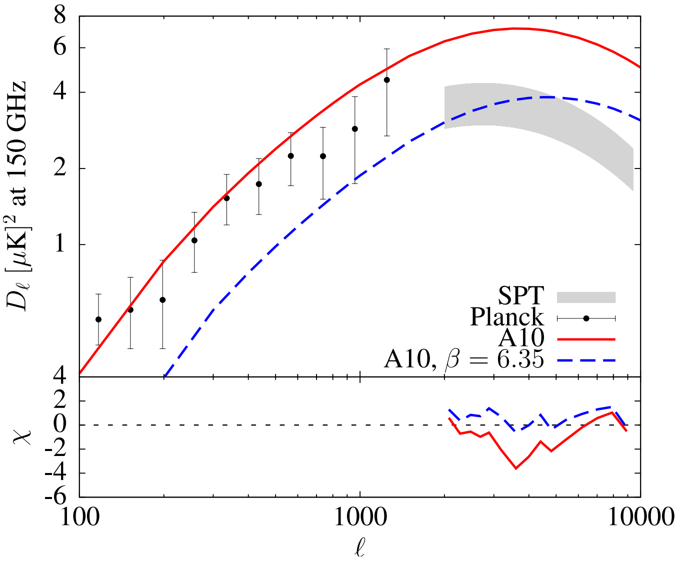

Figure 7.5: Predictions for the tSZ power spectrum for self-similar evolution. The red solid line is the tSZ power spectrum given by the A10 pressure profile (Eq. 7.9). The shaded gray region represent the 1σ constraints from the SPT based on the Shaw et al. (2010) template (see text for details). The blue dashed line represents the GNFW model with our best fit outer slope (β = 6.35), which provides good fit to the actual SPT data, as shown by the χ plot in the bottom panel. The black data points are the marginalized bandpowers of the Planck tSZ power spectrum, taken from Planck Collaboration et al. (2014c).

lower thermal pressure can be additional pressure support from gas bulk motions, usually triggered by infalling or merging sub-halos. Recent results from numerical simulations (Nagai et al. 2007; Lau et al. 2009; Nelson et al. 2014) as well as analytical modeling (Shi & Komatsu 2014) have shown that this non-thermal pressure contribution is small in the inner regions, but rapidly increases with radius. We therefore concentrate on modifying β, given the least amount of observational constraint on its value, while keeping the redshift evolution of the pressure amplitude at $E(z)^{8/3}$ as in Eq. 7.9.

The best fit value obtained from our MCMC sampling is $\beta = 6.35 \pm 0.19$, together with the CIB contribution terms $D^{\rm P}_{3000} = 7.58 \pm 0.28$ and $D^{\rm C}_{3000} = 6.42 \pm 0.54$. The resulting PTE= 0.80 suggests a good fit to the CMB bandpower data. This value of β is considerably higher than the one assumed by A10 ($\beta = 5.49$), implying a much lower thermal pressure support in the outskirts. This new value of β has very little effect on the inner pressure profile ($< 1\%$ at $r << r_{500}$), but reduces the pressure amplitude by $\sim 40\%$ at r_{500}. The effect is significant on the power spectrum after projection, especially on large scales, where the new tSZ power amplitude is lowered by $\sim 50\%$ compared to the A10 values (Fig. 7.5, blue dashed line). Furthermore, the peak of the tSZ power spectrum is shifted to smaller angular scales, near $\ell \sim 4500$. We note that the shape of the tSZ power spectrum differs strongly compared to the Shaw et al. (2010) template (gray band), but the new shape provides acceptable fit to the SPT data together with the above CIB power amplitudes.

Possible tension with *Planck* and *Bolocam* results

The marginalized value of the outer pressure profile slope, $\beta = 6.35 \pm 0.19$ with 68% confidence, is higher than the mean values obtained from direct cluster SZ profile measurement by *Bolocam* and *Planck* experiments. However, in a GNFW model fit the value of β generally highly degenerates with

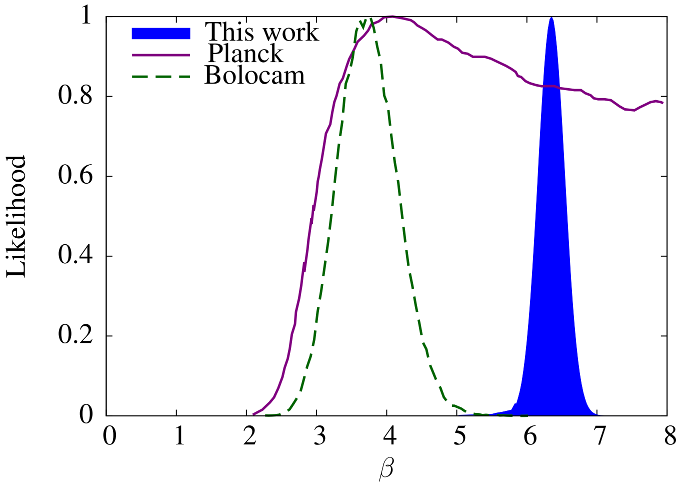

Figure 7.6: 1D likelihood curves for outer slope parameter β. The purple solid line shows the constraints from *Planck* . Results from *Bolocam* are shown by the green dashed line. The blue-filled curve represents our best fit constraint on β.

other parameters, in particular it anti-correlates with the scale radius (or equivalently, c_{500}), as shown by Planck Collaboration et al. (2013a). Therefore we must compare our best fit values with the marginalized errors on β from other experiments. This is shown in Fig. 7.6, where we plot the normalized likelihood distributions for the outer slope parameter β from *Planck* and *Bolocam* fits. As can be seen, there is significant tension for such a steep value of outer slope with *Bolocam* data, whereas it is consistent with the *Planck* measurement. A possible cause can be that the *Bolocam* team fixes the gas concentration parameter c_{500}, which restricts their likelihood range of β, even though both our modeling and the *Bolocam* work by Sayers et al. (2013b) use the same fixed value $c_{500} = 1.18$ from the A10 model. The sensitivity of the *Planck* measurement to the slope parameters is possibly lower due to its large beam, except for a few nearby clusters.

A general consequence of having a steeper outer slope is that it will inevitably reduce the tSZ power at low ℓ values ($\ell < 1000$), as seen in section 7.4.1. This then leads to some tension with the tSZ power measurements based on *Planck* data (Planck Collaboration et al. 2014c), which we show in Fig. 7.5. The *Planck* marginalized bandpower values are taken directly from the *Planck* collaboration paper. Without a knowledge of the covariance we cannot compute the χ^2 or the PTE value of our model from *Planck* data, but a clear tension can be seen from the figure.

7.4.2 Weakly self-similar: changing pressure normalization with redshift or mass

It is possible to imagine scenarios where the amplitude of the pressure distribution in galaxy clusters deviate from a strictly self-similar evolution, i.e., not scaling as $P(r) \propto M_{500}^{2/3}$ or/and $P(r) \propto E(z)^{8/3}$. In fact A10 already show that the mass scaling of the pressure profile is not strictly self-similar, there is an additional factor, $\alpha_P = 0.12$, in the mass-scaling power (see Eq. 7.9). The reason behind this deviation from self-similarity is the empirical calibration of the A10 pressure profile against the measured $Y_X - M_{500}$ scaling of Arnaud et al. (2007), which was based on a subset of REXCESS clusters at low redshifts. Therefore, while the small deviation in the mass exponent in Eq. 7.9 is well-measured in the local universe, its redshift dependence remains largely unexplored.

In this Section we explore scenarios where the redshift evolution of the pressure amplitude deviates from the $E(z)^{8/3}$ scaling, while keeping the shape (Eq. 7.10) constant. Physical motivation for such redshift dependence can be found from the observed scaling of the $L_X - T_X$ scaling relation (e.g., Reichert et al. 2011), possibly relating to a gas mass fraction, $f_{\rm gas}$, evolution in groups and clusters which we discuss subsequently. As an extension to this model, we consider cases where the redshift evolution depends also on mass, in line with the observed difference in the mass dependence of $f_{\rm gas}$ in groups and clusters.

Departure from self-similar redshift evolution

As discussed in Section 7.3.1, in the self-similar model the redshift evolution of the global properties of galaxy clusters is described by a simple power law of the $E(z)$ parameter. However, non-gravitational processes, like cooling and feedback, can alter the expected redshift evolution parametrization (e.g., Voit 2005). Such possible deviations from self-similarity can be considered through a $(1 + z)$ term lacking a better understanding of their origin. Recent semi-analytical works (Shaw et al. 2010; Battaglia et al. 2012a) have also used a power-law dependence of $(1 + z)$ for modeling the non-thermal pressure evolution.

Following the above argument, and keeping the functional form of the A10 pressure profile unchanged at low redshifts, we introduce an additional $(1 + z)$ dependence of the form

$$P_e(r) \propto E^{\frac{8}{3}}(z)(1+z)^{\alpha_z} M_{500}^{\frac{2}{3}+\alpha_p}. \tag{7.11}$$

The parameter α_z signifies the departure from the self-similar evolution, and we constrain its value by comparing with the SPT measurements (R12) through our MCMC method. The best fit value is $\alpha_z = -0.73 \pm 0.16$, $D^{\rm P}_{3000} = 7.69 \pm 0.27$, and $D^{\rm C}_{3000} = 6.35 \pm 0.49$, with a PTE of 0.78. The overall effect of such non self-similar evolution is to lower the amplitude of the tSZ power spectrum (purple-dotted line in Fig. 7.7), since as the negative value for α_z implies, the pressure amplitude in groups/clusters decreases with increasing redshift. The modified shape of the tSZ power spectrum is in good agreement with the Shaw et al. template (Fig. 7.7).

From a cosmological point of view, a power-law dependence of $E(z)$ is a more attractive parametrization for the non-self-similar evolution. Efstathiou & Migliaccio (2012) have proposed such a model by introducing the parameter ϵ into the $E(z)$ power for the pressure scaling:

$$P_e(r) \propto E(z)^{\frac{8}{3}-\epsilon} M_{500}^{\frac{2}{3}+\alpha_p}. \tag{7.12}$$

As before, we can constrain the value of ϵ by comparing with the SPT measurements. We find values of $\epsilon = 1.17 \pm 0.27$, $D^{\rm P}_{3000} = 7.69 \pm 0.26$, and $D^{\rm C}_{3000} = 6.40 \pm 0.51$, with a resulting PTE of 0.79 (blue-dashed line in Fig. 7.7). We cannot directly compare with the results of Efstathiou & Migliaccio (2012), since they constrained their ϵ value by comparing with simulated tSZ power spectrum templates (Battaglia et al. 2010; Trac et al. 2011), and incorporate another additional normalization parameter (A) for their model that should be highly degenerate with the redshift evolution term ϵ.

Depending on the physical origin of the non-self-similar evolution, either an $E(z)$ or a $(1 + z)$ power-law dependence will describe the pressure profile modification correctly. Since both these parametrizations

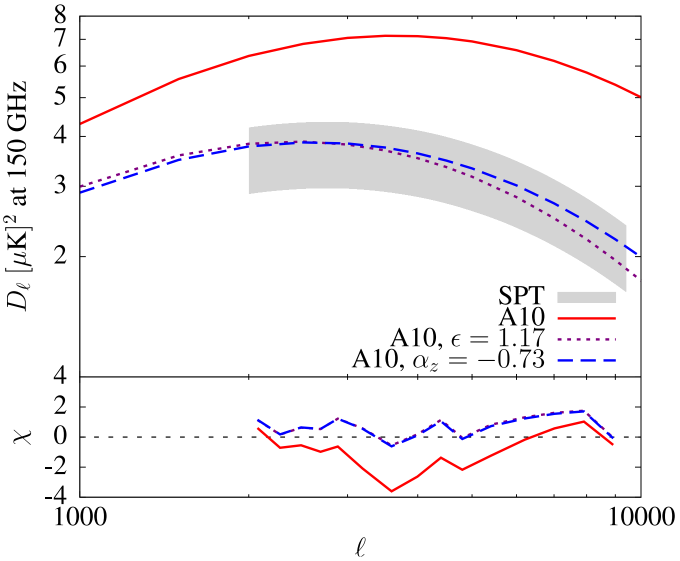

Figure 7.7: Predictions for the tSZ power spectrum for a weak departure from self-similarity, affecting only the pressure normalization. The red solid line is the tSZ power spectrum given by the A10 pressure model, and the shaded gray region is the 1σ scatter around the best fit Shaw model with SPT data. The blue dashed line represents the A10 model with $\epsilon = 1.17$ (Eq. 7.12). The purple dotted line represents A10 model with $\alpha_z = -0.73$ (Eq. 7.11). Both parameters, ϵ and α_z, modify the redshift evolution of the pressure profile to reduce its amplitude at high-z.

result in similar changes to the $P(r)$, and show similar relative errors, we have opted for keeping both cases in our analyses.

Association with $f_{\rm gas}$ and X-ray scaling laws

The pressure-mass, $P - M$, scaling relation has a direct dependence on the gas mass fraction, $f_{\rm gas}$: $P \propto f_{\rm gas} E^{8/3} M^{2/3}$. This quantity is usually assumed as constant, and the A10 work make no explicit statement on gas mass fraction either. However, the $P - M$ relation used by A10 deviates from the self-similar prediction, having a slightly stronger mass dependence: $P \propto E^{8/3} M^{2/3+0.12}$. By comparing the A10 $P - M$ relation with the self-similar prediction, we can assume that this excess is the result of the gas mass fraction: $f_{\rm gas} \propto M^{0.12}$. This is motivated by studies which have found that $f_{\rm gas}$ increases with mass of galaxy groups and clusters (Vikhlinin et al. 2006; Arnaud et al. 2007; Pratt et al. 2009; Sun et al. 2009), since non-gravitational processes (e.g., AGN feedback and star formation) produce a larger impact on galaxy groups than in clusters. Pratt et al. (2009), for example, found a relatively strong mass dependence of $f_{\rm gas}$ in the REXCESS sample: $f_{\rm gas} \propto M^{0.2}$; and for low mass regime, Sun et al. (2009) constrained the mass dependence in the range: $f_{\rm gas} \propto M^{0.16-0.22}$.

In order to assess the impact of different mass dependence of $f_{\rm gas}$ on the tSZ power spectrum, we introduce two distinct power laws for the mass dependence in the A10 pressure profile (Eq. 7.9): $f_{\rm gas} \propto M^{0.2}$ and $f_{\rm gas} \propto M^{0.12}$ for masses below and above $M_{500} = 10^{14}\ h^{-1}$ M$_\odot$, respectively. Fig. 7.8 shows the small effect of this broken power law for mass dependence on the tSZ power spectrum (green-dotted line), which is not enough to explain the discrepancy between tSZ power spectrum predictions and the SPT constraints. This shows that a small departure from the self-similar mass scaling, in accordance with the observational results, is not sufficient to explain the low amplitude of the tSZ power spectrum by itself; one needs to consider a modification to the redshift evolution as well. By using our MCMC

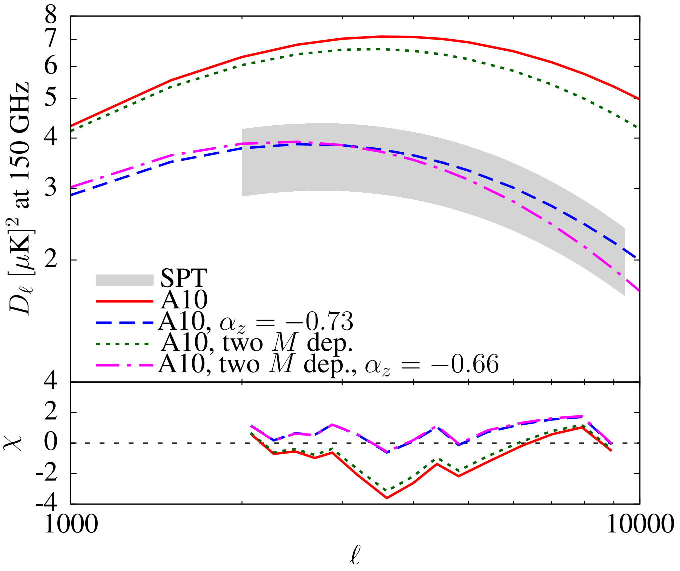

Figure 7.8: Predictions for the tSZ power spectrum for a weak departure from self-similarity, factoring in additional mass-dependence for the scaling. The red solid line and the gray shaded regions have the same meaning as in earlier figures. The blue dashed line represents the tSZ power spectrum with $\alpha_z = -0.73$ (Eq. 7.11), as in Fig. 7.7. The green dotted line is given by a modified A10 pressure profile that has double mass dependence: $f_{\rm gas} \propto M^{0.2}$ for masses below $M_{500} = 10^{14}\ h^{-1}\ {\rm M}_\odot$, and $f_{\rm gas} \propto M^{0.12}$ above this mass limit. Since this change alone is not enough to reach the SPT constraints, we need to introduce a redshift evolution, the result of which is shown by the magenta dash-dotted line.

method, we found that the necessary evolution is given by: $\alpha_z = -0.66 \pm 0.15$, $D^{\rm P}_{3000} = 7.70 \pm 0.21$, and $D^{\rm C}_{3000} = 6.38 \pm 0.47$, with a PTE of 0.79 (shown in Fig. 7.7 by the magenta dash-dotted line).

$f_{\rm gas}$ evolution vs. X-ray data and simulations

In the previous section we assumed that the weakly non-self-similar $P - M$ scaling used by A10 is due to the fact that $f_{\rm gas}$ has a mass dependence. In a similar manner, the non-self-similar evolution required to explain the discrepancy between the SPT measurements and the theoretical predictions of the tSZ power spectrum (section 7.4.2) can be attributed to an evolution in $f_{\rm gas}$. This assumption is motivated by recent observations that show scaling relations, which have a direct dependency on the $f_{\rm gas}$, do not always follow a self-similar evolution (see discussion in Böhringer et al. 2012). For example, Reichert et al. (2011) and Hilton et al. (2012) have measured the $L_X - T_X$ scaling relation in different redshift ranges, and they find it to be non-self-similar.

The X-ray bolometric luminosity scales with $f_{\rm gas}$ as

$$L_{\rm bol} \propto f_{\rm gas}^2 T^2 E(z). \tag{7.13}$$

If we assume that the temperature scaling remains self-similar, this would suggest an evolving baryon fraction in clusters. Thus, our tSZ power spectrum based on an evolving $f_{\rm gas}$ model, following the results from previous section 7.4.2, would suggest

$$E^{-1} L_{\rm bol} \propto T^{2.36} (1+z)^{-1.82 \pm 0.302}, \tag{7.14}$$

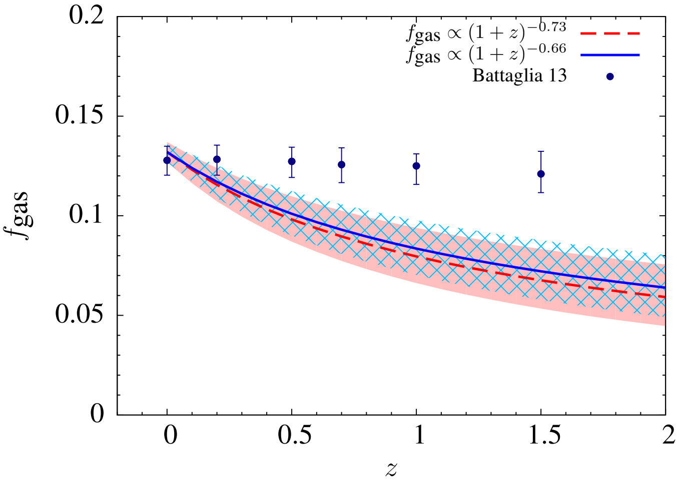

Figure 7.9: Redshift evolution of the gas mass fraction, $f_{\rm gas}$, based on our modeling. The blue solid line is for redshift-dependent $f_{\rm gas}$ following the $(1+z)^{\alpha_z}$ power law, and the red dashed line if the same but with two different mass scaling (see section 7.4.2). The hatched and shaded regions mark the 1σ confidence intervals around these lines, respectively. Points with error bars are taken from Battaglia et al. (2013) simulations, who compute the mean $f_{\rm gas}$ within r_{200}.

for the $(1+z)^{\alpha_z}$ scaling, or

$$L_{\rm bol} \propto T^{2.36} E^{-1.58\pm0.54}, \tag{7.15}$$

for the $E(z)^{8/3-\epsilon}$ scaling. We compare these results with the XCS cluster sample result from Hilton et al. (2012), and also from Reichert et al. (2011) who use an ad-hoc high-z cluster sample. Hilton et al. (2012) have found the scaling for the bolometric luminosity as $E^{-1}L_{\rm bol} \propto T^{3.18}(1+z)^{-1.7\pm0.4}$ or $L_{\rm bol} \propto T^{3.18}E^{-1.2\pm0.5}$. The result from Reichert et al. (2011) is a less significant change with redshift for the soft-band luminosity: $L_X \propto T^{2.70\pm0.24}E^{-0.23^{+0.12}_{-0.62}}$. We see that our results are generally consistent with those from Hilton et al. (2012), but there is disagreement with the Reichert et al. (2011) scaling. What is significant, however, is that the errors on the redshift evolution term from our modeling are similar to those available at present from direct X-ray observations. This illustrates the promise of tSZ power spectrum measurements to constrain cluster scaling relations, and we shall discuss its future prospects in section 7.5.2.

Currently there are no direct $f_{\rm gas}$ measurement in a mass-limited cluster sample out to high redshifts. The works by Allen et al. (2004, 2008) use carefully selected relaxed clusters from X-ray survey data, where they find that $f_{\rm gas}$ remains practically unchanged with redshift. The results from complete X-ray samples are restricted to low redshifts, for example the REXCESS sample by Pratt et al. (2009). Therefore, we make a comparison with recent results from N-body hydrodynamical simulations of clusters that have aimed at measuring the evolution of the baryonic component. Fig. 7.9 shows a comparison of the $f_{\rm gas}$ from Battaglia et al. (2013), who use hydrodynamical TreePM-SPH simulations including cooling, star-formation, and supernova and AGN feedback, with our results. Clearly both our single power law evolution and the broken mass-dependent evolution models are inconsistent with Battaglia et al. (2013) predictions, which show a negligible change in $f_{\rm gas}$ with redshift.

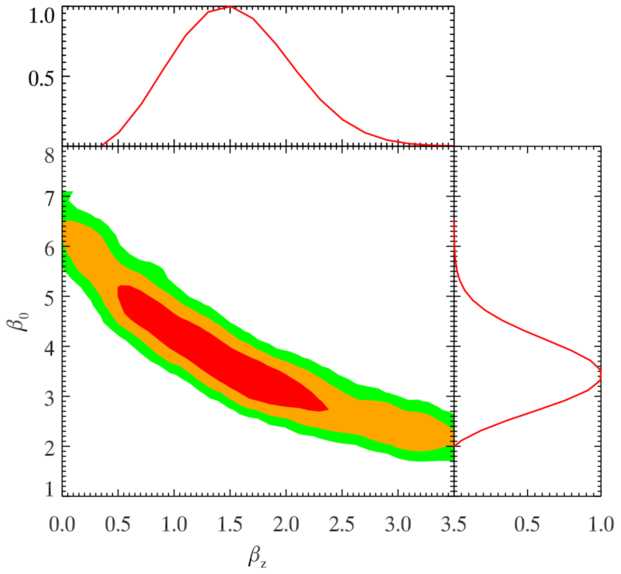

Figure 7.10: 2D Likelihood contours for the correlation between the β_0 (the outer slope parameter at $z = 0$) and β_z (its redshift evolution, see Eq. 7.16). The colored contours show the 1, 2, and 3σ constraints, and the marginalized values are shown in the side panels. Both β_0 and β_z tend to lower the tSZ power amplitude and hence anti-correlate.

7.4.3 Non-self-similar: an evolving shape of the pressure profile

In our study of a deviation from self-similarity, we have assumed the shape of the pressure profile remains constant with redshift, such that the outer pressure slope parameter β does not change with z. In reality this is unlikely to be true, since the cluster merger fraction steadily increases with redshift, meaning departure from hydrostatic equilibrium should become more significant at high-z, making non-thermal pressure support more prominent. Shaw et al. (2010) considered this effect and identified a redshift evolution of the non-thermal pressure support as potentially the most significant contributor to the lower amplitude of the tSZ power spectrum. An enhancement of the non-thermal pressure (random gas motions) with redshift is also shown by recent hydrodynamical simulations (Lau et al. 2009; Nelson et al. 2014), who in addition find that there is practically no mass dependence for this effect. Our treatment of a non-self-similar pressure shape, therefore, only consists of an evolution with redshift and no scaling with cluster mass.

We consider a model of this redshift-dependent steepening of the pressure profile using a simple, analytic form for the slope parameter β as follows:

$$\beta = \beta_0 (1 + z)^{\beta_z}, \tag{7.16}$$

Here β_0 is the outer slope parameter at $z = 0$, roughly reminiscent of the low-redshift measurements by A10 and Sun et al. (2011), and β_z is its redshift scaling. Fig. 7.10 shows the result of model constraints using this new redshift-dependent term. The parameter β_z is highly degenerate with β_0, with large errors on their marginalized values: $\beta_z = 1.50^{+0.60}_{-0.55}$ and $\beta_0 = 3.50^{+0.80}_{-0.70}$ with a PTE= 0.79. Likewise, if we

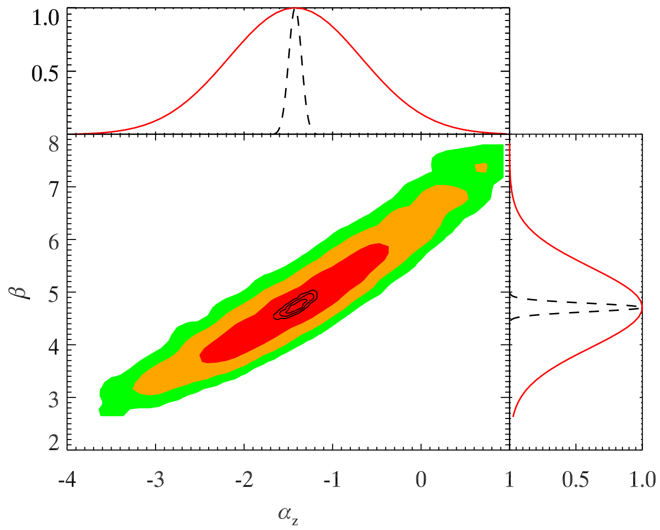

Figure 7.11: 2D likelihood contours for the β and α_z parameters and their marginalized values. The colored contours show the 1, 2, and 3σ constraints available from the SPT bandpowers of R12. The black solid lines show the expected constraints from the CCAT tSZ survey. The marginalized errors for CCAT (dashed lines) are almost an order of magnitude smaller.

parametrize the redshift evolution of β with an $E(z)$ power-law as

$$\beta = \beta'_0 E(z)^{\beta'_z}, \tag{7.17}$$

we obtain $\beta'_z = 2.12^{+1.19}_{-1.07}$ and $\beta'_0 = 3.79^{+0.79}_{-0.71}$ with a PTE= 0.76. This parameter degeneracy is a general conclusion whenever we try to constrain a pressure profile model parameter and its redshift evolution simultaneously from the current SPT data.

7.5 Discussion and outlook

In this Section, we discuss the limitations of the present generation tSZ power spectrum experiments to constrain multiple model parameters for the ICM pressure. We then make predictions for future experiments using simulated bandpower data, based on the same SPT baseline model but scaled to the expected sensitivities for those new tSZ surveys. Finally, we consider the impact of cosmological parameter uncertainties on our methodology of constraining the ICM pressure from current and future tSZ power measurements.

7.5.1 Need for better tSZ power spectrum measurements

In the course of our modification attempts for the ICM pressure profile from its universal shape and amplitude, we found several potential solutions that can bring the power spectrum amplitude in accordance with the SPT data, but none of these solutions are fully satisfactory in light of the current data or simulations. Evidently, more than one effect is responsible for the observed low tSZ power, such as a combination of steeper pressure profile in the cluster outskirts (and possibly its redshift evolution)

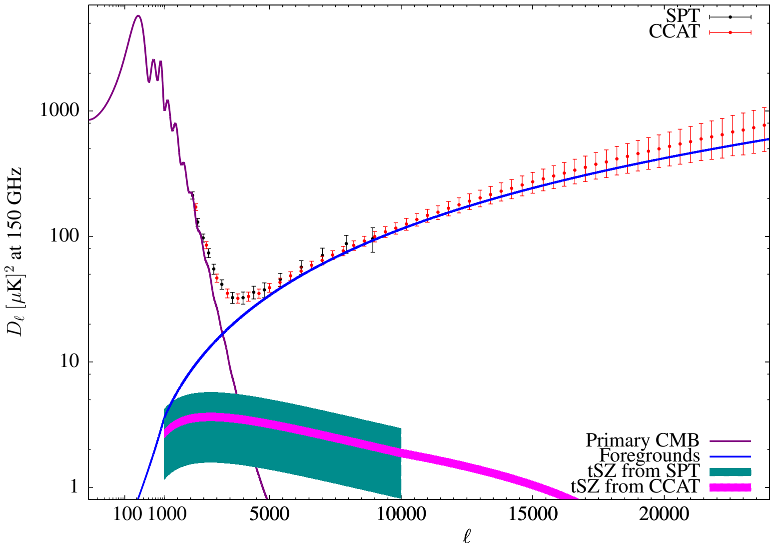

Figure 7.12: The current SPT bandpower measurements for the total CMB anisotropies (black data points, from R12), and the predicted bandpowers for CCAT (red points), shown with their respective $\pm 3\sigma$ errors. The thick blue line is the best fit SPT foreground model, and the purple line is the lensed CMB power spectrum. The cyan and magenta shaded regions represent the $\pm 3\sigma$ model uncertainties on the tSZ power spectrum from the SPT and CCAT, respectively. This figure illustrates how the improved sensitivity and angular resolution of CCAT can constrain both the amplitude and the shape of the tSZ power spectrum at the same time.

and a redshift-dependent baryonic fraction. Unfortunately, current ground- or space-based tSZ experiments do not have the requisite sensitivity and resolution to simultaneously constrain both the shape and the amplitude of the tSZ power spectrum, while separating it from the other multiple astrophysical components affecting the CMB bandpowers at 150 GHz.

As an illustration we pick up the two most prominent parameters featured in our analysis: the slope parameter β and the non-self-similar term α_z, to demonstrate this parameter degeneracy. Results are shown in Fig. 7.11 with colored contours, and marginalized values in red solid lines. When both parameters are varied simultaneously we obtain $\alpha_z = -1.42 \pm 0.75$ and $\beta = 4.71 \pm 0.71$. Clearly, none of these constraints are very informative, the non-self-similar evolution term is consistent with zero at 2σ. A similar case arises for any other parameter combination that can each individually attribute to the lower tSZ power measurement.

Upcoming SZ survey experiments, however, will have sufficient sensitivity and sky-coverage to place simultaneous constraints on the amplitude and the shape of the tSZ power spectrum. This will bring in a significant improvement in the parameter uncertainties (e.g., β or α_z), and help to break the current parameter degeneracies. Two such experiments are CCAT[1] and SPT-3G. In the following we use CCAT to demonstrate the improved parameter constraints from future SZ experiments.

7.5.2 Predictions for CCAT

CCAT is expected to be a 25 meter class submillimeter telescope that will perform high resolution microwave observations of the Southern sky (e.g., Woody et al. 2012). It will enable accurate measure-

---

[1] www.ccatobservatory.org

ments of the tSZ and kSZ power spectra in the multipole range between $2000 < \ell < 20000$. CCAT will be more sensitive than SPT in the location of tSZ power spectrum peak, and thus can better constrain the shape and the normalization of the spectrum. Figure 7.12 shows simulated CCAT bandpowers at 150 GHz from a 5 years survey, performed over 2000 deg^2 in approximately $10,000$ hours of integration. The nominal noise value at 150 GHz for this fiducial CCAT survey is 12 μK/beam. It is assumed that the wide frequency coverage of CCAT, in particular its 850 μm band, will effectively remove the dusty sub-mm galaxy confusion at lower frequencies.

We have used predicted CCAT bandpowers created using the baseline SPT model (C. Reichardt, priv. comm.). Assuming the same shapes for the foreground power spectra templates, the models were extrapolated to higher ℓ values to account for the factor two better resolution of CCAT. For our analysis we also only used the three auto-spectra frequencies (95, 150 and 220 GHz) as in SPT, and the three cross-spectra, since the higher frequencies mostly provide better constraints on the CIB spectra. The survey area was scaled from the SPT survey area used in R12 for improved statistical errors. Calibration and the beam uncertainties were included at 5% level. Although the increased frequency coverage of CCAT might enable a more precise modeling of the CIB background, we did not use any new foreground model for our predictions. The CCAT bandpowers thus reflect an experiment with better sensitivity and resolution but with our current knowledge of the microwave foreground templates.

As seen from Fig. 7.12, the combination of unprecedented sensitivity and angular resolution of CCAT can constrain the shape and normalization of the tSZ power spectrum accurately, sufficient to break parameter degeneracies. When varying simultaneously the evolution parameter α_z and the slope term β, we obtain $\alpha_z = -1.42 \pm 0.07$ and $\beta = 4.71 \pm 0.08$ (see Fig. 7.11, black contours). The marginalized errors on these two parameters thus show almost an order of magnitude improvement over the current SPT-based results. Similar tight constraints are obtained from other parameter combinations as well. This result is significant, since gaining an order of magnitude better accuracy through targeted observation of galaxy clusters, either in tSZ or in X-rays, will be very difficult, at least with the surveys planned for the coming decade. Through tSZ power spectrum measurements one can thus put the most stringent constraints on the mass and redshift scaling of the pressure profile in galaxy groups and clusters.

We can obtain very similar parameter constraints when using simulated bandpowers for the SPT-3G experiment. SPT-3G is the proposed third generation detector array on SPT (Bender et al. 2014), and will possibly have marginally better sky sensitivity than CCAT due to its longer survey duration. However, its resolution will be worse than the CCAT and may not resolve the shape of the tSZ power equally well. It may also be less efficient in the modeling and removal of foreground components due to a smaller number of submillimeter frequency channels. Nevertheless, as we use the same frequency bands and the same baseline model templates for computing the CCAT and SPT-3G results, the respective model constraints turn out to be very similar. Our results here are not intended as a comparison between experiments, rather as a general demonstration of how these upcoming experiments can help to model cluster astrophysics parameters precisely through the tSZ power spectrum.

7.5.3 Impact of cosmological uncertainties

The key assumption in our work had been that cosmological parameters like σ_8 and Ω_m are known to infinite accuracies, which is not realistic. In this final Section we discuss the issue of parameter priors instead of fixed values. The error in cosmology can be of two different types. First, there is uncertainty in the cosmological model parameter fits in any given data set (or a combination thereof), that is given by

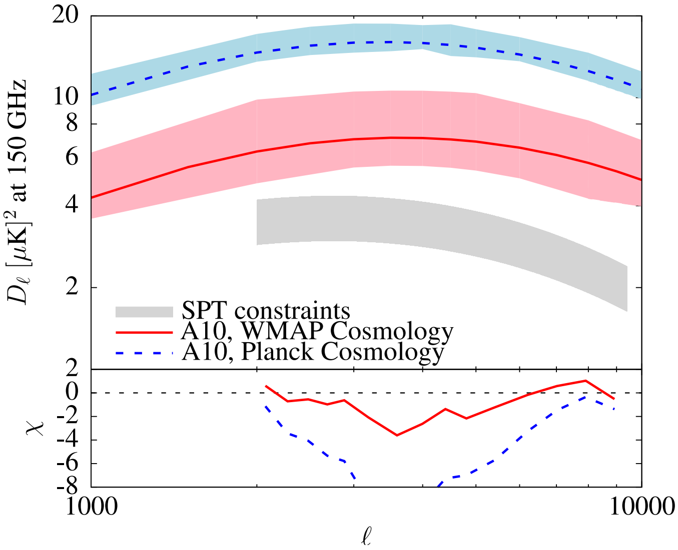

Figure 7.13: Prediction for the tSZ power spectrum amplitude from the A10 model, but using both the WMAP7 and *Planck* best fit cosmological model parameters. The higher predicted amplitude from the *Planck* cosmology comes primarily from the higher values of σ_8 and Ω_b. The shaded regions around the best-fit models are obtained using the respective parameters chains for these two parameters. The higher sensitivity of *Planck* clearly provides tighter constraints, although will require more drastic changes to the ICM pressure profile than we considered in this paper.

the parameter covariances. Second, there can be additional systematic uncertainties between the best fit values from different probes, like that between the current WMAP and *Planck* results based on the CMB analysis. In Fig. 7.13 we show the difference in amplitudes of the tSZ power spectrum, computed using the A10 model without modifications, from either the WMAP7 (Komatsu et al. 2011) or *Planck* (Planck Collaboration et al. 2015a) best fit cosmological parameters. The roughly factor 2 higher amplitude from *Planck* primarily comes from the higher values of σ_8 and Ω_b, since the tSZ amplitude roughly scales as $D_\ell^{\rm tSZ} \propto \sigma_8^{8.3}\Omega_b^{2.8}$ (e.g., R12). Consequently, choosing the present *Planck* cosmological parameters instead of the WMAP values would require all the pressure profile modification results presented in this paper to be even stronger.

It is not the purpose of this work to address the current tension between the WMAP and *Planck* cosmological parameters values. However, even if a concordance is reached, there will always remain the statistical uncertainties (and some unresolved systematics) in any specific cosmological model that will affect the pressure model predictions based on the tSZ power. This issue can be addressed through applying known parameter priors in the MCMC chain while computing the halo mass function and the volume element.

We set priors on the two cosmological parameters that affect the tSZ power spectrum most: Ω_m and σ_8. The priors are from the WMAP9 measurements (Hinshaw et al. 2013), $\Omega_m = 0.264 \pm 0.00973$ and $\sigma_8 = 0.81 \pm 0.014$, and we take care of the correlation between the parameters by using the actual parameter chains from WMAP9. We run our chains marginalizing over these two parameters, to constrain the redshift evolution parameter α_z, as well as the CIB amplitude parameters. We obtain $\alpha_z = -0.98 \pm 0.25$, $D_{3000}^{\rm P} = 7.69 \pm 0.24$, $D_{3000}^{\rm C} = 6.36 \pm 0.48$, whose values and errors are consistent with the ones obtained previously (see section 7.4.2). The use of *Planck* cosmological priors instead of WMAP9 provides a roughly factor 2 better constraints on these parameters, as can be seen from the

	SPT		CCAT	
Parameter	No priors	With priors	No priors	With priors
α_z	-0.73 ± 0.16	-0.98 ± 0.25	-0.73 ± 0.02	-0.79 ± 0.07
$D^{\rm P}_{3000}$	7.69 ± 0.27	7.69 ± 0.24	7.69 ± 0.01	7.54 ± 0.02
$D^{\rm C}_{3000}$	6.35 ± 0.49	6.36 ± 0.48	6.35 ± 0.04	6.26 ± 0.05

Table 7.2: Comparison of the redshift evolution parameter α_z (Eq. 7.11) and the CIB amplitudes with and without priors on the cosmological parameters. The adopted cosmology is from WMAP9 (Hinshaw et al. 2013), and we use the corresponding chains for cosmological parameters as priors, instead of fixed parameter values.

respective uncertainty intervals in Fig. 7.13. A similar conclusion was obtained by Hill & Pajer (2013), who obtained constraints for the outer-slope parameter β at $6\% - 8\%$ level, after marginalizing over cosmology, using a noise power model for *Planck* .

For the predicted CCAT bandpowers, we constrain the evolution parameter α_z in a similar way, with and without priors on the cosmological parameters. For the priors in this case we take a fiducial 1% uncertainty on σ_8 and $\Omega_{\rm m}$. This is assuming that by the time when CCAT will be in operation, the constraints on the cosmological parameters will be tighter thanks to some other experiments, like DES or *eROSITA*[2]. The results are displayed in Table 7.2. Clearly, switching from fixed cosmological values to realistic priors makes no major changes in the results, the same being true also for other pressure model parameters. The general conclusions presented in this work remain valid even when the parameter uncertainties are degraded by a factor $\sim 2 - 3$ while marginalizing over the cosmology.

7.6 Summary and conclusions

We have provided a systematic calibration of intracluster gas models against observational data for the tSZ power spectrum. In particular, we used the GNFW model for an analytical description of the gas pressure profile with empirically determined parameters from Arnaud et al. (2010, A10). We tested various extensions of this model against the SPT measured values of CMB bandpowers on arcminute scales (Reichardt et al. 2012, R12). We employed an MCMC based method following the baseline model of SPT to explore the parameter likelihoods.

Similar to earlier works, we found that the “universal” pressure model of A10 produces an amplitude of the tSZ power spectrum that is roughly a factor two higher than that measured by the SPT, ACT, and *Planck*. In addition to the A10 model itself, we tested the GNFW models fitted directly to the *Planck* and *Bolocam* data, which fail to account for the low tSZ power in the same way as the A10 model. The measurement errors in the *Planck* and *Bolocam* results are small compared to the current mismatch between model predictions and experimental results.

We considered three different modifications to the A10 pressure model: first, following a strictly self-similar evolution; second, applying a weakly self-similar evolution where only the amplitude of the pressure profile changes with redshift and mass; and third, having a non-self-similar evolution where both the amplitude and shape of $P(r)$ change with redshift. For the self-similar case, we only varied the cluster outer slope parameter, β, because it has the weakest observational constraint. The maximum likelihood value, which needed to reconcile model predictions with the SPT bandpowers, is $\beta = 6.3\pm0.2$. This is significantly higher than the most probable values measured by the *Bolocam* and *Planck* cluster

---

[2] http://www.mpe.mpg.de/eROSITA

tSZ observation. It also produces low-ℓ tSZ power that is inconsistent with the *Planck* tSZ bandpower measurements.

In a weak departure from self-similarity, we took the shape of the pressure profile as constant with redshift, but let the amplitude evolve differently than for self-similar models. We considered a power-law dependence of $(1 + z)$ or an additional exponent to $E(z)$ to model this evolution in the pressure scaling. Such a dependence on redshift could be due to an evolution of the gas mass fraction, f_{gas}, with redshift. We found that such models produce an excellent fit to the SPT data. However, an evolution of f_{gas} also affects the X-ray luminosity and would thereby produce some tension with the measured $L_X - T_X$ scaling relation of high-z clusters. Additionally, a strong decrease in f_{gas} with redshift appears to be inconsistent with some recent hydrodynamical simulations of cosmological halo samples.

In a final attempt to modify the GNFW pressure profile of A10, we let both its shape and amplitude vary with redshift in a strong departure from self-similarity. We considered a simple modeling for the redshift dependence of the pressure outer slope parameter β, as motivated by the recent simulations of random gas motions in the cluster outskirts. We found that in such cases the parameters are highly degenerate: neither the pressure slope at $z = 0$ nor its redshift evolution can be constrained accurately from the current tSZ power spectrum data.

The degeneracy between the model parameters is a general problem when using the currently available CMB bandpower measurements. For future CMB/tSZ experiments with better sensitivities, these degeneracies can be broken by measuring both the shape and the amplitude of the tSZ power spectrum to high accuracy. We used the simulated bandpower measurements for a CCAT 2000 deg^2 sky survey and found almost an order of magnitude improvement over the current model parameter uncertainties. This can, for example, enable simultaneous measurements of the outer slope parameter and the redshift evolution of f_{gas} to the level of a few percent.

We tested the impact of cosmological parameter uncertainties, in particular σ_8 and Ω_{m}, on our results. For the current SPT-data based results, we used the WMAP9 cosmological parameter uncertainties, directly using the chains for the relevant cosmological parameters as priors in our MCMC modeling. This degrades the uncertainties on the pressure profile parameters like β or α_z by roughly a factor two. For the CCAT fiducial survey, we reduced the cosmological errors by an additional 50%. This causes the ICM pressure model errors for CCAT to degrade roughly by a factor three, which will still be sufficient to place strong constraints on multiple model parameters. The large systematic difference between the current WMAP and *Planck* cosmological parameters remain an open question, although we note that adopting to the *Planck* cosmology will roughly cause a factor two higher prediction of the tSZ power amplitude, so will require more drastic modifications to the ICM pressure profile than we considered in this paper.

Acknowledgements

We acknowledge the help from Christian Reichardt and Daisuke Nagai in providing the simulated bandpower measurements for CCAT; Laurie Shaw for sharing his tSZ and kSZ power spectrum templates; and Jack Sayers for sharing the *Bolocam* cluster pressure profile fit results. The authors acknowledge financial support from the DFG (Deutsche Forschungsgemeinschaft), through the Transregio Programme TR33 “The Dark Universe”. FP acknowledges support from BMBF/DLR grant 50 OR 1117.

7.7 Appendix: Details of the R12 sky model

In this appendix, we summarize the models defined by Reichardt et al. (2012, R12) for the different components of the microwave sky diffuse emission. These are used as a baseline throughout the article while constraining parameters from the measured SPT bandpowers.

- *Lensed Primary CMB*. The lensed CMB is calculated with CAMB[3]. Gravitational lensing effects are important because they tend to increase the power of the CMB anisotropies on small angular scales, compared to the unlensed estimates.

- *Poisson infrared (IR) source power*. This term takes into account the shot-noise fluctuation power from randomly distributed microwave-emitting galaxies. It is given by

  $$D^{\mathrm{P}}_{\ell,\nu_1,\nu_2} = D^{\mathrm{P}}_{3000}\epsilon_{\nu_1\nu_2}\eta^{\alpha_\nu}_{\nu_1\nu_2}\left(\frac{\ell}{3000}\right)^2, \tag{7.18}$$

  where $D^{\mathrm{P}}_{3000} \equiv D^{\mathrm{P}}_{3000,\nu_0,\nu_0}$ is the amplitude of the Poisson power term for infrared galaxies at $\ell = 3000$ and at reference frequencies (ν_0): 97.9, 153.8, and 219.6 GHz. The coefficient

  $$\epsilon_{\nu_1,\nu_2} \equiv \frac{\frac{dB}{dT}|_{\nu_0}\frac{dB}{dT}|_{\nu_0}}{\frac{dB}{dT}|_{\nu_1}\frac{dB}{dT}|_{\nu_2}}, \tag{7.19}$$

  is the ratio of power in the $\nu_1 \otimes \nu_2$ cross-spectrum with respect to the $\nu_0 \otimes \nu_0$ auto-spectrum. $\eta_{\nu_1\nu_2} = (\nu_1\nu_2/\nu_0^2)$ is the ratio of the frequencies of the spectrum to the reference frequency. R12 obtained a best fit value for the spectral index of $\alpha_\nu = 3.45$. $B(T)$ is the CMB blackbody specific intensity.

- *Clustered IR source power*. Because the infrared galaxies trace the mass distribution, they are spatially correlated. This leads to a clustered term in the power spectrum of infrared galaxies given by

  $$D^{\mathrm{C}}_{\ell,\nu_1,\nu_2} = D^{\mathrm{C}}_{3000}\epsilon_{\nu_1\nu_2}\eta^{\alpha_c}_{\nu_1\nu_2}\left(\frac{\ell}{3000}\right)^{0.8}, \tag{7.20}$$

  where D^{C}_{3000} is defined as in the IR Poisson term, and $\alpha_c = 3.72$ is the best fit value taken from R12. Moreover, R12 adopted the power law model $\ell^{0.8}$ from Lyman-break correlated galaxies (Giavalisco et al. 1998; Scott & White 1999).

- *Radio source power*. The brightest point sources in the SPT maps coincide with known radio sources. To take this contribution into account, the Poisson radio term is given by

  $$D^{\mathrm{R}}_{\ell} = D^{\mathrm{R}}_{3000}\epsilon_{\nu_1\nu_2}\eta^{\alpha_{\mathrm{R}}}_{\nu_1\nu_2}\left(\frac{\ell}{3000}\right)^2, \tag{7.21}$$

  where D^{R}_{3000} is the amplitude of the radio Poisson power spectrum at $\ell = 3000$ with value $1.28 \pm 0.19\,\mu\mathrm{K}^2$ at 150 GHz. This value is based on the de Zotti et al. (2005) source count model. $\alpha_{\mathrm{R}} = -0.53$ is the mean spectral index from the Shirokoff et al. (2011) analysis.

---

[3] http://lambda.gsfc.nasa.gov/toolbox/tb_camb_form.cfm

- *Galactic cirrus.* An average Galactic cirrus contribution term is parametrized as

  $$D_\ell^{\rm cir} = D_{3000}^{{\rm cir},\nu_1,\nu_2}\left(\frac{\ell}{3000}\right)^{-1.2}. \tag{7.22}$$

  Following the cirrus treatment in Hall et al. (2010) and Keisler et al. (2011), R12 measured powers at $\ell = 3000$ to be 0.16, 0.21, and 2.19 μK^2 for 95, 150, and 220 GHz respectively.

- *kSZ power spectrum.* A homogeneous kSZ power spectrum is adopted, following the *cooling plus star-formation* (CSF) model of Shaw et al. (2012). This model is constructed by calibrating an analytic model with two hydrodynamical simulations. The CSF template predicts 1.6 μK^2 at $\ell = 3000$.

- *tSZ power spectrum.* R12 uses the analytical model of Shaw et al. (2010) as a template for the tSZ power, which relies on a physical cluster model coupled with halo formalism similar to the one presented in Section 7.2.1. Their cluster model mainly accounts for star formation, energy feedback (from supernovae and active galactic nuclei), and non-thermal pressure support. In our analysis, we replace the Shaw et al. model by a phenomenological description of the intracluster pressure profile that allow us for more freedom.

CHAPTER 8

Summary and future perspectives

In this work, different aspects of statistical studies based on the galaxy cluster population are explored. This work emphasizes the careful treatment of the detection capability and of the accuracy of physical characterisation of galaxy groups and clusters derived from present and future X-ray surveys. These considerations must be taken into account in order to achieve precision cosmology with future galaxy cluster surveys. Section 8.1 summarises the achieved results in this thesis work. Section 8.2 presents the expectations for the on-going and future galaxy cluster surveys.

8.1 Final summary of results

Chapter 4 is devoted to the future all-sky survey in X-ray band by the extended ROentgen Survey with an Imaging Telescope Array (*eROSITA*) mission. The goal of this work is to investigate wether the *eROSITA* mission will be able to deliver a pure galaxy cluster sample that helps to constrain the dark matter and dark energy content of the Universe. This is achieved by means of extensive and realistic *eROSITA* image simulations. These simulations are created with parameterised cluster morphologies. By using state-of-the-art source detection algorithms, a cluster selection function is calculated for a grid of cluster parameter values. It is found that the cluster selection function depends on various factors, the most important being the galaxy cluster morphology and the detection algorithm. The first result shows that wavelet-based detection algorithms are an excellent alternative to the current *eROSITA* detection tools, in particular regarding the detection of extended sources. It is also found that the cluster selection function highly depends on the cluster fluxes and sizes. This estimated cluster selection function is used to calculate the number of clusters to be detected by the *eROSITA* mission. The results give a cluster density of 5 clusters per square degree. Then, the *eROSITA* all-sky survey will allow the detection of $\sim 1.36 \times 10^5$ clusters. This cluster sample will have an additional contamination of $\sim 10\%$, which can be cleaned by multi-wavelength follow-up of the clusters. These findings confirm the theoretical predictions on the expected number of clusters detected by *eROSITA*, which will allow to put tight constraints on the dark matter and dark energy models. In summary, the work presented in this chapter shows that *eROSITA* will be able to detect $\sim 10^5$ galaxy clusters and that the detection and selection of clusters are not a trivial task, and need careful attention, for which possible solutions to improve on these matters are outlined.

Chapter 5 explores the detection feasibility of high-redshift ($z > 2.0$) galaxy groups ($M_{500} = 5 \times 10^{13}$ M$_\odot$) with the future Advanced Telescope for High ENergy Astrophysics (*ATHENA*) mission. This observatory is expected to have unprecedented sensitivity and a very good angular resolution. Such attributes will allow the study of the most energetic processes in the Universe up to high redshift. The capabilities of *ATHENA* on detecting high-redshift galaxy groups are measured through extensive and dedicated *ATHENA* image simulations. Current X-ray instruments have detected galaxy clusters up to $z \sim 1.5 - 2$, then our current knowledge about the thermo-dynamical state of high-redshift ($z > 2.0$) galaxy groups is very limited. To overcome this problem, different physically motivated models of X-ray emission are simulated and tested. Since the *ATHENA* mission is in study phase, distinct instrumental setups are also simulated. By using wavelet-based, state-of-the-art source detection and characterisation algorithms, the detection efficiency of high-redshift galaxy groups is determined. The results show that such galaxy groups can be detected and characterised by the future *ATHENA* mission as long as the instrumental setup possesses a large effective area (> 2.1 m^2 at 1.5 keV) and a good angular resolution over the entire field-of-view ($< 10''$). Moreover, it is shown that the detection of these high-redshift object by *ATHENA* will help to constrain structure formation and evolution models as well as feedback models in galaxy groups.

In Chapter 6, different aspects of wavelength-selection bias in high-redshift galaxy cluster samples are studied. The goal is to compare the physical properties of galaxy clusters in samples selected in different wavelengths, providing evidence that the astrophysics behind each selection technique can affect the content of the samples. For this research, 95 mid-infrared (MIR) clusters from the Spitzer Adaptation of the Red Sequence Cluster Survey (SpARCS) and 18 X-ray clusters from the *XMM-Newton* Large Scale Structure Survey (XMM-LSS) at $z > 0.8$ are used. In order to study MIR-selected clusters in X-rays, two techniques were developed: a Bayesian aperture photometry method and a faint source stacking procedure. Both methods implement a careful treatment of the Poisson and low-count statistics present in X-ray data. The analysis found that only 33% of the X-ray-selected clusters can be related to one of the MIR-selected clusters. The comparison of the properties of both distant cluster samples reveals a number of physical differences:

- At high redshifts, X-ray surveys select galaxy clusters that represent a dynamically relaxed subset of the massive cluster population, where the intra-cluster gas has settled and started to emit in X-ray. This is confirmed by their corresponding, compact MIR surface brightness distribution, meaning that these systems have a concentrated mass distribution.
- At high redshifts, MIR surveys identify clusters that exhibit a broader range of dynamical states and, therefore, offer a useful complement to X-ray studies. However, our comparison also identifies a population of low X-ray emission MIR clusters that represent non-virialized large-scale structures.

This study demonstrates that multi-wavelength studies of galaxy cluster populations are an effective method of revealing physical bias in cluster samples.

Chapter 7 shows a complementary method to study the intra-cluster properties. It consists in using an analytical prescription for the intra-cluster gas pressure distribution and constraining some of the model parameters by comparing the predicted power spectrum of the thermal Sunyaev-Zel'dovich effect (SZ) with measurements of the Cosmic Microwave Background (CMB). For this, the pressure of the intra-cluster gas is assumed to be spherically symmetric and its profile to follow the parametric GNFW model determined empirically by Arnaud et al. (2010). Different deviations from this model are tested and quantified, through a Markov chain Monte Carlo based method, against South Pole Telescope (SPT) measurements of the CMB. The results show that a steeper pressure profile in the cluster outskirts or an evolving gas mass fraction have mild-to-severe conflicts with experimental data. Moreover, it is found that varying more than one parameter in the pressure model leads to strong degeneracies that cannot be broken with current observational constraints. By using simulated bandpowers for future thermal SZ survey experiments, in particular, a possible 2000 $\deg^2$ CCAT survey, we show that such observations can provide almost an order of magnitude better precision on the same model parameters. These new instruments will allow us to break the current parameter degeneracies and place simultaneous constraints on, e.g. the gas pressure profile and its redshift evolution.

8.2 Perspectives on current and future galaxy cluster surveys

Currently, there are quite a number of finished and on-going galaxy cluster surveys across the electromagnetic spectrum: from sub-millimetre wavelengths, optical and infrared bands to X-rays. There have been a number of studies on the calibration of cluster scaling relations between different observables at distinct wavebands. Optical spectroscopic and photometric observations are still the best way to confirm and extract redshift information of clusters detected in X-rays and through the SZ-effect. Therefore, galaxy cluster studies make use of multi-wavelength data. However, the important problem of observational bias still persists and is usually treated crudely in the analysis of cluster surveys.

Deep surveys can help to improve the accuracy of the cluster selection function. Since such surveys detect also a large number of low-mass systems, they are useful for a better understanding of the non-gravitational processes in galaxy groups and clusters. On the other hand, wide-angle surveys are useful to obtain larger samples of clusters, with medium to high masses, depending on the depth and sensitivity of the survey. Given the large number of systems in these surveys, it is *easier* to model their selection function, and thereby place precise cosmological constraints by means of the cluster mass function.

More and more cluster surveys have a multi-wavelength coverage, making the future of low-bias cluster samples very promising. Large SZ experiments, such as the SPT, the Atacama Cosmology Telescope (ACT) and the *Planck* mission have already produced large cluster catalogues, and some comparison with optical and X-ray data has been done. In the optical bands, several on-going surveys promise a great wealth of cluster data: GAMA, VIPERS, the KIlo-Degree Survey (KIDS), the VST ATLAS and the Dark Energy Survey (DES). In X-rays, the XXL survey is delivering the first results of a dedicated multi-follow up programme.

Although these surveys have their own strengths and challenges, the ultimate goal is to combine them and use their synergies to get a sufficiently complete view of the cluster populations and their place in the hierarchy of cosmic large-scale structure formation. Our goal is to have a better understanding of the observational bias in cluster samples before the final *eROSITA* all-sky survey catalogue is released. Only if we succeed with this challenge, the large *eROSITA* galaxy cluster sample can be reliably used for competitive, precision cosmological constraints.

Bibliography

Abell, G. O. (1958), ApJS, 3, 211

Abell, G. O. et al. (1989), ApJS, 70, 1–138

Aird, J. et al. (2013), arXiv: 1306.2325

Allen, S. W. et al. (2004), MNRAS, 353, 457–467, eprint: astro-ph/0405340

Allen, S. W. et al. (2008), MNRAS, 383, 879–896, arXiv: 0706.0033

Allen, S. W. et al. (2011), ARA&A, 49, 409–470, arXiv: 1103.4829

Anderson, M. E. et al. (2013), ApJ, 762, 106, arXiv: 1211.5140

Anderson, M. E. et al. (2015), MNRAS, 449, 3806–3826, arXiv: 1409.6965

Arnaud, K. A. (1996), *Astronomical Data Analysis Software and Systems V*, ed. by G. H. Jacoby & J. Barnes, vol. 101, Astronomical Society of the Pacific Conference Series 17

Arnaud, M. et al. (2005), A&A, 441, 893–903, eprint: astro-ph/0502210

——— (2007), A&A, 474, L37–L40, arXiv: 0709.1561

Arnaud, M. et al. (2010), A&A, 517, A92, arXiv: 0910.1234

Bacchi, M. et al. (2003), A&A, 400, 465–476, eprint: astro-ph/0301206

Baganoff, F. K. et al. (2001), Nature, 413, 45–48, eprint: astro-ph/0109367

Baldi, A. et al. (2002), ApJ, 564, 190–195, eprint: astro-ph/0108514

Barret, D. et al. (2013), arXiv: 1308.6784

Battaglia, N. et al. (2010), ApJ, 725, 91–99, arXiv: 1003.4256

Battaglia, N. et al. (2012a), ApJ, 758, 74, arXiv: 1109.3709

——— (2012b), ApJ, 758, 75, arXiv: 1109.3711

——— (2013), ApJ, 777, 123, arXiv: 1209.4082

Bavdaz, M. et al. (2010), X-Ray Optics and Instrumentation, 2010. Special Issue on X-Ray Focusing: Techniques and Applications, id.295095, 2010, 9

Bayliss, M. B. et al. (2014), ApJ, 794, 12, arXiv: 1307.2903

Beijersbergen, M. et al. (2004), *UV and Gamma-Ray Space Telescope Systems*, ed. by G. Hasinger & M. J. Turner, vol. 5488, Society of Photo-Optical Instrumentation Engineers (SPIE) Conference Series 868–874

Bender, A. N. et al. (2014), *Society of Photo-Optical Instrumentation Engineers (SPIE) Conference Series*, vol. 9153, Society of Photo-Optical Instrumentation Engineers (SPIE) Conference Series 1, arXiv: 1407.3161

Bergé, J. et al. (2008), MNRAS, 385, 695–707, arXiv: 0712.3293

Bertin, E. & S. Arnouts (1996), A&AS, 117, 393–404

Bhattacharya, S. et al. (2011), ApJ, 732, 122, arXiv: 1005.2239

Bhattacharya, S. et al. (2012), ApJ, 760, 5, arXiv: 1203.6368

Birkinshaw, M. (1991), *Physical Cosmology*, ed. by A. Blanchard et al. 177

Bocquet, S. et al. (2015), arXiv: 1502.07357
Bode, P. et al. (2009), ApJ, 700, 989–999, arXiv: 0905.3748
Böhringer, H. & N. Werner (2010), A&A Rev., 18, 127–196
Böhringer, H. et al. (2000), ApJS, 129, 435–474, eprint: astro-ph/0003219
Böhringer, H. et al. (2001), A&A, 369, 826–850, eprint: astro-ph/0012266
Böhringer, H. et al. (2012), A&A, 539, A120, arXiv: 1112.5035
Böhringer, H. et al. (2014), ArXiv e-prints, arXiv: 1403.5886
Bonafede, A. et al. (2014), ApJ, 785, 1, arXiv: 1402.1492
Borgani, S. et al. (2004), MNRAS, 348, 1078–1096, eprint: astro-ph/0310794
Borkowski, K. J. et al. (2006), ApJ, 652, 1259–1267, eprint: astro-ph/0608297
Bouwens, R. J. et al. (2009), ApJ, 705, 936–961, arXiv: 0909.4074
Brandt, W. N. et al. (2001), AJ, 122, 2810–2832, eprint: astro-ph/0108404
Branduardi-Raymont, G. et al. (2013), arXiv: 1306.2332
Bryan, G. L. & M. L. Norman (1998), ApJ, 495, 80–99, eprint: astro-ph/9710107
Bullock, J. S. et al. (2001), MNRAS, 321, 559–575, eprint: astro-ph/9908159
Burenin, R. A. et al. (2007), ApJS, 172, 561–582, eprint: astro-ph/0610739
Byram, E. T. et al. (1966), Science, 152, 66–71
Campana, S. et al. (1999), ApJ, 524, 423–433, eprint: astro-ph/9904375
Canning, R. E. et al. (2015), arXiv: 1505.05790
Cappi, M. et al. (2013), arXiv: 1306.2330
Cash, W. (1979), ApJ, 228, 939–947
Castander, F. J. et al. (1995), Nature, 377, 39–41
Cavaliere, A. & R. Fusco-Femiano (1976), A&A, 49, 137–144
Chiappetti, L. et al. (2013), MNRAS, 429, 1652–1673
Clerc, N. et al. (2012a), MNRAS, 423, 3545–3560, arXiv: 1109.4440
Clerc, N. et al. (2012b), MNRAS, 423, 3561–3583, arXiv: 1109.4441
Clowe, D. et al. (2006), ApJLett, 648, L109–L113, eprint: astro-ph/0608407
Collins, C. A. et al. (1997), ApJLett, 479, L117–L120, eprint: astro-ph/9701143
Croston, J. H. et al. (2013), arXiv: 1306.2323
Dai, X. et al. (2007), ApJ, 658, 917–928, eprint: astro-ph/0606002
Damiani, F. et al. (1997), ApJ, 483, 370–389
Davis, M. & P. J. Peebles (1983), ApJ, 267, 465–482
de Zotti, G. et al. (2005), A&A, 431, 893–903, eprint: astro-ph/0410709
Decourchelle, A. et al. (2013), arXiv: 1306.2335
Dodelson, S. (2003), Academic Press, ISBN: 9780122191411, Academic Press
Donahue, M. et al. (2002), ApJ, 569, 689–719, eprint: astro-ph/0112529
Dovciak, M. et al. (2013), arXiv: 1306.2331
Driver, S. P. et al. (2011), MNRAS, 413, 971–995, arXiv: 1009.0614
Dunkley, J. et al. (2009), ApJS, 180, 306–329, arXiv: 0803.0586
Dunkley, J. et al. (2011), ApJ, 739, 52, arXiv: 1009.0866
Ebeling, H. et al. (1998), MNRAS, 301, 881–914, eprint: astro-ph/9812394
Ebeling, H. et al. (2000), ApJ, 534, 133–145, eprint: astro-ph/9905321
Ebeling, H. et al. (2001), ApJ, 553, 668–676, eprint: astro-ph/0009101
Eckert, D. et al. (2012), A&A, 541, A57, arXiv: 1111.0020
Eckmiller, H. J. et al. (2011), A&A, 535, A105, arXiv: 1109.6498
Eddington, A. S. (1913), MNRAS, 74, 5

Edge, A. C. (2004), Clusters of Galaxies: Probes of Cosmological Structure and Galaxy Evolution, 58, eprint: astro-ph/0307150

Efstathiou, G. & M. Migliaccio (2012), MNRAS, 423, 2492–2497, arXiv: 1106.3208

Elvis, M. et al. (2009), ApJS, 184, 158–171, arXiv: 0903.2062 `[astro-ph.CO]`

Erfanianfar, G. et al. (2013), ApJ, 765, 117, arXiv: 1302.5114

Ettori, S. et al. (2013), arXiv: 1306.2322

Fabian, A. C. (1994), ARA&A, 32, 277–318

Fabian, A. C. et al. (2000), MNRAS, 318, L65–L68, eprint: astro-ph/0007456

Fakhouri, O. et al. (2010), MNRAS, 406, 2267–2278, arXiv: 1001.2304

Fassbender, R. et al. (2011), New Journal of Physics, 13,12 125014, arXiv: 1111.0009 `[astro-ph.CO]`

Ferrarese, L. & D. Merritt (2000), ApJLett, 539, L9–L12, eprint: astro-ph/0006053

Finoguenov, A. et al. (2007), ApJS, 172, 182–195, eprint: astro-ph/0612360

Finoguenov, A. et al. (2010), MNRAS, 403, 2063–2076, arXiv: 0912.0039

Freeman, P. E. et al. (2002), ApJS, 138, 185–218, eprint: astro-ph/0108429

Fritz, G. et al. (1971), ApJLett, 164, L81

Fruscione, A. et al. (2006), *Society of Photo-Optical Instrumentation Engineers (SPIE) Conference Series*, vol. 6270, Society of Photo-Optical Instrumentation Engineers (SPIE) Conference Series 1

Galametz, A. et al. (2009), ApJ, 694, 1309–1316, arXiv: 0901.1109

Georgakakis, A. et al. (2013), arXiv: 1306.2328

George, E. M. et al. (2014), arXiv: 1408.3161

Ghizzardi, S. (2001), (Internal report)

Giacconi, R. et al. (1962), Physical Review Letters, 9, 439–443

Giacconi, R. et al. (2002), ApJS, 139, 369–410

Giacintucci, S. et al. (2011), ApJ, 732, 95, arXiv: 1103.1364

Giavalisco, M. et al. (1998), ApJ, 503, 543–552, eprint: astro-ph/9802318

Gierliński, M. et al. (2008), Nature, 455, 369–371

Gilli, R. et al. (2007), A&A, 463, 79–96, eprint: astro-ph/0610939

Gilmour, R. et al. (2009), MNRAS, 392, 1509–1531, arXiv: 0901.2810

Giodini, S. et al. (2013), Space Sci. Rev., 177, 247–282, arXiv: 1305.3286

Gioia, I. M. et al. (2001), ApJLett, 553, L105–L108, eprint: astro-ph/0102332

Gitti, M. et al. (2012), Advances in Astronomy, 2012, 6, arXiv: 1109.3334

Gladders, M. D. & H. K. Yee (2000), AJ, 120, 2148–2162, eprint: astro-ph/0004092

Gobat, R. et al. (2011), A&A, 526, A133, arXiv: 1011.1837

Green, P. J. et al. (2003), Astronomische Nachrichten, 324, 93–96

Guth, A. H. (1981), Phys. Rev. D, 23, 347–356

Guzzo, L. & The Vipers Team (2013), The Messenger, 151, 41–46, arXiv: 1303.3930 `[astro-ph.CO]`

Gwyn, S. D. (2012), AJ, 143, 38

Hall, N. R. et al. (2010), ApJ, 718, 632–646, arXiv: 0912.4315

Hasinger, G. (2004), Nuclear Physics B Proceedings Supplements, 132, 86–96, eprint: astro-ph/0310804

Hasinger, G. et al. (2005), A&A, 441, 417–434, eprint: astro-ph/0506118

Hasinger, G. et al. (2007), ApJS, 172, 29–37, eprint: astro-ph/0612311

Hayashi, M. et al. (2011), MNRAS, 415, 2670–2687, arXiv: 1104.2121

Henry, J. P. et al. (2001), ApJLett, 553, L109–L113

Hernández-Monteagudo, C. et al. (2006), ApJLett, 652, L1–L4, eprint: astro-ph/0606172

Hill, J. C. & E. Pajer (2013), Phys. Rev. D, 88,6 063526, arXiv: 1303.4726 `[astro-ph.CO]`

Hilton, M. et al. (2012), MNRAS, 424, 2086–2096, arXiv: 1205.5570

Hinshaw, G. et al. (2013), ApJS, 208, 19, arXiv: 1212.5226

Horner, D. J. et al. (2008), ApJS, 176, 374–413
Hu, W. & A. V. Kravtsov (2003), ApJ, 584, 702–715, eprint: astro-ph/0203169
Jenkins, A. et al. (1998), ApJ, 499, 20–40, eprint: astro-ph/9709010
Jenkins, A. et al. (2001), MNRAS, 321, 372–384, eprint: astro-ph/0005260
Jonker, P. et al. (2013), arXiv: 1306.2336
Kaastra, J. et al. (2013), arXiv: 1306.2324
Kaiser, N. (1986), MNRAS, 222, 323–345
Keisler, R. et al. (2011), ApJ, 743, 28, arXiv: 1105.3182
Kellogg, E. et al. (1975), ApJ, 199, 299–306
King, I. (1962), AJ, 67, 471
Kolokotronis, V. et al. (2006), MNRAS, 366, 163–170, eprint: astro-ph/0503409
Komatsu, E. & T. Kitayama (1999), ApJLett, 526, L1–L4, eprint: astro-ph/9908087
Komatsu, E. & U. Seljak (2002), MNRAS, 336, 1256–1270, eprint: astro-ph/0205468
Komatsu, E. et al. (2011), ApJS, 192, 18, arXiv: 1001.4538
Kron, R. G. (1980), ApJS, 43, 305–325
Laird, E. S. et al. (2009), ApJS, 180, 102–116, arXiv: 0809.1349
Larsson, J. et al. (2011), Nature, 474, 484–486, arXiv: 1106.2300 `[astro-ph.SR]`
Lau, E. T. et al. (2009), ApJ, 705, 1129–1138, arXiv: 0903.4895
Lehmann, I. et al. (2001), A&A, 371, 833–857, eprint: astro-ph/0103368
Lehmer, B. D. et al. (2005), ApJS, 161, 21–40, eprint: astro-ph/0506607
Lehmer, B. D. et al. (2007), ApJ, 657, 681–699, eprint: astro-ph/0612003
Linde, A. D. (1982), Physics Letters B, 108, 389–393
Liske, J. et al. (2015), MNRAS, 452, 2087–2126, arXiv: 1506.08222
Lloyd-Davies, E. J. et al. (2011), MNRAS, 418, 14–53, arXiv: 1010.0677
Lonsdale, C. J. et al. (2003), PASP, 115, 897–927, eprint: astro-ph/0305375
Lovisari, L. et al. (2015), A&A, 573, A118, arXiv: 1409.3845
Lueker, M. et al. (2010), ApJ, 719, 1045–1066, arXiv: 0912.4317
Malmquist, K. (1920), Lund Medd. Ser. II, 22, 1–39
Mann, A. W. & H. Ebeling (2012), MNRAS, 420, 2120–2138, arXiv: 1111.2396
Mantz, A. B. et al. (2014), ApJ, 794, 157, arXiv: 1401.2087
Mantz, A. et al. (2010a), MNRAS, 406, 1759–1772, arXiv: 0909.3098
Mantz, A. et al. (2010b), MNRAS, 406, 1773–1795, arXiv: 0909.3099
Marconi, A. & L. K. Hunt (2003), ApJLett, 589, L21–L24, eprint: astro-ph/0304274
Martini, P. et al. (2013), ApJ, 768, 1, arXiv: 1302.6253
Mason, K. O. et al. (2000), MNRAS, 311, 456–484
Maughan, B. J. et al. (2012), MNRAS, 421, 1583–1602, arXiv: 1108.1200
McCarthy, I. G. et al. (2014), MNRAS, 440, 3645–3657, arXiv: 1312.5341
McNamara, B. R. & P. E. Nulsen (2007), ARA&A, 45, 117–175, arXiv: 0709.2152
Meekins, J. F. et al. (1971), Nature, 231, 107–108
Merloni, A. et al. (2004), MNRAS, 354, L37–L42, eprint: astro-ph/0409187
Merloni, A. et al. (2012), ArXiv e-prints, arXiv: 1209.3114 `[astro-ph.HE]`
Moretti, A. et al. (2003), ApJ, 588, 696–703, eprint: astro-ph/0301555
Motch, C. et al. (2013), arXiv: 1306.2334
Murray, S. S. et al. (2005), ApJS, 161, 1–8, eprint: astro-ph/0504084
Muzzin, A. V. (2008), PhD thesis: University of Toronto, Canada
Nagai, D. et al. (2007), ApJ, 668, 1–14, eprint: astro-ph/0703661
Nandra, K. et al. (2002), ApJ, 576, 625–639, eprint: astro-ph/0205215

Nandra, K. et al. (2013), arXiv: 1306.2307
Nastasi, A. et al. (2011), A&A, 532, L6, arXiv: 1106.5784
Navarro, J. F. et al. (1995), MNRAS, 275, 720–740, eprint: astro-ph/9408069
——— (1997), ApJ, 490, 493–508, eprint: astro-ph/9611107
Nelson, K. et al. (2014), ApJ, 792, 25, arXiv: 1404.4636
Pacaud, F. et al. (2006), MNRAS, 372, 578–590, eprint: astro-ph/0607177
Pacaud, F. et al. (2015), ArXiv e-prints, arXiv: 1512.04264
Panzera, M. R. et al. (2003), A&A, 399, 351–364, eprint: astro-ph/0211201
Park, T. et al. (2006), ApJ, 652, 610–628, eprint: astro-ph/0606247
Pavlinsky, M. et al. (2014), *Society of Photo-Optical Instrumentation Engineers (SPIE) Conference Series*, vol. 9144, Society of Photo-Optical Instrumentation Engineers (SPIE) Conference Series 1
Peacock, J. A. (1999), Cambridge: Cambridge Univ., URL: https://cds.cern.ch/record/879495
Perlman, E. S. et al. (2002), ApJS, 140, 265–301, eprint: astro-ph/0112190
Peterson, J. R. et al. (2001), A&A, 365, L104–L109, eprint: astro-ph/0010658
Pierre, M. et al. (2004), JCAP, 9, 11, eprint: astro-ph/0305191
Pierre, M. et al. (2015), ArXiv e-prints, arXiv: 1512.04317
Piffaretti, R. & R. Valdarnini (2008), A&A, 491, 71–87, arXiv: 0808.1111
Pillepich, A. et al. (2012), MNRAS, 422, 44–69, arXiv: 1111.6587
Planck Collaboration et al. (2013a), A&A, 550, A131, arXiv: 1207.4061
——— (2013b), A&A, 557, A52, arXiv: 1212.4131
Planck Collaboration et al. (2014a), A&A, 571, A12, arXiv: 1303.5072
——— (2014b), A&A, 571, A20, arXiv: 1303.5080
——— (2014c), A&A, 571, A21, arXiv: 1303.5081
Planck Collaboration et al. (2015a), arXiv: 1502.01589
Planck Collaboration et al. (2015b), ArXiv e-prints, arXiv: 1504.03339
Pointecouteau, E. et al. (2005), A&A, 435, 1–7, eprint: astro-ph/0501635
Pointecouteau, E. et al. (2013), arXiv: 1306.2319
Pratt, G. W. et al. (2009), A&A, 498, 361–378, arXiv: 0809.3784
Press, W. H. & P. Schechter (1974), ApJ, 187, 425–438
Press, W. H. et al. (1992)
Puccetti, S. et al. (2006), A&A, 457, 501–515, eprint: astro-ph/0607107
Ramos-Ceja, M. E. et al. (2015), A&A, 583, A111, arXiv: 1412.6023
Rau, A. (2013), (Internal report)
——— (2014), (Internal report)
Rau, A. et al. (2013), arXiv: 1308.6785
Read, A. M. & T. J. Ponman (2003), A&A, 409, 395–410, eprint: astro-ph/0304147
Reed, D. S. et al. (2007), MNRAS, 374, 2–15, eprint: astro-ph/0607150
Reed, D. et al. (2003), MNRAS, 346, 565–572, eprint: astro-ph/0301270
Refregier, A. et al. (2010), arXiv: 1001.0061
Reichardt, C. L. et al. (2012), ApJ, 755, 70, arXiv: 1111.0932
Reichert, A. et al. (2011), A&A, 535, A4, arXiv: 1109.3708
Reiprich, T. H. & H. Böhringer (2002), ApJ, 567, 716–740, eprint: astro-ph/0111285
Robotham, A. S. et al. (2011), MNRAS, 416, 2640–2668, arXiv: 1106.1994
Romer, A. K. et al. (2000), ApJS, 126, 209–269, eprint: astro-ph/9907401
Romer, A. K. et al. (2001), ApJ, 547, 594–608
Rosati, P. et al. (1995), ApJLett, 445, L11–L14, eprint: astro-ph/9503064
Rosati, P. et al. (2002), ARA&A, 40, 539–577, eprint: astro-ph/0209035

Rosati, P. et al. (2009), A&A, 508, 583–591, arXiv: 0910.1716
Rozo, E. et al. (2014), MNRAS, 438, 78–96, arXiv: 1204.6305
Rubiño-Martín, J. A. & R. A. Sunyaev (2003), MNRAS, 344, 1155–1174, eprint: astro-ph/0211430
Ruderman, J. T. & H. Ebeling (2005), ApJLett, 623, L81–L84, eprint: astro-ph/0503204
Rykoff, E. S. et al. (2008), ApJ, 675, 1106–1124, arXiv: 0709.1158
Rykoff, E. S. et al. (2014), ApJ, 785, 104, arXiv: 1303.3562
Sadibekova, T. et al. (2014), A&A, 571, A87, arXiv: 1403.4100
Sarazin, C. L. (1986), Reviews of Modern Physics, 58, 1–115
Sayers, J. et al. (2013a), ApJ, 778, 52, arXiv: 1312.3680
Sayers, J. et al. (2013b), ApJ, 768, 177, arXiv: 1211.1632
Schneider, P. (2006), Springer
Schneider, P. et al. (1993), Astronomische Nachrichten, 314, 314
Sciortino, S. et al. (2013), arXiv: 1306.2333
Scott, D. & M. White (1999), A&A, 346, 1–6, eprint: astro-ph/9808003
Sehgal, N. et al. (2010), ApJ, 709, 920–936, arXiv: 0908.0540
Sekiguchi, K. & et al. (2004), *Astrophysics and Space Science Library*, ed. by M. Plionis, vol. 301, Astrophysics and Space Science Library 169
Seward, F. D. & P. A. Charles (2010)
Shaw, L. D. et al. (2010), ApJ, 725, 1452–1465, arXiv: 1006.1945
Shaw, L. D. et al. (2012), ApJ, 756, 15, arXiv: 1109.0553
Sheth, R. K. & G. Tormen (1999), MNRAS, 308, 119–126, eprint: astro-ph/9901122
Shi, X. & E. Komatsu (2014), MNRAS, 442, 521–532, arXiv: 1401.7657
Shirokoff, E. et al. (2011), ApJ, 736, 61, arXiv: 1012.4788
Sievers, J. L. et al. (2013), JCAP, 10, 60, arXiv: 1301.0824
Slezak, E. et al. (1994), AJ, 108, 1996–2008
Springel, V. et al. (2005), Nature, 435, 629–636, eprint: astro-ph/0504097
Starck, J.-L. & F. Murtagh (2006)
Starck, J.-L. & M. Pierre (1998), A&AS, 128, 397–407, eprint: astro-ph/9707305
Starck, J.-L. et al. (1998)
Starikova, S. et al. (2014), ApJ, 786, 125
Suárez-Velásquez, I. F. et al. (2013), MNRAS, 431, 342–348, arXiv: 1301.6546
Šuhada, R. et al. (2012), A&A, 537, A39, arXiv: 1111.0141 `[astro-ph.CO]`
Sun, M. et al. (2009), ApJ, 693, 1142–1172, arXiv: 0805.2320
Sun, M. et al. (2011), ApJLett, 727, L49, arXiv: 1012.0312
Sunyaev, R. A. & Y. B. Zel’dovich (1972), CoASP, 4, 173
——— (1980), MNRAS, 190, 413–420
Takey, A. et al. (2011), A&A, 534, A120, arXiv: 1109.1743 `[astro-ph.CO]`
Tinker, J. et al. (2008), ApJ, 688, 709–728, arXiv: 0803.2706
Trac, H. et al. (2011), ApJ, 727, 94, arXiv: 1006.2828
Truemper, J. (1993), Science, 260, 1769–1771
Trümper, J. E. & G. Hasinger (2008)
Valtchanov, I. et al. (2001), A&A, 370, 689–706, eprint: astro-ph/0102297
van Dyk, D. A. et al. (2001), ApJ, 548, 224–243, eprint: astro-ph/0008170
Vikhlinin, A. et al. (1997), ApJLett, 474, L7–L10, eprint: astro-ph/9610151
Vikhlinin, A. et al. (1998), ApJ, 502, 558–581, eprint: astro-ph/9803099
Vikhlinin, A. et al. (2006), ApJ, 640, 691–709, eprint: astro-ph/0507092
Vikhlinin, A. et al. (2009a), ApJ, 692, 1033–1059, arXiv: 0805.2207

Vikhlinin, A. et al. (2009b), ApJ, 692, 1060–1074, arXiv: 0812.2720
Voit, G. M. (2005), AdSpR, 36, 701–705
von der Linden, A. et al. (2014), MNRAS, 439, 2–27, arXiv: 1208.0597
Warren, M. S. et al. (2006), ApJ, 646, 881–885, eprint: astro-ph/0506395
Werner, N. et al. (2008), A&A, 482, L29–L33, arXiv: 0803.2525
Willis, J. P. et al. (2013), MNRAS, 430, 134–156, arXiv: 1212.4185
Wilson, M. J. et al. (2012), Phys. Rev. D, 86,12 122005, arXiv: 1203.6633
Wolter, H. (1952), Annalen der Physik, 445, 94–114
Woody, D. et al. (2012), *Society of Photo-Optical Instrumentation Engineers (SPIE) Conference Series*, vol. 8444, Society of Photo-Optical Instrumentation Engineers (SPIE) Conference Series 2
Wylezalek, D. et al. (2013), ApJ, 769, 79, arXiv: 1304.0770
Yang, Y. et al. (2004), AJ, 128, 1501–1523, eprint: astro-ph/0409087
Zinn, P.-C. et al. (2012), A&A, 547, A50, arXiv: 1210.4188
Zwicky, F. (1933), Helvetica Physica Acta, 6, 110–127
——— (1937), ApJ, 86, 217

List of Figures

List of Tables

Acknowledgements

It has been a long way to achieving two of my major dreams: doing a Ph.D. in Astrophysics and live in Deutschland. Although it has been very hard to be far away from home, I have been very lucky to have the support of many wonderful people. I hope I do not forget to mention anybody, apologies if this happens.

My deepest gratitude goes to my adviser, Florian Pacaud, for trusting me this Ph.D. work and giving me big responsibilities in so many different projects. Thanks Florian for your professional guidance, for sharing tons of knowledge and ideas that made my research experience very rewarding. Thanks for offering me the opportunity to get involved in so many scientific collaborations (XXL, *eROSITA* and *ATHENA*), and to encourage me to present my work in different meetings, which allowed me to meet many great scientists from around the world.

I would like to express my sincere acknowledgement to my supervisor Frank Bertoldi for giving me the opportunity of being part of his group and financially supporting me during this thesis. Thanks a lot for all the advice on my multiple presentations and financial applications, and for giving me the freedom in the kind of research I have pursued. I am also very grateful to my second supervisor Thomas Reiprich for *adopting* me as part of his research group, for entrusting me the *ATHENA* work regarding the detection of high redshift galaxy groups, and for all the advice, help and patience.

I would like to thank Kaustuv Basu, for our close collaboration and for the enlightening discussions we had in the course of our work.

This thesis could not be possible to finish without the help and close collaboration with many people: Nicolas Clerc, thanks for the synthetic *eROSITA* simulations; Georg Lamer thanks for all the back and forth emails regarding the use of the eSASS detection pipeline; Herman Brunner thanks for helping in the installation of eSASS; Jon Willis for giving me the opportunity of closely collaborate in the multi-wavelength analysis of high redshift galaxy groups. Thanks to Florian, Martin, Jens, Ana, Franz, Miguel, Frank, Gerrit, Bharad, Eric and Kaustuv for the proofreads and useful suggestions for this manuscript.

I want to thank the International Max-Planck Research School for Astronomy and Astrophysics for sponsoring my travels to different consortium meetings and international conferences. Special thanks to Manolis Angelakis and Simone Pott for their support and help. I also want to thank the Bonn-Cologne Graduate School for supporting financially some other scientific meetings I have attended. My sincere gratitude to Christina Stein-Schmitz for all the help in the bureaucracy as well for her moral support.

I also want to thank all current and former members of the SZ research group: Frank, Kaustuv, Florian, Martin, Matthias, Sandra, Aarti, Jens and Ana; and the same for the Dark Energy group: Thomas,

Lorenzo, Gerrit, Katharina, Alberto, Bharad and Yuying; for their experience and help in different science aspects. I did not only learn great astrophysics with all you but also made excellent friends. The same goes for my (former) officemates: Milan and Benjamin, for putting up with me and for the nice work atmosphere.

Special thanks to all those who already left AIfA/Bonn, but made my life at and outside the institute so fun: Franz, Ines, Karl and Elli, I am very glad to have you as my friends and grateful for your support. Milan and Agustina for those excellent meals we have shared. Matthias and Snezhi for the nice parties. Felipe, Andrés and Brenda for all the fun chats we used to have. I miss you all!

Last but not least. Mis más sinceros agradecimientos a ti Miguel, la vida de Ph.D. de este lado del charco contigo ha sido una de las mejores experiencias en mi vida. Gracias por aguantarme todos los días, darme tantos consejos y rica comida. Ma' y Pa', gracias por tanto amor, apoyo y consejos que me han dado durante toda mi vida, no tengo palabras para expresarles mi gratitud y amor. Ustedes son el motor que impulsa mi vida y estaré en deuda con ustedes por esto y más. Gus y Monse, gracias por apoyarme, cada día que pasa los extraño más y más. A mis abuelitas y abuelitos, gracias por tanto cariño y por estar siempre al pendiente de mí. A mis tíos y tías, primos y primas, por ser parte de la mejor familia que pude haber tenido y por apoyarme en muchas y diferentes formas.